Efficient Integral Equation Solutions for Electromagnetic Modelling of Complex Printed Circuit Boards

by

K.J. Scott, M.A.

Department of Electronic and Electrical Engineering
University College London

A thesis submitted for the degree of
Doctor of Philosophy of the University of London

August 1990

ProQuest LLC.
789 East Eisenhower Parkway
P.O. Box 1346
Ann Arbor, MI 48106 – 1346

Abstract

Frequencies of 1 GHz or more and high packing densities are becoming common in much electronic equipment, such as mobile communication systems. In these situations, the effect of electromagnetic coupling in the interconnections can seriously degrade performance, and leads to many repeated attempts at a satisfactory design if not understood. This thesis describes several aspects of a method to analyse the complex three dimensional electromagnetic behaviour of printed circuit boards, which is used to understand and correct these problems. An approximate solution to Maxwell's equations in terms of a lumped element equivalent circuit model, using capacitors, inductors and resistors, is first developed.

The method employs Green's functions for the electric scalar and magnetic vector potentials. Series solutions for these in situations where there are up to three infinite, planar dielectric layers and two ground planes are developed. They are shown to have good convergence properties, and their use makes the method very efficient.

The concept of inductance is examined, and developed to model the inductance of the vias used to connect different layers together. For more general cases of modelling inductance and capacitance, basis functions for rectangular and triangular elements are examined, and efficient subroutines to calculate the potentials due to them are described.

The modelling of more general metal shapes than tracks is tackled by describing them in terms of polygons. A comprehensive method for processing these into a set of rectangular and triangular elements is developed, and possible enhancements to this discussed.

Results are presented to show that the methods described yield excellent agreement with experimental results, while being extremely efficient in terms of computer time and resources.

Acknowledgements

I would like to express my thanks to Bob Milsom at Philips Research Laboratories, whose advice and encouragement has helped me greatly throughout the course of this work. Many others within Philips have also offered help and advice. Thanks are due to Giles Clark, Bas Michielsen and other PRL researchers for many discussions on electromagnetic theory; Joe Morice for his help with mathematical problems; Julian McEntegart and colleagues from OTIB(UK), who designed and coded much of the FACET software; Steve Watkinson and John Batten of PRCS Cambridge, who designed and measured a number of test layouts, and were a useful source of advice; and Professor E. Wehrhahn of PKI Nuremburg, who provided the design and measured response of his microstrip filter.

I would also like to thank Brian Davies and Anibal Fernandez at University College London, for their interest and guidance. I am grateful to the College authorities of UCL for allowing me to take advantage of their expertise, and to form contacts with the College under the Public Research Institutions and Industrial Research Laboratories Scheme.

My thanks are due to Philips Research Laboratories, who have funded this research, and supported my connection with University College.

Last, but not least, my thanks to all those (too numerous to mention) who have made the last few years enjoyable, especially my long-suffering wife Fiona, who will doubtless be most relieved when all this is over!

Contents

List of Figures

List of Tables

Chapter 1
Introduction

1.1 Introduction

The design of circuits has long been something of an art. In the past, circuits were first designed on paper, with component values calculated by hand. When a satisfactory design had been reached, the circuit was implemented as a breadboard, with the components interconnected by wires (often a tangled mass of wires!). Unexpected behaviour of the circuit often occurred at this stage, so a certain amount of "try it and see" changing took place, until the circuit performed satisfactorily, and the design could be transferred to a printed circuit board (PCB). This transfer would also be done by hand, leaving considerable scope for more errors to creep in, necessitating one or more redesigns.

Nowadays, electronic design is usually carried out using computer aided design (CAD) packages, both for the design of the circuit and the layout of PCBs and integrated circuits (ICs). These packages include circuit simulation facilities, which predict the performance of the schematic circuit and thus replace the breadboard stage. However, the ability to simulate any unwanted effects introduced by the PCB layout is not usually found in such packages. Analogue and digital systems are now using higher frequencies (up to a few GHz), for example in radio communications or high performance computers, while the emphasis on miniaturisation means that components are becoming more and more tightly packed, thus increasing unwanted coupling. The problems on PCBs are more severe than in ICs at the present time, and so this work has concentrated on the former.

A PCB consists of a dielectric substrate with one or more layers of printed metallisation pattern. PCBs with internal layers of conductors are fabricated as several separate substrates, which are then bonded together. Discrete components, such as capacitors, resistors, transistors and ICs, are mounted on the substrate, and use the metallisation pattern to provide the necessary connections between themselves for the circuit to function. As a result of the trends discussed above, it is often not a good approximation to ignore the effects of the PCB metallisation pattern in the circuit simulation. Instead, the combination of metallisation

pattern and dielectric must be treated as a complex, multi-terminal component, which will in general have a very complex transfer characteristic. In addition, such a model should be integrated into the CAD system.

The work described in this thesis forms part of a project at Philips Research Laboratories, Redhill (PRL) to produce a computer package, known as FACET, which is able to predict unwanted effects caused by layout. Its use will help to prevent costly design mistakes, and to speed up the design process. Additionally, the availability of such a powerful tool enables design aspects to be explored much more thoroughly than has been possible before, which should lead to more robust designs. A summary of the main achievements made during this research appears as section 9.2 in the concluding chapter.

The next section describes the approaches that have been used for electromagnetic modelling, and the following section gives more information about the computer package developed.

1.2 Electromagnetic Modelling

Electromagnetic modelling has a long history, going back to Maxwell at least. Before the advent of computers, the problems that could be tackled were limited by the complexity of the calculations to simple, symmetrical geometries. An example of this is the capacitance of a thin rectangular plate, investigated by Maxwell [1893], and many others since, eg. [Reitan and Higgins, 1957]. The method they used was the method of subareas, essentially dividing up the plate into a number of smaller areas, imposing a constant charge density on each area and solving for these charge densities. This method has some resemblance to that used here, as will become apparent later.

With the advent of high speed computers, there has been an explosion of interest in the field, and a large associated literature has built up. There are many numerical approaches which have been used for electromagnetic modelling. All numerical methods convert the continuous field problem to a discrete equivalent. General numerical analysis techniques such as the finite difference method (FDM) [Zienkiewicz and Morgan, 1983, Chapter 1] or finite element method (FEM) [Zienkiewicz and Morgan, 1983, Chapters 3 and 4] have been widely used in many fields. Essentially, these work from the differential form of Maxwell's equations. The problem is discretised by creating a mesh of points covering the region of

the PCB and surrounding space. This mesh must be fine enough to represent the electric and magnetic fields with reasonable accuracy. The methods then relate the field values at each mesh point to those at adjacent mesh points to produce a set of simultaneous equations to be solved. Unfortunately, for a PCB of moderate size and complexity, a 3D mesh with many tens of millions of nodes is likely to be produced because of the rapid spatial variations in the metallisation pattern, and consequently the fields. This is much too large to be feasible, even with today's computers.

An alternative approach, which is rather more promising for this application, is to work from the integral form of Maxwell's equations, for instance using the electric field integral equation [Wang and Drane, 1982]. This method breaks up the pattern of conductors into patches, on each of which charge or current sources of unknown amplitude are defined. The unknown amplitudes can then be found by forcing the fields to obey the relevant boundary conditions. The number of simultaneous equations produced is equal to the number of unknown amplitude terms. Since unknown sources are only present on conducting surfaces, the number of simultaneous equations produced is many times smaller than for the FDM or FEM. The penalty is that the individual terms in the simultaneous equations are rather more complex to obtain, and the set of equations is non-sparse, since each source in principle affects every other source. However, the reduction in problem size is of much greater importance here, and such methods make the problem feasible.

In such integral methods, the continuous field problem is typically reduced to a set of discrete simultaneous equations using the method of moments [Harrington, 1968]. The simplest implementation of this is the wire grid model [Moore and Pizer, 1984], where the surfaces are modelled as a mesh of thin wires. This method has been used successfully for the modelling of radar cross-sections, because the far field pattern is fairly accurately predicted. The method is less well suited to modelling coupling and impedance on PCBs. This is because of the need for a fine grid of wires to model the rapid variations in current density within conductors at radio frequencies (RF), and the difficulty in obtaining the correct values for the near fields. PCB radiation and irradiation is another important subject, but this is not addressed here.

A better approach, and the one adopted in this work, is to use physically realistic charge and current distributions to model the actual distributions. The behaviour of charge and current in tracks and at conductor edges has been investigated [van Nie, 1977; Mittra and Lee, 1971; Kobayashi, 1985], so these results can be incorporated in the assumed distributions. With

this approach adopted, the next problem is to find the fields or potentials due to these charge and current distributions. Several authors have provided solutions for a variety of situations [Wei et al, 1984; Yamashita, 1968; Farrar and Adams, 1974; Crampagne et al, 1978].

The final problem with which this work is concerned is to produce a model suitable for analysis with a standard circuit analysis package. This enables the results of the simulation to be displayed in a way meaningful to an electronic designer. One way to do this, and the method adopted here, is to associate the elements into which the layout is subdivided with components in an equivalent circuit. This method was pioneered by Ruehli [1972, 1979, 1987] and co-workers at IBM, and has the great advantage of producing inductance and capacitance values for identifiable parts of the layout. Such components are meaningful to an electronic designer. Alternatives are possible, such as expressing the results as an admittance matrix, but these are generally harder to implement and to interpret.

Commercially available packages are rather limited in this field. Touchstone [EEsof], the most commonly used package for microstrip simulation, has good models for junctions and pairs of coupled tracks, but cannot handle multi-layer boards and non-parallel tracks. Greenfield2 [Quantic] will simulate multi-layer boards, but is also restricted to parallel tracks. The lack of a capability for non-parallel tracks is the most serious limitation for all but the most regular of digital PCBs, and the lack of a model for irregularly shaped metallisation areas is also a serious limitation for RF PCBs. There are several published papers addressing specific problems, such as crossing tracks [Koike et al, 1987], or corners and T junctions [Silvester and Benedek, 1973], but only the IBM work referred to above addresses more general problems. This is, however, aimed specifically at IC simulation, and is not available as a commercial package.

The problem of a general 3D analysis capability for PCBs is addressed in the FACET system, described in the next section. The work presented in this thesis has investigated several of the areas necessary for this system, and the results of this work have been incorporated into the system.

1.3 The FACET System

FACET, standing for Functional Analysis of Circuits using Electromagnetic Theory, is the name of the CAD package developed at PRL for PCB simulation. The package is described

in the paper by Milsom et al [1989], provided as additional material to this thesis. FACET has much greater functionality than other commercially available packages, such as those mentioned in the previous section. It can handle a large number of non-parallel conductors in a multi-layer configuration, with models for all the conductor features commonly found on PCBs. A brief description of the functionality of the package is given in the remainder of this section.

FACET treats the PCB layout information held in the CAD system used for design as follows. The description of the layout contains the following types of conductor features:

- Pads, or places where components can be attached. There are two types of these. Rectangular pads are for the attachment of surface mounted devices (SMDs), which are compact discrete components, such as resistors or capacitors, and surface mounted integrated circuits. Their use is becoming more and more widespread, principally because of their small size. Circular pads are for the attachment of the more traditional wire ended components, and consist of a circular area of metal (for the solder connection) together with a via, or hole through the PCB (for the component lead). Although the use of wire ended components is reducing, they will continue to be used for several specific applications, such as high power inductors, and for vias connecting different PCB conductor layers.
- Tracks form the majority of the conductors on a typical PCB. Their principal use is to provide connections between components. However, they can also be used to realise printed components such as inductors and resistors. This latter use is becoming increasingly common, and will become more so with the availability of accurate models for these components.
- Polygons are areas of metal which are many sided and irregular in shape. They are often used as partial ground planes, in an attempt to improve the isolation between different parts of the layout. The modelling of polygons is described in detail in Chapter 7.
- Vias are holes through the PCB substrate, usually metallised. They provide electrical interconnections between different conductor layers, and are also used for the attachment of wire ended components, as mentioned above.
- Ground planes may also be present, either on one surface of the PCB or remote from it (usually the equipment package). One ground plane parallel to the PCB surface, modelled as a perfect conductor, can be taken into account in the current version of FACET.

These features are processed into sets of elements as the first stage in the modelling process, an element being a portion of conductor area. FACET represents the electrical behaviour of the PCB by an equivalent circuit, consisting of capacitors, inductors and resistors. An appropriate topology for the equivalent circuit is automatically generated, and each component in this circuit is associated with a set of FACET elements. The degree of subdivision performed is controlled predominantly by the maximum frequency at which the model is required to be valid, a higher frequency requiring more subdivision to maintain the accuracy of the representation. The geometrical complexity also has an effect on the degree of subdivision.

FACET then solves for the values of the equivalent circuit components. The electromagnetic analysis required for this is the heart of FACET, and the methods used are described in Chapter 2. The output from this stage is an equivalent circuit, written in the input language of an appropriate circuit simulator, at present PHILPAC or PANACEA, which are in-house Philips packages, although SPICE could in principle also be used.

The equivalent circuit model of the PCB is then combined with details of the circuit components to be attached to the PCB to form the complete circuit representing the behaviour of the PCB and its components. Using PHILPAC or PANACEA, any simulation required can now be performed in the same way as for the schematic circuit without PCB effects. The results can be viewed in the same way as the designer would the results of a simulation of the components alone, to see the effect of layout on the circuit performance. There are additional post processing options in FACET to aid in diagnosing problems with a layout. The most important of these is a power flow plotting facility, which shows plots of the distribution of electromagnetic power at a particular frequency superimposed on the layout diagram.

The work described in this thesis addresses several of the areas within FACET, to which it has made a major contribution.

1.4 Outline of Thesis

Chapter 2 is a theoretical overview. It begins by taking Maxwell's equations and rewriting them in terms of an electric scalar potential and a magnetic vector potential. The equations for these can be solved by using appropriate Green's functions (effectively the potential due

to a point charge or current source), the derivation of which is described in Chapter 3. The process of forming an equivalent circuit model for the conductors on the PCB is then described, showing how the layout is subdivided into elements, which are then associated with equivalent circuit components. This association is shown to satisfy Maxwell's equations given certain approximations, which are justified by reference to the class of problems tackled.

Chapter 3 discusses the derivation of the set of Green's functions for the scalar and vector potentials required by the previous chapter for geometrical arrangements suitable for PCB modelling. The Green's functions are derived through a Fourier transform method and expressed as infinite series of charges or currents, which can be regarded as image sources. The association of these series with the classical method of images is shown explicitly for a few simple cases, then the convergence properties of the series are examined. The series are shown to converge well for most practical cases, which is an important factor in obtaining simulation results in a reasonable time.

Chapter 4 begins by demonstrating the equivalence of the standard definition of inductance in terms of magnetic flux through closed loops to a definition in terms of the vector potential, as used in Chapter 2. It then takes one of the simplest of the Green's functions derived in Chapter 3, that for the vector potential in free space, and uses it to illustrate how the computation of inductance is performed for a particular example. The example is the inductance of vias, which can be modelled as hollow, cylindrical conductors. Efficient expressions are developed for the self inductance of a via and the mutual inductance between vias.

Chapter 5 goes on to describe the computation of scalar and vector potentials for the elements used to model the charge and current distributions in polygons and tracks, and also the mutual inductance between the rectangular elements used in the polygon model. A large set of subroutines has been implemented to compute these potentials for a variety of types of elements and arrangements of PCB and ground planes. These are shown to be extremely efficient, which is vital since they are the major time consuming factor in the field analysis part of a typical simulation.

Chapter 6 details a variety of tests that have been performed on these subroutines, both on their own and within FACET. These tests include some checks on the internal consistency

of the models and some checks against known results, to show that the correct behaviour is indeed predicted.

Chapter 7 describes the development of a model for polygons, which are large or irregularly shaped areas of metal on a PCB, thus bringing together the work of the previous chapters. A detailed scheme for subdividing a polygon into elements is described. This produces the three sets of elements described in Chapter 2, and performs various other tasks needed for the production of the final equivalent circuit. Some inefficiencies in the present model are identified, principally the production of an excessive number of elements in some circumstances or the production of extremely large equivalent circuits. Several approaches to solve these problems are suggested, and a small test described to show the possibilities. The implementation of these methods will be the subject of future work.

Chapter 8 gives the results of comparisons between the methods described so far, when incorporated into FACET, and either experimental data or literature results. Excellent agreement is demonstrated, at frequencies of up to 10 GHz, providing confirmation of the accuracy of the approach taken in this thesis and in FACET. Some timing information is also given to show that the methods are also extremely efficient. The main problem with speed (when there is one) is identified as being due to circuit simulation rather than the 3D field analysis. The methods suggested in Chapter 7 could help reduce this problem considerably.

Chapter 9 gives a summary of the work described in this thesis and discusses its usefulness. Several ideas for future research, to enhance the efficiency of the models and for extensions into other areas, are presented.

1.4.1 Notes on Computations

All of the code referred to in this thesis has been written in FORTRAN 77, using double precision (8 byte) numbers where appropriate, and compiled using Release 4.1 of IBM's VS FORTRAN compiler. The compiler options OPT(2), which performs a considerable amount of optimisation, and NOSDUMP, which suppresses some internally generated code, were used. The code was run on an IBM 4381/14 computer running the VM/CMS operating system, which can perform approximately 3 million floating point operations per second. References to the time taken for simulations refer to the CPU time used on this system.

Chapter 2

Theoretical Overview

2.1 Introduction

This chapter provides the theoretical basis for the models developed. The analysis begins with Maxwell's equations, which are rewritten in terms of scalar and vector potentials. The solutions for these potentials are by means of Green's functions, and this forms the subject of Chapter 3. The basic method for subdividing the PCB layout into sets of elements which represent components in the equivalent circuit model is described. This is done initially for polygon areas, and then simplified to cover the model for tracks.

A detailed analysis demonstrates that the equivalent circuit model for the layout is a valid solution to Maxwell's equations, given the approximations introduced. The principal approximations are the forms of charge and current distribution imposed in the layout, and the assumption that the dominant coupling effects take place at spatial separations of rather less than a wavelength. Both of these approximations are well founded, and their use is borne out by the accuracy of the results obtained.

2.2 Scalar and Vector Potentials

The starting point for the analysis is Maxwell's equations [Ramo et al, 1965, pp. 234-236]

$$\begin{aligned} \nabla \times \mathbf{E} &= -\frac{\partial \mathbf{B}}{\partial t} && (a) \\ \nabla \times \mathbf{H} &= \mathbf{J} + \frac{\partial \mathbf{D}}{\partial t} && (b) \\ \nabla . \mathbf{D} &= \rho && (c) \\ \nabla . \mathbf{B} &= 0 && (d) \end{aligned} \qquad (2.1)$$

where **E** and **H** are the electric and magnetic field vectors, **D** and **B** are the electric and magnetic flux density vectors, ρ and **J** are charge and conduction current densities, and t is time.

The metals and dielectric substrates used in printed circuit boards can be considered to be isotropic, so the following relations between vectors can be applied

$$\begin{aligned} \mathbf{B} &= \mu\mathbf{H} \\ \mathbf{D} &= \varepsilon\mathbf{E} \\ \mathbf{J} &= \sigma\mathbf{E} \end{aligned} \tag{2.2}$$

where μ is the permeability, ε is the permittivity and σ is the conductivity at any given point.

Taking the divergence of equation 2.1 (b) and combining it with equation 2.1 (c) yields the current continuity equation, which is a consequence of the conservation of charge

$$\nabla.\mathbf{J} = -\frac{\partial \rho}{\partial t} \tag{2.3}$$

The vectors **E** and **B** can be expressed in terms of an electric scalar potential ϕ and a magnetic vector potential **A** as [Ramo et al, 1965, pp. 259-261]

$$\begin{aligned} \mathbf{E} &= -\nabla\phi - \frac{\partial \mathbf{A}}{\partial t} \\ \mathbf{B} &= \nabla \times \mathbf{A} \end{aligned} \tag{2.4}$$

The divergence of the vector potential is arbitrary [Ramo et al, 1965, pp. 259-261]. Here it is convenient to impose the Lorentz condition, which sets

$$\nabla.\mathbf{A} = -\mu\varepsilon\frac{\partial \phi}{\partial t} \tag{2.5}$$

If equations 2.4 and 2.5 are substituted into Maxwell's equations 2.1, the following pair of Helmholtz equations for the potentials result:

$$\begin{aligned} \nabla^2\phi - \mu\varepsilon\frac{\partial^2\phi}{\partial t^2} &= -\frac{\rho}{\varepsilon} \\ \nabla^2\mathbf{A} - \mu\varepsilon\frac{\partial^2\mathbf{A}}{\partial t^2} &= -\mu\mathbf{J} \end{aligned} \tag{2.6}$$

The final step is to ignore the time dependent terms in equation 2.6. This amounts to assuming that the dominant interaction effects take place at spatial separations of rather less than a wavelength. In practice this seems to be a very good approximation for circuit boards. Note that time dependence and coupling between electric and magnetic fields are still retained in the solution through equations 2.3 and 2.4. The resulting expressions for the potentials are the Poisson equations

$$\begin{aligned} \nabla^2\phi &= -\frac{\rho}{\varepsilon} \\ \nabla^2\mathbf{A} &= -\mu\mathbf{J} \end{aligned} \tag{2.7}$$

Each of these equations is then solved to find the potential for a given distribution of charge or current density, as described in Chapters 3 and 5. This yields the integral representations

$$\begin{aligned} \phi(\mathbf{r}) &= \iiint G_\phi(\mathbf{r}\,|\,\mathbf{r}')\,\rho(\mathbf{r}')\,d^3\mathbf{r}' \\ \mathbf{A}(\mathbf{r}) &= \iiint G_\mathbf{A}(\mathbf{r}\,|\,\mathbf{r}')\,\mathbf{J}(\mathbf{r}')\,d^3\mathbf{r}' \end{aligned} \tag{2.8}$$

where the integrals are over a volume which includes all the sources under consideration, $\mathbf{r}$ is the object point, where the potential is required, and $\mathbf{r}'$ is the source point. The Green's functions G_ϕ and $G_\mathbf{A}$ can be considered to be the potential due to a unit point charge and a unit point current respectively. In free space they assume the particularly simple forms

$$\begin{aligned} G_\phi(\mathbf{r}\,|\,\mathbf{r}') &= \frac{1}{4\pi\varepsilon_0|\mathbf{r}-\mathbf{r}'|} \\ G_\mathbf{A}(\mathbf{r}\,|\,\mathbf{r}') &= \frac{\mu_0\mathbf{i}}{4\pi|\mathbf{r}-\mathbf{r}'|} \end{aligned} \tag{2.9}$$

where $\mathbf{i}$ is a unit vector directed parallel to the point current. In more general situations, with arbitrary arrangements of dielectric material and grounded metal bodies, the Green's functions are rather more complex.

Within FACET, a restricted set of configurations is allowed, a generalised view of which is shown in Figure 1. The substrate of the printed circuit board is modelled as an infinite parallel-sided slab of dielectric of thickness c. There is also an infinite, ideal ground plane parallel to the PCB surface and separated from the rear surface of the PCB by a distance d_1. This distance is allowed to take any value between zero and infinity. Most practical

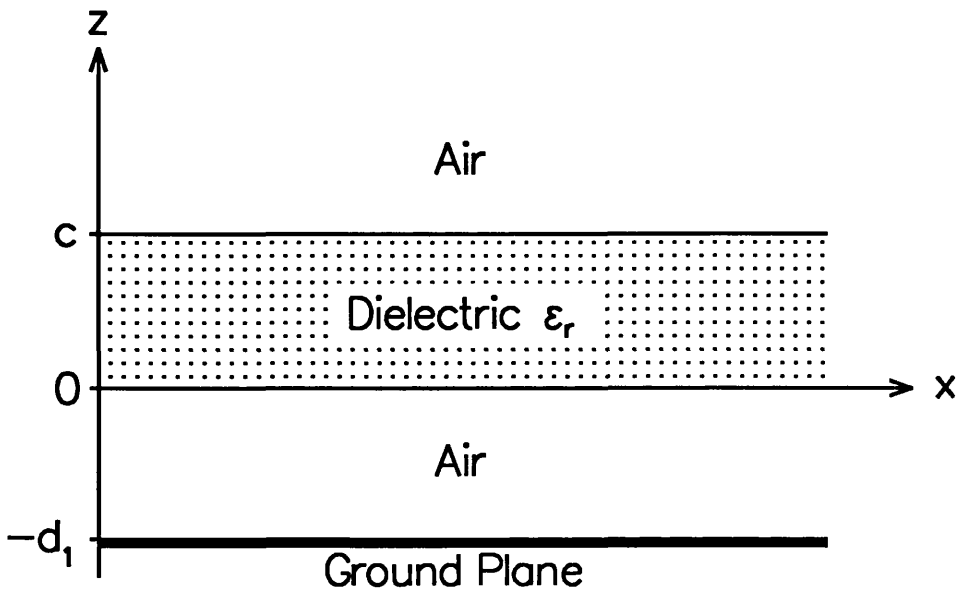

Figure 1. Vertical section through PCB structure

situations can be modelled by this arrangement. Green's functions for these cases are derived in Chapter 3 as infinite series of terms similar to those in equation 2.9.

2.3 Equivalent Circuit Model

The aim of this analysis is to produce an equivalent circuit model for the conductors on the PCB, in terms of a set of inductors, capacitors and resistors. The resistors represent both dielectric and resistive losses. The flows of current in the inductors and charge in the capacitors give an approximation to the real charge and current distributions.

There are two types of equivalent circuit model used. The first is for large or irregularly shaped areas of conductor, which are modelled as polygons. The second is for tracks, which are thin sections of conductor where the current flow can be considered to be purely longitudinal, leading to a simplified model. There is no restriction on track orientation. These models are discussed in turn.

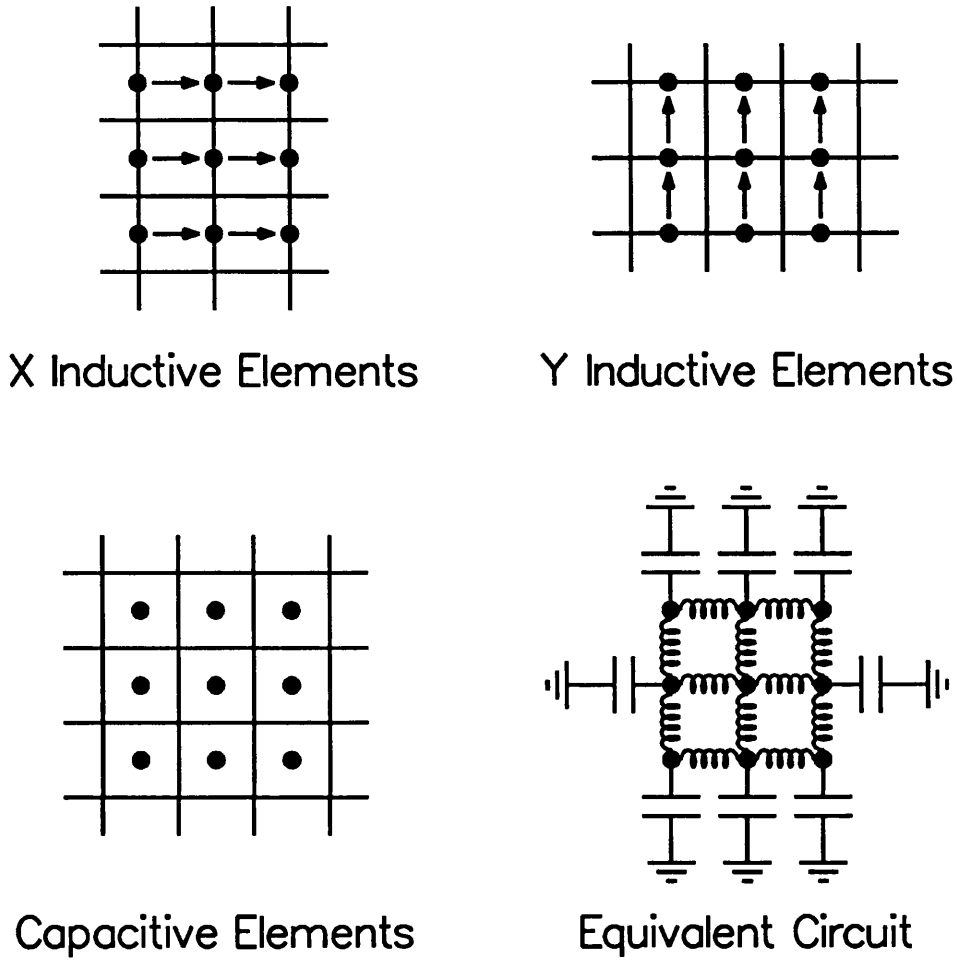

Figure 2. Elements and equivalent circuit for the interior of a polygon

2.3.1 Polygons

The formation of an equivalent circuit begins with the creation of a rectangular grid within each polygon, discussed in detail in Chapter 7. This creates rows of physical nodes, at the intersections of grid lines, with each row parallel to either the global X or global Y axis. These nodes are identified with circuit nodes, to which the equivalent circuit components forming the model of the polygon are attached. The individual equivalent circuit components are represented by rectangular and triangular elements (or patches). These are formed by the subdivision, and basis functions which model the charge and current distributions in the polygon are defined on each element [Ruehli, 1979].

Figure 2 shows part of the interior of a polygon, with the subdivision into elements. The circles represent the nodes, and are in the same position in all four diagrams. The location and spacing of these nodes is determined by the geometry of the polygon and the maximum frequency for which the model is required. Chapter 7 describes how they are produced, and describes the more complex arrangements necessary at the polygon edges. For this example the grid of nodes is regular, but this need not be the case.

Current flowing in the polygon is considered by splitting it into two orthogonal components, parallel to the global X and Y axes. Two sets of elements are generated, one for each direction of current flow, called the X and Y inductive elements respectively. The X inductive elements have basis functions which model the flow of current from one node to the next parallel to the global X axis. Each element therefore extends from one node to the next in this direction, and halfway to the next row of nodes at larger and smaller Y co-ordinates. These elements are shown as the first picture in Figure 2, with the arrows indicating the direction of current flow. They are represented as self inductances in the equivalent circuit model, with series resistors to represent the resistive loss. Inductive couplings between elements are represented by mutual inductances.

The Y inductive elements are similar, this time modelling the current flow parallel to the global Y axis. These elements are shown as the second picture in Figure 2, with the arrows indicating the direction of current flow. They are also represented as self inductances in the equivalent circuit model.

The distribution of charge can be modelled by just one set of elements as it is a scalar quantity. Each element has basis functions to model the charge density distribution around a node. These elements are called the capacitive elements, and are shown in the third picture in Figure 2. Each element can be considered as representing one plate of a capacitor, and the ground plane is also represented as a capacitor plate. In the equivalent circuit model, capacitors are formed by taking all pairs of capacitor plates in turn, with a resistor placed in parallel to model the dielectric loss.

The final picture in Figure 2 shows a simplified version of the equivalent circuit model generated for this section of the polygon. Only the self inductances and the capacitances to ground from the edge nodes are shown, to avoid making the diagram too cluttered. The full model has the resistors described above, capacitors between each pair of nodes, and mutual inductances between each pair of parallel inductors - the mutual inductance between

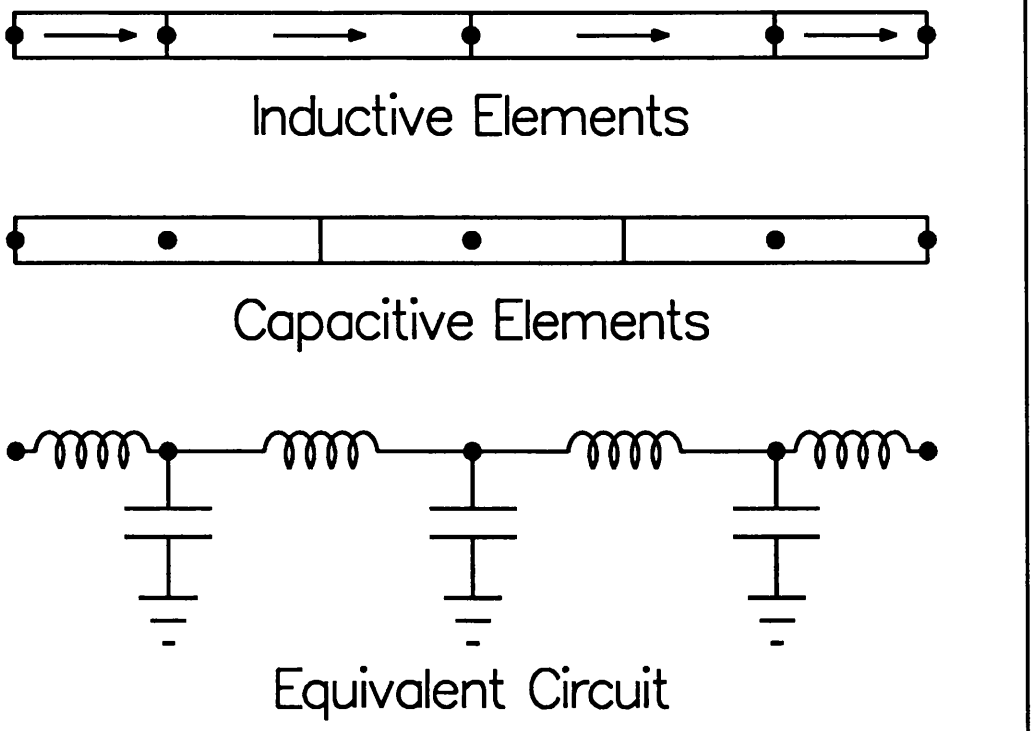

Figure 3. Elements and equivalent circuit for a track section

perpendicular inductors is zero, as orthogonal currents do not interact inductively with one another.

The model developed to date treats each capacitive element as having a constant charge density on it, and each inductive element as having a constant current density in it. The analysis that follows allows for more general charge and current distributions, which may be implemented in future work to improve the accuracy and efficiency of the model, if necessary.

2.3.2 Tracks

The model for tracks is somewhat simpler, as the flow of current is assumed to be purely longitudinal. As for polygons, a set of nodes is defined along the track with a spacing determined by the maximum frequency for which the model is required. Figure 3 shows the arrangement of nodes and elements for a short section of track. Only one set of elements,

the inductive elements, is required to model the current flow in the track, with each element modelling the current flowing between two nodes, in the same way as in a polygon. These are shown as the first picture in Figure 3. The two inductive elements at the end of the track section are half the length of the other elements. The second set of elements, the capacitive elements, model the charge density distribution around a node, again in the same way as for a polygon. These are shown as the second picture in Figure 3.

The equivalent circuit model is just a one dimensional version of that developed for polygons. A simplified version of this, showing only the self inductances and capacitances to ground, is shown as the third picture in Figure 3.

The following treatment is developed for polygons, but the results are readily specialised to cover tracks as well.

2.4 Capacitance

Consider first the i^{th} capacitive element. This has N_i charge basis functions ψ_{in} defined within it, giving a total charge density distribution ρ_i

$$\rho_i(\mathbf{r}) = \sum_{n=1}^{N_i} Q_{in}\, \psi_{in}(\mathbf{r})\, e^{j\omega t} \tag{2.10}$$

where Q_{in} are the amplitudes of the basis functions. Harmonic time dependence, of angular frequency ω, has been assumed, and the common factor $e^{j\omega t}$ will be dropped from subsequent equations. More complex time dependence could be taken into account using Fourier analysis, superposing the solutions for several different frequencies. The total charge in the element, Q_i, is found by integrating the charge density of equation 2.10 over the volume of the i^{th} capacitive element, giving

$$Q_i = \sum_{n=1}^{N_i} Q_{in} \iiint_i \psi_{in}(\mathbf{r})\, d^3\mathbf{r} \tag{2.11}$$

where the integrals are over the volume of the i^{th} element.

A solution is required for the charge density distribution necessary to produce a given voltage distribution over the layout. This cannot be done exactly with a finite set of basis functions. An approximate solution is found using the point collocation method. This samples the value of potential at N_i points in each element (the same number of points as the number of basis functions). The value of the potential at each of these points is the sum of the potentials due to every basis function. The n^{th} collocation point in the i^{th} capacitive element is located at $\mathbf{r}_{in}$ The potential here is ϕ_{in}, given by the summation

$$\phi_{in} = \sum_{j=1}^{N_{cel}} \sum_{n=1}^{N_j} Q_{jn} \int\int\int_j G_\phi(\mathbf{r}_{in} | \mathbf{r}') \, \psi_{in}(\mathbf{r}') \, d^3\mathbf{r}' \qquad (2.12)$$

where the total number of capacitive elements is N_{cel}, and the integral is over the volume of the j^{th} capacitive element. For a given set of ϕ_{in}, the above equation yields a set of simultaneous equations which can be solved for the coefficients of the basis functions Q_{jn} for all values of j.

To find the matrix of capacitances between elements, appropriate sets of ϕ_{in} are used. For the i^{th} column of the capacitance matrix, the voltage at all collocation points within the i^{th} element (the source element) is set to to 1V, and the voltage at all other collocation points is set to 0V. When the simultaneous equations have been solved for the coefficients of the basis functions, the capacitance between the i^{th} and j^{th} capacitive elements, C_{ij}, is simply minus the charge on the j^{th} capacitive element,

$$C_{ij} = -Q_j \qquad \phi_i = 1 \ , \ i \neq j \qquad (2.13)$$

where Q_j is found using equation 2.11.

This above procedure is then repeated with each element in turn acting as the source element. The capacitance to ground of the i^{th} capacitive element, C_{ii}, is the charge on this element when the whole polygon is at a uniform potential of 1V. It is therefore found as the sum of the charges on the i^{th} capacitive element, accumulated over the set of N_{cel} solutions.

More complex voltage distributions could be used to model the actual distribution more accurately. The only condition for a set of capacitances to be produced is that the superposition of all the voltage distributions in the N_{cel} solutions is a uniform 1V over the

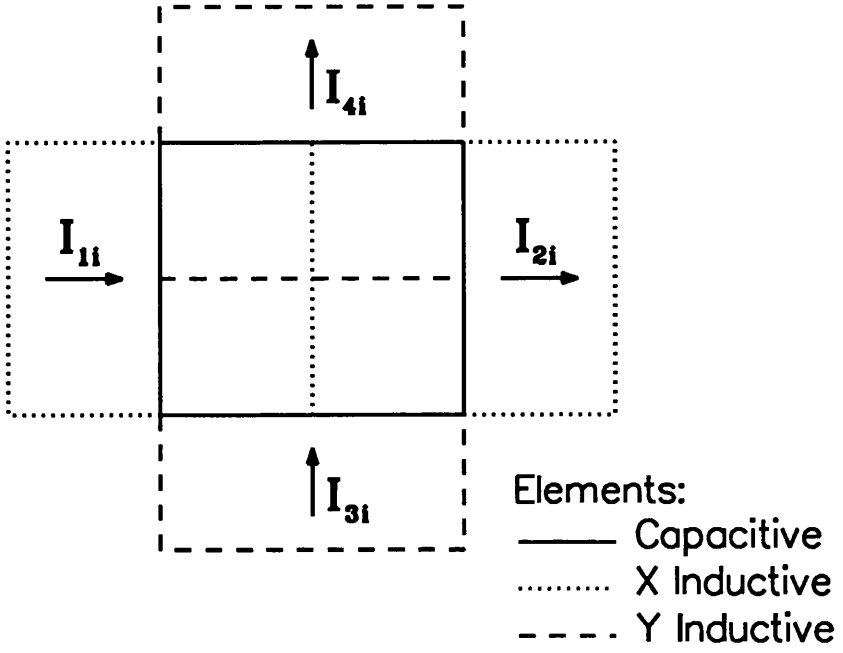

Figure 4. Inductive elements overlapping a capacitive element

whole structure. Other possibilities have been examined for tracks, where the conclusion was that although improvements are possible, the effects are of second order importance.

The set of capacitances has been produced from purely electrostatic considerations, using a piecewise constant approximation to the charge distribution. For a circuit solution, the current continuity condition of equation 2.3 must also be satisfied. The solution method above can only do this in an average sense over the volume of each capacitive element, because of the approximations used. Integrating equation 2.3 for the conservation of charge over the volume of the i^{th} capacitive element, and substituting for the total charge and potential in the element using equations 2.11 and 2.12 gives

$$\begin{aligned} \iiint_i \nabla.\mathbf{J}(\mathbf{r}')\, d^3\mathbf{r}' &= -\iiint_i \frac{\partial}{\partial t} \sum_{n=1}^{N_i} Q_{in}\, \psi_{in}(\mathbf{r}')\, d^3\mathbf{r}' \\ &= -\frac{\partial Q_i}{\partial t} \\ &= -\sum_j C_{ij} \frac{\partial \phi_j}{\partial t} \end{aligned} \qquad (2.14)$$

The left hand side can be transformed to a surface integral using the divergence theorem, and evaluates to the net current leaving the volume of the i^{th} capacitive element.

Figure 4 shows the arrangement of the four inductive elements overlapping the i^{th} capacitive element in a polygon. The four currents defined in the figure are the total current in each of the inductive elements. With this definition equation 2.14 becomes,

$$I_{2i} - I_{1i} + I_{4i} - I_{3i} = -\sum_j C_{ij} \frac{\partial \phi_j}{\partial t} \tag{2.15}$$

The set of equations for all i is just Kirchhoff's first law, for the continuity of current, applied to the equivalent circuit for the polygon. This means that the model developed is consistent with both the electromagnetic laws of Maxwell's equations and Kirchhoff's first law from circuit theory, and so the representation is valid providing Kirchhoff's second law is also obeyed. This will be demonstrated shortly.

At the edges of the polygon the arrangement of elements becomes more complex: there may be fewer inductive elements overlapping a particular capacitive element, and the capacitive element itself may be triangular in shape. Similarly, tracks only have two inductive elements overlapping each capacitive element. However, if the left hand side of equation 2.15 is considered as the total current leaving the i^{th} capacitive element, then the above analysis is still valid.

2.4.1 Dielectric Loss

Dielectric loss is accounted for by placing a resistor of value $1/(\omega C \tan \delta)$ in parallel with each capacitor C , where $\tan \delta$ is the loss tangent of the PCB material, and $\omega = 2\pi f$ is the angular frequency. This is not rigorous, since there are fields outside the PCB material, and the loss is therefore slightly over estimated. However, the computational costs of a full analysis is much greater, and the difference in accuracy is very small. This model requires the circuit simulator to permit frequency dependent resistors, which both PHILPAC and PANACEA do for AC analysis. Where these are not allowed, a resistor value computed at the expected dominant frequency would have to be selected, with a consequent loss in accuracy. Note that this approximation is required for all transient analysis, even in PHILPAC and PANACEA.

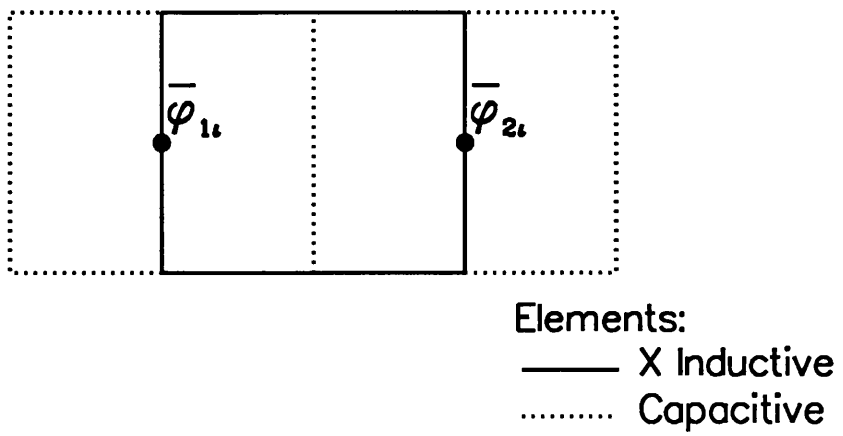

Figure 5. Capacitive elements overlapping an X inductive element

2.5 Inductance

The previous section examined the model for charge, leading to equations for the equivalent circuit capacitances. This section examines the model for current, and will lead to equations for the equivalent circuit inductances. Equation 2.2, relating electric field and current, and equation 2.4, relating electric field and potentials, can be combined to yield

$$\frac{\mathbf{J}}{\sigma} + \nabla\phi + \frac{\partial \mathbf{A}}{\partial t} = 0 \qquad (2.16)$$

This equation simply shows that the current density at any point is proportional to the electric field there.

In isotropic materials the vector potential A is always parallel to the current producing it, as illustrated by equation 2.6 which defines the vector potential. Since the current flow in the polygon has been partitioned into two orthogonal sets, only one of these need be considered. That considered is the set of X inductive elements. Figure 5 shows the arrangement of the i^{th} X inductive element and the two capacitive elements which overlap it. Writing the x component of equation 2.16 as

$$\frac{J_x}{\sigma} + \frac{\partial\phi}{\partial x} + \frac{\partial A_x}{\partial t} = 0 \qquad (2.17)$$

and taking the line integral of this equation along the length of the element (ie. parallel to the x axis) results in

$$\frac{1}{\sigma}\int_{l_i} J_x\,dx + \phi_{2i} - \phi_{1i} + \frac{\partial}{\partial t}\int_{l_i} A_x\,dx = 0 \qquad (2.18)$$

where ϕ_{2i} and ϕ_{1i} are the potentials at the two ends of the line along the i^{th} inductive element, which is of length l_i . Let the width of the element be w, and assume for the moment that the variation of fields in the thickness of the element can be ignored. Averaging equation 2.18 across the width of the element, taken as the y direction, gives

$$\frac{1}{\sigma w}\int\int J_x\,dx\,dy + \left[\overline{\phi_{2i}} - \overline{\phi_{1i}}\right] + \frac{\partial}{\partial t}\left[\frac{1}{w}\int\int A_x\,dx\,dy\right] = 0 \qquad (2.19)$$

This can be viewed as a form of Ohm's law, relating the mean current density in the element to the applied voltage across the element and the voltage across the element due to current flow elsewhere. The three terms in this equation are now examined in turn.

The first term represents the potential drop across the internal or surface impedance of the element. Let this impedance be Z_i in the i^{th} element, and let the magnitude of the current flowing in the i^{th} element be I_i. Then,

$$Z_i = \frac{1}{\sigma w l_i}\int\int J_x\,dx\,dy \qquad (2.20)$$

This is considered in detail in Appendix A, where it is shown that the internal impedance function Z_i is complex and varies with frequency. The real part represents conductor loss and is incorporated in the model as a resistor in series with the inductor of the appropriate element. The imaginary part is ωL_{int}, where L_{int} is the internal inductance, due to the presence of magnetic flux within the conductor itself, and is frequency dependent. This is incorporated in the model by adding it to the frequency independent external inductance derived below, which is due to magnetic flux outside the conductor. The effect of a finite conductor thickness was also examined, and included within the internal impedance function Z_i.

The second term is just the mean voltage difference between the two ends of the element, as shown in Figure 5.

Turning to the third term, it is shown in Chapter 4 that the mutual inductance between two elements, L_{ij}, can be written as

$$L_{ij} = \frac{1}{a_i} \int\int_{a_i} \int_{l_i} \mathbf{A}_j \cdot \mathbf{dl}_i \; dy \, dz \tag{2.21}$$

where a_i is the cross sectional area of the i^{th} element (assumed constant); l_i is the length of the i^{th} element; $\mathbf{A}_j$ is the vector potential due to a current of 1 amp flowing in the j^{th} element; $\mathbf{dl}_i$ is directed parallel to the direction of current flow in the i^{th} element (along its length); and y and z are respectively the width and thickness directions in this element. If the current flow directions in the two elements are at an angle θ to one another, the width of the i^{th} element is w_i, and its thickness is negligible, equation 2.21 can be rewritten as

$$L_{ij} = \frac{\cos\theta}{w_i} \int_{w_i} \int_{l_i} |\mathbf{A}_j| \; dx \, dy \tag{2.22}$$

where the integral is over the area of the i^{th} element, and x is the length direction in the i^{th} element. This is the form in which the inductance is calculated.

Equation 2.19 can therefore be written as,

$$I_i Z_i + \overline{\phi_{2i}} - \overline{\phi_{1i}} + \sum_{j=1}^{N_{xel}} L_{ij} \frac{\partial I_j}{\partial t} = 0 \tag{2.23}$$

where N_{xel} is the total number of X inductive elements. The set of all such equations for X and Y inductive elements is just Kirchhoff's second law, for the voltage drop around a loop, applied to the equivalent circuit for the polygon. In conjunction with equation 2.15, which was Kirchhoff's first law for the polygon, this demonstrates that the electromagnetic and circuit representations are equivalent, and so the equivalent circuit is a valid model.

At the edges of the polygon the arrangement of elements can be more complex, but the above analysis remains valid for rectangular elements. In a track, two capacitive elements overlap each inductive element in exactly the same way as shown in Figure 5, so the above analysis is also valid for tracks.

Some attention needs to be paid to differences with triangular elements, which can be created at the edges of the polygon. Figure 6 shows a triangular element, of length l and width w.

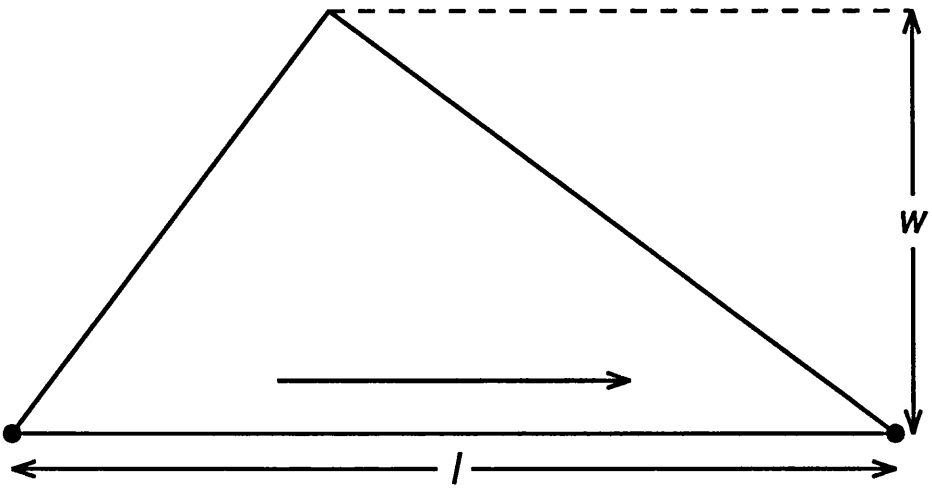

Figure 6. Triangular element for inductance: current flow direction shown by arrow, nodes shown by filled circles

These elements are right angled triangles, with the current flow direction assumed parallel to the hypotenuse and a circuit node placed conceptually at each end of the hypotenuse, between which the equivalent circuit self inductance is connected. For the purposes of analysis, the current density in such elements is defined to be uniform, with a peak current of 1 amp at the widest point (and hence a mean current of 0.5 amp). When equation 2.18, relating current density and applied voltage, is averaged over the width of the element to obtain equation 2.19, the third term in equation 2.19 will contain a factor of $1/(w/2)$ rather than $1/w$. Equation 2.22 for the inductance between elements becomes,

$$L_{ij} = \frac{2\cos\theta}{w} \int\int |\mathbf{A}_j| \, dx\, dy \qquad (2.24)$$

where the integral is over the area of the triangle. With this result, equation 2.23 is valid for both rectangular and triangular elements.

2.6 Conclusions

The treatment in this chapter began with Maxwell's equations, which were rewritten in terms of scalar and vector potentials. The basic concept of the subdivision of a layout into elements which are modelled by components in an equivalent circuit was described, and it

was shown that this model led to Kirchhoff's first and second laws (equations 2.15 and 2.23), and is therefore a valid representation of the electrical behaviour of the layout. A detailed description of how polygonal areas are subdivided into elements is given in Chapter 7.

The development of this model involved two main approximations:

1. The dominant interactions are assumed to take place at spatial separations of rather less than a wavelength, which is nearly always the case for PCBs.

2. The actual charge and current distributions in the layout are modelled by a finite set of basis functions. In a polygon, the sets of elements and basis functions chosen give a piecewise constant approximation to the actual charge and current distributions. In tracks, the distributions are piecewise constant along the length of the track, while the distribution across the width produces a flat scalar or vector potential distribution in that direction.

Further confirmation of the validity of these approximations is given by comparing results from simulations with experimental data or previously published work. Chapter 8 does this for several examples, and the excellent accuracy obtained there shows that the approximations are indeed reasonable.

The next chapter derives a set of Green's functions for the scalar and vector potentials, required in the computation of the values of the equivalent circuit components. These are derived for a set of configurations which is able to model most PCB structures.

Chapter 3
Green's Functions for Scalar and Vector Potentials

3.1 Introduction

Scalar and vector potential Green's functions were briefly introduced in Chapter 2 as the potential due to a unit point charge or current respectively. For the simplest possible case of a point source in free space, the solution to this problem is well known [Bleaney and Bleaney, 1976, p.4], and was given as equation 2.9. This chapter is concerned with the much more complicated configuration shown in Figure 7, consisting of three layers of isotropic dielectric, bounded by two perfectly conducting ground planes. The three layers are of dielectric constant ε_1 for $-d_1 \le z \le 0$, ε_2 for $0 \le z \le c$ and ε_3 for $c \le z \le c + d_2$. All three layers have the same relative permeability, assumed here to be 1.0. The dielectric layers and the ground planes are assumed to be of infinite extent in the x and y directions, with boundaries between them parallel to the xy plane.

This structure can be used to model a PCB, with layer 2 representing the substrate, layers 1 and 3 representing the air gaps above and below the PCB, and the ground planes representing two surfaces of a metal package. The analysis is, however, performed for the general case. Simpler cases of the results are then generated by:

- Placing one or both ground planes at infinity
- Setting two or three of the dielectric constants equal to one another
- Placing the point source at $z = 0$ or $z = c$, and determining the potential at $z = 0$ or $z = c$

Published results have only treated the complete structure shown in Figure 7 in two dimensions in the spectral domain [Yamashita, 1968], or much simpler cases in the spatial domain (three dielectric layers with no ground planes [Silvester, 1968], or two dielectric layers with one ground plane [Chow, 1980]). This chapter covers all these cases with one general formulation, which gives results for three dimensions in the spatial domain.

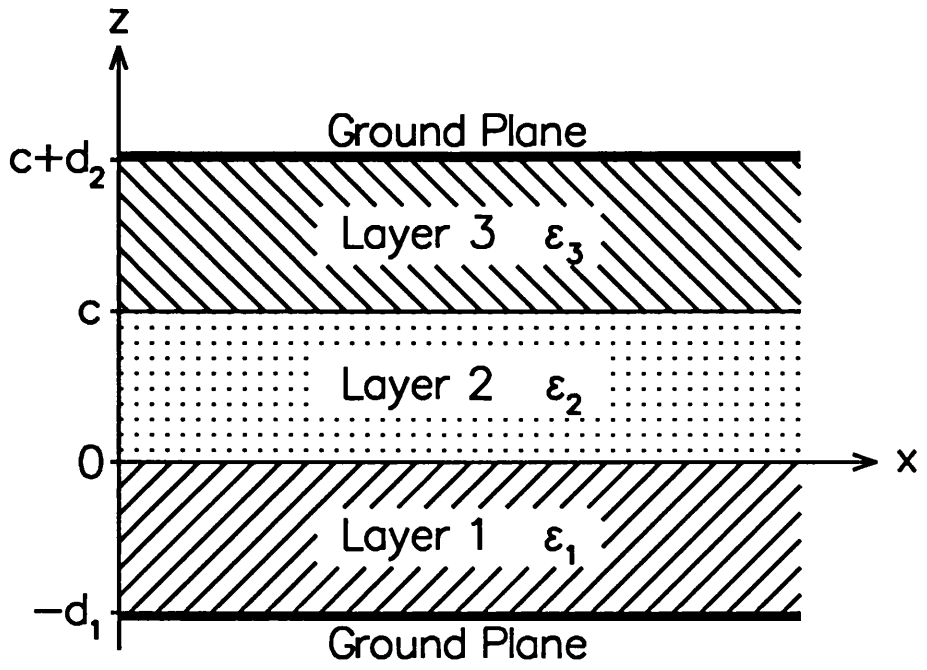

Figure 7. Structure to be analysed: section through the x-z plane

Section 3.2 gives a general description of the approach used. This approach is then used in section 3.3 to derive the scalar potential for all locations of the source charge and of the object point (ie. the point where the potential is required). Sections 3.4, 3.5 and 3.6 specialise these general results to simpler cases, by the methods listed above. Section 3.7 derives similar results for the vector potential. These are much simpler, because the vector potential is not affected by discontinuities in the dielectric constant. The results in these sections are enclosed in boxes for ease of identification, since there are inevitably a great many cases to be considered.

The results produced can be interpreted as the potentials due to series of image charges, as in the classical method of images [Bleaney and Bleaney, 1976, pp.48-56]. Section 3.8 shows this correspondence exactly for some of the simpler cases, and describes the remaining cases qualitatively.

The solutions for the potential are obtained in the form of infinite series. For practical purposes it is therefore necessary to know how quickly the series converge. This question is examined in section 3.9 for various representative cases.

Some of the results described here have been used in FACET, where they have proved their usefulness and accuracy. There, they are spatially convolved with known basis functions for the charge and current distributions over track and polygon elements on a PCB to give the potentials due to these elements. This process is described in Chapter 5. The form of solution obtained here enables this convolution to be performed very efficiently.

3.2 General Approach

3.2.1 Scalar Potential

The scalar potential Green's function can be written as,

$$G_\phi(x\,|\,x_0, y\,|\,y_0, z\,|\,z_0) \tag{3.1}$$

This represents the scalar potential at the point (x, y, z) due to a point charge placed at (x_0, y_0, z_0). In this chapter, the solution for the potential $\phi(x, y, z)$ due to a unit point charge placed at $(0, 0, z_0)$ is found. No loss of generality results from this simplification. The Green's function is related to this by,

$$G_\phi(x\,|\,x_0, y\,|\,y_0, z\,|\,z_0) \;=\; \phi(x-x_0, y-y_0, z) \tag{3.2}$$

At zero frequency, the (electrostatic) scalar potential required is the solution of the Poisson equation,

$$\nabla^2\phi = -\frac{1}{\varepsilon}\,\delta(x)\,\delta(y)\,\delta(z-z_0) \tag{3.3}$$

This is also valid approximately for non-zero frequencies when the spatial dimensions involved are rather less than the wavelength of signals at the maximum frequency of interest, as discussed in Chapter 2. To solve for the potential, apply the two dimensional Fourier transform,

$$\tilde{f}(k_x, k_y) \;=\; \frac{1}{2\pi}\int_{-\infty}^{\infty}\int_{-\infty}^{\infty} f(x,y)\; e^{-jk_x x} e^{-jk_y y}\; dx\; dy \tag{3.4}$$

to equation 3.3. Also, set

$$k^2 = k_x^2 + k_y^2 \tag{3.5}$$

since the transformed equation only contains k_x and k_y as $k_x^2 + k_y^2$. The transformed equation is now an ordinary differential equation in the spectral domain,

$$\frac{d^2}{dz^2}\tilde{\phi}(k,z) - k^2\tilde{\phi}(k,z) = -\frac{1}{2\pi\varepsilon}\delta(z-z_0) \tag{3.6}$$

The term on the right hand side of equation 3.6 is only non-zero in the plane $z = z_0$. This plane is parallel to the other boundaries in the geometry, so by treating it as another boundary a problem with N dielectric layers can be modelled in terms of $N+1$ regions. The problem therefore reduces to a set of $N+1$ Laplace's equations,

$$\frac{d^2}{dz^2}\tilde{\phi}_i(k,z) - k^2\tilde{\phi}_i(k,z) = 0 \qquad (i = 1...N+1) \tag{3.7}$$

with appropriate boundary conditions enforced at all the boundaries. The general solution of this set of equations is,

$$\tilde{\phi}_i(k,z) = A_i^+ e^{kz} + A_i^- e^{-kz} \tag{3.8}$$

where A_i^+ and A_i^- are initially unknown functions of k. In the solution for the problem with three dielectric layers, there will therefore be four separate regions in which to solve equation 3.7, giving eight unknown functions of k to be determined. Section 3.3 details the solution of this problem.

3.2.2 Vector Potential

The vector potential Green's function can be written in a similar way to equation 3.1 as

$$G_A(x|x_0, y|y_0, z|z_0) \tag{3.9}$$

This represents the vector potential at the point (x, y, z) due to a point current placed at (x_0, y_0, z_0). Just as for the scalar potential, the solution is found for the potential $A(x,y,z)$ due to a unit point current source placed at $(0,0, z_0)$. The Green's function is then

$$G_A(x|x_0, y|y_0, z|z_0) = A(x-x_0, y-y_0, z) \tag{3.10}$$

At zero frequency, the (magnetostatic) vector potential required is the solution of the Poisson equation,

$$\nabla^2 \mathbf{A} = -\mu_0 \mathbf{I} \delta(x)\, \delta(y)\, \delta(z - z_0) \tag{3.11}$$

where **I** is a unit vector in the direction of the current at the current source.

This equation can then be solved in the same way as for the scalar potential. The results are simpler, however, because all three layers have the same relative permeability. Hence, only two Laplace's equations analogous to equation 3.7 have to be solved. This derivation is detailed in section 3.7.

3.3 Scalar Potential Solution for the General Case

3.3.1 Source Charge in Layer 1

The source charge is located at $z = z_0$, in layer 1. An extra boundary is therefore introduced at $z = z_0$. The solutions to the four Laplace's equations can be written in a similar way to equation 3.8 as

$$\begin{aligned}
\tilde{\phi}_a(k,z) &= A^+ e^{kz} + A^- e^{-kz} && -d_1 \le z \le z_0 \\
\tilde{\phi}_b(k,z) &= B^+ e^{kz} + B^- e^{-kz} && z_0 \le z \le 0 \\
\tilde{\phi}_c(k,z) &= C^+ e^{kz} + C^- e^{-kz} && 0 \le z \le c \\
\tilde{\phi}_d(k,z) &= D^+ e^{kz} + D^- e^{-kz} && c \le z \le c + d_2
\end{aligned} \tag{3.12}$$

where A^+ to D^- are initially unknown functions of arbitrary wavenumber k. These are determined by the Fourier transformed boundary conditions, which are

$$
\begin{aligned}
\tilde{\phi}_a(k,-d_1) &= 0 && (i)\\
\tilde{\phi}_d(k,c+d_2) &= 0 && (ii)\\
\tilde{\phi}_b(k,z_0) &= \tilde{\phi}_a(k,z_0) && (iii)\\
\tilde{\phi}_c(k,0) &= \tilde{\phi}_b(k,0) && (iv)\\
\tilde{\phi}_d(k,c) &= \tilde{\phi}_c(k,c) && (v)\\
\varepsilon_2 \frac{d}{dz}\tilde{\phi}_c(k,0) &= \varepsilon_1 \frac{d}{dz}\tilde{\phi}_b(k,0) && (vi)\\
\varepsilon_3 \frac{d}{dz}\tilde{\phi}_d(k,c) &= \varepsilon_2 \frac{d}{dz}\tilde{\phi}_c(k,c) && (vii)\\
\frac{d}{dz}\tilde{\phi}_b(k,z_0) &= \frac{d}{dz}\tilde{\phi}_a(k,z_0) - \frac{1}{2\pi\varepsilon_0\varepsilon_1} && (viii)
\end{aligned}
\qquad (3.13)
$$

The first two conditions enforce zero potential on the ground planes at $z=-d_1$ and $z=c+d_2$, which is the only solution possessing a Fourier transform. The next three enforce continuity of potential at the boundaries between the four regions. The last three enforce continuity of the normal component of electric flux density **D** at the boundaries where no free charge is present, and a discontinuity equal to the charge density at the boundaries where free charge is present [Bleaney and Bleaney, 1976, p.121].

Equations 3.12 and 3.13 are combined to solve for the functions A^+ to D^-. For convenience, set

$$\alpha = \frac{\varepsilon_2-\varepsilon_1}{\varepsilon_2+\varepsilon_1} \quad , \quad \beta = \frac{\varepsilon_2-\varepsilon_3}{\varepsilon_2+\varepsilon_3} \qquad (3.14)$$

For the situation described in the introduction to this chapter, layer 1 and layer 3 are both air, with dielectric constant $\varepsilon_1=\varepsilon_3=1$, and layer 2 is the PCB material, with dielectric constant $\varepsilon_2>1$. α and β are written in the above way so that they are both positive for this case. Also define z_d and z_s by

$$z_d = |z-z_0| \quad , \quad z_s = z+z_0 \qquad (3.15)$$

The full solution to this problem is detailed in Appendix B. For clarity of presentation of the results, define the function $\xi(l,m,n,z)$ as,

$$\xi(l,m,n,z) = \frac{1}{\sqrt{x^2+y^2+(2ld_2+2md_1+2nc+z)^2}} \qquad (3.16)$$

Writing ϕ_{ij} to represent the potential in layer j due to a charge in layer i, and using the notation of equation 3.16, the space domain potentials are given by,

$$\begin{aligned}\phi_{11}(x,y,z) = \frac{1}{4\pi\varepsilon_0\varepsilon_1}\sum_{l=0}^{\infty}\sum_{m=0}^{\infty}\sum_{n=0}^{\infty}K_{mn}(\alpha)\,K_{ln}(\beta)\,\times \\ \Big[\quad \xi(\,l\,,\,m\,,\,n\,,z_d) + \xi(l+1,m+1,n+1,-z_d) \\ -\xi(\,l\,,m+1,\,n\,,z_s) - \xi(l+1,\,m\,,n+1,-z_s) \\ +\alpha\,\{\,\xi(l+1,\,m\,,n+1,z_d) + \xi(\,l\,,m+1,\,n\,,-z_d) \\ -\xi(l+1,m+1,n+1,z_s) - \xi(\,l\,,\,m\,,\,n\,,-z_s)\,\} \\ +\beta\,\{\,\xi(l+1,m+1,\,n\,,z_s) + \xi(\,l\,,\,m\,,n+1,-z_s) \\ -\xi(l+1,\,m\,,\,n\,,z_d) - \xi(\,l\,,m+1,n+1,-z_d)\,\} \\ +\alpha\beta\{\,\xi(\,l\,,m+1,n+1,z_s) + \xi(l+1,\,m\,,\,n\,,-z_s) \\ -\xi(\,l\,,\,m\,,n+1,z_d) - \xi(l+1,m+1,\,n\,,-z_d)\,\}\,\Big]\end{aligned} \tag{3.17}$$

$$\begin{aligned}\phi_{12}(x,y,z) = \frac{1+\alpha}{4\pi\varepsilon_0\varepsilon_2}\sum_{l=0}^{\infty}\sum_{m=0}^{\infty}\sum_{n=0}^{\infty}K_{mn}(\alpha)\,K_{ln}(\beta)\,\times \\ \Big[\quad \xi(\,l\,,\,m\,,n,z_d) + \xi(l+1,m+1,n+1,-z_d) \\ -\xi(\,l\,,m+1,n,z_s) - \xi(l+1,\,m\,,n+1,-z_s) \\ +\beta\,\{\,\xi(l+1,m+1,n,z_s) + \xi(\,l\,,\,m\,,n+1,-z_s) \\ -\xi(l+1,\,m\,,n,z_d) - \xi(\,l\,,m+1,n+1,-z_d)\,\}\,\Big]\end{aligned} \tag{3.18}$$

$$\begin{aligned}\phi_{13}(x,y,z) = \frac{(1+\alpha)(1+\beta)}{4\pi\varepsilon_0\varepsilon_2}\sum_{l=0}^{\infty}\sum_{m=0}^{\infty}\sum_{n=0}^{\infty}K_{mn}(\alpha)\,K_{ln}(\beta)\,\times \\ \Big[\quad \xi(l,\,m\,,n,z_d) + \xi(l+1,m+1,n+1,-z_d) \\ -\xi(l,m+1,n,z_s) - \xi(l+1,\,m\,,n+1,-z_s)\,\Big]\end{aligned} \tag{3.19}$$

Scalar potentials with three dielectric layers, two ground planes

The coefficients $K_{ij}(\eta)$ are given by equation B.5,

$$K_{ij}(\eta) = \sum_{r=0}^{\min\{i,j\}}(-1)^r\frac{(i+j-r)!}{r!\,(i-r)!\,(j-r)!}\eta^{i+j-2r} \tag{B.5}$$

Interestingly, $K_{ij}(\eta)$ can also be written as a Jacobi polynomial, which simplifies its computation for large values of i and j. This derivation is detailed in Appendix C.

$$\phi_{22}(x,y,z) = \frac{1}{4\pi\varepsilon_0\varepsilon_2}\sum_{l=0}^{\infty}\sum_{m=0}^{\infty}\sum_{n=0}^{\infty}K_{mn}(\alpha)\,K_{ln}(\beta)\times$$
$$\begin{aligned}
&\Big[\quad \xi(\,l\,,\,m\,,n,z_d) + \xi(l+1,m+1,n+1,-z_d)\\
&\quad - \xi(\,l\,,m+1,n,z_s) - \xi(l+1,\,m\,,n+1,-z_s)\\
&\quad +\alpha\,\{\,\xi(\,l\,,\,m\,,n,z_s) + \xi(l+1,m+1,n+1,-z_s)\\
&\quad\quad - \xi(\,l\,,m+1,n,z_d) - \xi(l+1,\,m\,,n+1,-z_d)\,\}\\
&\quad +\beta\,\{\,\xi(l+1,m+1,n,z_s) + \xi(\,l\,,\,m\,,n+1,-z_s)\\
&\quad\quad - \xi(l+1,\,m\,,n,z_d) - \xi(\,l\,,m+1,n+1,-z_d)\,\}\\
&\quad +\alpha\beta\{\,\xi(l+1,m+1,n,z_d) + \xi(\,l\,,\,m\,,n+1,-z_d)\\
&\quad\quad - \xi(l+1,\,m\,,n,z_s) - \xi(\,l\,,m+1,n+1,-z_s)\,\}\,\Big]
\end{aligned} \tag{3.20}$$

$$\phi_{23}(x,y,z) = \frac{1+\beta}{4\pi\varepsilon_0\varepsilon_2}\sum_{l=0}^{\infty}\sum_{m=0}^{\infty}\sum_{n=0}^{\infty}K_{mn}(\alpha)\,K_{ln}(\beta)\times$$
$$\begin{aligned}
&\Big[\quad \xi(l,\,m\,,n,z_d) + \xi(l+1,m+1,n+1,-z_d)\\
&\quad - \xi(l,m+1,n,z_s) - \xi(l+1,\,m\,,n+1,-z_s)\\
&\quad +\alpha\,\{\,\xi(l,\,m\,,n,z_s) + \xi(l+1,m+1,n+1,-z_s)\\
&\quad\quad - \xi(l,m+1,n,z_d) - \xi(l+1,\,m\,,n+1,-z_d)\,\}\,\Big]
\end{aligned} \tag{3.21}$$

$$\phi_{33}(x,y,z) = \frac{1}{4\pi\varepsilon_0\varepsilon_3}\sum_{l=0}^{\infty}\sum_{m=0}^{\infty}\sum_{n=0}^{\infty}K_{mn}(\alpha)\,K_{ln}(\beta)\times$$
$$\begin{aligned}
&\Big[\quad \xi(l,\,m\,,\,n\,,z_d) + \xi(l+1,m+1,n+1,-z_d)\\
&\quad - \xi(l,m+1,\,n\,,z_s) - \xi(l+1,\,m\,,n+1,-z_s)\\
&\quad +\alpha\,\{\,\xi(l,\,m\,,\,n\,,z_s) + \xi(l+1,m+1,n+1,-z_s)\\
&\quad\quad - \xi(l,m+1,\,n\,,z_d) - \xi(l+1,\,m\,,n+1,-z_d)\,\}\\
&\quad +\beta\,\{\,\xi(l,m+1,n+1,z_d) + \xi(l+1,\,m\,,\,n\,,-z_d)\\
&\quad\quad - \xi(l,\,m\,,n-1,z_s) - \xi(l+1,m+1,n+2,-z_s)\,\}\\
&\quad +\alpha\beta\{\,\xi(l,m+1,n-1,z_s) + \xi(l+1,\,m\,,n+2,-z_s)\\
&\quad\quad - \xi(l,\,m\,,n+1,z_d) - \xi(l+1,m+1,\,n\,,-z_d)\,\}\,\Big]
\end{aligned} \tag{3.22}$$

Scalar potentials with three dielectric layers, two ground planes

3.3.2 Source Charge in Layer 2 or 3

Similar analysis is used for the cases with the source charge in layer 2 or in layer 3. The details of the calculations are presented in Appendix B. Applying the theorem of reciprocity [Morse and Feshbach, 1953, p.883], only three distinct new cases for the potential are generated. These are given in equations 3.20, 3.21 and 3.22.

3.4 Simpler Geometries - Fewer Ground Planes

The general results of sections 3.3.1 and 3.3.2 are now applied to simpler geometries. This section examines the results when one or both of the ground planes are removed (or placed at infinity).

3.4.1 One Ground Plane

The case with one ground plane is treated by letting $d_2 \rightarrow \infty$. Then, $e^{-2kd_2} \rightarrow 0$, and so the second term in equation B.2 becomes,

$$\frac{(\beta - e^{-2kd_2})^n}{(1 - \beta e^{-2kd_2})^{n+1}} = \beta^n \tag{3.23}$$

The function $\psi(k)$ in Appendix B can then be written as a double summation instead of the triple summation in equation B.6, ie.

$$\psi(k) = \sum_{m=0}^{\infty} \sum_{n=0}^{\infty} \beta^n K_{mn}(\alpha)\, e^{-2nkc} e^{-2mkd_1} \tag{3.24}$$

The potentials ϕ_{11} - ϕ_{33} can now be derived from their general forms in equations 3.17 - 3.19 and 3.20 - 3.22. Firstly, terms of the form $\xi(l,m,n,z)$ are replaced by $\xi(0,m,n,z)$, as they are zero when $l \neq 0$. All terms of the form $\xi(l+1,m,n,z)$ can be deleted as they simplify to $\xi(1,m,n,z)$, which becomes zero as $d_2 \rightarrow \infty$. The previous results therefore simplify to

$$\phi_{11}(x,y,z) = \frac{1}{4\pi\varepsilon_0\varepsilon_1}\sum_{m=0}^{\infty}\sum_{n=0}^{\infty}\beta^n K_{mn}(\alpha)\times$$
$$\begin{aligned}[\quad & \xi(0,\ m\ ,\ n\ ,z_d) - \xi(0,m+1,\ n\ ,z_s)\\ &+\alpha\{\ \xi(0,m+1,\ n\ ,-z_d) - \xi(0,\ m\ ,\ n\ ,-z_s)\ \}\\ &+\beta\{\ \xi(0,\ m\ ,n+1,-z_s) - \xi(0,m+1,n+1,-z_d)\ \}\\ &+\alpha\beta\{\ \xi(0,m+1,n+1,z_s) - \xi(0,\ m\ ,n+1,z_d)\ \}\ ]\end{aligned} \tag{3.25}$$

$$\phi_{12}(x,y,z) = \frac{1+\alpha}{4\pi\varepsilon_0\varepsilon_2}\sum_{m=0}^{\infty}\sum_{n=0}^{\infty}\beta^n K_{mn}(\alpha)\times$$
$$\begin{aligned}[\quad & \xi(0,m,\ n\ ,z_d) - \xi(0,m+1,\ n\ ,z_s)\\ &+\beta\{\ \xi(0,m,n+1,-z_s) - \xi(0,m+1,n+1,-z_d)\ \}\ ]\end{aligned} \tag{3.26}$$

$$\phi_{13}(x,y,z) = \frac{(1+\alpha)(1+\beta)}{4\pi\varepsilon_0\varepsilon_2}\sum_{m=0}^{\infty}\sum_{n=0}^{\infty}\beta^n K_{mn}(\alpha)\times$$
$$[\ \xi(0,m,n,z_d) - \xi(0,m+1,n,z_s)\ ] \tag{3.27}$$

$$\phi_{22}(x,y,z) = \frac{1}{4\pi\varepsilon_0\varepsilon_2}\sum_{m=0}^{\infty}\sum_{n=0}^{\infty}\beta^n K_{mn}(\alpha)\times$$
$$\begin{aligned}[\quad & \xi(0,m,\ n\ ,z_d) - \xi(0,m+1,\ n\ ,z_s)\\ &+\alpha\{\ \xi(0,m,\ n\ ,z_s) - \xi(0,m+1,\ n\ ,z_d)\ \}\\ &+\beta\{\ \xi(0,m,n+1,-z_s) - \xi(0,m+1,n+1,-z_d)\ \}\\ &+\alpha\beta\{\ \xi(0,m,n+1,-z_d) - \xi(0,m+1,n+1,-z_s)\ \}\ ]\end{aligned} \tag{3.28}$$

$$\phi_{23}(x,y,z) = \frac{1+\beta}{4\pi\varepsilon_0\varepsilon_2}\sum_{m=0}^{\infty}\sum_{n=0}^{\infty}\beta^n K_{mn}(\alpha)\times$$
$$\begin{aligned}[\quad & \xi(0,m,n,z_d) - \xi(0,m+1,n,z_s)\\ &+\alpha\{\ \xi(0,m,n,z_s) - \xi(0,m+1,n,z_d)\ \}\ ]\end{aligned} \tag{3.29}$$

$$\phi_{33}(x,y,z) = \frac{1}{4\pi\varepsilon_0\varepsilon_3}\sum_{m=0}^{\infty}\sum_{n=0}^{\infty}\beta^n K_{mn}(\alpha)\times$$
$$\begin{aligned}[\quad & \xi(0,\ m\ ,\ n\ ,z_d) - \xi(0,m+1,\ n\ ,z_s)\\ &+\alpha\{\ \xi(0,\ m\ ,\ n\ ,z_s) - \xi(0,m+1,\ n\ ,z_d)\ \}\\ &+\beta\{\ \xi(0,m+1,n+1,z_d) - \xi(0,\ m\ ,n-1,z_s)\ \}\\ &+\alpha\beta\{\ \xi(0,m+1,n-1,z_s) - \xi(0,\ m\ ,n+1,z_d)\ \}\ ]\end{aligned} \tag{3.30}$$

Scalar potentials with three dielectric layers, one ground plane

$$\phi_{11}(x,y,z) = \frac{1}{4\pi\varepsilon_0\varepsilon_1}\sum_{n=0}^{\infty}(\alpha\beta)^n \times \left[\xi(0,0,n,z_d) - \alpha\,\xi(0,0,n,-z_s) + \beta\,\xi(0,0,n+1,-z_s) - \alpha\beta\,\xi(0,0,n+1,z_d) \right] \quad (3.31)$$

$$\phi_{12}(x,y,z) = \frac{1+\alpha}{4\pi\varepsilon_0\varepsilon_2}\sum_{n=0}^{\infty}(\alpha\beta)^n \left[\xi(0,0,n,z_d) + \beta\,\xi(0,0,n+1,-z_s) \right] \quad (3.32)$$

$$\phi_{13}(x,y,z) = \frac{(1+\alpha)(1+\beta)}{4\pi\varepsilon_0\varepsilon_2}\sum_{n=0}^{\infty}(\alpha\beta)^n\,\xi(0,0,n,z_d) \quad (3.33)$$

$$\phi_{22}(x,y,z) = \frac{1}{4\pi\varepsilon_0\varepsilon_2}\sum_{n=0}^{\infty}(\alpha\beta)^n \times \left[\xi(0,0,n,z_d) + \alpha\,\xi(0,0,n,z_s) + \beta\,\xi(0,0,n+1,-z_s) + \alpha\beta\,\xi(0,0,n+1,-z_d) \right] \quad (3.34)$$

$$\phi_{23}(x,y,z) = \frac{1+\beta}{4\pi\varepsilon_0\varepsilon_2}\sum_{n=0}^{\infty}(\alpha\beta)^n \left[\xi(0,0,n,z_d) + \alpha\,\xi(0,0,n,z_s) \right] \quad (3.35)$$

$$\phi_{33}(x,y,z) = \frac{1}{4\pi\varepsilon_0\varepsilon_3}\sum_{n=0}^{\infty}(\alpha\beta)^n \times \left[\xi(0,0,n,z_d) + \alpha\,\xi(0,0,n,z_s) - \beta\,\xi(0,0,n-1,z_s) - \alpha\beta\,\xi(0,0,n+1,z_d) \right] \quad (3.36)$$

Scalar potentials with three dielectric layers, no ground planes

3.4.2 No Ground Planes

The case with no ground plane is treated by taking the results from section 3.4.1 and letting $d_1 \to \infty$. Then, $e^{-2kd_1} \to 0$, and so the first term in equation B.6 becomes,

$$\frac{\left(\alpha - e^{-2kd_1}\right)^n}{\left(1-\alpha e^{-2kd_1}\right)^{n+1}} = \alpha^n \quad (3.37)$$

The function $\psi(k)$ can then be written as a single summation, instead of the double summation in equation 3.24, ie.

$$\psi(k) = \sum_{n=0}^{\infty} (\alpha\beta)^n e^{-2nkc} \tag{3.38}$$

The potentials ϕ_{11} - ϕ_{33} can now be derived from their previous forms in equations 3.25 - 3.30. For the same reasons as in section 3.4.1, terms of the form $\xi(0,m,n,z)$ are replaced by $\xi(0,0,n,z)$, and terms of the form $\xi(0,m+1,n,z)$ become zero. The previous results therefore reduce to those in equations 3.31 - 3.36.

3.5 Simpler Geometries - Fewer Dielectric Layers

This section examines the results when the number of dielectric layers is reduced to two or one, in each case with either two, one or no ground planes.

3.5.1 Two Dielectric Layers, Two Ground Planes

This case is treated by letting $d_1 \rightarrow 0$, so that $e^{-2kd_1} \rightarrow 1$. The first term in equation B.2 simplifies to

$$\frac{(\alpha - e^{-2kd_1})^n}{(1-\alpha e^{-2kd_1})^{n+1}} = \frac{(-1)^n}{1-\alpha} \tag{3.39}$$

The function $\psi(k)$ can then be simplified to the double summation,

$$\psi(k) = \frac{1}{1-\alpha} \sum_{l=0}^{\infty} \sum_{n=0}^{\infty} (-1)^n K_{ln}(\beta)\, e^{-2nkc} e^{-2lkd_2} \tag{3.40}$$

Since $d_1 = 0$, terms of the form $\xi(l,m,n,z)$ or $\xi(l,m+1,n,z)$ can both be replaced by $\xi(l,0,n,z)$. If the source charge is in layer 1 (which is now of zero thickness), then $z_d = z_s$. Hence, ϕ_{11}, ϕ_{12} and ϕ_{13} in equations 3.17 - 3.19 all become zero, as must be the case since the source is coincident with the lower ground plane. The remaining three cases are

$$\phi_{22}(x,y,z) = \frac{1}{4\pi\varepsilon_0\varepsilon_2}\sum_{l=0}^{\infty}\sum_{n=0}^{\infty}(-1)^n K_{ln}(\beta)\times$$
$$\begin{aligned}[\quad & \xi(\ l\ ,0,n,z_d) + \xi(l+1,0,n+1,-z_d) \\ & -\xi(\ l\ ,0,n,z_s) - \xi(l+1,0,n+1,-z_s) \\ & +\beta\ \{\ \xi(l+1,0,n,z_s) + \xi(\ l\ ,0,n+1,-z_s) \\ & -\xi(l+1,0,n,z_d) - \xi(\ l\ ,0,n+1,-z_d)\ \}\ ]\end{aligned} \tag{3.41}$$

$$\phi_{23}(x,y,z) = \frac{1+\beta}{4\pi\varepsilon_0\varepsilon_2}\sum_{l=0}^{\infty}\sum_{n=0}^{\infty}(-1)^n K_{ln}(\beta)\times$$
$$\begin{aligned}[\quad & \xi(l,0,n,z_d) + \xi(l+1,0,n+1,-z_d) \\ & -\xi(l,0,n,z_s) - \xi(l+1,0,n+1,-z_s)\ ]\end{aligned} \tag{3.42}$$

$$\phi_{33}(x,y,z) = \frac{1}{4\pi\varepsilon_0\varepsilon_3}\sum_{l=0}^{\infty}\sum_{n=0}^{\infty}(-1)^n K_{ln}(\beta)\times$$
$$\begin{aligned}[\quad & \xi(l,0,\ \ n\ \ ,z_d) + \xi(l+1,0,n+1,-z_d) \\ & -\xi(l,0,\ \ n\ \ ,z_s) - \xi(l+1,0,n+1,-z_s) \\ & +\beta\ \{\ \xi(l,0,n+1,z_d) + \xi(l+1,0,\ \ n\ \ ,-z_d) \\ & -\xi(l,0,n-1,z_s) - \xi(l+1,0,n+2,-z_s)\ \}\ ]\end{aligned} \tag{3.43}$$

Scalar potentials with two dielectric layers, two ground planes

3.5.2 Two Dielectric Layers, One Ground Plane

This case is treated by letting $d_1 \to 0$ and $d_2 \to \infty$. Using equations 3.23 and 3.39, the function $\psi(k)$ can be simplified to the single summation,

$$\psi(k) = \frac{1}{1-\alpha}\sum_{n=0}^{\infty}(-\beta)^n e^{-2nkc} \tag{3.44}$$

As in section 3.5.1, there are now only three cases for the potential. These are derived from equations 3.28 - 3.30 as,

$$\phi_{22}(x,y,z) = \frac{1}{4\pi\varepsilon_0\varepsilon_2}\sum_{n=0}^{\infty}(-\beta)^n \times \left[\xi(0,0,n,z_d) - \xi(0,0,n,z_s) + \beta \{ \xi(0,0,n+1,-z_s) - \xi(0,0,n+1,-z_d) \} \right] \quad (3.45)$$

$$\phi_{23}(x,y,z) = \frac{1+\beta}{4\pi\varepsilon_0\varepsilon_2}\sum_{n=0}^{\infty}(-\beta)^n \left[\xi(0,0,n,z_d) - \xi(0,0,n,z_s) \right] \quad (3.46)$$

$$\phi_{33}(x,y,z) = \frac{1}{4\pi\varepsilon_0\varepsilon_3}\sum_{n=0}^{\infty}(-\beta)^n \times \left[\xi(0,0,n,z_d) - \xi(0,0,n,z_s) + \beta \{ \xi(0,0,n+1,z_d) - \xi(0,0,n-1,z_s) \} \right] \quad (3.47)$$

Scalar potentials with two dielectric layers, one ground plane

3.5.3 Two Dielectric Layers, No Ground Planes

This case is treated by putting $\varepsilon_2 = \varepsilon_3$ in the results of section 3.4.2. Hence, from equation 3.14, $\beta = 0$, and so $\psi(k) = 1$. Also, $\phi_{12} = \phi_{13}$, and $\phi_{22} = \phi_{23} = \phi_{33}$, as would be expected since layer 2 and layer 3 can no longer be distinguished. The three cases therefore reduce to,

$$\phi_{11}(x,y,z) = \frac{1}{4\pi\varepsilon_0\varepsilon_1}\left[\xi(0,0,0,z_d) - \alpha\, \xi(0,0,0,-z_s) \right] \quad (3.48)$$

$$\phi_{12}(x,y,z) = \frac{1+\alpha}{4\pi\varepsilon_0\varepsilon_2}\, \xi(0,0,0,z_d) \quad (3.49)$$

$$\phi_{22}(x,y,z) = \frac{1}{4\pi\varepsilon_0\varepsilon_2}\left[\xi(0,0,0,z_d) + \alpha\, \xi(0,0,0,z_s) \right] \quad (3.50)$$

Scalar potentials with two dielectric layers, no ground planes

These results are the same as those obtained from classical image theory [Bleaney and Bleaney, 1976, pp.48-56].

3.5.4 One Dielectric Layer, Two Ground Planes

This case is treated by taking the results of section 3.5.1, and additionally letting $d_2 \to 0$. Then, $e^{-2kd_2} \to 1$, and the second term in equation B.2 simplifies to

$$\frac{(\beta - e^{-2kd_2})^n}{(1-\beta e^{-2kd_2})^{n+1}} = \frac{(-1)^n}{1-\beta} \tag{3.51}$$

Combining equations 3.40 and 3.51, the function $\psi(k)$ can be simplified to the single summation,

$$\psi(k) = \frac{1}{(1-\alpha)(1-\beta)} \sum_{n=0}^{\infty} e^{-2nkc} \tag{3.52}$$

Since $d_2 = 0$, terms of the form $\xi(l,0,n,z)$ or $\xi(l+1,0,n,z)$ can both be replaced by $\xi(0,0,n,z)$. If the source charge is in layer 3 (which is now of zero thickness), and the potential is required at z,

$$z_s = c+z \quad , \quad z_d = c-z \tag{3.53}$$

Using this relationship, it is seen that ϕ_{23} and ϕ_{33} in equations 3.42 and 3.43 both become zero, as would be expected. The remaining case is,

$$\phi_{22}(x,y,z) = \frac{1}{4\pi\varepsilon_0\varepsilon_2} \sum_{n=0}^{\infty} \left[\xi(0,0,n,z_d) + \xi(0,0,n+1,-z_d) - \xi(0,0,n,z_s) - \xi(0,0,n+1,-z_s) \right] \tag{3.54}$$

Scalar potential with one dielectric layer, two ground planes

3.5.5 One Dielectric Layer, One Ground Plane

This case is treated by putting $\varepsilon_2 = \varepsilon_3$ in the results of section 3.5.2. Since $\beta = 0$,

$$\psi(k) = \frac{1}{1-\alpha} \tag{3.55}$$

As in section 3.5.4, there is now only one case for the potential, equivalent to equations 3.45 - 3.47,

$$\phi_{22}(x,y,z) = \frac{1}{4\pi\varepsilon_0\varepsilon_2}\left[\ \xi(0,0,0,z_d) - \xi(0,0,0,z_s)\ \right] \qquad (3.56)$$

Scalar potential with one dielectric layer, one ground plane

This is just the potential due to a unit (positive) point charge at $(0, 0, z_0)$ and a unit (negative) point charge at $(0, 0, -z_0)$, as predicted by classical image theory [Bleaney and Bleaney, 1976, pp.48-56].

3.5.6 One Dielectric Layer, No Ground Planes

This case is treated by putting $\varepsilon_1 = \varepsilon_2$ in the results of section 3.5.3. Hence, from equation 3.14, $\alpha = 0$. Also, $\phi_{11} = \phi_{12} = \phi_{22}$, as would be expected since layer 1 and layer 2 can no longer be distinguished. The remaining case is the potential due to a point charge in an infinite medium of dielectric constant ε_2.

$$\phi_{22}(x,y,z) = \frac{1}{4\pi\varepsilon_0\varepsilon_2}\ \xi(0,0,0,z_d) \qquad (3.57)$$

Scalar potential with one dielectric layer, no ground planes

3.6 Simpler Results - Particular Source and Object Point Positions

This section presents the results of positioning both z and z_0 on the boundaries of layer 2. This results in simpler forms for the formulae presented earlier. These are useful for the case mentioned in the introduction, where layer 2 represents the PCB material, when the metallisation patterns are on the top or bottom surface of the PCB. The results presented will be:

- $\phi_{00}(x, y)$ for $z = z_0 = 0$, so $z_d = z_s = 0$. This can be derived from ϕ_{11}, ϕ_{12} or ϕ_{22}
- $\phi_{0c}(x, y)$ for $z = 0$, $z_0 = c$ (or vice versa), so $z_d = z_s = c$. This can be derived from ϕ_{12}, ϕ_{13}, ϕ_{22} or ϕ_{23}
- $\phi_{cc}(x, y)$ for $z = z_0 = c$, so $z_d = 0$ and $z_s = 2c$. This can be derived from ϕ_{22}, ϕ_{23} or ϕ_{33}

The results are derived from those for all the situations presented in sections 3.3, 3.4 and 3.5. They will be given without further explanation.

$$\phi_{00}(x,y) = \frac{1+\alpha}{4\pi\varepsilon_0\varepsilon_2}\sum_{l=0}^{\infty}\sum_{m=0}^{\infty}\sum_{n=0}^{\infty}K_{mn}(\alpha)\,K_{ln}(\beta)\times$$
$$\Big[\ \xi(l,m,n,0) + \xi(l+1,m+1,n+1,0) - \xi(l,m+1,n,0) - \xi(l+1,m,n+1,0) + \beta\ \{\ \xi(l+1,m+1,n,0) + \xi(l,m,n+1,0) - \xi(l+1,m,n,0) - \xi(l,m+1,n+1,0)\ \}\ \Big] \tag{3.58}$$

$$\phi_{0c}(x,y) = \frac{(1+\alpha)(1+\beta)}{4\pi\varepsilon_0\varepsilon_2}\sum_{l=0}^{\infty}\sum_{m=0}^{\infty}\sum_{n=0}^{\infty}K_{mn}(\alpha)\,K_{ln}(\beta)\times$$
$$\Big[\ \xi(l,m,n,c) + \xi(l+1,m+1,n,c) - \xi(l,m+1,n,c) - \xi(l+1,m,n,c)\ \Big] \tag{3.59}$$

$$\phi_{cc}(x,y) = \frac{1+\beta}{4\pi\varepsilon_0\varepsilon_2}\sum_{l=0}^{\infty}\sum_{m=0}^{\infty}\sum_{n=0}^{\infty}K_{mn}(\alpha)\,K_{ln}(\beta)\times$$
$$\Big[\ \xi(l,m,n,0) + \xi(l+1,m+1,n+1,0) - \xi(l,m+1,n+1,0) - \xi(l+1,m,n,0) + \alpha\ \{\ \xi(l,m,n+1,0) + \xi(l+1,m+1,n,0) - \xi(l,m+1,n,0) - \xi(l+1,m,n+1,0)\ \}\ \Big] \tag{3.60}$$

Scalar potentials with three dielectric layers, two ground planes

$$\phi_{00}(x,y) = \frac{1+\alpha}{4\pi\varepsilon_0\varepsilon_2}\sum_{m=0}^{\infty}\sum_{n=0}^{\infty}\beta^n\,K_{mn}(\alpha)\times$$
$$\Big[\ \xi(0,m,n,0) - \xi(0,m+1,n,0) + \beta\ \{\ \xi(0,m,n+1,0) - \xi(0,m+1,n+1,0)\ \}\ \Big] \tag{3.61}$$

$$\phi_{0c}(x,y) = \frac{(1+\alpha)(1+\beta)}{4\pi\varepsilon_0\varepsilon_2}\sum_{m=0}^{\infty}\sum_{n=0}^{\infty}\beta^n\,K_{mn}(\alpha)\times$$
$$\Big[\ \xi(0,m,n,c) - \xi(0,m+1,n,c)\ \Big] \tag{3.62}$$

$$\phi_{cc}(x,y) = \frac{1+\beta}{4\pi\varepsilon_0\varepsilon_2}\sum_{m=0}^{\infty}\sum_{n=0}^{\infty}\beta^n\,K_{mn}(\alpha)\times$$
$$\Big[\ \xi(0,m,n,0) - \xi(0,m+1,n+1,0) + \alpha\ \{\ \xi(0,m,n+1,0) - \xi(0,m+1,n,0)\ \}\ \Big] \tag{3.63}$$

Scalar potentials with three dielectric layers, one ground plane

$$\phi_{00}(x,y) = \frac{1+\alpha}{4\pi\varepsilon_0\varepsilon_2}\sum_{n=0}^{\infty}(\alpha\beta)^n\left[\,\xi(0,0,n,0) + \beta\,\xi(0,0,n+1,0)\,\right] \tag{3.64}$$

$$\phi_{0c}(x,y) = \frac{(1+\alpha)(1+\beta)}{4\pi\varepsilon_0\varepsilon_2}\sum_{n=0}^{\infty}(\alpha\beta)^n\,\xi(0,0,n,c) \tag{3.65}$$

$$\phi_{cc}(x,y) = \frac{1+\beta}{4\pi\varepsilon_0\varepsilon_2}\sum_{n=0}^{\infty}(\alpha\beta)^n\left[\,\xi(0,0,n,0) + \alpha\,\xi(0,0,n+1,0)\,\right] \tag{3.66}$$

Scalar potentials with three dielectric layers, no ground planes

$$\phi_{cc}(x,y) = \frac{1+\beta}{4\pi\varepsilon_0\varepsilon_2}\sum_{l=0}^{\infty}\sum_{n=0}^{\infty}(-1)^n K_{\ln}(\beta)\times \left[\,\xi(l,0,\;n\;,0) + \xi(l+1,0,n+1,0) - \xi(l,0,n+1,0) - \xi(l+1,0,\;n\;,0)\,\right] \tag{3.67}$$

Scalar potential with two dielectric layers, two ground planes

$$\phi_{cc}(x,y) = \frac{1+\beta}{4\pi\varepsilon_0\varepsilon_2}\sum_{n=0}^{\infty}(-\beta)^n\left[\,\xi(0,0,n,0) - \xi(0,0,n+1,0)\,\right] \tag{3.68}$$

Scalar potential with two dielectric layers, one ground plane

The formulae in equations 3.61 - 3.66 and equation 3.68 can be rewritten in a form that is efficient for computation. The details of this are presented in Appendix D.

3.7 Vector Potential Solution

An arbitrarily directed current source between the ground planes in Figure 7 can be resolved into two components, one parallel to the ground planes and one normal to them. This section details how the vector potential is obtained for both cases.

3.7.1 Source Current Parallel to the Ground Planes

The point current source is located at $z = z_0$ between the two ground planes, directed parallel to the x axis. The Poisson equation 3.11 for the vector potential shows that the vector potential is parallel to the current source producing it, and is therefore also parallel to the x axis. Hence, only the x component A_x of the vector potential is considered.

Because all three dielectric layers have a relative permeability of 1.0, only two Laplace's equations are required to solve for the vector potential. These are

$$\begin{aligned} \tilde{A}_{xa}(k,z) &= A^+e^{kz} + A^-e^{-kz} \qquad -d_1 \le z \le z_0 \\ \tilde{A}_{xb}(k,z) &= B^+e^{kz} + B^-e^{-kz} \qquad z0 \le z \le c + d_2 \end{aligned} \tag{3.69}$$

where $\tilde{A}_{xa}$ is the Fourier transformed x component of the vector potential for $z \le z_0$, $\tilde{A}_{xb}$ is the same for $z \ge z_0$, and A^+ to B^- are initially unknown functions of arbitrary wavenumber k. These are determined by the Fourier transformed boundary conditions, which are,

$$\begin{aligned} \tilde{A}_{xa}(k,-d_1) &= 0 && (i) \\ \tilde{A}_{xb}(k,c+d_2) &= 0 && (ii) \\ \tilde{A}_{xa}(k,z_0) &= \tilde{A}_{xb}(k,z_0) && (iii) \\ \frac{d}{dz}\tilde{A}_{xb}(k,z_0) &= \frac{d}{dz}\tilde{A}_{xa}(k,z_0) - \frac{\mu_0}{2\pi} && (iv) \end{aligned} \tag{3.70}$$

The first two conditions enforce zero vector potential on the ground planes at $z = -d_1$ and $z = c + d_2$, which is the only solution possessing a Fourier transform. The next condition enforces continuity of potential at the boundary between the two regions. The last condition enforces a discontinuity in **H** equal to the current density at the boundary between the two regions [Bleaney and Bleaney, 1976, p.121].

The solution of these equations is performed in an identical manner to that for the scalar potential, and so the details are omitted. There are three cases to be considered, with two, one and no ground planes respectively. The x component of the vector potential, A_x, for each of these cases is:

$$A_x(x,y,z) = \frac{\mu_0}{4\pi} \sum_{n=0}^{\infty} [\ \xi(0,0,n,z_d) + \xi(0,0,n+1,-z_d) - \xi(0,0,n,z_s) - \xi(0,0,n+1,-z_s)\ ] \quad (3.71)$$

x component of vector potential with two ground planes

$$A_x(x,y,z) = \frac{\mu_0}{4\pi} [\ \xi(0,0,0,z_d) - \xi(0,0,0,z_s)\ ] \quad (3.72)$$

x component of vector potential with one ground plane

$$A_x(x,y,z) = \frac{\mu_0}{4\pi} \xi(0,0,0,z_d) \quad (3.73)$$

x component of vector potential with no ground planes

3.7.2 Source Current Perpendicular to the Ground Planes

The point current source is located at $z = z_0$ between the two ground planes, directed parallel to the z axis. The vector potential is therefore also parallel to the z axis, so only its z component, A_z, is considered. This component produces a magnetic field parallel to the ground planes, which is not constrained by any boundary conditions [Bleaney and Bleaney, 1976, p.121]. The ground planes therefore have no effect, and the z component of the vector potential is given by,

$$A_z(x,y,z) = \frac{\mu_0}{4\pi} \xi(0,0,0,z_d) \quad (3.74)$$

z component of vector potential

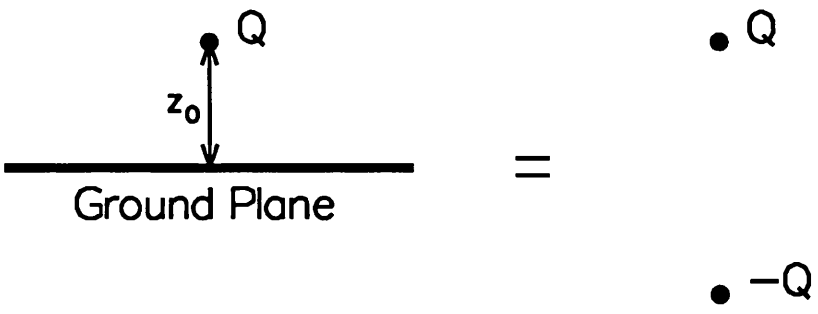

Figure 8. Image representation of a point charge above a ground plane

3.8 Correspondence with Image Series

The method of images [Bleaney and Bleaney, 1976, pp.48-56] is a technique which, in some cases, enables the effect of material boundaries on the scalar potential to be accounted for. This is done by defining a system of "image" charges in a homogeneous medium, of appropriate strength and location, which have the same combined effect as the original charge in the inhomogeneous medium. The simplest example of this is a point charge above an infinite ground plane. The effect of the ground plane is the same as that of a point charge of equal magnitude and opposite sign to the original charge, placed the same distance from the ground plane and on the opposite side. This is where the image of the original charge would be if the ground plane were a mirror, hence the name of the method. This situation is illustrated in Figure 8.

If the potential is required at (x, y, z), then this point has a separation in the z-direction of $|z - z_0| = z_d$ from the original charge, and a separation of $z + z_0 = z_s$ from the image charge. Hence, for any $z \geq 0$, the potential can be written as,

$$\phi(x,y,z) = \frac{1}{4\pi\varepsilon_0}\left[\, \xi(0,0,0,z_d) - \xi(0,0,0,z_s) \,\right] \tag{3.75}$$

which is the same as equation 3.56, the potential for one dielectric layer and one ground plane, when $\varepsilon_2 = 1$. Note that the potential is only given correctly in the space above the original ground plane; below the ground plane, the potential is zero. This illustrates the point that, in general, a different image series will be required to yield the potential in each region of the original problem, because there can only be one charge in the region of interest. If

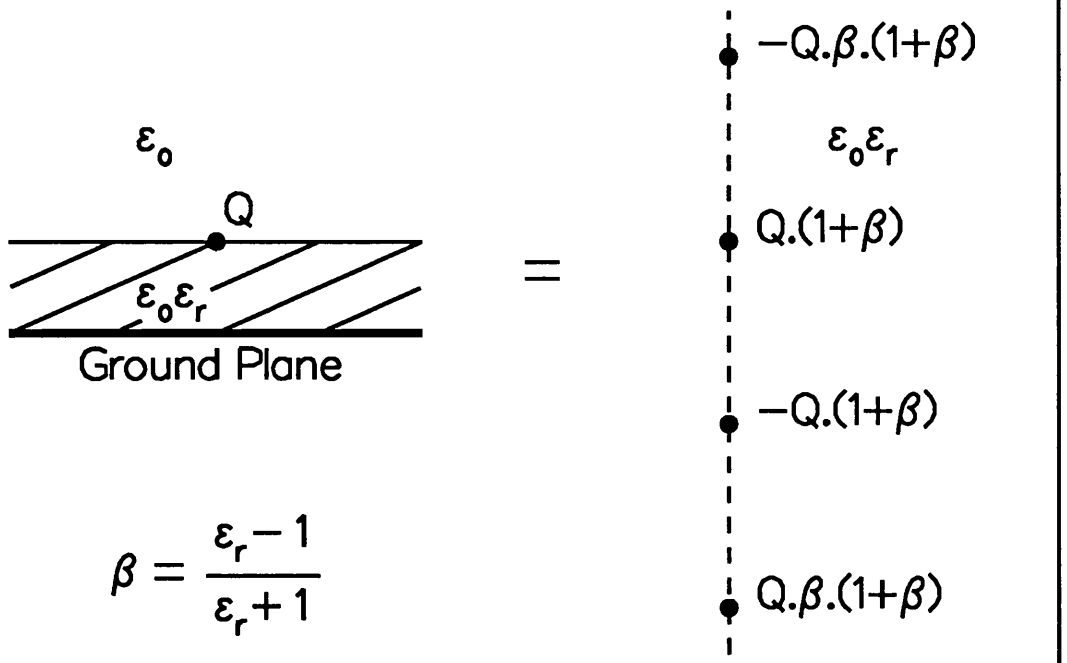

Figure 9. Infinite image series for two dielectric layers, one ground plane

this were not the case, there would be additional singularities in the potential, not present in the original situation.

A similar correspondence is found between the results of equations 3.48 - 3.50, for two dielectric layers and no ground planes, and those in Bleaney and Bleaney [1976, pp.48-56] for a point charge above a semi-infinite dielectric, but this will not be detailed here. When these two cases are combined, the situation shown in Figure 9 results. There are now in effect two "mirrors", a perfectly reflecting one (the ground plane) and a partially reflecting one (the air-dielectric interface). The combination of these two produces an infinite series of images, the first few of which are shown in Figure 9 [Chow, 1980]. This series is valid for evaluating the potential within the dielectric. A different image series would be needed to evaluate the potential above the dielectric, with no image charges in this region. Both series give the same result for the potential on the air-dielectric interface, which can be written as,

$$\phi_{cc}(x,y) = \frac{1+\beta}{4\pi\varepsilon_0\varepsilon_r} \sum_{n=0}^{\infty} (-\beta)^n \left[\xi(0,0,n,0) - \xi(0,0,n+1,0) \right] \qquad (3.76)$$

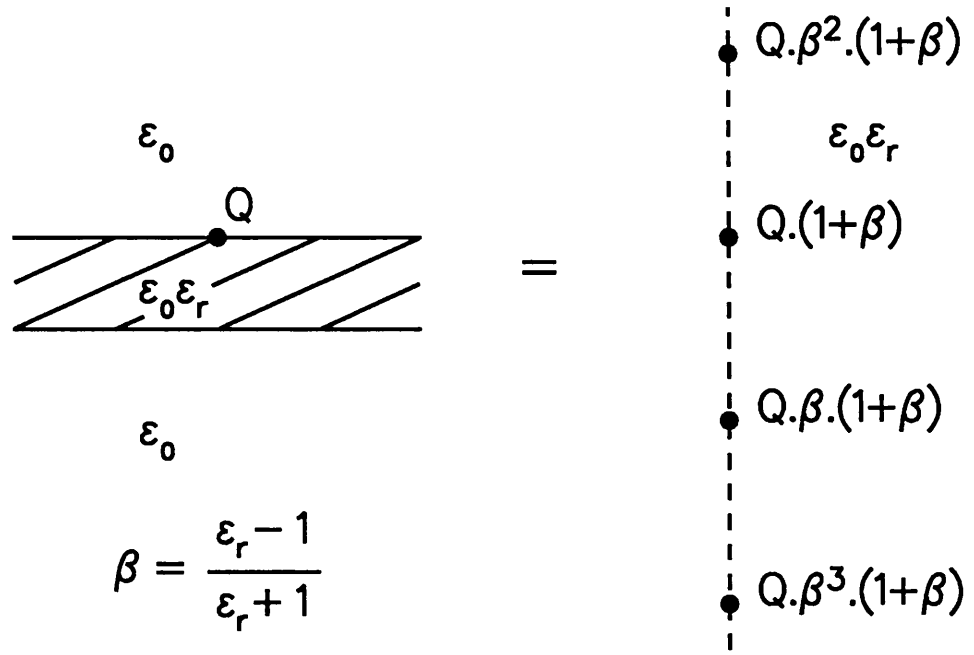

Figure 10. Infinite image series for three dielectric layers, no Ground planes

which is the same as equation 3.68 when $\varepsilon_2 = \varepsilon_r$ and $\varepsilon_3 = 1$.

Another case is that shown in Figure 10. Again, there are two reflecting surfaces, but this time both of them are partially reflecting. This results in the infinite series of images shown, also only valid within the dielectric, first derived by Silvester [1968]. The potential on the top air-dielectric interface can be written as,

$$\phi_{cc}(x,y) = \frac{1+\beta}{4\pi\varepsilon_0\varepsilon_r} \sum_{n=0}^{\infty} \beta^{2n} \left[\xi(0,0,n,0) + \beta\, \xi(0,0,n+1,0) \right] \qquad (3.77)$$

This is the same as equation 3.66 when $\varepsilon_2 = \varepsilon_r$ and $\varepsilon_1 = \varepsilon_3 = 1$ (so that $\alpha = \beta$).

More complicated geometries have not been dealt with by image theory, to the author's knowledge, but general principles can be deduced. Since two reflecting surfaces produce an infinite series of images, it would be expected that three reflecting surfaces would produce a doubly infinite series of images, four reflecting surfaces a trebly infinite series of images, and so on. The results in previous sections, with doubly and trebly infinite series, are of the form expected. This suggests that they too could be interpreted as image series,

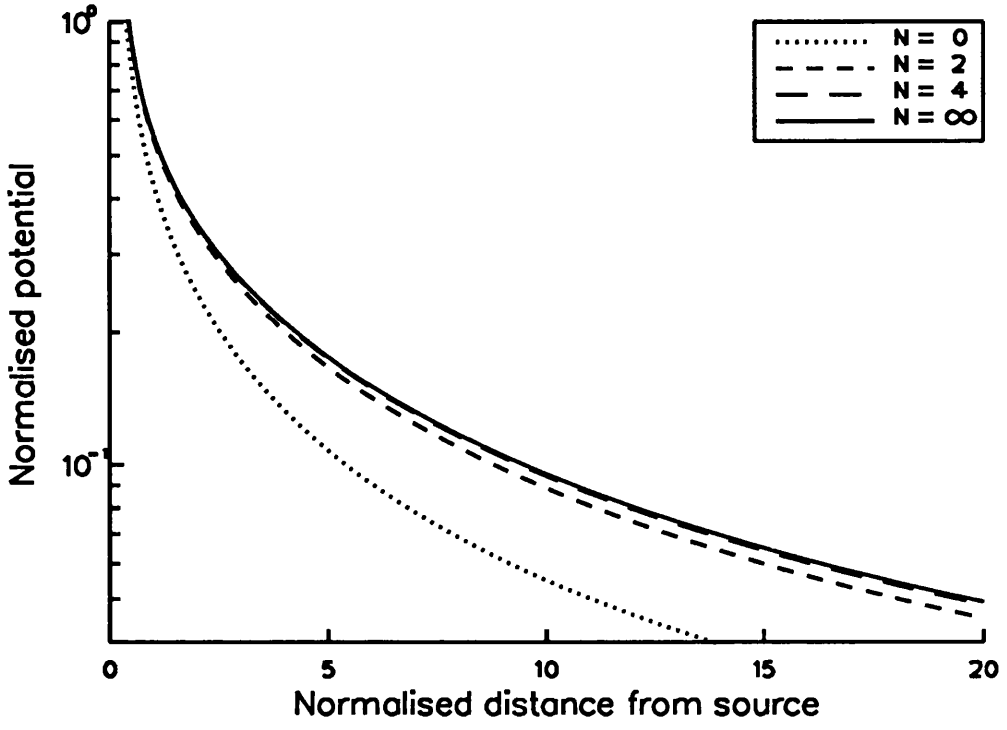

Figure 11. Potential for a PCB with no ground planes: $\varepsilon_2 = 5$

if so desired. However, because of their complexity, it would be unattractive to derive them in the same way as Silvester did [1968] for a singly infinite series.

3.9 Rate of Convergence of Series

Convergence is a vital consideration in determining the optimum trade-off between accuracy and efficiency in the FACET simulations. The rate of convergence of the infinite series derived so far is now examined for a few examples, with two, one or no ground planes and two or three dielectric layers. Only the behaviour of the scalar potential formulae is examined, since the vector potential formulae are so similar.

To obtain potentials for these examples, layer 2 in the general geometry of Figure 7 is taken to be a PCB material, and layers 1 and 3 are taken to be air. Hence, $\varepsilon_1 = \varepsilon_3 = 1$ and so $\alpha = \beta$. The source charge and object point are both placed at $z = c$, the boundary between layers 2 and 3. The potentials examined are therefore all ϕ_{cc}, as derived in section 3.6. These

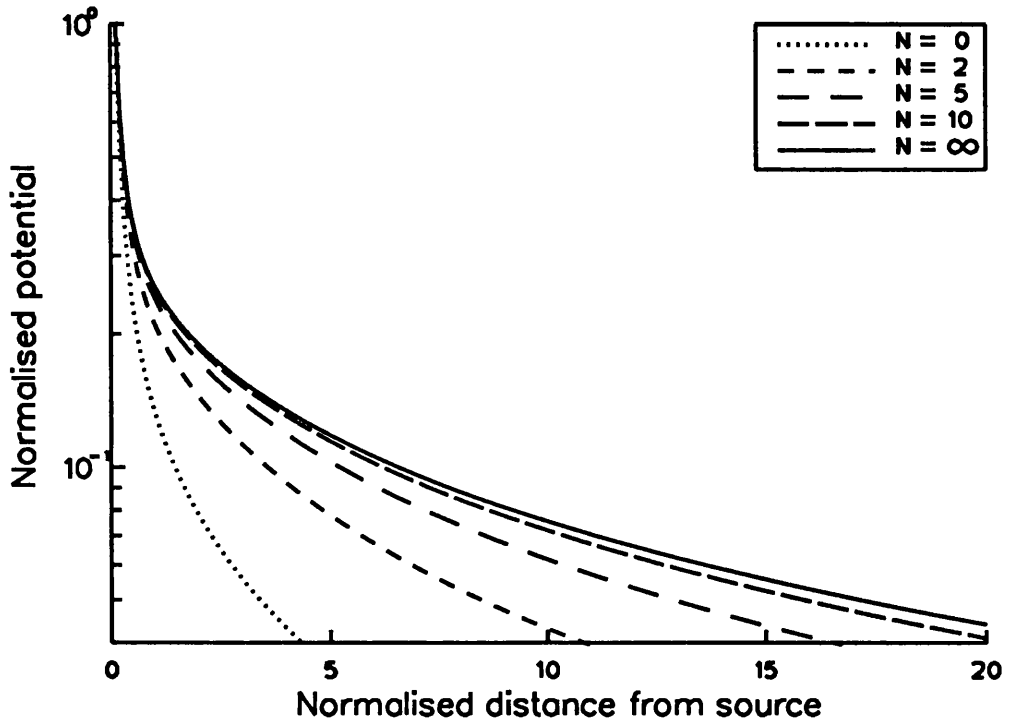

Figure 12. Potential for a PCB with no ground planes: $\varepsilon_2 = 20$

results can be extrapolated readily to more general cases if required, but the general conclusions will be similar for all geometries with the same structure.

Plots are presented in the following sections of the potential (on a logarithmic scale) against the distance from the source point charge. The potential is normalised by the potential one PCB thickness away from a unit point charge in free space, ie. $(4\pi\varepsilon_0 c)^{-1}$, and the distance from the point charge is normalised by the thickness of the PCB, ie. c. These definitions enable the results from the various cases examined below to be compared easily.

3.9.1 No Ground Planes, Three Dielectric Layers

The first case examined is a PCB with no ground planes present. The potential is derived from equation 3.66 by setting $\alpha = \beta$ and changing the upper limit of summation from infinity to N,

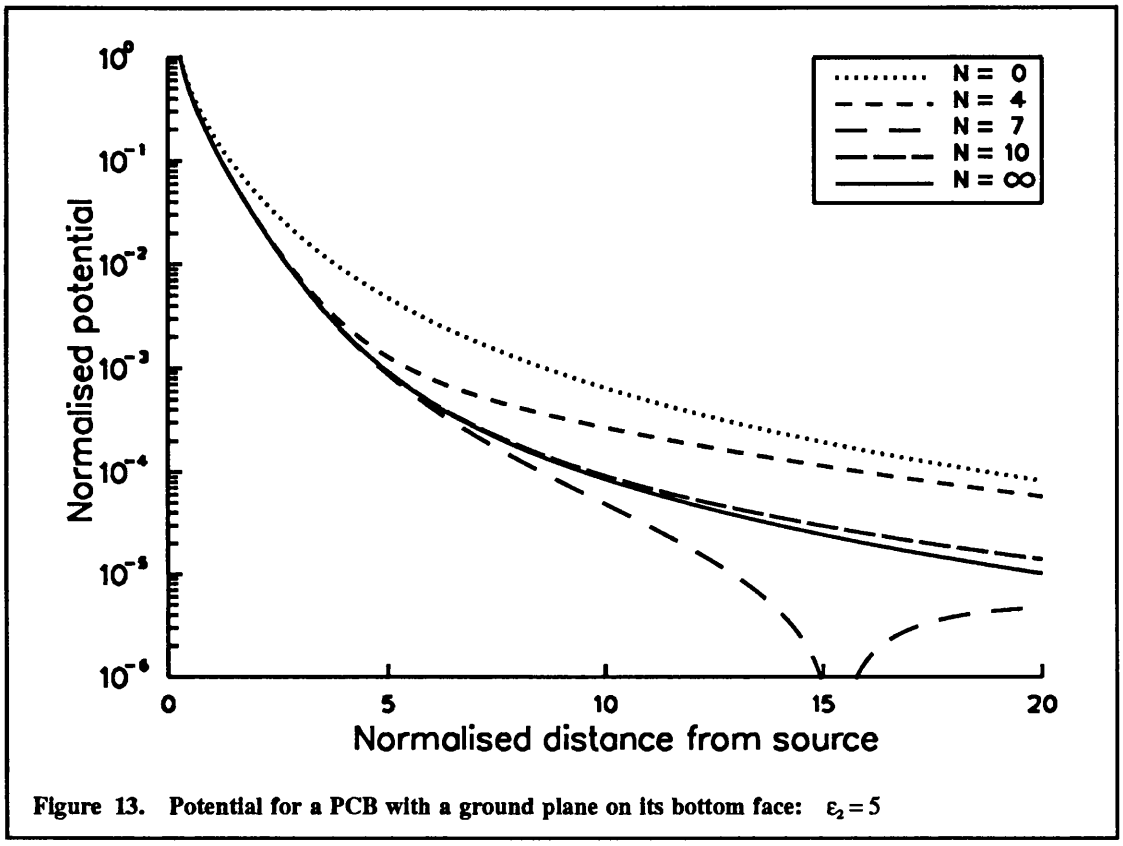

Figure 13. Potential for a PCB with a ground plane on its bottom face: $\varepsilon_2 = 5$

$$\phi_{cc}(x,y) = \frac{1+\beta}{4\pi\varepsilon_0\varepsilon_2} \sum_{n=0}^{N} \beta^{2n} \left[\xi(0,0,n,0) + \beta\, \xi(0,0,n+1,0) \right] \qquad (3.78)$$

Figure 11 shows the results for various values of the upper limit of summation N when $\varepsilon_2 = 5$, Figure 12 shows the same for $\varepsilon_2 = 20$. In the first case, the convergence is rapid, and putting $N = 4$ produces a nearly exact answer. The second case converges rather more slowly, but using $N = 10$ still gives a very good answer. This difference is because for $\varepsilon_2 = 5$, $\beta = 0.67$, whereas for $\varepsilon_2 = 20$, $\beta = 0.90$. Hence, for the latter case the series coefficients decrease more slowly with increasing n, so the higher terms in the series are given more weight than before, and more of them need to be included before their effect becomes negligible. As a partial compensation though, in the second case the potential drops off more rapidly close to the source, showing the confinement of the field by the high dielectric constant and reducing the effect of inaccuracies in the value of the potential.

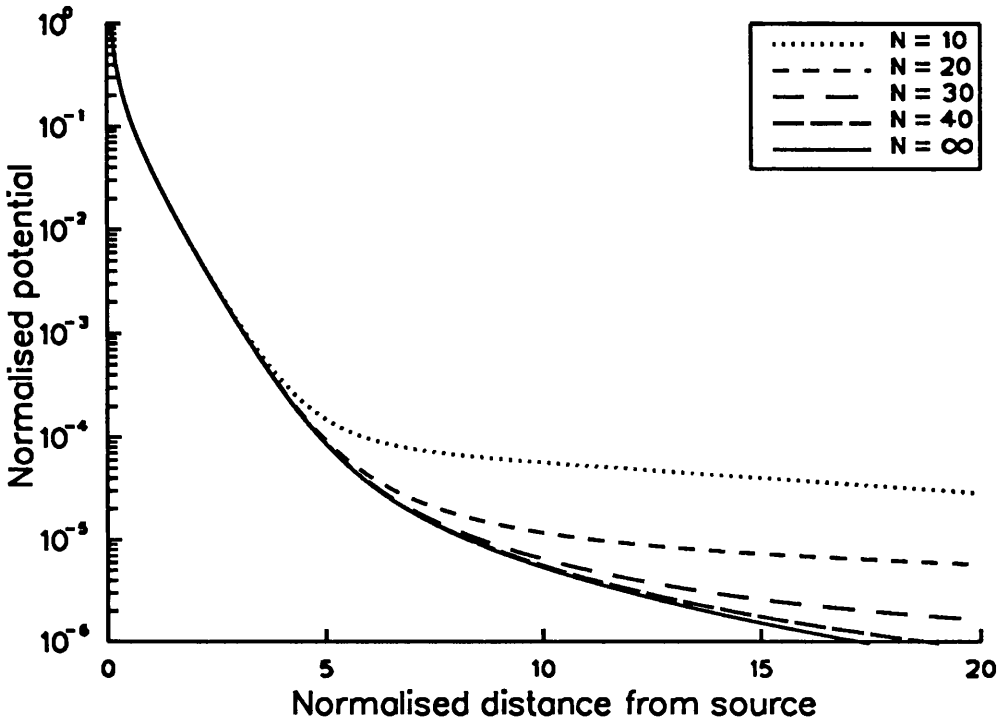

Figure 14. Potential for a PCB with a ground plane on its bottom face: $\varepsilon_2 = 20$

In both cases the series converge rapidly. Since the dielectric constant of typical PCB material is rarely much more than 5, putting $N=4$ should be accurate enough for most situations.

3.9.2 One Ground Plane, Two Dielectric Layers

This case is a PCB with a ground plane on its bottom face. The potential is derived from equation 3.68, using the same conditions as the previous section,

$$\phi_{cc}(x,y) = \frac{1+\beta}{4\pi\varepsilon_0\varepsilon_2} \sum_{n=0}^{N} (-\beta)^n \left[\xi(0,0,n,0) - \xi(0,0,n+1,0) \right] \qquad (3.79)$$

Figure 13 shows the results for various values of N when $\varepsilon_2 = 5$, and Figure 14 the same for $\varepsilon_2 = 20$. In both cases the convergence is slower than it was without a ground plane. This is partly because the magnitude of the series coefficients decreases less rapidly than before, falling off as β^n rather than β^{2n}, and partly because the coefficients now alternate in

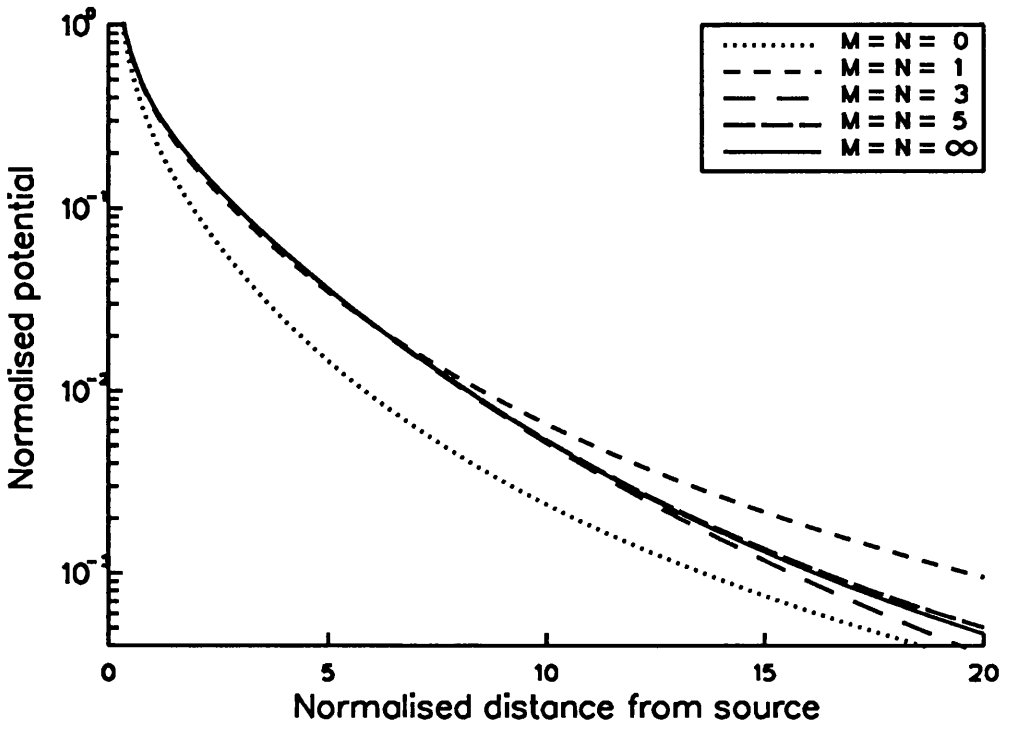

Figure 15. Potential for a PCB with a ground plane 1 board thickness from its bottom face

sign. This also accounts for the sharp dip in potential for $N = 7$ in Figure 13, which is where the calculated potential becomes negative. Note that sharp dips on a logarithmic scale only correspond to small changes on a linear scale, and the actual change is from a very small positive value to a very small negative value. This is possible with a series of alternating sign, but is not a problem here since it only appears to affect the results for a few values of N. The convergence is still quite fast when $\varepsilon_2 = 5$, and using $N = 10$ gives a very good answer. When $\varepsilon_2 = 20$ the convergence is slower, as before, and it is necessary to set $N = 40$ to achieve the same level of accuracy.

Note, however, that the potential is much reduced compared to the case with no ground plane - by a factor of about 5000 for $\varepsilon_2 = 5$, and of about 70,000 for $\varepsilon_2 = 20$ at a distance of 20 board thicknesses from the source. Hence, the slower convergence may not matter greatly in real problems as the potential may not be significant further than, say, five PCB thicknesses from the source charge.

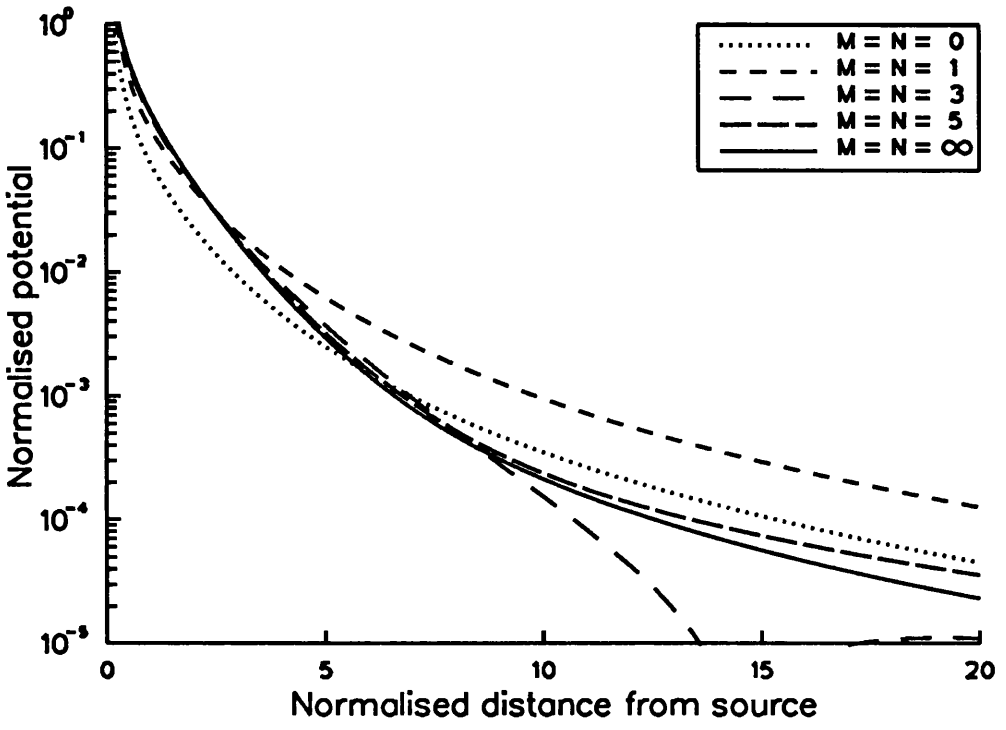

Figure 16. Potential for a PCB with a ground plane 0.1 board thicknesses from its bottom face

3.9.3 One Ground Plane, Three Dielectric Layers

This case is a PCB with a ground plane removed a distance d_1 from its bottom face. The potential is derived from equation 3.63 by setting $\alpha = \beta$ and changing the upper limits of the summations from infinity to M and N,

$$\phi_{cc}(x,y) = \frac{1+\beta}{4\pi\varepsilon_0\varepsilon_2} \sum_{m=0}^{M} \sum_{n=0}^{N} \beta^n K_{mn}(\beta) \times \left[\xi(0,m,n,0) - \xi(0,m+1,n+1,0) + \beta \{ \xi(0,m,n+1,0) - \xi(0,m+1,n,0) \} \right] \tag{3.80}$$

In this section the dielectric constant of layer 2 is fixed at $\varepsilon_2 = 5$, about that of typical PCB material, and the effect of varying the distance from the bottom face of the PCB to the ground plane is examined.

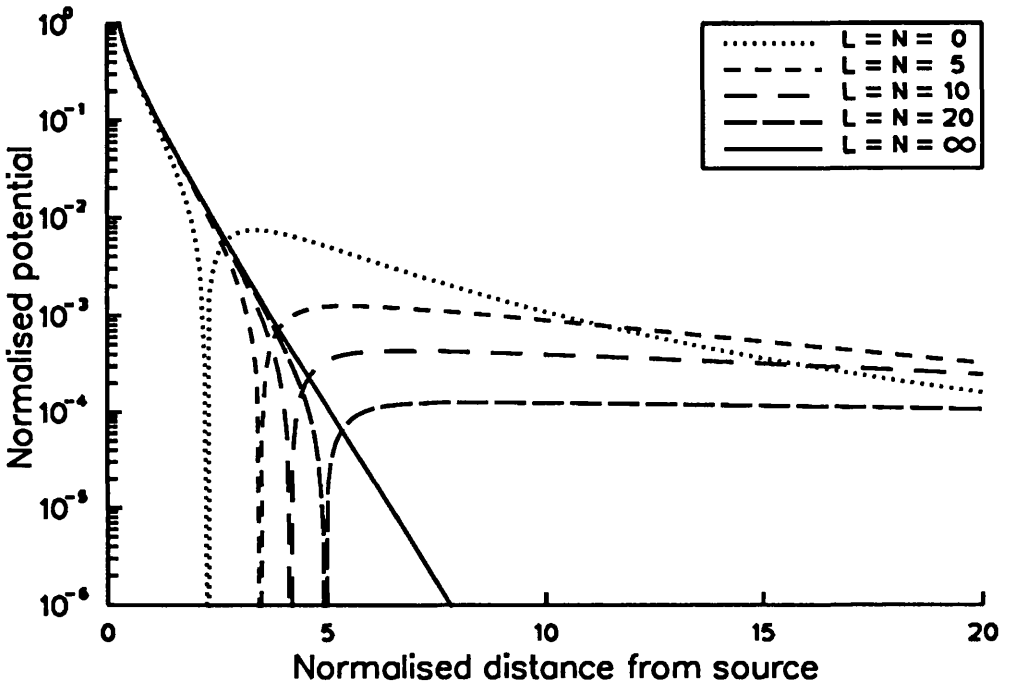

Figure 17. Potential for a PCB with a ground plane 1 board thickness from its top face and a ground plane on its bottom face

Figure 15 shows the results for $d_1 = c$, ie. placing the ground plane one board thickness from the bottom face of the PCB, and Figure 16 shows the results for $d_1 = 0.1c$. The convergence is better with the ground plane further away, which might be anticipated since the convergence of the previous cases was faster with no ground plane than with the ground plane on the bottom face of the PCB. In both cases the results are very good for $M = N = 5$, and in the first case putting $M = N = 3$ also gives very good results. The total number of terms needed is not many more than before, $M = N = 3$ corresponding to 16 terms and $M = N = 5$ to 36 terms.

The values of the potentials fall between the previous results for $\varepsilon_2 = 5$ (in Figure 11 and Figure 13), that with $d_1 = c$ being closer to the case with three dielectric layers, no ground planes and that with $d_1 = c$ being closer to the case with two dielectric layers and one ground plane. Because the potential falls off rather more rapidly with the closer ground plane, the slightly worse convergence in this case may be of reduced importance in practice.

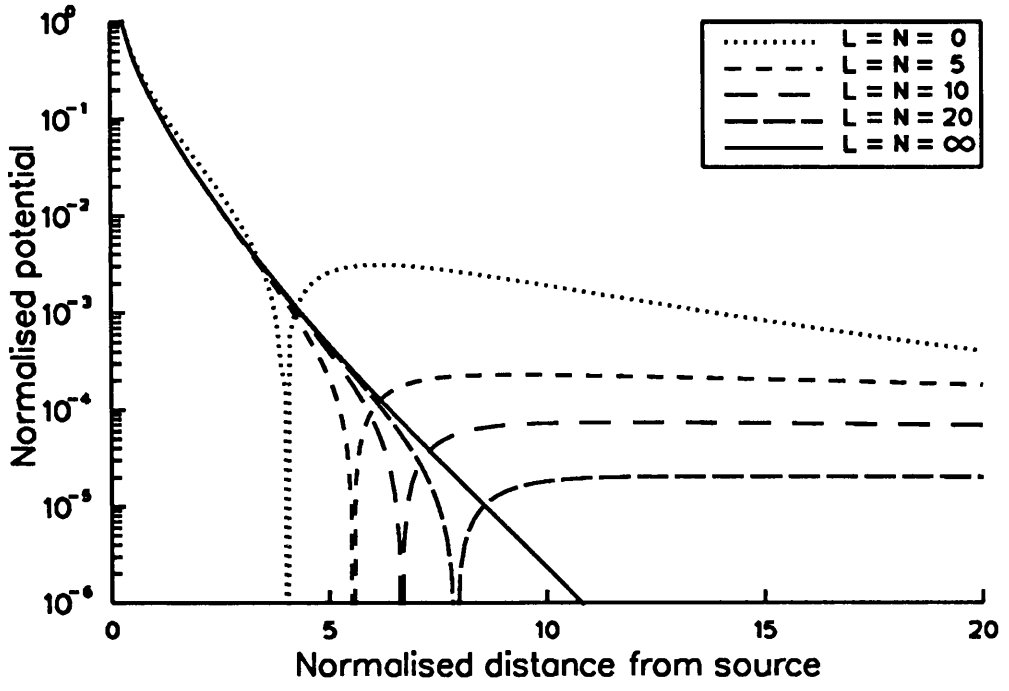

Figure 18. Potential for a PCB with a ground plane 3 board thicknesses from its top face and a ground plane on its bottom face

3.9.4 Two Ground Planes, Two Dielectric Layers

This case is a PCB with one ground plane on its bottom face and a second one placed a distance d_2 from its top face. The potential is derived from equation 3.67, setting the upper limits of summation to L and N,

$$\phi_{cc}(x,y) = \frac{1+\beta}{4\pi\varepsilon_0\varepsilon_2}\sum_{l=0}^{L}\sum_{n=0}^{N}(-1)^n K_{ln}(\beta) \times \left[\xi(l,0,n,0) + \xi(l+1,0,n+1,0) - \xi(l,0,n+1,0) - \xi(l+1,0,n,0) \right] \tag{3.81}$$

In this section the dielectric constant of layer 2 is again fixed at $\varepsilon_2 = 5$, and the effect of varying the distance from the top face of the PCB to the second ground plane is examined.

Figure 17 shows the results for $d_2 = c$, ie. placing the ground plane one board thickness from the top face of the PCB, and Figure 18 shows the results for $d_2 = 3c$. It is immediately

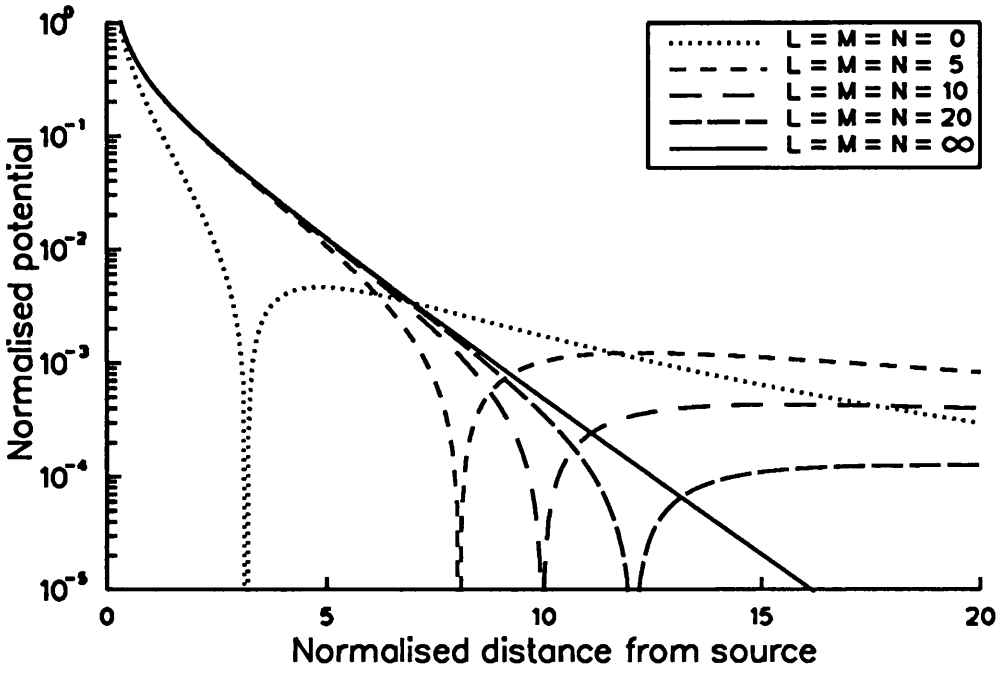

Figure 19. Potential for a PCB with ground planes 1 board thickness from its top face and 1 board thickness from its bottom face

apparent that the presence of the second ground plane has a large effect on both the value of the potential and the convergence of the series. The potential now falls away vary much more rapidly than for the previous cases, and faster for $d_2 = c$ than for $d_2 = 3c$, as would be expected. There are also sharp dips in the potential, where it becomes negative, as noted before. Here, this is a more serious effect, occurring for all values of L and N, but at a greater distance from the source as the number of terms is increased. The effect is rather worse for the ground plane one board thickness from the top PCB surface than with it three board thicknesses away, as would be expected from the behaviour of previous results.

Because the potential does fall off very rapidly, taking $L = N = 5$ and setting the potential to zero when it is computed with a negative value will produce an approximation as accurate as those suggested in previous cases, which may be useful for practical situations.

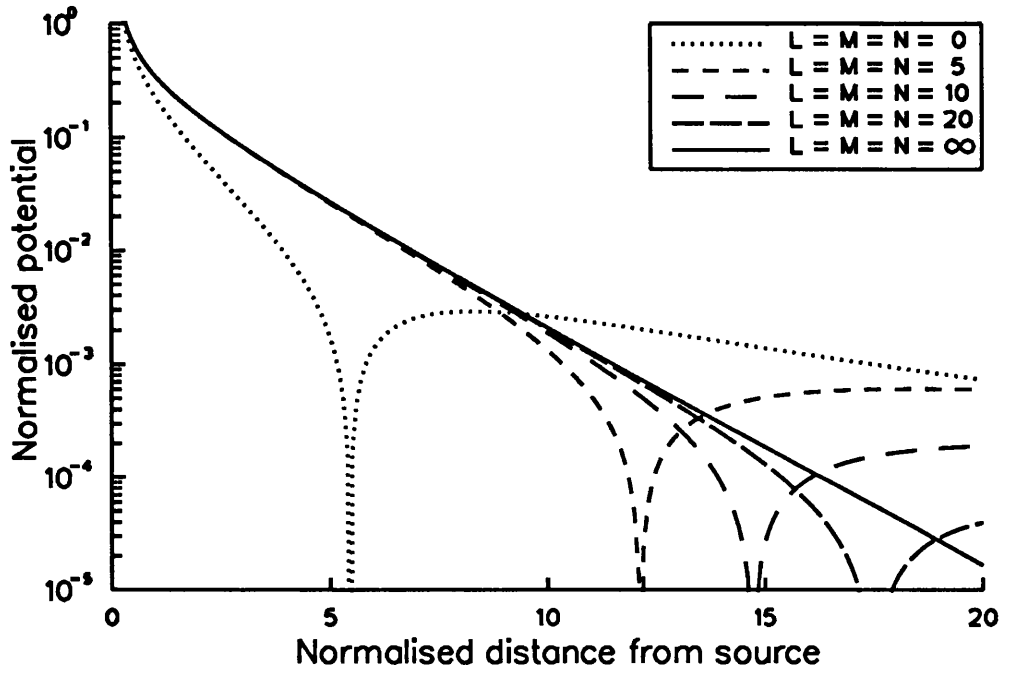

Figure 20. Potential for a PCB with ground planes 3 board thicknesses from its top face and 1 board thickness from its bottom face

3.9.5 Two Ground Planes, Three Dielectric Layers

This case is the most general one of a PCB with ground planes above and below it, separated by air gaps from the PCB dielectric. The potential is derived from equation 3.60, setting the upper limits of summation to L, M and N,

$$\begin{aligned}\phi_{cc}(x,y) = \frac{1+\beta}{4\pi\varepsilon_0\varepsilon_2}\sum_{l=0}^{L}\sum_{m=0}^{M}\sum_{n=0}^{N}K_{mn}(\alpha)\,K_{ln}(\beta)\,\times \\ \Big[\quad \xi(l,\ m\ ,\ n\ ,0) + \xi(l+1,m+1,n+1,0) \\ - \xi(l,m+1,n+1,0) - \xi(l+1,\ m\ ,\ n\ ,0) \\ +\alpha\ \{\ \xi(l,\ m\ ,n+1,0) + \xi(l+1,m+1,\ n\ ,0) \\ - \xi(l,m+1,\ n\ ,0) - \xi(l+1,\ m\ ,n+1,0)\ \}\ \Big]\end{aligned} \tag{3.82}$$

The results shown are for the dielectric constant of layer 2 fixed at $\varepsilon_2 = 5$, d_1 fixed at one board thickness, and d_2 set to one board thickness (in Figure 19) and three board thicknesses (in Figure 20).

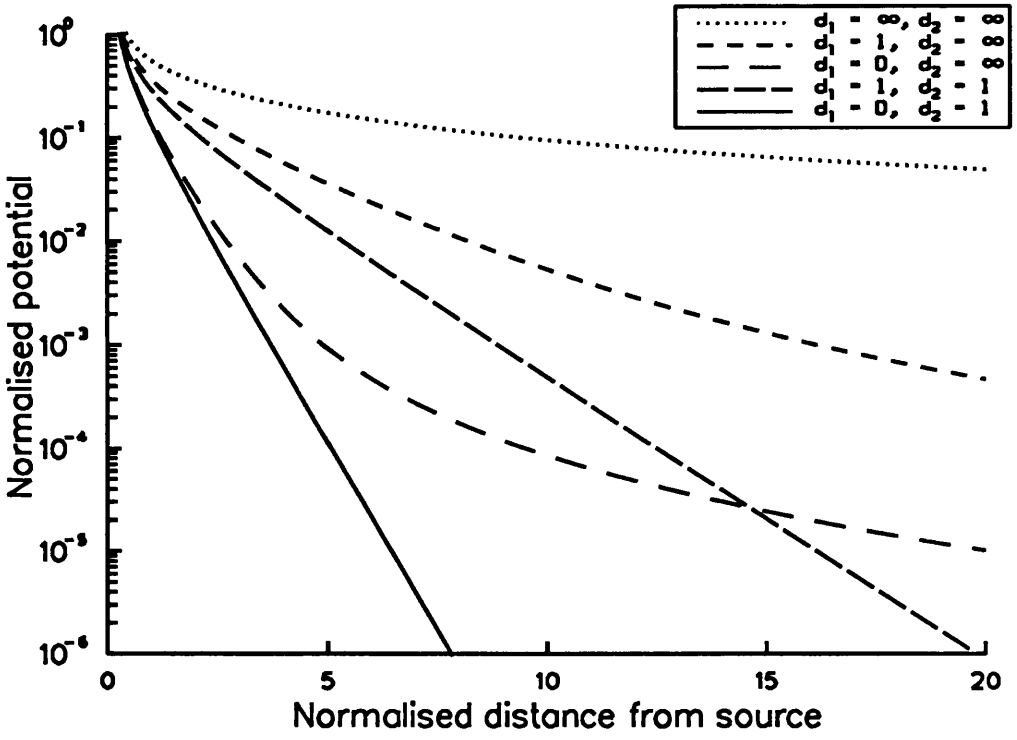

Figure 21. Potentials for various cases of ground plane positions

The potential is now obtained from a triple summation. As might be expected from previous results, the convergence is reasonably slow, and has the same behaviour as that for two ground planes and two dielectric layers in the previous section. Setting $L=M=N=5$ may be sufficiently accurate for use in practical problems, but even this results in 216 terms in the summation.

3.9.6 Summary

The discussion in this section has shown the behaviour of the solutions derived for the potential. The forms ranged from the simplest, with no ground planes and a single summation, to the most complex, with two ground planes and a triple summation. Figure 21 shows the solutions for several of these cases, all with $\varepsilon_2 = 5$ and $\varepsilon_1 = \varepsilon_3 = 1$, put together for ease of comparison. This also illustrates that the more ground planes that are present, and the closer they are to the PCB, the faster the potential is attenuated.

3.10 Conclusions

This chapter has considered the problem of evaluating the potential due to a unit point charge or point current, which yield the electrostatic scalar potential Green's function and the magnetostatic vector potential Green's function respectively. This problem was posed for a region consisting of three dielectric layers bounded by two ground planes, all of infinite extent in two dimensions (x and y). Solutions for the potential anywhere in the structure due to a point source placed anywhere were found. The solutions were obtained in the spectral domain, and by expanding these as infinite series the transform back to the spatial domain was made possible.

The results obtained were then used to generate results for simpler cases, with fewer dielectric layers or fewer ground planes. The convergence of the series was examined, and they were found to converge rapidly, with the partial exception of the most general case. Another advantage of the simpler cases was demonstrated by this: as well as being expressed in a simpler form, their expansions converged more rapidly. This method could, in principle, be used for any number of dielectric layers, but the mathematical complexity would become too great and the resulting series would not converge rapidly enough to be of practical use.

The next two chapters make use of the Green's functions developed here, describing the way they are incorporated into FACET. Chapter 4 uses the vector potential Green's function in the computation of the inductance of vias. Chapter 5 uses both scalar and vector potential Green's functions, convolving them with various basis functions defined on rectangular and triangular elements. In both these applications, the ease of computation and accuracy of the Green's functions has been very useful.

Chapter 4
Modelling the Inductance of Vias

4.1 Introduction

Vias are holes in the dielectric material of a printed circuit board (PCB), perpendicular to its surface and usually plated with solder. They are either used to connect different layers of metallisation or as a point of attachment for the leads of wire ended components. The inductance of these vias is assumed to be much more significant than their capacitance to other conductors. In particular, when a via is part of an ground return path its impedance, due mainly to inductance at radio frequencies, may be critical. This chapter describes the model developed for the inductance of vias. These are treated as hollow thin-walled cylinders, with a uniform current flow along their surface in an axial direction.

The model is developed in the following way. Firstly the basic definitions of inductance are derived in an appropriate form. The equation for the vector potential due to current flow along a hollow cylinder, used in the computation of the inductances, is derived from the results of Chapter 3, and the numerical method chosen for its evaluation described. This is then used to derive the self inductance of a via and the mutual inductance between two parallel vias. For the case of the mutual inductance approximate expressions are also derived, which can be evaluated much more rapidly than the exact forms, and their accuracy is examined. Finally, the internal impedance of a via is examined.

4.2 Definitions of Inductance

4.2.1 Mutual Inductance

Consider a set of current-carrying conductor loops in free space. A current I_i flowing in the i^{th} loop produces a magnetic field $\mathbf{B}_i$. This results in a magnetic flux ψ_{ij} linking the j^{th} loop, where

$$\psi_{ij} = \int_{S_j} \mathbf{B}_i \cdot d\mathbf{S}_j \tag{4.1}$$

The integral is over any open surface S_j bounded by the j^{th} loop, and $d\mathbf{S}_j$ is the outward normal to this surface. The mutual inductance L_{ij} between the two loops is defined as the flux linking the j^{th} loop due to a unit current flowing in the i^{th} loop,

$$L_{ij} = \frac{\psi_{ij}}{I_i} \tag{4.2}$$

It can be shown from the theorem of reciprocity [Morse and Feshbach, 1953, p.883] that $L_{ij} = L_{ji}$. The magnetic field **B** is expressed in terms of a vector potential **A**, in the same way as in Chapter 2, where

$$\mathbf{B} = \nabla \times \mathbf{A} \tag{4.3}$$

The solutions for the vector potential which will be needed later in this chapter were derived in section 3.7. Equation 4.1 can be rewritten in terms of the vector potential using Stokes' Law [Morse and Feshbach, 1953, p.43]. For a unit current flowing in the i^{th} loop, this can be combined with equation 4.2 to give the mutual inductance between the two loops as

$$L_{ij} = \int_{l_j} \mathbf{A}_i \cdot d\mathbf{l}_j \tag{4.4}$$

where the integral is now around the j^{th} loop and $d\mathbf{l}_j$ is directed around this loop in the direction of current flow. If the conductor forming the loop cannot be assumed to be thin, then the above equation must be modified to average the contributions to the integral over its cross section. If the cross sectional area is taken to be a constant, a_j, and y and z are the co-ordinates normal to the local current flow direction, the result is,

$$L_{ij} = \frac{1}{a_j} \int\int_{a_j} \int_{l_j} \mathbf{A}_i \cdot d\mathbf{l}_j \, dy \, dz \tag{4.5}$$

This is the form used to calculate inductances in this chapter, and is also the form used in equation 2.21 of Chapter 2.

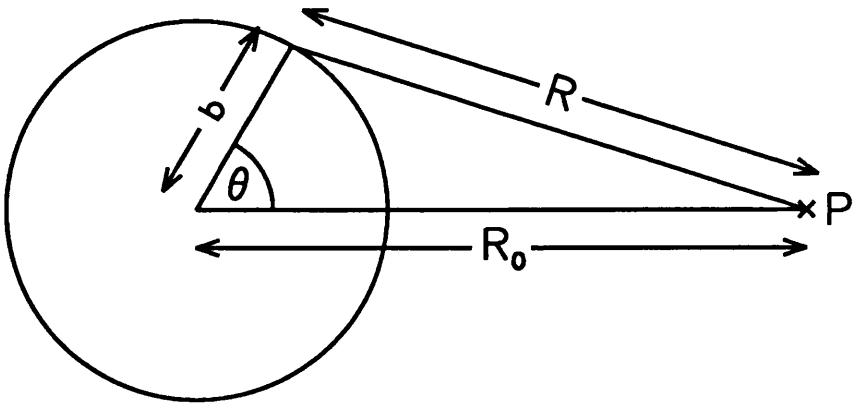

Figure 22. Co-ordinates used for via geometry

4.2.2 Partial Inductance

The discussion so far has related to current loops. However, it is often convenient to consider the constituent parts of these loops separately. For example, part of a loop might consist of PCB tracks, part of vias (the subject of this chapter) and part of external connections. Equation 4.5 involves the integral of the vector potential around the j^{th} current loop, and could with no loss of generality be partitioned into several integrals, each over a part of this loop. Equally, the i^{th} loop could be split into several parts, each contributing independently to $\mathbf{A}_i$.

Each inductance defined by equation 4.5 can therefore be partitioned into a set of *partial inductances*, as defined by Ruehli [1987]. These can then be manipulated as inductances in their own right. With these definitions the inductance problem for a general set of conductors breaks down into three parts:

- Split the conductors into a number of suitable elements
- Compute the vector potential due to unit current flow in these elements
- Compute the full set of partial inductances between elements

When these partial inductances are combined and used in a circuit simulator, the correct behaviour of the current loops will be obtained.

4.3 Computation of the Vector Potential

Figure 22 shows a section perpendicular to the axis of the via, which is of length $2a$ and radius b. The vector potential is required at an observation point P. The local co-ordinates which will be used are cylindrical. The x axis is coincident with the axis of the via, and the via extends from $x=-a$ to $x=a$. The angle co-ordinate θ is measured anticlockwise from the line between the centre of the via and the observation point P. In these co-ordinates, (r, θ, x) the observation point is situated at $(R_0, 0, x_0)$. The via is assumed to be a hollow, thin walled cylinder, with a uniform current density around its circumference directed parallel to the x axis. The current per unit length around the circumference is of magnitude $\frac{1}{2\pi b} A$, so that a total current of 1 amp flows through the via. This value is used entirely for convenience, since inductance is then numerically equal to flux, as shown by equation 4.2.

Because the current is directed parallel to the x axis, the only component of the vector potential A that is non-zero is the x component A_x, as can be seen from equation 3.11 for the vector potential. The PCB material is assumed to have the same permeability as air, μ_0, so the region being considered is homogeneous. This remains true even if there is an ideal infinite ground plane parallel to the PCB (allowed in a FACET simulation), since this is perpendicular to the vias and therefore has no effect, as discussed in section 3.7. The walls of the cylinder are thin, so no integration over r is needed to find this component, which is

$$\begin{aligned} A_x &= \frac{\mu_0}{8\pi^2 b} \int_0^{2\pi} \int_{-a}^{a} \frac{b\, dx\, d\theta}{\sqrt{R^2 + (x - x_0)^2}} \\ &= \frac{\mu_0}{4\pi^2} \int_0^{\pi} \ln\left[\frac{a - x_0 + \sqrt{R^2 + (a - x_0)^2}}{-a - x_0 + \sqrt{R^2 + (a + x_0)^2}} \right] d\theta \end{aligned} \tag{4.6}$$

R in the above equation is a function of θ. The cosine rule can be used to express it in terms of b and R_0 (which are constants) and θ,

$$R^2 = b^2 + R_0^2 - 2bR_0 \cos\theta \tag{4.7}$$

The substitution $\alpha = \theta/2$ is useful. In terms of α, R is

$$R^2 = (R_0 - b)^2 + 4bR_0 \sin^2\alpha \tag{4.8}$$

Noting also that $d\theta = 2d\alpha$, equation 4.6 is transformed into the form used for computations,

$$A_x = \frac{\mu_0}{2\pi^2} \int_0^{\frac{\pi}{2}} \ln\left[\frac{a - x_0 + \sqrt{(R_0 - b)^2 + 4bR_0 \sin^2\alpha + (a - x_0)^2}}{-a - x_0 + \sqrt{(R_0 - b)^2 + 4bR_0 \sin^2\alpha + (a + x_0)^2}} \right] d\alpha \tag{4.9}$$

4.3.1 Evaluation of the Integral

Equation 4.9 has to be integrated numerically. Two methods have been used: Simpson's rule [Matthews and Walker, 1970, pp.349-353], and a set of rules due to Patterson[1968]. The use of these is discussed in more detail in Chapter 5. Both these methods are used in an iterative way, using more integrand values until the required level of convergence is achieved. This is usually after only two or three rules, involving at most 15 or so integrand evaluations. The subroutine takes about 0.75ms to run using three rules and about 0.35ms using two rules.

4.4 Self Inductance of a Via

Equation 4.5 shows that the self inductance of the via is found by integrating the x component of the vector potential over its surface. The via is thin walled, so the cross-sectional area a_j in equation 4.5 is replaced by the circumference of the via, $2\pi b$ and no radial integration is performed. Since the vector potential was derived for unit current, the self inductance of the via is numerically equal to the flux linking the via. Denoting the self inductance by L_{ii}, and noting that $\mathbf{A}.\mathbf{dl} = A_x dx_0$, equation 4.5 becomes

$$L_{ii} = \frac{1}{2\pi b}\int_{-a}^{a}\int_{0}^{2\pi} A_x\, b\, d\theta\, dx_0 = \int_{-a}^{a} A_x\, dx_0 \tag{4.10}$$

since A_x is independent of θ. The problem now is to perform the integration. This can be tackled by setting up a function

$$f(\xi, R) = \ln\left[\xi + \sqrt{R^2+\xi^2}\,\right] \tag{4.11}$$

which when integrated with respect to ξ gives

$$\int f(\xi, R)\, d\xi = \xi \ln\left[\xi + \sqrt{R^2+\xi^2}\,\right] - \sqrt{R^2+\xi^2} \tag{4.12}$$

Using the function $f(\xi, R)$, the self inductance of equation 4.10 can be written as

$$L_{ii} = \frac{\mu_0}{4\pi^2}\int_{0}^{\pi}\left[\int_{0}^{2a} f(\xi, R)\, d\xi - \int_{-2a}^{0} f(\xi, R)\, d\xi\right] d\theta \tag{4.13}$$

Using equation 4.12, performing the two inner integrations and combining the results then gives for the inner term

$$\left[\int_{0}^{2a} f(\xi, R)\, d\xi - \int_{-2a}^{0} f(\xi, R)\, d\xi\right] = 2a \ln\left[\frac{2a+\sqrt{R^2+4a^2}}{-2a+\sqrt{R^2+4a^2}}\right] - 2\sqrt{R^2+4a^2} + 2R \tag{4.14}$$

For the self inductance, R_0 in Figure 22 is constant and equal to the radius of the via, b. From equation 4.7, the expression for R to be used in the above equation is therefore $R^2 = 2b^2(1-\cos\theta)$.

Equation 4.14 now has to be integrated over θ. No analytic solution to this integral has been found, but it can be written in a simplified form, the derivation of which is detailed in Appendix E. Briefly, the second term results in an elliptic integral of the second kind (see

formula 2.576.2 in Gradshteyn and Ryzhik [1980]), and the integration of the third term is trivial. The resulting expression for the self inductance is

$$L_{ii} = \frac{2\mu_0}{\pi^2}\left[a\int_0^{\frac{\pi}{2}} \ln\left[\frac{2a}{b} + \sqrt{\frac{4a^2}{b^2} + 4\sin^2\alpha}\right] d\alpha \right. \\ \left. - \sqrt{a^2+b^2}\, E\left(\frac{b}{\sqrt{a^2+b^2}}\right) + b \right] \tag{4.15}$$

where E is the complete elliptic integral of the second kind.

4.4.1 Evaluation of the Numerical Integral

The first term in equation 4.15 has to be integrated numerically. This is done in the same way as for the vector potential in section 4.3.1, with the exception that the number of rules in the numerical integration is fixed at 2. This has been found to give better than 0.1% accuracy provided that the length of the via is at least a tenth of its radius, which is always the case. Only 7 integrand evaluations are required to give this answer, so the routine is fast - taking about 23ms to run.

4.4.2 Evaluation of the Elliptic Integral

The second term in equation 4.15 involves the complete elliptic integral of the second kind. This is evaluated using a four term expansion given by Cody [1965]. For the integral $E(k)$ this is

$$E(k) \approx 1 + 0.4630106\eta + 0.1077857\eta^2 \\ + [\,0.2452740\eta + 0.04125321\eta^2\,] \times \ln\left(\frac{1}{\eta}\right) \tag{4.16}$$

where $\eta = 1 - k^2$. The maximum error in this approximation is 3.91×10^{-5}. Since $1 \le E(k) \le \frac{\pi}{2}$, this is perfectly acceptable.

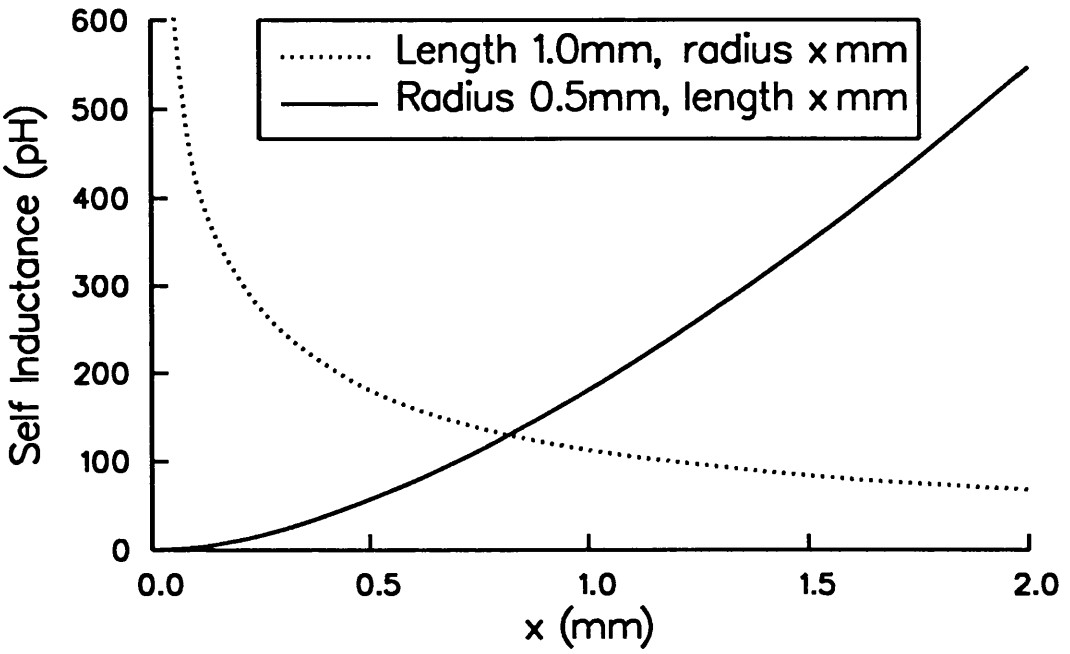

Figure 23. Self inductance of a via of varying size

4.4.3 Results

Two sets of results are shown in Figure 23 to show the behaviour of the model. The first is for a via of length 1mm and radius between 0 and 2mm. The self inductance approaches infinity as the radius approaches zero, which is to be expected because of the terms in $1/b$ in equation 4.15.

The second set of results is for a via of radius 0.5mm and length between 0 and 2mm. The self inductance of a very long via would be expected to be proportional to its length. For shorter vias doubling the length more than doubles the self inductance because of the extra mutual inductance between the two halves. This reinforcing effect reduces with length because of the reduction in mutual inductance with separation.

These results show that the predicted self inductance varies in a reasonable manner when the length and radius of the via are varied. The values predicted are also reasonable when compared with those predicted for tracks in FACET, although details are not given here.

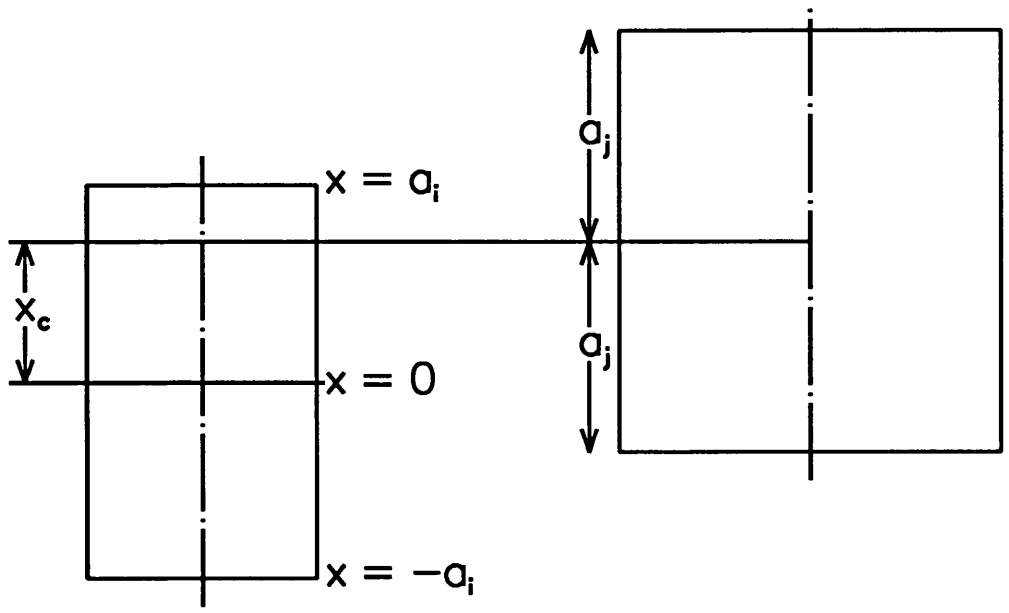

Figure 24. Geometry used for mutual inductance calculations: section through via axes

4.5 Computation of the Mutual Inductance Between Vias

Expressions for the mutual inductance between two vias can now be worked out, proceeding along similar lines to the derivation of the self inductance. In practical cases all vias are parallel to one another: here both vias are assumed to be parallel to the x axis. A section through the via axes is shown in Figure 24, and a section through the vias perpendicular to their axes is shown in Figure 25. The first via is of length $2a_i$ and radius b_i. It is centred at $x=0$, and so extends from $x=-a_i$ to $x=a_i$. The second via is of length $2a_j$ and radius b_j. It is centred at $x=x_c$, and so extends from $x=x_c-a_i$ to $x=x_c+a_i$.

The full solution for the mutual inductance is derived below, treating both vias as hollow cylinders and resulting in some rather complex expressions. Various approximations are then investigated to find an approach that gives results much faster and with sufficient accuracy.

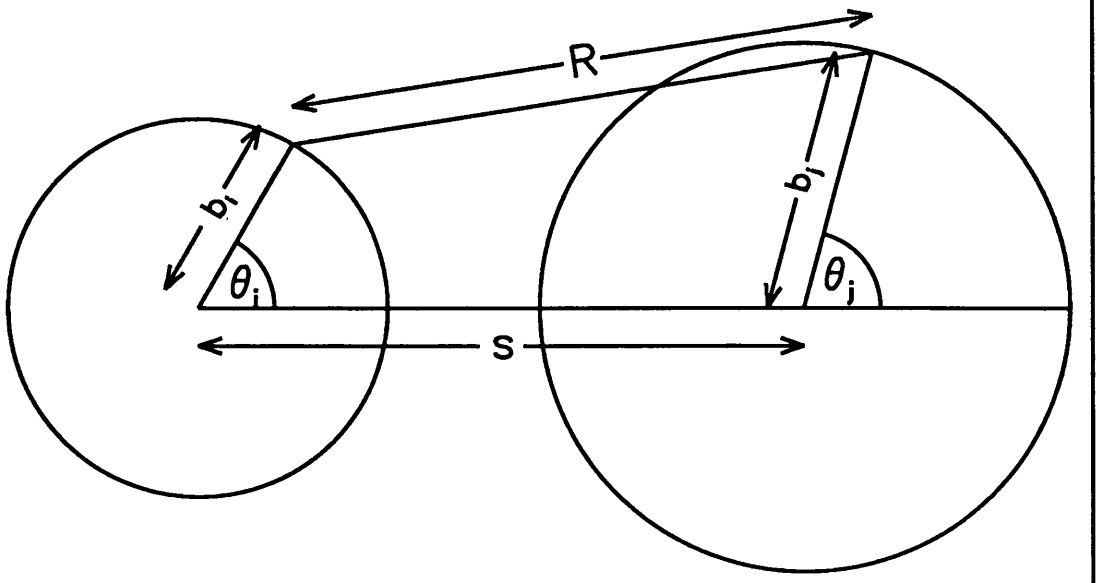

Figure 25. Geometry used for mutual inductance calculations: section perpendicular to via axes

4.5.1 Full Calculation

To calculate the mutual inductance, the distance R between two arbitrary points on the via circumferences in the plane perpendicular to their axes is needed. With θ_i and θ_j as defined in Figure 25, and s as the separation of the via axes in this plane, this distance can be shown to be,

$$R^2 = s^2 + b_i^2 + b_j^2 - 2b_i b_j \cos(\theta_i - \theta_j) + 2s(b_j \cos\theta_j - b_i \cos\theta_i) \tag{4.17}$$

Denoting the x component of the vector potential due to unit current flow in the first via by A_{x_i}, the mutual inductance between the two vias is

$$\begin{aligned} L_{ij} &= \frac{1}{2\pi b_j} \int_0^{2\pi} \int_{x_c - a_j}^{x_c + a_j} A_{x_i}\, b_j\, dx_j\, d\theta_j \\ &= \frac{1}{2\pi} \int_0^{2\pi} \int_{x_c - a_j}^{x_c + a_j} A_{x_i}\, dx_j\, d\theta_j \end{aligned} \tag{4.18}$$

The integral over θ_j cannot be reduced to $2\int_0^{\pi}$ as before because the vector potential is no longer symmetrical about $\theta_j = \pi$. Similarly, the integral to give the vector potential is

asymmetrical about $\theta_i = 0$. The vector potential A_x at the point (b_j, θ_j, x_j) on the second via is therefore

$$A_{x_i} = \frac{\mu_0}{8\pi^2} \int_0^{2\pi} \ln\left[\frac{a_i - x_j + \sqrt{R^2 + (a_i - x_j)^2}}{-a_i - x_j + \sqrt{R^2 + (a_i + x_j)^2}} \right] d\theta_i \tag{4.19}$$

The full expression for the mutual inductance between the two vias is therefore

$$L_{ij} = \frac{\mu_0}{16\pi^3} \int_0^{2\pi} \int_0^{2\pi} \int_{x_c - a_j}^{x_c + a_j} \ln\left[\frac{a_i - x_j + \sqrt{R^2 + (a_i - x_j)^2}}{-a_i - x_j + \sqrt{R^2 + (a_i + x_j)^2}} \right] dx_j d\theta_i d\theta_j \tag{4.20}$$

The inner integral, over x_j, is identical in form to that already evaluated for the self inductance, but with more complicated limits. Call this integral I'. It is turned into the required form (equation 4.11) by splitting the logarithm into two parts, and performing the substitutions $\xi = a_i - x_j$ and $\xi = -a_i - x_j$ respectively on the two halves. This gives

$$I' = \int_{\xi_1}^{\xi_2} f(\xi, R)\, d\xi - \int_{\xi_3}^{\xi_4} f(\xi, R)\, d\xi \tag{4.21}$$

where the limits ξ_1 to ξ_4 are given by

$$\begin{aligned} \xi_1 &= a_i - a_j - x_c & \xi_2 &= a_i + a_j - x_c \\ \xi_3 &= -a_j - a_i - x_c & \xi_4 &= a_j - a_i - x_c \end{aligned} \tag{4.22}$$

The discussion is simplified by introducing the functions $I'_1(\xi)$ and $I'_2(\xi)$

$$\begin{aligned} I'_1(\xi) &= \xi \ln\left[\xi + \sqrt{R^2 + \xi^2} \right] \\ I'_2(\xi) &= \sqrt{R^2 + \xi^2} \end{aligned} \tag{4.23}$$

Using equation 4.12 and the above functions, I' can be written as

$$I' = I'_1(\xi_2) - I'_1(\xi_1) - I'_1(\xi_4) + I'_1(\xi_3) - I'_2(\xi_2) + I'_2(\xi_1) + I'_2(\xi_4) - I'_2(\xi_3) \tag{4.24}$$

This result now has to be integrated with respect to θ_i and θ_j to give the mutual inductance. No analytic solution for the integration of $I'_1(\xi)$ has been found, and so this has to be performed numerically (using the NAG subroutine D01DAF [NAG, 1988]). However, some progress can be made with the second function $I'_2(\xi)$. Equation 4.17 for R can be expanded and rearranged to

$$\begin{aligned} R^2 = {} & \{s^2 + b_i^2 + b_j^2 + 2sb_j \cos\theta_j\} - \{2b_i(b_j \cos\theta_j + s)\} \cos\theta_i \\ & - \{2b_i b_j \sin\theta_j\} \sin\theta_i \end{aligned} \tag{4.25}$$

Formula 3.032.1 in Gradshteyn and Ryzhik [1980] is

$$\int_0^{2\pi} f(p\cos x + q\sin x)\,dx = 2\int_0^{\pi} f\left(\sqrt{p^2+q^2}\cos x\right) dx \tag{4.26}$$

Therefore set

$$\begin{aligned} c_1 &= s^2 + b_i^2 + b_j^2 + 2sb_j\cos\theta_j \\ c_2 &= \sqrt{\{2b_i(b_j\cos\theta_j + s)\}^2 + \{2b_i b_j \sin\theta_j\}^2} \end{aligned} \tag{4.27}$$

The integral of I'_2 over θ_i can now be performed, using formula 2.576.1 in Gradshteyn and Ryzhik [1980], to give

$$\begin{aligned} \int_0^{2\pi} \sqrt{R^2+\xi^2}\,d\theta_i &= 2\int_0^{\pi} \sqrt{c_1 + \xi^2 + c_2\cos\theta_i}\,d\theta_i \\ &= 4\sqrt{c_1 + c_2 + \xi^2}\, E\left(\sqrt{\frac{2c_2}{c_1 + c_2 + \xi^2}}\right) \end{aligned} \tag{4.28}$$

where E is the complete elliptic integral of the second kind. When c_1 and c_2 are expanded as functions of θ_j, the resulting expression is rather complicated, and no analytic solution for the integral over θ_j has been found. This remaining single integral is therefore performed numerically, using the method described in section 4.3.1.

This section presented in some detail the full calculation of the mutual inductance between two vias when both are treated as hollow cylinders. This result takes rather a long time to compute, principally because of the double numerical integration of I'_1. The main use for the results obtained from this section is therefore to compare with the results from the following sections, where various approximations are used, as a check on their accuracy.

4.5.2 Approximations for the Mutual Inductance

An approximation to the mutual inductance can be obtained by treating one or both vias as a filament of current, or a thin wire. The expressions derived above can then be greatly simplified.

4.5.2.1 Treating One Via as a Thin Wire

For this case, the second via is treated as a thin wire, so $b_j = 0$. The expression for R in equation 4.17 simplifies to

$$R^2 = s^2 + b_i^2 - 2sb_i \cos\theta_i \tag{4.29}$$

This is no longer a function of θ_j, so the integration over θ_j can be replaced with a multiplication by 2π. The integration of I'_1 over θ_i still has to be performed numerically, although it is now symmetrical about $\theta_i = \pi$. This is done in the same way as for the self inductance in section 4.4.1. Again, only 7 integrand evaluations are needed for results of sufficient accuracy. The integration of I'_2 results in a simpler form of the elliptic integral in equation 4.28

$$I^{el}(\xi) = \int_0^{2\pi} \sqrt{R^2 + \xi^2}\, d\theta_i = 4\sqrt{(b_i+s)^2 + \xi^2}\, E\left(\sqrt{\frac{4b_i s}{(b_i+s)^2 + \xi^2}}\right) \tag{4.30}$$

The full expression for the mutual inductance can therefore be written as

$$\begin{aligned} L_{ij} = {} & \frac{\mu_0}{4\pi^2} \int_0^{\pi} \left[I'_1(\xi_2) - I'_1(\xi_1) - I'_1(\xi_4) + I'_1(\xi_3)\right] d\theta_i \\ & - \frac{\mu_0}{2\pi^2} \left[I^{el}(\xi_2) - I^{el}(\xi_1) - I^{el}(\xi_4) + I^{el}(\xi_3)\right] \end{aligned} \tag{4.31}$$

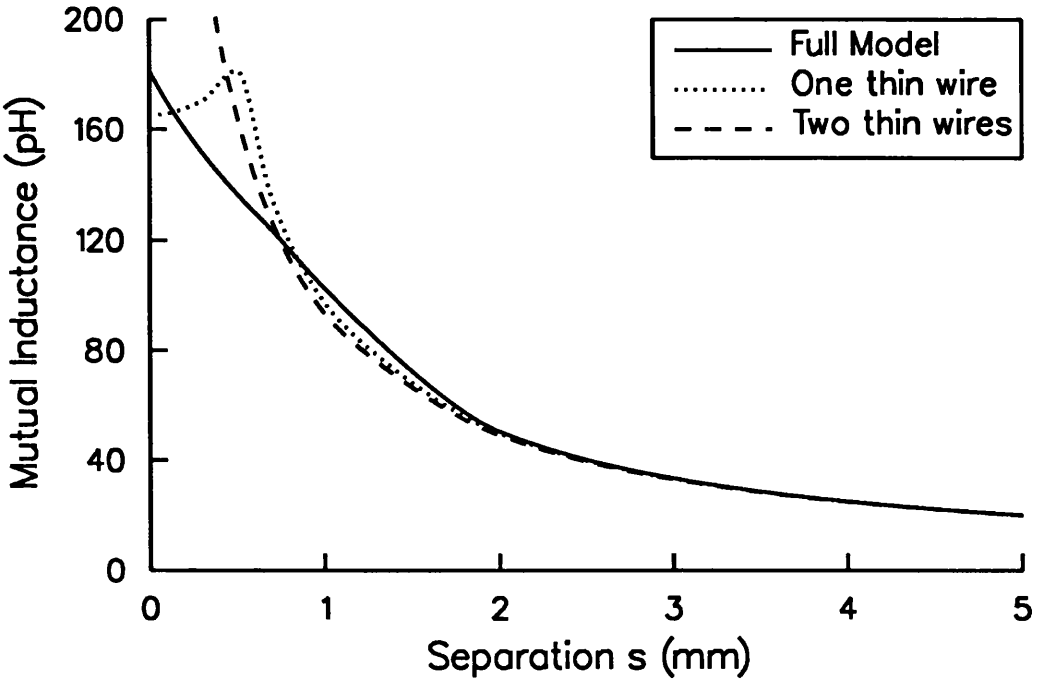

Figure 26. Mutual inductance between two vias: length = 1.0mm, radius = 0.5mm, separation of centres = s mm

4.5.2.2 Treating Both Vias as Thin Wires

With both vias treated as thin wires, $b_i = b_j = 0$. The expression for R in equation 4.17 simplifies to

$$R^2 = s^2 \tag{4.32}$$

This is no longer a function of θ_i or θ_j, so the integrations over these can be replaced with a multiplication by $4\pi^2$. Using I' as defined in equation 4.24, with R^2 replaced by s^2, the full expression for the mutual inductance is now

$$L_{ij} = \frac{\mu_0}{4\pi} I' \tag{4.33}$$

4.5.3 Results and Comparison of Methods

Figure 26 shows results from the full integrations and the two approximations detailed above for the mutual inductance between two vias. Both vias had length and radius 1mm, and the second via was positioned with $x_c = 0$, separated from the first via by s mm.

A separation of 0 corresponds to the self inductance of the via. The full integrations give exactly the same answer for this as was obtained in the previous section. Approximating one via as a thin wire gives a result which is about 10% less than the correct answer. Approximating both vias as thin wires gives an infinite result. This would be expected from the results of the previous section: for $s = 0$, $I'_2(\xi) = -\infty$ when ξ is negative, and with $x_c = 0$ one or more of the limits ξ_1 to ξ_4, given by equation 4.22, is negative.

Separations of between 0 and 1mm are not physically realistic in this case, since they correspond to the vias overlapping. For separations of more than 1mm, the answers given by the three methods quickly converge: at a separation of 3mm the differences from the full integration result are 0.7% for the one thin wire approximation and 1.3% for the two thin wires approximation.

The times taken by these different methods are (approximately):

Two thin wires	0.10ms
One thin wire	0.87ms
Full integration	100ms or more

Hence, the approximate methods are greatly preferred. Since the one thin wire approximation is the more accurate of the two, and still takes less than 1ms to evaluate, it is the method adopted for inclusion in FACET. If the two vias have different diameters, the smaller of them is considered as the thin wire.

4.6 Internal Impedance of a Via

The results derived so far have been for the external impedance of a via, due to the fields set up in space by the current flowing through it. Also of interest is its internal impedance, due to the fields set up in the metal of the via itself. This depends on the conductivity of the via metallisation and the frequency. The via has been assumed to be thin walled, so to calculate the internal impedance it can be modelled to a good approximation as a flat sheet

Frequency	R_i (mΩ)	ωL_i (mΩ)	L_i (pH)
1 MHz	0.549	0.005	0.750
10 MHz	0.550	0.047	0.750
100 MHz	0.625	0.453	0.720
1 GHz	1.974	1.969	0.313
10 GHz	6.226	6.226	0.099
100 GHz	19.695	19.695	0.031

Table 1. Surface impedances for a via of length 1.5mm and radius 0.5mm

of metal, of length $2a$ and width $2\pi b$, with the current distribution assumed symmetrical in the thickness (ie. the metal sheet is assumed to have two current carrying skins). The necessary skin effect theory is detailed in Appendix A, so the results will just be summarised here.

The impedance of a square region (of any size) in a conducting sheet with defined thickness and conductivity is called the surface impedance, Z_s. This has units of Ohms per square, and can be written as

$$Z_s = R_s + j\omega L_s \tag{4.34}$$

where R_s and L_s are respectively the surface resistance and inductance. To obtain the internal impedance, Z_i, of a particular via, the surface impedance is multiplied by the number of squares (where the subdivision is in the direction of the current), giving

$$Z_i = \frac{a}{\pi b} Z_s \tag{4.35}$$

At low frequencies, when the skin depth of the conductor is much greater than its thickness, both R_s and L_s are constant. At higher frequencies, R_s increases as $\sqrt{f}$ while L_s falls off as $1/\sqrt{f}$, so that at very high frequencies the real and imaginary parts of the surface impedance, R_s and ωL_s, are equal.

As an example, consider a via with radius 0.5mm and length 1.5mm (ie. $a = 0.75$mm and $b = 0.5$mm). The metallisation is taken to be be 15 μm of copper, which has a conductivity of 5.8×10^7 S m^{-1}. For this metal the skin depth is equal to its thickness at a frequency

of 19.4 MHz. Table 1 shows how R_i, ωL_i and L_i vary with frequency. They all behave in the manner expected.

The resistance of this via is small at all frequencies likely to be used. Its internal inductance is also small compared with its external self inductance of 349 pH, and reduces with increasing frequency. Hence, modelling the via as a flat sheet to calculate its internal impedance is quite accurate enough.

4.7 Conclusions

This chapter outlined the calculation of the vector potential due to a via, the self inductance of a via and the mutual inductance between two vias. The necessary theory of inductance was derived from first principles. All the above quantities are calculated very efficiently, none taking more than 1ms of CPU time. The results obtained behave as would be expected for various limiting cases, and have reasonable values. The internal impedance of a via was also examined, and shown to be of much less importance than the external inductance.

The next chapter goes on to describe the computation of scalar and vector potentials due to track and polygon elements, used in the computation of the values of capacitors and inductors in the equivalent circuit model. For polygon elements, the mutual inductance between elements can be computed analytically, using similar methods to those developed in this chapter.

Chapter 5
Evaluation of Potentials and Inductance

5.1 Introduction

This chapter is concerned with the algorithms which calculate the scalar and vector potentials, both for track and polygon elements, the self inductance of a rectangular polygon element, and the mutual inductance between two rectangular polygon elements, and with the FORTRAN 77 subroutines which implement them in FACET. The nomenclature is discussed briefly, and then the expressions used to calculate the potentials and inductance are derived.

The assumed charge or current density distributions within each element are known as basis functions, and two types of these are used in the algorithms described here. Each polygon element has just one basis function, which is a constant charge or current density as appropriate. This is because these elements are designed to describe part of a large area of metal, where variations in charge and current density occur relatively slowly.

In contrast, track elements have up to six basis functions, each of which has a singular behaviour in the width of the element. This behaviour produces a potential distribution which is approximately flat across the width of the element, which is close to the actual distribution expected. The additional basis functions, only included for charge, allow for some "leaning" of the charge density distribution in an attempt to model better the capacitance between tightly spaced tracks. The use of these additional basis functions is optional in FACET, as there can be a considerable time penalty associated with it.

It is important that the algorithms are computationally efficient, since they consume a large fraction of the computer time used in a typical FACET simulation. The expressions derived here for the polygon elements are all analytic, for maximum efficiency. Those for the track elements have as much of the expression as possible derived analytically, leaving just a single integration to be performed numerically. Special attention has been paid to this numerical integration, to ensure that it is performed accurately and efficiently. Timings are

presented to show that high efficiency has indeed been obtained in all the implemented subroutines, and to demonstrate the time savings that result from the analytical approach, where it can be applied.

5.2 Subroutine Naming Conventions

A naming convention for the full set of subroutines was adopted, giving each subroutine a five or six character name. The naming convention is described in detail in Appendix F, so only the names of the subroutines implemented are listed here. Note that there are additional subroutines in FACET which conform to the convention, but which are not relevant to the work reported here.

Six subroutines are implemented in FACET Version 3.0 to calculate vector potentials. Four of these are for potentials due to polygon elements. These are:

VPR1G VPR1N VPT1G VPT1N

The remaining two subroutines are for potentials due to track elements. These are:

VTR1G VTR1N

More cases have to be considered for the scalar potential, and 36 subroutines are implemented in FACET, split evenly between those for polygon elements and those for track elements. Those for polygon elements are:

SPR1CB	SPT1CB
SPR1CM	SPT1CM
SPR1CS	SPT1CS
SPR1GB	SPT1GB
SPR1GD	SPT1GD
SPR1GM	SPT1GM
SPR1NB	SPT1NB
SPR1ND	SPT1ND
SPR1NM	SPT1NM

and those for track elements are:

STR1CB	STR6CB
STR1CM	STR6CM
STR1CS	STR6CS

STR1GB	STR6GB
STR1GD	STR6GD
STR1GM	STR6GM
STR1NB	STR6NB
STR1ND	STR6ND
STR1NM	STR6NM

The remaining subroutines are for the calculation of inductance of polygon rectangles. There are two subroutines, called:

SIPR MIPRPR

5.3 Rectangular Polygon Elements - Vector Potential

The Green's function G_A for an point current source with a ground plane parallel to the bottom face of the PCB and placed a distance d_1 below it was given by equation 3.72. This can be written as,

$$G_A(x|x_0, y|y_0, z|z_0) = \frac{\mu_0 i}{4\pi}\left[\frac{1}{\sqrt{(x-x_0)^2+(y-y_0)^2+(z-z_0)^2}} - \frac{1}{\sqrt{(x-x_0)^2+(y-y_0)^2+(z+z_0+2d_1)^2}}\right] \quad (5.1)$$

where the x and y co-ordinates are in the plane of the PCB faces and the z co-ordinate is perpendicular to the PCB. This represents the vector potential at the point (x,y,z) due to a unit point current i at the point (x_0, y_0, z_0). The second term is due to the image current, which models the induced current in the ground plane, and can be ignored if there is no ground plane present. Equation 2.22 for the mutual inductance between two elements requires the x component of the vector potential due to a uniform current density distribution, A_x, in a rectangular element, with a total current of 1 amp.

The location of the origin and the orientation of the x and y axes in equation 5.1 are arbitrary, so they can be defined locally with respect to an element. The plane $z=0$, however, corresponds to the bottom face of the PCB at all times. Figure 27 shows the local co-ordinate axes for a rectangular element of length $2a$ and width $2b$. The origin of these co-ordinates is the centre of the rectangle, which therefore extends from $-a$ to a in the x

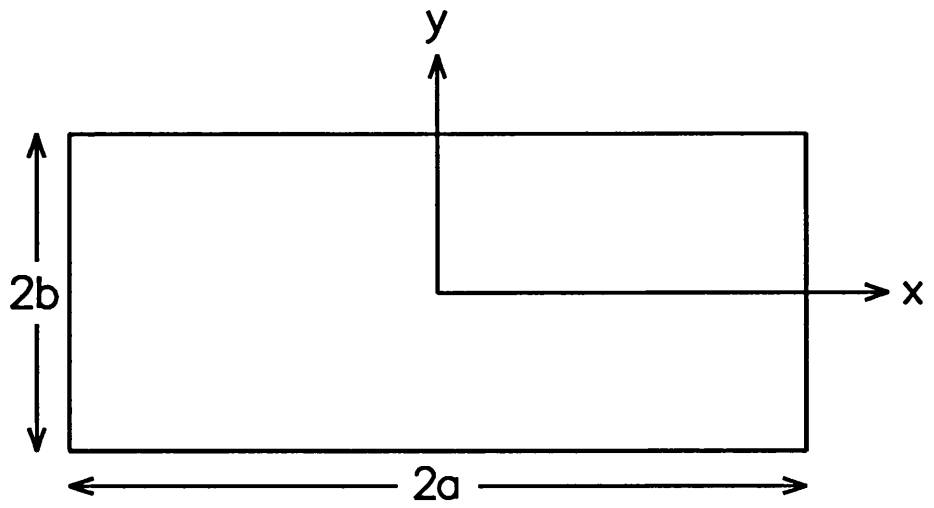

Figure 27. Rectangular element and local co-ordinate axes

co-ordinate and from $-b$ to b in the y co-ordinate. A uniform current is assumed to flow parallel to the x axis. At a point (x,y,z) in these co-ordinates, the vector potential due to this current is parallel to the x axis, and is given by

$$\mathbf{A} = \frac{\mathbf{i}}{2b}\int_{-a}^{a}\int_{-b}^{b} G_A(x\,|\,x_0, y\,|\,y_0, z\,|\,z_0)\,dy_0\,dx_0 \tag{5.2}$$

where **i** is now a unit vector parallel to the x axis, and the $1/2b$ factor is to normalise the total current to 1 amp. It is shown in Appendix G how the integral I

$$I(x_1, x_2, y_1, y_2, z) = \int_{y_1}^{y_2}\int_{x_1}^{x_2} \frac{dx\,dy}{\sqrt{x^2 + y^2 + z^2}} \tag{5.3}$$

can be evaluated analytically, the result being given in equation G.21. In terms of this integral, equation 5.2 becomes

$$\begin{aligned}\mathbf{A} = A_x = \frac{\mu_0}{8\pi b}\Big(& I(-a-x, a-x, -b-y, b-y, |z-z_0|) \\ & - I(-a-x, a-x, -b-y, b-y, z+z_0+2d_1) \Big)\end{aligned} \tag{5.4}$$

This is the function implemented in the subroutine VPR1G. When there is no ground plane present, the second term in equation 5.4 is zero, and this simplified form is implemented in the subroutine VPR1N.

5.4 Rectangular Polygon Elements - Scalar Potential

For the scalar potential, the formulae are slightly more complicated. In FACET, a single sided PCB is defined as one with a ground plane on its bottom face. For an element on the top surface of a single sided PCB of thickness c, Appendix D shows that the Green's function G_ϕ can be written as

$$G_\phi(x|x_0, y|y_0, c|c) = \sum_{n=0}^{N+1} \frac{P_n}{R_n} \tag{5.5}$$

where

$$R_n = \sqrt{(x-x_0)^2 + (y-y_0)^2 + 4n^2c^2} \tag{5.6}$$

and the P_n are functions of ε_r, the dielectric constant of the PCB. They are therefore constant for any given PCB material. The upper limit of summation, $N+1$, is chosen to give the required accuracy. This matter was discussed in some detail in section 3.9. Hence, the scalar potential ϕ at the point (x,y,c) is

$$\phi = \sum_{n=0}^{N+1} P_n I(-a-x, a-x, -b-y, b-y, 2nc) \tag{5.7}$$

This is implemented in the subroutine SPR1CS. The other subroutines with names of the form SPR1xx are for different ground plane and element locations. They are very similar in form, but with different expressions for the Green's functions. The full set of Green's functions needed to implement the subroutines was derived in Chapter 3.

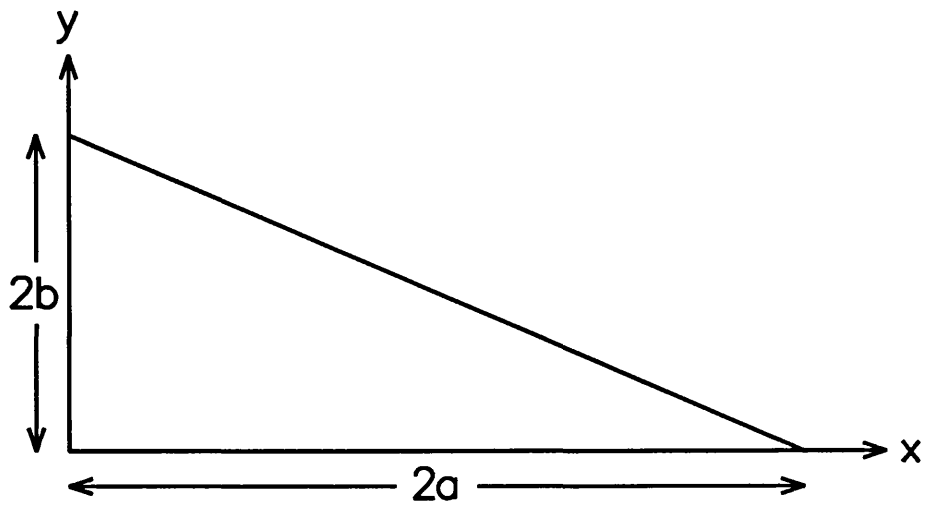

Figure 28. Type 2 triangular element and local co-ordinate axes

5.5 Triangular Polygon Elements - Vector Potential

Figure 28 shows the local co-ordinate axes for a triangular element. The origin of these co-ordinates is at the right angle corner. The triangle extends from 0 to $2a$ in the x co-ordinate and from 0 to $2b$ in the y co-ordinate. In the terminology to be introduced in Chapter 7, this is a type 2 triangular element. There are four types of triangular element, the other three being reflections of the type 2 element in one or both of the X and Y axes. The other types of triangle have local co-ordinates with the origin at the right angle corner. Table 2 shows their extent in these local co-ordinates.

The vector potential due to current flow in a triangle, **A**, is obtained from an expression similar to equation 5.2. However, in this case the current flow is assumed to be parallel to the hypotenuse, because this is always part of the edge of the polygon, and clearly current cannot flow over such an edge. The vector potential is therefore also parallel to the hypotenuse, and is given by integrating G_A over the area of the triangle. This results in

$$\mathbf{A} = \frac{\sqrt{a^2+b^2}}{2ab} \int_{x_1}^{x_2} \int_{y_1}^{y_1+\frac{y_2-y_1}{x_2-x_1}(x-x_1)} G_A(x\,|\,x_0, y\,|\,y_0, z\,|\,z_0)\, dy_0\, dx_0 \qquad (5.8)$$

The normalising factor is chosen so that the peak current in the triangle is 1 amp. In section 6.8 it is confirmed that this is the correct choice. The integration limits are different for each

Element Type	Minimum X Co-ordinate	Maximum X Co-ordinate	Minimum Y Co-ordinate	Maximum Y Co-ordinate
1	-2a	0	0	2b
2	0	2a	0	2b
3	-2a	0	-2b	0
4	0	2a	-2b	0

Table 2. Minimum and maximum local co-ordinates for triangles

of the four types of triangle. Table 3 gives the limits necessary to obtain the potential at the point (x,y) in local co-ordinates.

It is shown in Appendix G how the integral I'

$$I'(x_1, x_2, y_1, y_2, z) = \int_{x_1}^{x_2} \int_{y_1}^{y_1 + \frac{y_2 - y_1}{x_2 - x_1}(x - x_1)} \frac{dy\,dx}{\sqrt{x^2 + y^2 + z^2}} \tag{5.9}$$

can be evaluated analytically, the result being given in equation G.42. With the limits provided by Table 3 for the appropriate type of triangle, equation 5.8 can be written in terms of the integral I' as

$$\mathbf{A} = \frac{\mu_0 i \sqrt{a^2 + b^2}}{4\pi ab} \Big(I(x_1, x_2, y_1, y_2, |z - z_0|) - I(x_1, x_2, y_1, y_2, z + z_0 + 2d_1) \Big) \tag{5.10}$$

This is the function implemented in the subroutine VPT1G. When there is no ground plane present, the second term in equation 5.10 is zero, and this simplified form is implemented in the subroutine VPT1N.

Element Type	x_1	x_2	y_1	y_2
1	-x-2a	-x	-y	-y+2b
2	x-2a	x	-y	-y+2b
3	-x-2a	-x	y	y+2b
4	x-2a	x	y	y+2b

Table 3. Integration limits for triangles

5.6 Triangular Polygon Elements - Scalar Potential

The scalar potential is obtained in almost the same manner as for a rectangular element, with the charge density assumed constant over the triangle. Considering again an element on the top surface of a single sided PCB, the scalar potential ϕ at the point (x,y) can be written in a similar way to equation 5.7 as

$$\phi = \sum_{n=0}^{N+1} P_n I'(x_1, x_2, y_1, y_2, 2nc) \tag{5.11}$$

This is implemented in the subroutine SPT1CS. The other subroutines with names of the form SPT1xx are for different ground plane and element locations. They are very similar in form, but with different expressions for the Green's functions. The full set of Green's functions needed to implement the subroutines was derived in Chapter 3.

5.7 Rectangular Polygon Elements - Self Inductance

The self inductance of a rectangle is obtained by integrating the vector potential given by equation 5.4 over the area of the rectangle, as shown by equation 2.22. The derivation of this result is detailed in Appendix G in two parts. The first part, with the result given in equation G.72, gives the self inductance of a rectangle with no ground plane present. The second part, with the result given in equation G.86, gives the mutual inductance between the rectangle and its image: if a ground plane is present, this must be subtracted from the first

result to give the true value of the self inductance. This result is implemented in the subroutine SIPR, the name standing for Self Inductance of a Polygon Rectangle.

5.8 Rectangular Polygon Elements - Mutual Inductance

The mutual inductance between two parallel rectangles with parallel current flow directions is obtained by integrating the vector potential due to the first rectangle, given by equation 5.4, over the area of the second rectangle, as shown by equation 2.22. The derivation of this is considered in Appendix G, with the result being given by equation G.103. This equation gives the same inductance with the rectangles labelled either way round, as would be expected from reciprocity. If a ground plane is present, the mutual inductance between the first rectangle and the image of the second rectangle needs to be subtracted to give the correct answer. This result is implemented in the subroutine MIPRPR, the name standing for Mutual Inductance between Polygon Rectangle and Polygon Rectangle.

5.9 Rectangular Track Elements - Scalar Potential

A track rectangle is described using exactly the same co-ordinate system as for a polygon rectangle, shown in Figure 27. However, these elements are used to represent tracks, which are typically long, narrow sections of metal, rather than the interior of a large area of metal, so different basis functions are appropriate. The basis functions selected have two parts. It has been shown [Mittra and Lee, 1971] that the charge density distribution near a conductor edge varies inversely as the square root of the distance from that edge. The resultant singularities at the two edges $y=\pm b$ are modelled by including a factor of

$$\frac{1}{\sqrt{(b-y)(b+y)}} = \frac{1}{\sqrt{b^2-y^2}} \tag{5.12}$$

in the basis functions. The $\sqrt{(b-y)(b+y)}$ results in a scalar potential distribution that is virtually flat across the width of the element, provided that this width is less than about $2(c+d_1)$. This is almost always the case for PCB tracks. Figure 29 shows this charge distribution and the resulting scalar potential distribution for an element 10mm long and 2mm wide on a single sided board with dielectric constant 5 and a coincident ground plane.

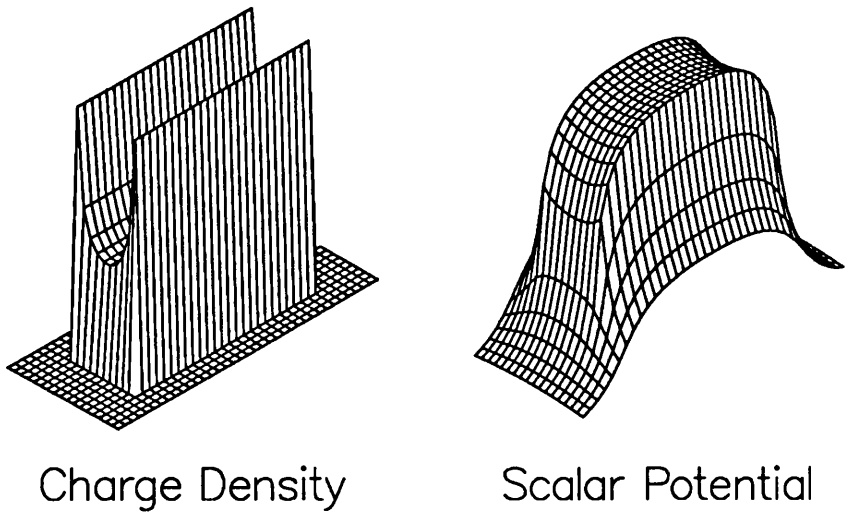

Figure 29. Charge density distribution and resulting scalar potential

This is almost flat across the width of the track; the variation from flatness is due to the presence of the ground plane and dielectric, but the effect is not very large.

The ends $x = \pm a$ will not usually represent the edge of a conductor, and so do not need to have singularities modelled. The remaining variation is built into the basis functions by a bivariate polynomial in x and y, of the form $x^i y^j$. In FACET, i can take the values 0, 1 or 2 and j can take the values 0 or 1, so these are therefore the only cases considered here. These terms allow for the slower spatial variations in the charge density caused by mutual attraction or repulsion of charge in neighbouring elements, and propagation effects when tracks have significant electrical length. The resulting set of basis functions is,

$$\rho_{ij}(x, y) = \frac{x^i y^j}{\sqrt{b^2 - y^2}} \tag{5.13}$$

Considering for the moment an element on the top surface of a single sided PCB, the Green's function given by equation 5.5 is convolved with the set of basis functions given by equation 5.13 to yield the potential ϕ at the point (x,y,c) due to the $(i,j)^{th}$ basis function in the element. This is,

$$\phi(i,j,x,y) = \int_{-b}^{b} \frac{{y_0}^j}{\sqrt{b^2-{y_0}^2}} \int_{-a}^{a} \sum_{n=0}^{N+1} \frac{P_n {x_0}^i \, dx_0 \, dy_0}{\sqrt{(x-x_0)^2+(y-y_0)^2+4n^2c^2}} \tag{5.14}$$

The inner integral, over x_0, can be performed analytically, while the integral over y_0 has to be performed numerically. The evaluation of these integrals is described below.

The results are implemented in the subroutine STR6CS, with a simplified version, which only computes the potential due to the $i=j=0$ basis function, implemented in STR1CS. As for the polygon elements, the other subroutines with names of the form STR6xx and STR1xx are for different ground plane and element locations. They are very similar in form, differing only in the expressions for the Green's functions, derived for all cases in Chapter 3.

5.9.1 Evaluation of the Analytic Integral

The general form of the integral with respect to x_0 (ie. along the length of the element) is,

$$\mathrm{I}_i^x(x,y,y_0) = \int_{-a}^{a} \sum_{n=0}^{N+1} \frac{P_n {x_0}^i \, dx_0}{\sqrt{(x-x_0)^2+(y-y_0)^2+4n^2c^2}} \tag{5.15}$$

The evaluation of this integral is considered for $i=0, 1, 2$. Performing the substitution $\xi = x_0 - x$ and setting $R'^2_n = (y-y_0)^2 + 4n^2c^2$ results in the simpler form,

$$\mathrm{I}_i^x(x,y,y_0) = \int_{-a}^{a} \sum_{n=0}^{N+1} \frac{P_n (\xi+x)^i \, d\xi}{\sqrt{\xi^2+R'^2_n}} \tag{5.16}$$

Expanding the numerator results in up to three integrals, of standard form. In terms of these, the three original integrals I_i^x can be written as,

$$\begin{aligned} I_0^x &= \sum_{n=0}^{N+1} P_n I'_{0n} \\ I_1^x &= \sum_{n=0}^{N+1} P_n [I'_{1n} + xI'_{0n}] \\ I_2^x &= \sum_{n=0}^{N+1} P_n [I'_{2n} + 2xI'_{1n} + x^2 I'_{0n}] \end{aligned} \tag{5.17}$$

The three new integrals I'_{in} can all be evaluated to give

$$I'_{0n} = \int_{-a-x}^{a-x} \frac{d\xi}{\sqrt{\xi^2 + R'^2_n}} = \log\left[\frac{a-x+\sqrt{(a-x)^2+R'^2_n}}{-a-x+\sqrt{(a+x)^2+R'^2_n}} \right] \tag{5.18}$$

$$I'_{1n} = \int_{-a-x}^{a-x} \frac{\xi d\xi}{\sqrt{\xi^2 + R'^2_n}} = \sqrt{(a-x)^2+R'^2_n} - \sqrt{(a+x)^2+R'^2_n} \tag{5.19}$$

$$\begin{aligned} I'_{2n} = \int_{-a-x}^{a-x} \frac{\xi^2 d\xi}{\sqrt{\xi^2 + R'^2_n}} = \frac{1}{2}\Big[& (a-x)\sqrt{(a-x)^2+R'^2_n} \\ & + (a+x)\sqrt{(a+x)^2+R'^2_n} - R'^2_n I'_0 \Big] \end{aligned} \tag{5.20}$$

The integrand in equation 5.18 is singular when $|x| < a$, $\xi = 0$ and $R'_n = 0$. This can only occur when $n = 0$ and the point (x, y) is inside the source element, but will require special treatment in the numerical part of the integration which follows. Physically, this singularity occurs for the point within the distributed source which is coincident with the observation point. The other integrands are always finite and smooth.

5.9.2 Evaluation of the Numerical Integral

The remaining integral with respect to y_0 (ie. across the width of the element) is,

$$I_{ij} = \int_{-b}^{b} I_i^x(x, y, y_0) \frac{y_0^{\,j}\, dy_0}{\sqrt{b^2 - y_0^{\,2}}} \tag{5.21}$$

No analytic solution to this integral has been found, so the integration has to be performed numerically. The integrand can be made smoother by applying the substitution $y_0 = b \sin\theta$. This removes the singularities at $y_0 = \pm b$, resulting in

$$I_{ij} = \int_{-\frac{\pi}{2}}^{\frac{\pi}{2}} I_i^x(x, y, b \sin\theta)\ (b \sin\theta)^j\ d\theta \tag{5.22}$$

The logarithm, square root and sine terms in the integrands take much more CPU time to evaluate than additions and multiplications. For any given θ, these terms are the same in all the integrands. In addition the possible values of θ are known in advance, so the $\sin\theta$ terms need only be computed once, and stored for later use. For each set of six integrand evaluations only one logarithm and two square root terms need calculating (for each value of n), whereas calling a standard numerical integration subroutine for each in turn would result in 24 calculations, taking at least eight times as long. The integrations are therefore all performed together inside the subroutines.

Any numerical integration rule can be expressed as

$$\int_{x_1}^{x_2} f(x)\, dx = \sum_{t=1}^{T} w_t f(x_t) \tag{5.23}$$

where the w_t are weighting factors and the integrand is evaluated at the T abscissae x_t. In general, the accuracy of the final answer increases as the number of abscissae is increased.

In the subroutines, an iterative approach is adopted to obtain the required accuracy as efficiently as possible. This uses a set of integration rules, with increasing T, and applies them in turn until the difference between the answers produced by two consecutive rules is

less than the maximum error permitted. For the greatest efficiency, it is preferable to use a set of *interlacing* integration rules. This means that each rule uses the same set of abscissae x_i as the previous rule, and then adds a new set of abscissae intermediate between each of the old pairs of abscissae, so that no integrand evaluations are wasted.

Two such methods have been used. These are Simpson's rule [Matthews and Walker, 1970], and a set of rules due to Patterson [1968]. Both methods are implemented identically in the subroutines. The choice of subroutine is made by setting up three arrays, containing the number of points per rule, and the abscissae positions and their associated weights for each rule, all containing information for the appropriate method. Patterson's method is generally preferred, as it is the more powerful of the two. The option of using Simpson's rule has been retained so that the two methods can be compared if any doubt arises. This also means that if a better integration method is found it can be incorporated with very little effort.

5.9.2.1 Handling the Singular Integral

As mentioned in the previous section, the function I'_{00} is singular when the object point is inside the source element. This is handled by setting it to zero in the first part of the numerical integration, and then evaluating its contribution to the potentials separately. The two integrals S_j

$$S_0 = \int_{-\frac{\pi}{2}}^{\frac{\pi}{2}} I'_{00}\, d\theta \qquad \text{and} \qquad S_1 = \int_{-\frac{\pi}{2}}^{\frac{\pi}{2}} I'_{00}\, b \sin\theta\, d\theta \tag{5.24}$$

are integrated using the NAG subroutine D01AHF [NAG, 1988]. This implements a version of Patterson's rules, and is adapted to handle singularities. Its accuracy (for a given number of integrand evaluations) is greatly improved by submitting each integral as two parts, split at the singularity (which is at $y_0 = b \sin\theta = y$).

Denote the potential calculated without the I'_{00} term by $\phi'(i,j,x,y)$. Noting that $P_0 x^i$ is the coefficient of the I'_{00} term in equation 5.17, the complete potential is

$$\phi(i,j,x,y) = \phi'(i,j,x,y) + P_0 x^i S_j \tag{5.25}$$

The non-singular integral $\phi'(i,j,x,y)$ is evaluated as described above.

5.10 Rectangular Track Elements - Vector Potential

The calculations for the vector potential are rather simpler. Only the x-directed component of current density is considered, and the model for inductance only uses the $i=j=0$ basis function. The current density basis function is therefore,

$$J_x(x,y) = \frac{1}{\sqrt{b^2-y^2}} \tag{5.26}$$

The Green's function for the vector potential was given by equation 5.1. As was the case for polygon elements, there are only two different subroutines needed. The subroutine VTR1G is for the case with a ground plane present, while the subroutine VTR1N is for the case without a ground plane. Both of these are implemented in exactly the same way as those for the scalar potential, described in the previous section.

5.11 Speed of the Subroutines

It is important that the subroutines developed are as efficient as possible in their use of computer time, as the time spent in the evaluation of potentials and inductance is one of the major components of the time taken for a typical FACET analysis. Three approaches have been taken to ensure maximum efficiency:

1. Analytic expressions have been derived for all the integrals required in the subroutines for polygon elements, and for as much of the integrals as possible in the subroutines for track elements. Considerable effort has been made to ensure that these expressions are as compact as possible, even though some are rather complicated. Even the most complicated expressions are still quicker to evaluate than they would be if evaluated using a numerical integration method. Also, there are none of the convergence problems which have to be addressed using numerical methods.
2. Where numerical integration methods do have to be used, considerable attention has been paid to both the method selected and the efficiency of its implementation.
3. Considerable attention has been paid to the structure of the subroutines, to ensure that no unnecessary calculations were performed. In conjunction with the use of optimising compilers, this has resulted in subroutines which have their speed limited mainly by the

speed of the intrinsic functions (logarithms, sines, etc.) provided as part of the FORTRAN 77 language.

The subroutines are divided into four sets, computing the potentials due to polygon rectangles and triangles, the inductance between polygon rectangles, and the potentials due to track rectangles. These are now examined in turn.

5.11.1 Polygon Rectangle Potential Subroutines

These subroutines implement the results of equations 5.4 and 5.7. Examination of equation G.21 shows that to evaluate the integral *I* of equation 5.3, it is necessary to compute 8 square roots, 4 logarithms and 4 arcsines. These are much more costly to evaluate than simple arithmetic operations. The times taken to evaluate these functions are approximately:

- 11.4μs for a square root
- 12.1μs for a logarithm
- 13.6μs for an arcsine

whereas an addition or multiply operation takes only about 0.3μs. Hence, each evaluation of *I* would be expected to take at least 194μs.

The calculation of the vector potential due to a constant current density in a rectangle requires one or two evaluations of *I*. The evaluation of the scalar potential due to a constant charge basis function requires one evaluation of *I* for each term in the series in equation 5.7 or its equivalent. The number of terms in these series can be varied. Here the default values used in FACET are assumed. The evaluation of these functions would therefore be expected to be the dominant factor in the time taken by each subroutine if the subroutines are working efficiently.

Table 4 shows, for each of the subroutines for rectangular polygon elements, the number of evaluations of *I* required, together with the time taken for the function evaluations and the time taken for the complete subroutine to execute. This shows that, apart from the vector potential subroutines, where other overheads are becoming important, the function evaluations occupy around 87% of the subroutine execution time. It is therefore unlikely that these times can be improved on without faster algorithms for function evaluations or faster hardware.

Subroutine Name	Number of Evaluations of I	Time in ms		Proportion of Time in Functions
		Functions	Full Subroutine	
VPR1N	1	0.194	0.263	73.8%
VPR1G	2	0.340	0.424	80.2%
SPR1CS	12	2.227	2.58	86.3%
SPR1ND	12	2.328	2.69	86.5%
SPR1CB SPR1NB	22	4.268	4.91	86.9%
SPR1CM SPR1NM	44	8.536	9.84	86.7%
SPR1GD	49	9.506	11.10	85.6%
SPR1GB	144	27.936	31.90	87.6%
SPR1GM	288	55.872	63.70	87.7%

Table 4. Times for polygon rectangle potential subroutines

The subroutine VPR1G amalgamates some terms from the two evaluations of I , and the subroutine SPR1CS does not perform some of the function calls for the first evaluation of I, which is why the time for function evaluations is not an exact multiple of 194μs. These changes save approximately 48μs and 100μs respectively, which is a worthwhile improvement.

These times are substantially faster than those for the rectangular track elements, as will be demonstrated shortly - typically by a factor of three or four. This indicates that the analytic solutions are giving the improvement in efficiency that might be expected, and also that the subroutines for track rectangular elements are efficient, given their use of numerical integration.

Subroutine Name	Number of Evaluations of I'	Time in ms		Proportion of Time in Functions
		Functions	Full Subroutine	
VPT1N	1	0.253	0.354	71.5%
VPT1G	2	0.446	0.585	76.2%
SPT1CS	12	2.612	3.38	77.3%
SPT1ND	12	2.612	3.44	75.9%
SPT1CB SPT1NB	22	5.071	6.58	77.1%
SPT1CM SPT1NM	44	10.131	13.10	77.3%
SPT1GD	49	11.281	14.70	76.7%
SPT1GB	144	33.131	42.90	77.2%
SPT1GM	288	66.251	85.40	77.6%

Table 5. Times for polygon triangle potential subroutines

5.11.2 Polygon Triangle Potential Subroutines

These subroutines implement the results of equations 5.10 and 5.11. Examination of equation G.42 shows that to evaluate the integral I' of equation 5.9, it is necessary to compute 7 square roots, 3 logarithms, 4 arcsines and 4 arctangents. One additional square root, $\sqrt{1+\alpha^2}$, only needs to be evaluated once for each triangle. The additional function, an arctangent, takes approximately 14.8μs to evaluate. Hence, each evaluation of I' would be expected to take at least 230μs, with an additional 11.4μs for each triangle.

Table 5 shows, for each of the subroutines for triangular polygon elements, the number of evaluations of I' required, together with the time taken for the function evaluations and the

time taken for the complete subroutine to execute. For these subroutines, the function evaluations occupy about 77% of the subroutine execution time. This is less than was the case for the rectangular elements because the evaluation is rather more complicated, so other parts of the calculation occupy a more significant amount of time. The fact that the proportions are nearly the same for all the subroutines indicates that the implementation has been performed efficiently.

The vector potential subroutines VPT1G and VPT1N also involve one extra square root, to normalise the answer, and VTR1G has some of the logarithm terms amalgamated - saving approximately 36μs. The subroutines SPT1CS and SPT1ND do not perform some of the function calls for the first evaluation of I'. This saves approximately 159μs, although SPT1ND takes slightly longer to run because it has greater overheads.

5.11.3 Polygon Rectangle Inductance Subroutines

These subroutines implement the results of equations G.72 and G.84 for the self inductance of a rectangular element, and of equation G.103 for the mutual inductance between two parallel rectangular elements.

For the self inductance, equation G.72 shows that 1 square root and 2 logarithms need to be evaluated when there is no ground plane present. Equation B.84 shows that in addition, 3 square roots, 4 logarithms and 1 arcsine need to be evaluated when a ground plane is present.

For the mutual inductance, equation G.103 shows that 24 square roots, 64 logarithms and 16 arcsines need to be evaluated when there is no ground plane present, and twice the number when a ground plane is present. For the special case of the elements being coplanar and no ground plane present, only 16 square roots and 32 logarithms need to be evaluated.

Table 6 shows for each of these situations the time taken for the function evaluations and the time taken for the complete subroutine to execute. The self inductance subroutine SIPR is very fast, and so the function evaluations only occupy 52% or 65% of the execution time. The mutual inductance subroutine MIPRPR takes rather longer to run, and here the function evaluations occupy nearly 90% of the execution time.

Subroutine Name	Ground Plane	Time in ms		Proportion of Time in Functions
		Functions	Full Subroutine	
SIPR	absent	0.034	0.065	52.3%
SIPR	present	0.130	0.200	65.0%
MIPRPR elements coplanar	absent	0.570	0.64	89.1%
MIPRPR	absent	1.266	1.44	87.9%
MIPRPR	present	2.531	2.84	89.1%

Table 6. Times for polygon rectangle inductance subroutines

These times need to be contrasted with the time it would take to compute the self and mutual inductances by a numerical integration of the vector potential due to one element over the area of the second element - the way it still has to be done for triangles. The computation of the self inductance is very much faster than this would be - SIPR takes rather less time to run than VPR1N or VPR1G. The difference is rather less pronounced for the mutual inductance, which could be evaluated using an integration rule involving only four or six evaluations of the vector potential for elements spaced well apart. This gives approximately equal times using either method. However, the analytic method is always accurate whilst the numerical method can have errors of up to several percent, and so it is preferable to use the analytic method here.

5.11.4 Track Rectangle Potential Subroutines

These subroutines implement the results of section 5.9. Examination of equations 5.18 - 5.20 shows that each evaluation of the three functions I'_{ik} requires the computation of 2 square roots and 1 logarithm. Each integrand evaluation for the numerical integration requires these functions to be computed once for each term in the series for the Green's function in equation

Subroutine Name	Number of Evaluations of I'_{in}	Time in ms		Proportion of Time in Functions
		Functions	Full Subroutine	
VTR1N	15	0.524	0.746	70.2%
VTR1G	30	1.047	1.41	74.3%
STR6CS STR6ND	180	6.282	10.0	62.8%
SPT1CB SPT1NB	330	11.517	16.5	69.8%
SPT1CM SPT1NM	660	23.034	34.8	66.2%
SPT1GD	735	25.652	40.8	62.9%
SPT1GB	2160	75.384	108	69.8%
SPT1GM	4320	150.768	222	67.9%

Table 7. Times for track rectangle potential subroutines

5.7, or its equivalent for other board structures. The number of integrand evaluations required is variable, but 15 is a typical number.

Table 7 shows, for each of the subroutines for rectangular track elements, the number of evaluations of the I'_{in} required, together with the time taken for the square roots and logarithms, and the time taken for the complete subroutine to execute. These times are for the six basis function subroutines. The times for the single basis function routines are about 15% less. The difference is not very large because these subroutines still have to compute two square roots and one logarithm for each evaluation of I'_{0n}, so the time saving just results from the remaining computation that is avoided.

The subroutines take about three or four times longer to run than the analytic subroutines for the polygon rectangles, which indicates that their efficiency is good, given the much more rapid spatial variation of the fields. The time spent in intrinsic function evaluations, at an average of about 65% of the subroutine time, is a smaller fraction of the time than for the polygon subroutines. This is because there are more calculations performed in the track subroutines, and more trips around loops, giving generally larger overheads. The figures indicate that the performance of the subroutines would be hard to improve significantly.

5.12 Conclusions

This chapter examined the algorithms used in the computation of potentials and inductance. Careful attention was paid to the implementation of these formulae, and the resultant subroutines are extremely efficient, particularly those which were able to use analytic results. The use of analytic formulae was shown to be faster than using numerical techniques, although the latter still performed very efficiently.

The next chapter takes the subroutines described here and performs a variety of checks to see that their behaviour is reasonable and consistent. In conjunction with the accuracy of the results obtained, as described in Chapter 8, this gives good confidence in the correct implementation of the approach developed in this thesis.

Chapter 6

Verification of Subroutines

6.1 Introduction

This chapter examines several checks that have been performed on the subroutines described in the previous chapter, both on their own and when incorporated into FACET. These include some checks for consistency, for instance between rectangular and triangular polygon elements, and some checks to see that the solutions behave in a physically realistic manner. These tests give a high degree of confidence that the coding of the subroutines has been performed correctly.

6.2 Check on Symmetry with Rectangular Elements

6.2.1 Polygon Elements

Because the basis functions used for charge and current densities in polygon elements are constant, the potential at each of the four points $(\pm x, \pm y)$ in the local co-ordinates of a polygon rectangle should be identical. This was checked using the subroutine SPR1CS. The rectangle used has a half length of $a = 3.2$ mm, and a half width of $b = 0.8$ mm. The potential was computed with $x = \pm 3.3$ mm and $y = \pm 0.9$ mm, for a PCB 1.6mm thick with a dielectric constant of 4.55. The computations were performed using double precision numbers, which provide approximately 18 decimal digits. For comparison, they were also performed using extended precision numbers, which provide approximately 35 decimal digits.

```
Local x    Local y          Potential
 3.3mm      0.9mm     5 428 129.086 160 898 91 V
-3.3mm      0.9mm     5 428 129.086 160 961 77 V
 3.3mm     -0.9mm     5 428 129.086 160 900 07 V
-3.3mm     -0.9mm     5 428 129.086 160 963 17 V

Extended precision: 5 428 129.086 160 965 28... V
```

The variation between double precision results only occurs in the last five digits, and as such is just a consequence of the finite precision of the numbers used for the calculation. The extended precision results are all identical for the first 18 digits, and similarly close to the other results. For comparison, check the potential at a nearby point:

```
   Local x       Local y          Potential
3.300 001mm      0.9mm     5 428 122.479 857 250 82 V
```

This point is only 1nm away from the previous point, but the difference in potential is much greater than the difference between the previous four results. Hence, the subroutine can be considered to be sufficiently symmetrical. Similar tests can be performed on all the other potential subroutines, and similar answers are found.

6.2.2 Track Elements

The basis functions used for charge and current densities in track elements are not constant. The $(i,j)^{th}$ charge density basis function ρ_{ij} was given by equation 5.13 as

$$\rho_{ij}(x,y) = \frac{x^i y^j}{\sqrt{b^2 - y^2}} \qquad (5.13)$$

where x and y are the local co-ordinates of the element, $0 \le i \le 2$ and $0 \le j \le 1$. These give a charge distribution which is crowded towards the edges of the track, whereas the charge density basis function used for polygon rectangles gives a constant charge across the width of the element.

For the lowest order basis function, with $i=j=0$, the same symmetry relations as for a polygon rectangle should hold. This was checked using the subroutine STR1CS, with the

same rectangle and PCB dimensions as in the previous section. Also as before, the computations were performed using double precision numbers and extended precision numbers for comparison. The numerical integrations all used 15 points.

Local x	Local y	Potential
3.3mm	0.9mm	11 441 980 242.576 960 6 V
-3.3mm	0.9mm	11 441 980 242.576 637 3 V
3.3mm	-0.9mm	11 441 980 242.576 959 6 V
-3.3mm	-0.9mm	11 441 980 242.576 636 3 V

Extended precision: 11 441 980 242.576 644 4... V

The variation between double precision results is very similar to that found with the polygon rectangle subroutine, so the subroutine is sufficiently symmetrical. The extended precision results are all identical for the first 18 digits, and similarly close to the other results.

The difference in the absolute values of the potential for track and polygon rectangles is due to the different amounts of charge represented by each basis function. The total charge in a track rectangle is $2\pi a$, while that in a polygon rectangle is $4ab$, a factor of $\pi/2b$ less. For this example, $\pi/2b = 1963$, while the ratio of the two potentials is 2108:1, so the answers are similar when the total amount of charge is taken into account. They are not identical because of the different charge density distributions in the two basis functions.

6.3 Comparison of Potentials due to Polygon Rectangles and Triangles

A rectangular polygon element can be decomposed into two triangular polygon elements, as shown in Figure 30, and this decomposition can be performed in two different ways. Since constant charge and current densities have been used for the calculation of scalar and vector potential, the potential due to the pair of triangular elements should be identical to that due to the single rectangular element, when any difference in normalisation has been taken into account.

The subroutines which evaluate the scalar potential perform no normalisation, and so are the simplest ones to compare. The first comparison uses the subroutines SPR1CS and SPT1CS,

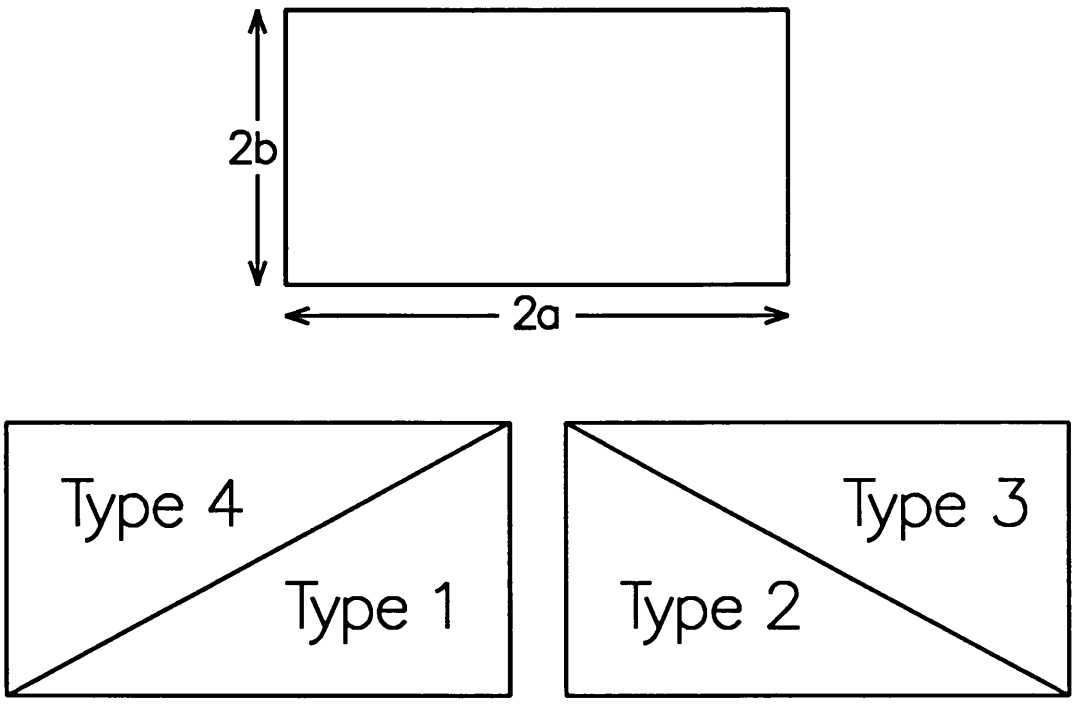

Figure 30. Rectangular polygon element split into triangular elements in two ways

with the same rectangle as in the previous section. In the local co-ordinates of the various triangles (ie. relative to the right angle corner), the point at which the potential is required is:

Triangle Type	Local x	Local y
1	0.1mm	1.7mm
2	6.5mm	1.7mm
3	0.1mm	0.1mm
4	6.5mm	0.1mm

The various potentials are found to be:

```
      Potential due to rectangle: 5 428 129.086 160 898 91 V

Potential due to type 1 triangle: 4 285 007.923 697 420 16 V
Potential due to type 4 triangle: 1 143 121.162 464 107 62 V
 Sum of the above two potentials: 5 428 129.086 161 527 78 V

Potential due to type 2 triangle:   566 739.439 298 289 86 V
Potential due to type 3 triangle: 4 861 389.646 863 202 33 V
 Sum of the above two potentials: 5 428 129.086 161 492 19 V
```

The sum of the potentials due to the triangular elements is very close to that due to the rectangular element in both cases. There is more difference than there was between symmetrical points for the rectangle in the previous section, but much less difference than that caused by moving the object point 1nm. Hence, this test demonstrates that the subroutines SPR1CS and SPT1CS are consistent with one another. Similar tests with the other subroutines give similar results.

6.4 Variation of Potential in the Plane of an Element

The scalar or vector potential due to a polygon element would be expected to vary smoothly in the plane of that element, peaking at the centre of the element. This has been checked by examining the variation of potential over the area of a rectangular or triangular polygon element. Figure 31 shows both surface and contour plots of the scalar potential on a rectangular and a triangular element. These were computed using the subroutines SPR1CS and SPT1CS, again for a PCB 1.6mm thick with a dielectric constant of 4.55. The rectangular element was 2.4mm square, and the triangular element had the same side lengths.

The plots show the potential over an area 2.5mm square, with the outline of the elements superimposed on the contour plot. They demonstrate that the potential is changing smoothly, and exhibiting the expected peak in the centre of the element, falling off toward the edges. The plot for the triangular element shows that the potential falls off rapidly outside the element. These plots also give added confirmation of the correct symmetry of the potential.

In contrast, the potential due to a track element has a rather different behaviour, as illustrated in Figure 32. The difference is principally in the behaviour of the potential across the width of the element, where it is somewhat flatter than for the polygon elements, and falls off more

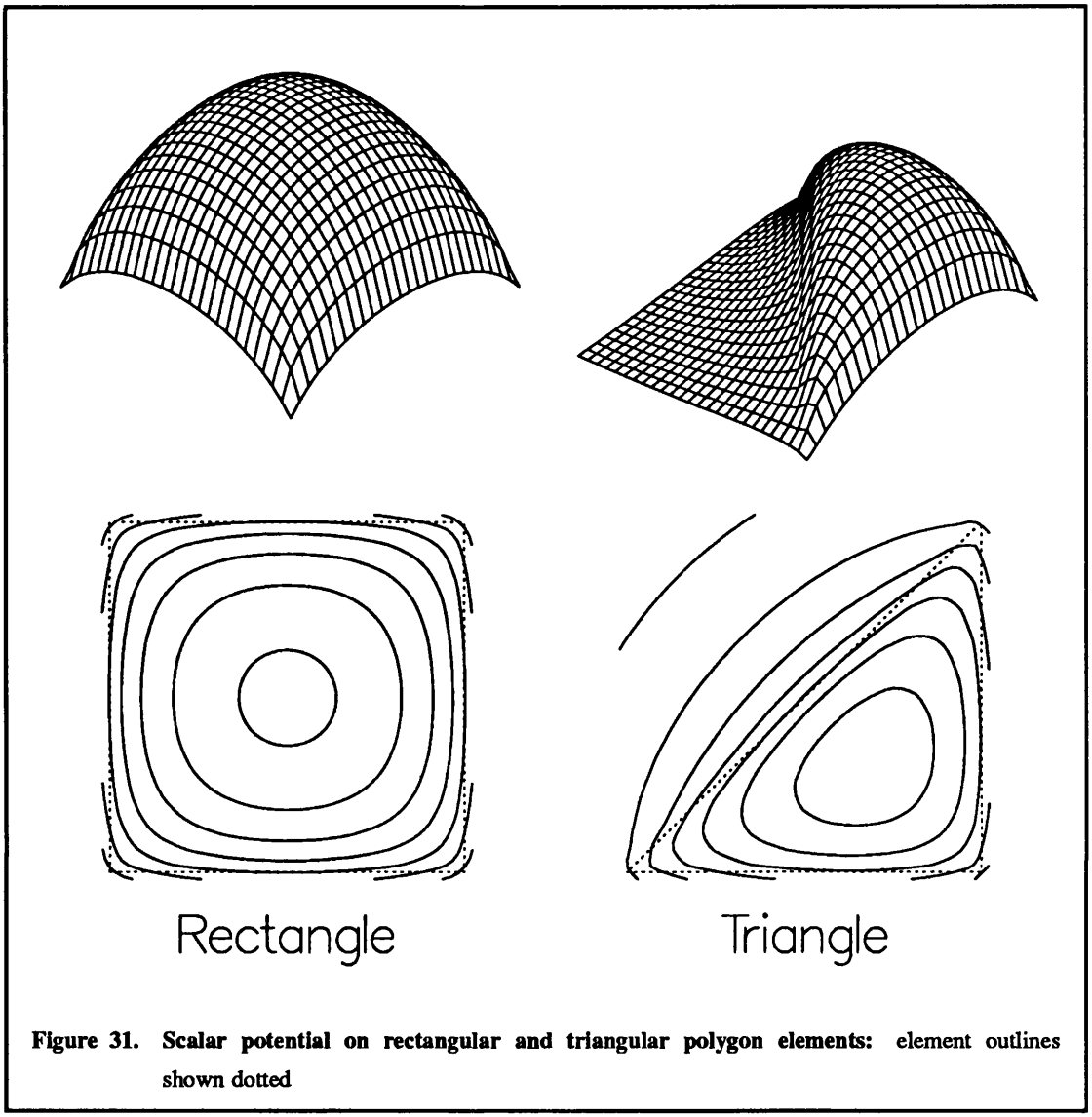

Figure 31. Scalar potential on rectangular and triangular polygon elements: element outlines shown dotted

rapidly outside the element. This is because of the singularity in the charge density basis functions given by equation 5.13. For narrow tracks, this gives a potential distribution which is flat across the element, as discussed in section 5.9. Here, the element is rather short and wide (1.5 times the PCB thickness), which is why the potential distribution is not quite flat.

The same sort of plots can be used to demonstrate that the other subroutines behave in a similar manner.

Far away from the element, the potential should approach that due to a point charge of the same total magnitude. Figure 33 illustrates this for the same rectangle as before, using the subroutines SPR1CS and STR1CS. The results for the track element have been normalised

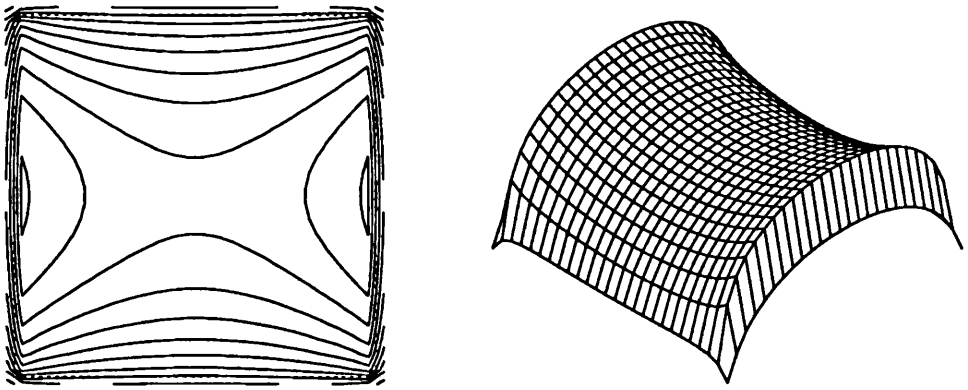

Figure 32. Scalar potential on rectangular track element: element outline shown dotted

to represent the same total charge as the polygon element. The graph shows the potentials at the point (0,*y*), with *y* between 0 and 10mm, due to the rectangular elements, and compares them with the potential due to a point charge of magnitude $4ab$, the total charge in the element. The three potentials approach each other quite rapidly. The difference is less than 10% when y = 6 mm, and less than 1% when y = 16 mm. This demonstrates that the subroutines have the correct behaviour for more distant points.

In the near field of the rectangle, the potentials due to the rectangular element behave much more realistically than that due to the point charge, as would be expected. The exact result would be a potential flat over the width of the track then falling off sharply. Neither result has quite this shape: the element is rather wide for a track, while a polygon element is usually surrounded by other elements which contribute to the production of a flat potential. It can again be shown that the other subroutines behave in a similar manner.

6.5 Variation of Potential Perpendicular to an Element

The potential variation along a line perpendicular to the plane of an element would be expected to be smooth except at the following places, where there is a discontinuity in the derivative of the potential (ie. the electric field normal to the PCB):

- At the element itself. Here the discontinuity is due to the presence of charge or current, which causes the gradient of the potential to reverse in sign. Note that the elements are

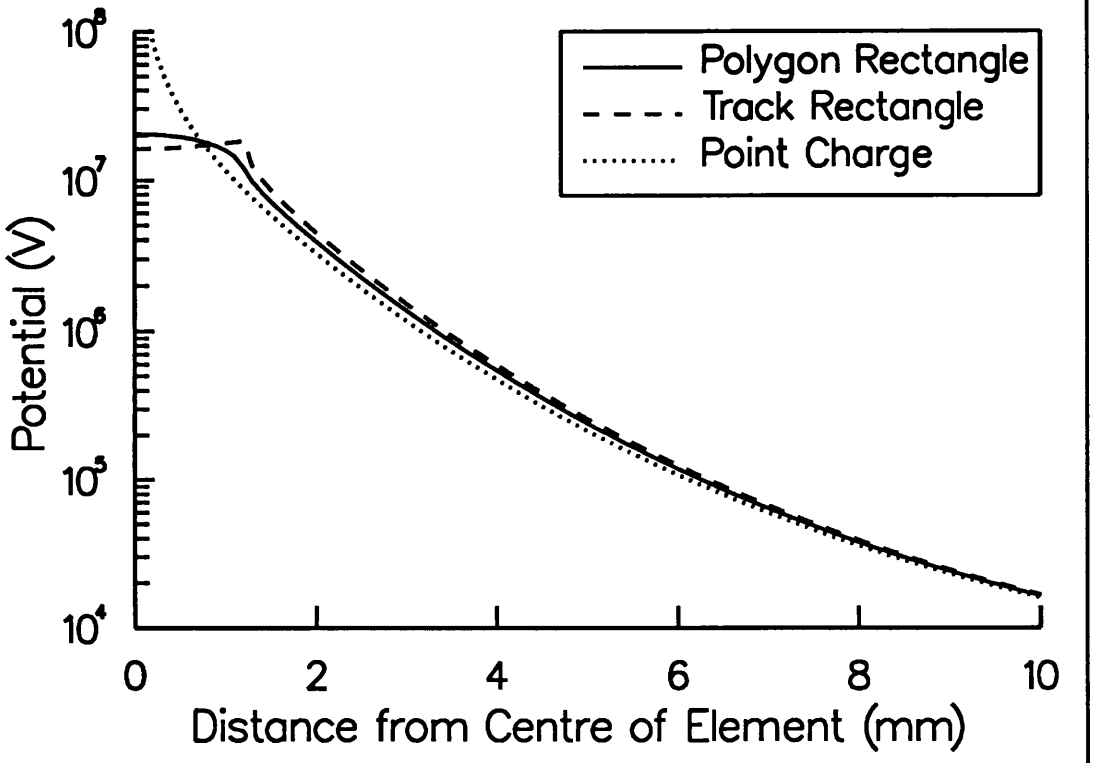

Figure 33. Scalar potential for polygon and track rectangular element and a point charge

assumed infinitesimally thin in these calculations, so variation inside the conductor is not considered. This is dealt with separately, in Appendix A.

- At the boundary between two dielectric layers, for the scalar potential only. Here the ratio of the derivatives of the potential on either side of the boundary is equal to the ratio of the two dielectric constants.

This was examined for a rectangular polygon element using the subroutines SPR1CM, SPR1CS and SPR1CB, for a rectangular track element using the subroutines STR1CM, STR1CS and STR1CB, and for a triangular polygon element using the subroutines SPT1CM, SPT1CS and SPT1CB. All the elements had a half length of a = 5.0 mm and a half width of b = 0.5 mm, and were on the top surface of a PCB 2mm thick with a dielectric constant of 4.55 and a ground plane on its bottom surface.

The potential was computed along a series of sections normal to the PCB surfaces, at local co-ordinates of (0,*y*) for the rectangle and (5mm,*y*) for the triangle. The vertical sections began at the ground plane on the bottom of the PCB and extended up to 3mm above the

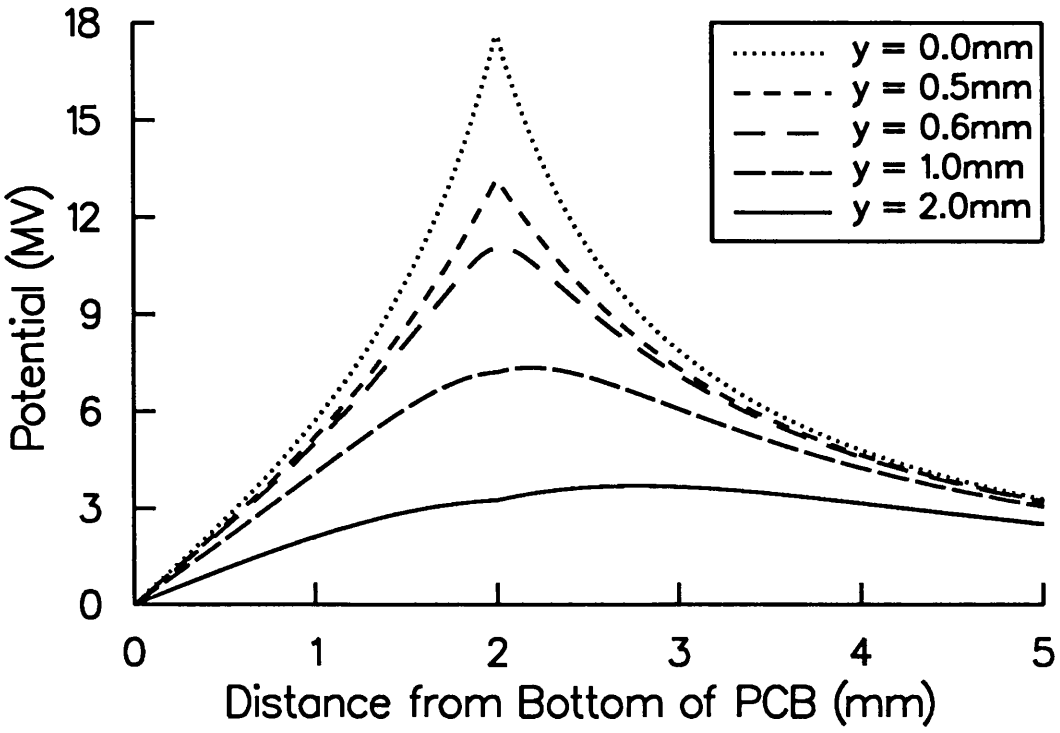

Figure 34. Scalar potential on vertical sections ymm from centre of rectangular polygon element

PCB. Five different sections were used for each case. The first of these was at the centre of the element, the next on the edge, followed by one just outside the element, and another two further away. The following diagram shows a view looking down on the PCB. Each dot indicates where a vertical section passes up through the PCB.

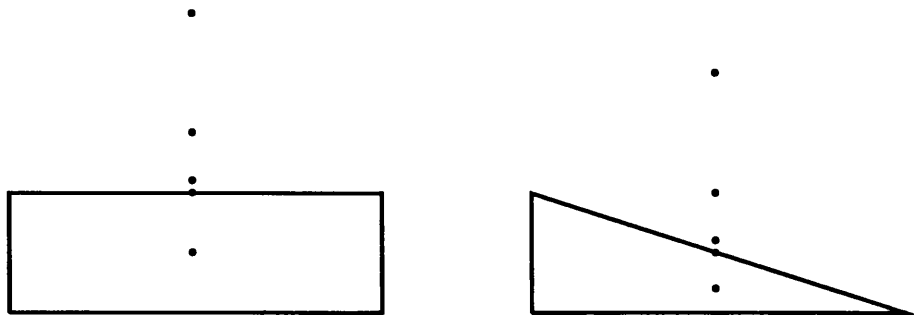

Figure 34 shows the potentials on these sections for the rectangular polygon element, Figure 35 shows the potentials for the rectangular track element, and Figure 36 shows the potentials for the triangular element. These demonstrate the expected features. The plots for the rectangular track element are normalised so that they represent the same total charge as the rectangular polygon element. All three sets of plots are similar, although the plots

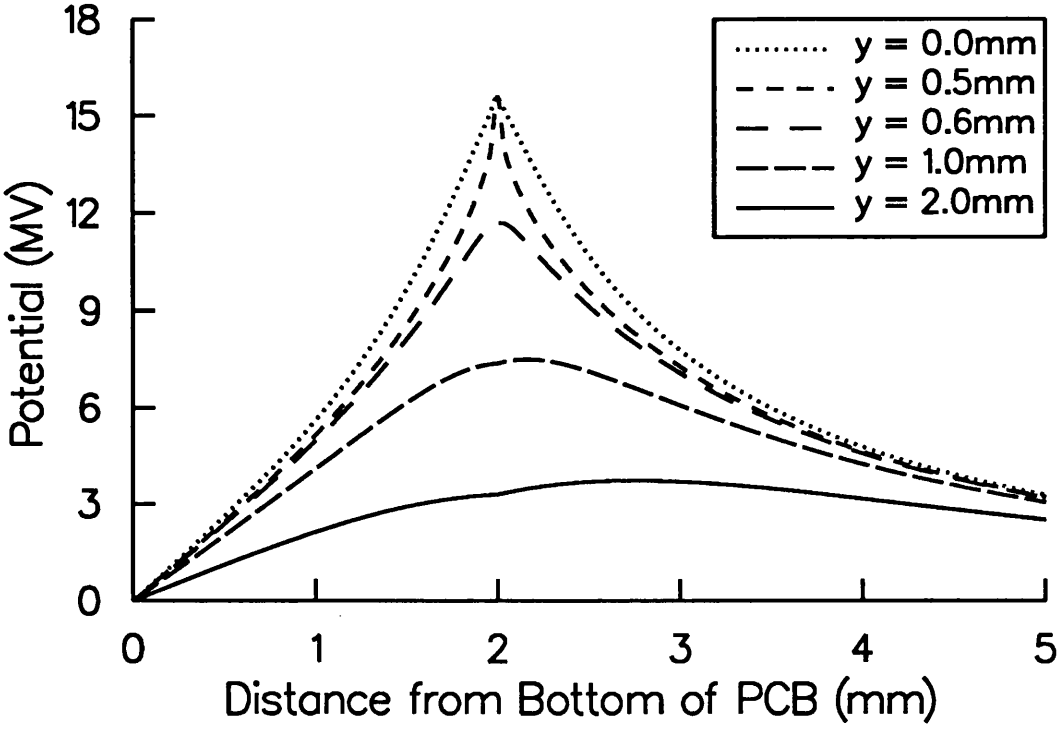

Figure 35. Scalar potential on vertical sections ymm from centre of rectangular track element

for the triangular element have a smaller potential since this element contains half the charge of the rectangular element.

The first section, at the centre of the element, has the largest potential, and this shows a discontinuity of gradient, in the form of a sharp peak, at the vertical position of the element. The second section, at the edge of the element, also exhibits this sharp peak, and this is at almost the same level for the track element. The remaining sections show no sharp discontinuity.

The second effect expected is the discontinuity in the gradient of the potential at the boundary between the two dielectric layers. This can only become apparent if the gradient of the potential is non-zero at the boundary. This is the case for the final two sections, where the peak in potential moves above the PCB, and this discontinuity of gradient can be seen clearly, particularly for the $y = 2$ mm section. This can be examined more closely for the rectangular polygon element. Denoting the distance from the bottom of the PCB by z, the potentials immediately adjoining the boundary are:

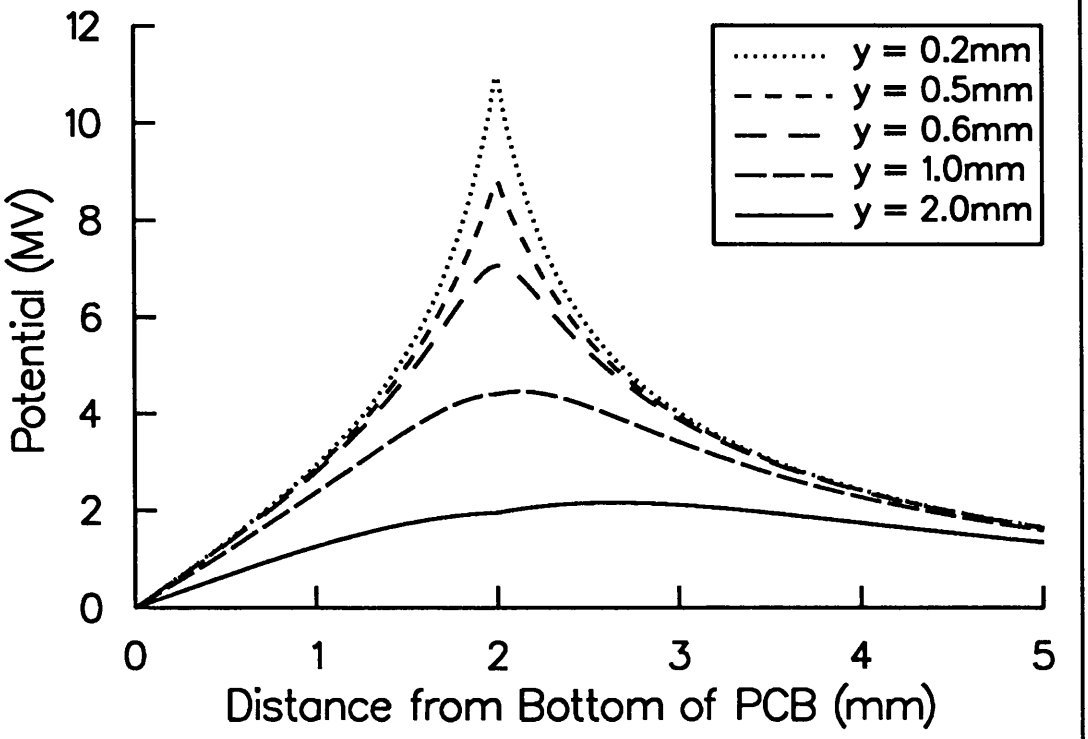

Figure 36. Scalar potential on vertical sections ymm from edge of triangular element

z	Potential	Difference	Subroutine
1.9999mm	3 252 623.140 V	27.849 V	SPR1CM
2.0000mm	3 252 650.989 V		SPR1CS
2.0001mm	3 252 777.582 V	126.593 V	SPR1CB

The difference column shows the difference between the potential and that at $z = 2$ mm. The ratio of these two differences is 4.55, the ratio of the dielectric constant of the board (4.55) to that of free space (1.00), which is the expected answer. This therefore demonstrates that the three subroutines involved match correctly at the boundary between their regions of validity.

Similar results have been obtained for the ground plane parallel to the bottom of the PCB or absent altogether, and for the vector potential, enabling considerable confidence to be placed in all the potential subroutines.

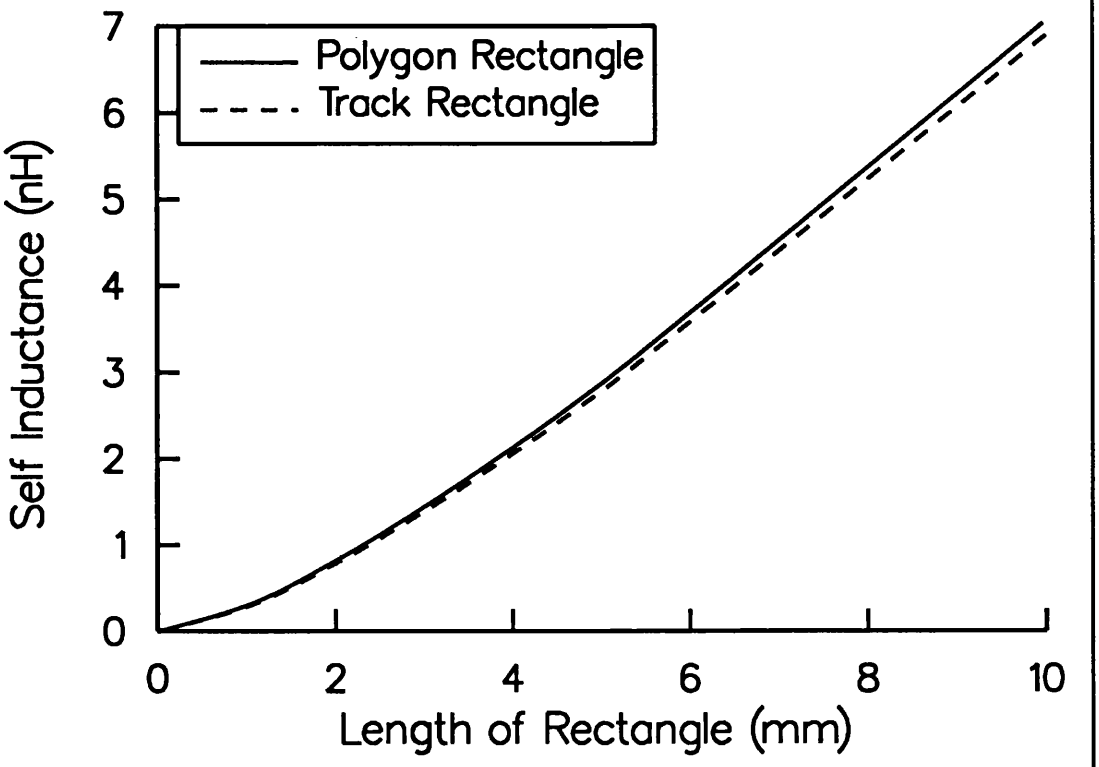

Figure 37. Self inductance of a polygon rectangle compared with that of a track rectangle

6.6 Self Inductance of a Rectangle

The self inductance of a polygon rectangle can be checked by comparing its value with that computed for a track of the same dimensions by FACET. Figure 37 shows this comparison for a rectangle 1mm wide, with a length of between 0 and 10mm. The results are very close. The difference ranges from 5.5% at a length of 1mm to just 1% at a length of 10mm.

This difference is probably due to the different basis functions used. The current density basis function for tracks in FACET was given by equation 5.26 as

$$J_x = \frac{1}{\sqrt{b^2 - y^2}} \tag{5.26}$$

where J_x is the current density, b is the half width of the track and y is the distance from the centre of the track in the width direction. This gives a current distribution which is crowded towards the edges of the track, whereas the current density basis function used for polygon

rectangles gives a constant current across the width of the track. This probably accounts for most of the difference between the two results.

Good confidence can therefore be placed in the correctness of the formula used for the self inductance of a polygon rectangle, and also of the implementation of self inductance for track rectangles in FACET. It can also be shown that the formula for the self inductance of a rectangle given in equation G.72 is equivalent to that given by Ruehli [1972] when applied to a rectangle of zero thickness.

6.7 Mutual Inductance between Rectangles

The mutual inductance between polygon rectangles for which the assumed directions of current flow are parallel can also be checked by comparison with the results for track rectangles of the same dimensions from FACET, and by comparison with the formulae developed for the mutual inductance between vias in Chapter 4.

This was done for two rectangles, one on either side of a PCB. The location of the rectangles is shown on the following plan, with the co-ordinates given in mm:

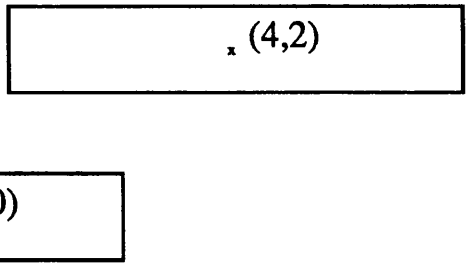

The first rectangle is centred at the origin, and is of length 5mm and width 1mm. The second rectangle is centred at (4mm,2mm), and is of length 6mm and width 1mm. The thickness of the PCB was varied from 0mm to 100mm, this giving a variable separation of the two rectangles in the plane perpendicular to the PCB surfaces. The results are shown in Table 8. The results for the track rectangles were derived using FACET, which employs a six point numerical integration instead of the analytic integration performed for polygon rectangles. The results for the polygon rectangles were obtained directly from the subroutine MIPRPR. The two sets of results are extremely close. The largest difference is for the zero thickness PCB, and this is only 0.2%.

Thickness of PCB (mm)	Mutual Inductance (pH)	
	Polygon Rectangles	Track Rectangles
0.0	772.83	774.55
0.5	761.69	763.07
1.0	732.70	733.44
2.0	652.35	652.32
5.0	443.87	443.72
10.0	270.19	270.15
20.0	145.58	145.58
50.0	59.701	59.700
100.0	29.962	29.962

Table 8. Mutual inductance between two rectangles

Another check is provided by comparing the results from polygon rectangles to those from vias, which are modelled as hollow cylinders. This has been done for two rectangular elements, each 10mm long and 1mm wide. The elements are separated either vertically (ie. perpendicular to the surface of the PCB) or horizontally (ie. in the plane of the PCB and perpendicular to the current flow direction). A separation of 0 corresponds to the elements being coincident. The pair of vias used for comparison were each 10mm long with a 1mm diameter. Here the separation is defined to be that in a direction perpendicular to their axes.

Figure 38 shows the results. When the elements are coincident, the mutual inductance between them is just the self inductance of one of them, as would be expected (the value is the same as that for a 10mm long rectangle in Figure 37). The self inductance of the via is less than that of the rectangle, because the current is spread out over a greater volume.

As the elements are separated, their mutual inductance changes in different ways. The vertical separation of rectangles produces the fastest initial decrease in inductance. This is because in the other two cases, the elements remain partially overlapping (a situation not possible in reality) until the element centres are separated by 1mm or more. This means that the current distributions reflect the closer proximity for a given separation for these two cases than for the vertical separation, and so the mutual inductance falls off more slowly.

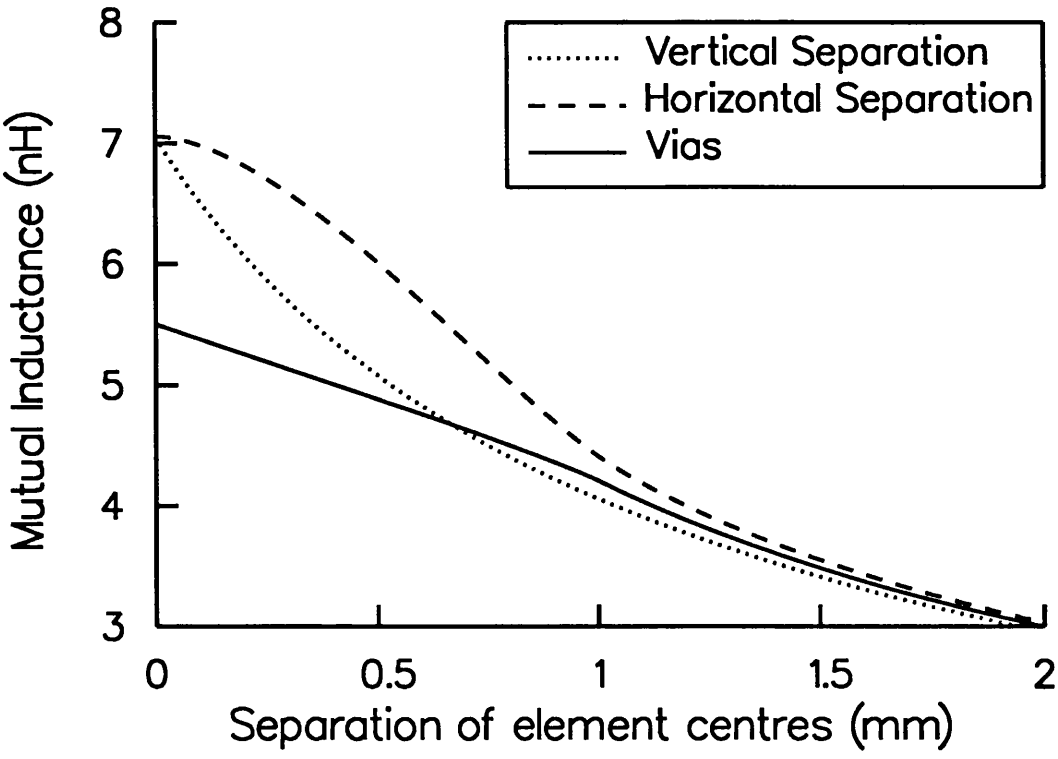

Figure 38. Mutual inductance between elements with varying separations

At a separation of 2mm, all three cases have nearly the same mutual inductance, and at larger separations they converge completely. This is because at large separations, the distances over which the current is spread are small in comparison with the separation, and so the details of the current distribution become unimportant.

These two checks indicate that the mutual inductance calculated by the subroutine MIVIVI has reasonable values, and exhibits the correct behaviour both at small and large element separations.

6.8 Vector Potential and Self Inductance of Triangles

In order to demonstrate that the correct normalisations have been applied to the vector potential, a set of triangular elements in a form very similar to a rectangle was created. This arrangement is shown in Figure 39, where the co-ordinates are given in mm, and are the local co-ordinates of the bottom left triangle. It consists of ten triangles, each having sides

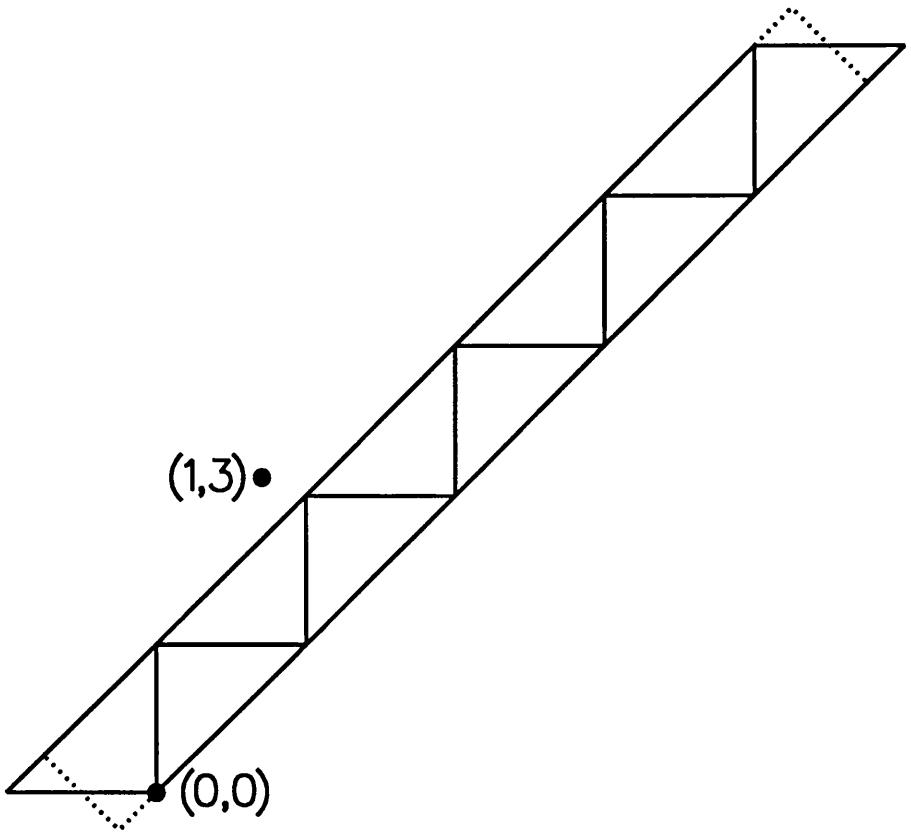

Figure 39. Set of triangular elements, with equivalent rectangular element shown dotted

of length $2a = 2b = \sqrt{2}$ mm = 1.41421 mm. This is virtually the same as a rectangle 10mm long and 1mm wide aligned at 45° to the global X axis. This rectangle is shown dotted in Figure 39. The only differences are at the two ends. The vector potentials are compared at the point shown, which is at (1,3)mm in the local co-ordinates of the bottom left triangle and at (-1.67157 , 0.91421)mm in the local co-ordinates of the equivalent rectangle. The vector potentials are:

```
Triangle:  0.24790 x 10^-6
Rectangle: 0.24778 x 10^-6
```

The difference is only 0.05%, indicating that the correct normalisation for the vector potential has been chosen. The existence of any difference at all is due to the effects of the two ends.

The second comparison which can be made is for the self inductance, using the same equivalent rectangle for comparison. The results here are:

```
Triangle:  4.9383 nH
Rectangle: 4.8143 nH
```

These results are not quite so close - the difference is about 2.5%. However, the self inductance of the rectangle was computed analytically, while that of the set of triangles was computed by numerical integration, with four points per triangle. The error resulting from this can be as much as a few percent, so the results agree as well as could be expected.

6.9 Conclusions

This chapter described a variety of tests that have been performed on the subroutines described in Chapter 5. These included checks on internal consistency, comparison of results from tracks, polygon elements and vias, and comparison with known results. All these tests were passed satisfactorily, indicating that the results generated can be used with confidence.

Before the subroutines can be of use in FACET, the input geometry, consisting of a description of the PCB layout in terms of tracks, pads, polygons and vias, has to be processed into a set of elements. The next chapter describes how this is performed for polygons, producing the necessary set of rectangular and triangular elements.

Chapter 7

Modelling of Arbitrarily-Shaped Metallisation Areas

7.1 Introduction

In addition to tracks and pads, radio frequency PCBs often contain other areas of metallisation. These may be of irregular shape, or may be rectangular in shape but so wide that the assumptions made in modelling them as tracks would not be valid.

This chapter describes how the input geometry, ie. the polygon shape, is processed to produce the sets of inductive and capacitive elements introduced in Chapter 2, which provided a theoretical basis to the modelling of such areas as polygons. These elements are represented by rectangles or right angled triangles. The sections follow fairly closely the computer code written to perform this function, and illustrate the method by following a particular example through all the stages.

The strategy adopted is firstly to form a grid of nodes over the polygon. Elements are then created between and around the nodes, in as similar a manner as possible to the idealised set of elements described in Chapter 2. At the edges of the polygon, the element formation is slightly different. Effectively, an element is created in the normal way, and then truncated by the side of the polygon. This results in either truncated rectangles or triangles for elements. Considerable effort has been applied to this method, to cover the great variety of possible input geometries and to produce an efficient solution.

Each self inductance in the equivalent circuit is represented by just one inductive element. However, a capacitor plate can be represented by up to three capacitive elements, because some capacitive elements at the polygon edge can be created with a complex shape. These elements have to be subdivided to produce just rectangles and right angled triangles, so that the subroutines described in Chapter 5 can be used. This will be seen when elements are created for the example polygon.

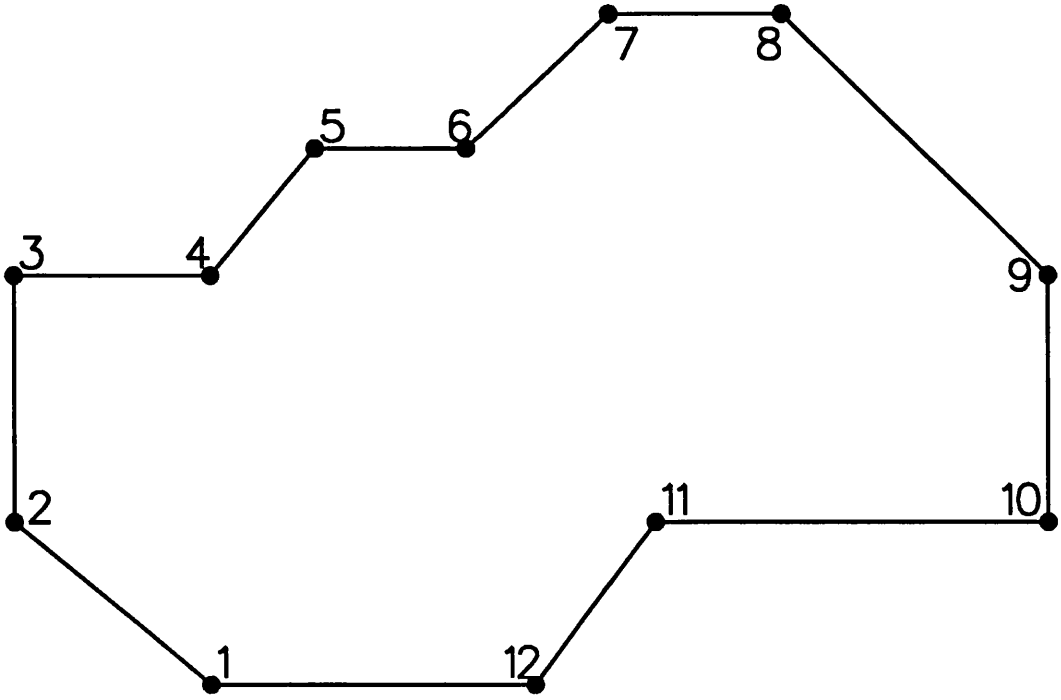

Figure 40. Outline of example polygon, showing order and location of corners

When the geometry processing has been described, ways in which the efficiency of the model could be improved are discussed. This is because in some situations the time taken for the simulations can become excessive, particularly when polygons are being used to model non-ideal ground conductors. Several methods which could be of use are identified and assessed.

7.2 Input and Grid Definition

The polygon geometry is described by an ordered list of the (x,y) co-ordinates of its corners. These can be provided in either a clockwise or an anti-clockwise sense, but they are always translated into a clockwise order. A set of bondpoints can also be provided. These are points within the polygon where components may be connected. They are specified by their location and a node number, which is used to identify the bondpoint in the input file of the

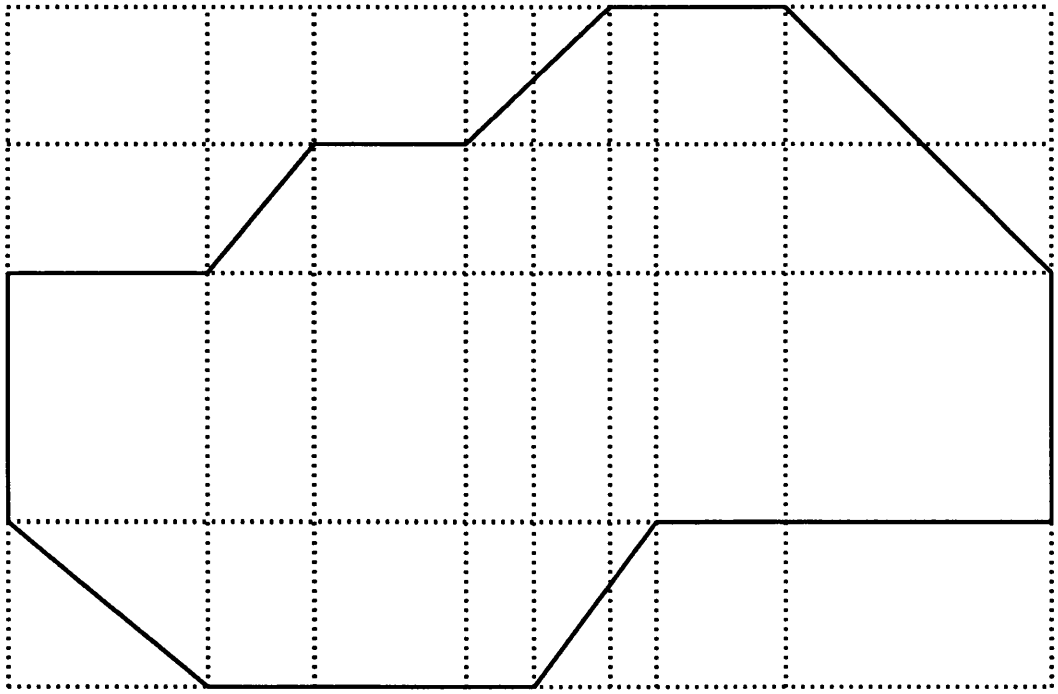

Figure 41. Initial set of grid lines produced for the example polygon

circuit analysis package (PHILPAC or PANACEA), which is automatically generated by FACET.

Figure 40 shows one example of a set of twelve corners and the polygon shape associated with them. The aim of the grid definition is to produce a set of lines parallel to the global X and Y axes, which subdivides the polygon into a set of rectangles and right angled triangles.

The first task is to form two arrays, containing all the distinct x co-ordinates and all the distinct y co-ordinates present in the set of input corners. These provide the initial set of grid lines. A grid line parallel to the Y axis is produced at each x co-ordinate, called an X grid line. Similarly, at each y co-ordinate a Y grid line, parallel to the X axis, is produced. The situation is then as shown in Figure 41.

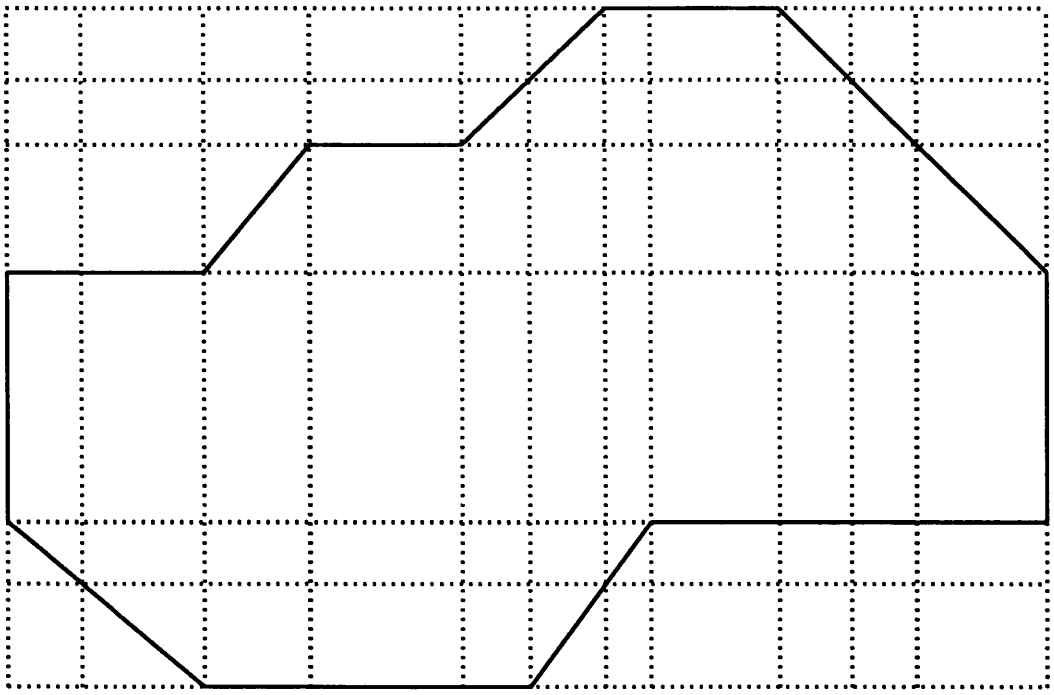

Figure 42. Final set of grid lines produced for the example polygon

It can be seen that the set of grid lines just produced creates trapezia, as well as rectangles and right angled triangles. To correct this, an X grid line needs to be produced where a Y grid line intersects a diagonal side (if one is not already present), and vice versa. This process of creating new grid lines continues until there are no points on a diagonal side where it is intersected by just one grid line. The full set of grid lines for the example polygon is shown in Figure 42 - three extra X grid lines and two extra Y grid lines have been produced in the second part of the process just described.

For the equivalent circuit produced to represent the polygon to be an accurate model of propagation effects, the grid lines must be separated by no more than one tenth of a wavelength at the highest frequency of interest. This is so that the piecewise constant approximations to the charge and current distributions in the polygon have sufficient flexibility to model the actual distributions fairly accurately. If any grid lines are separated by more than this amount, the appropriate number of extra grid lines are inserted between

them. When this has been done, the check for grid lines intersecting diagonal sides needs to be performed again, and any extra grid lines that are found to be necessary are generated.

The above process means that it is possible to generate an input geometry which results in a very large number of grid lines being generated. An example of this is a square with a corner placed at the origin and one side orientated at 46° to the X axis. However, analysis of several RF board designs found no geometries likely to cause such trouble. If any are found, the methods described in section 7.7 could be used to eliminate the problem.

This completes the definition of a grid for the polygon. It is now possible to work with integer co-ordinates. An integer x co-ordinate of 1 is assigned to the X grid line with the smallest x co-ordinate, a co-ordinate of 2 to the line with the next smallest x co-ordinate and so on. The same operation is then performed for the integer y co-ordinates from the Y grid lines. The positions of all the corners and bondpoints can now be expressed in these integer co-ordinates, which makes the subsequent processing much more efficient.

7.3 Classification of Sides and Corners

To proceed further, it is necessary to have some method for classifying the orientation of sides of the polygon and the shape of corners. Working in integer co-ordinates, there are four possible orientations for a line (one parallel to each of the two axes, two diagonal at any intermediate angle). Here, the direction of a line is also important. This is because each line joining two corners has metal to one side of it and not the other. Because the corners are provided in a clockwise direction, on progressing from one corner (the n^{th}) to the next (the $(n+1)^{th}$) the metal is always to the right. There are hence eight distinct orientations of a side needed here (the four referred to above, each with metal to one side or the other of it), illustrated in Figure 43, for the side between corners n and $n+1$. They are assigned the labels 1 to 8, in order of their angle to the global Y axis. Those with labels 1 and 5 are parallel to the Y axis, those with labels 3 and 7 are parallel to the X axis, while the others can have any intermediate orientation.

A corner is created at the junction between two sides. The scheme adopted to classify corners is similar to that used to classify sides. Each type of corner has a two digit label. For the n^{th} corner, the first digit is the orientation label of its first side, joining the $(n-1)^{th}$ and n^{th}corners. Similarly, the second digit is the orientation label of its second side, joining

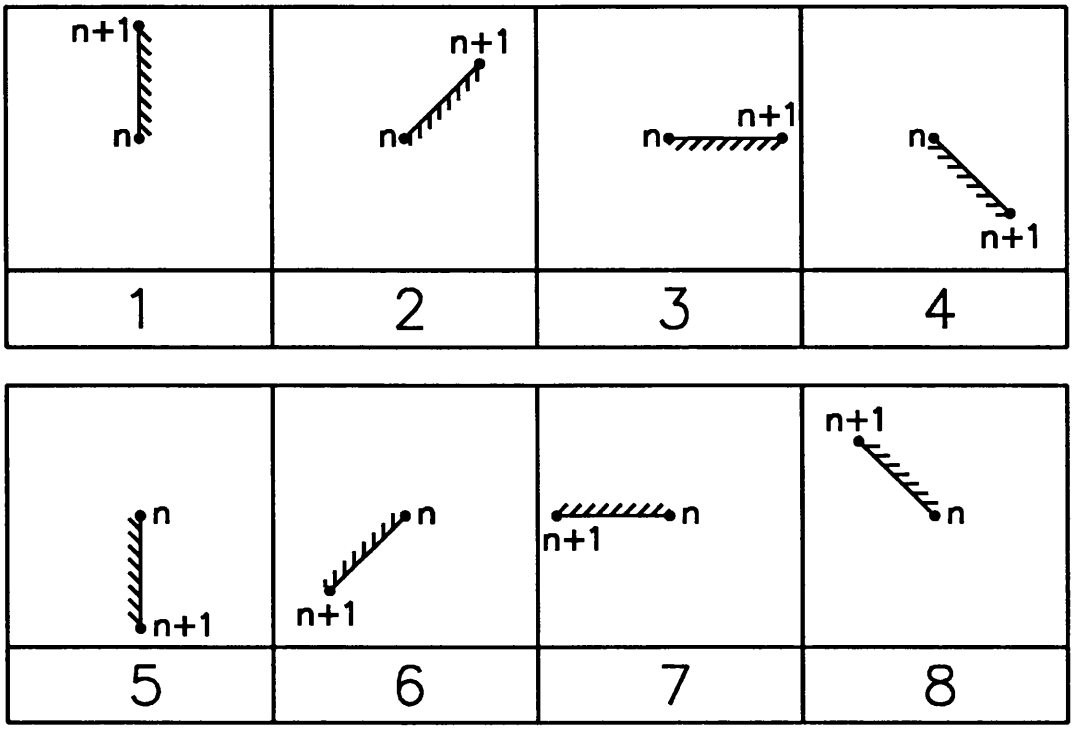

Figure 43. Classification of sides: the shaded side indicates the interior of the polygon

the n^{th} and $(n+1)^{th}$ corners. It follows that there are 64 possible corner type labels, the full set of which is illustrated in Figure 44. Of these 64 possible labels, 12 are not allowed and have a cross through them in the figure. There are several reasons for this:

- Labels 11, 33, 55 and 77 correspond to three corners in a straight line, parallel to one of the axes. This situation is considered an input error, as prohibiting it simplifies the geometry processing.
- Labels 15, 37, 51 and 73 correspond to three corners in a straight line which doubles back on itself. This corresponds to a piece of metal of zero thickness, and is therefore not allowed.
- Labels 26, 48, 62 and 84 correspond to a possible geometry. This is because the orientations of the two sides do not have to be the same and so they could form an acute angle at the corner where they meet. However, the algorithm described earlier for the creation of a grid will produce an infinite number of grid lines if such corners are present, and so they are forbidden. No such geometries have been observed in any real layout.

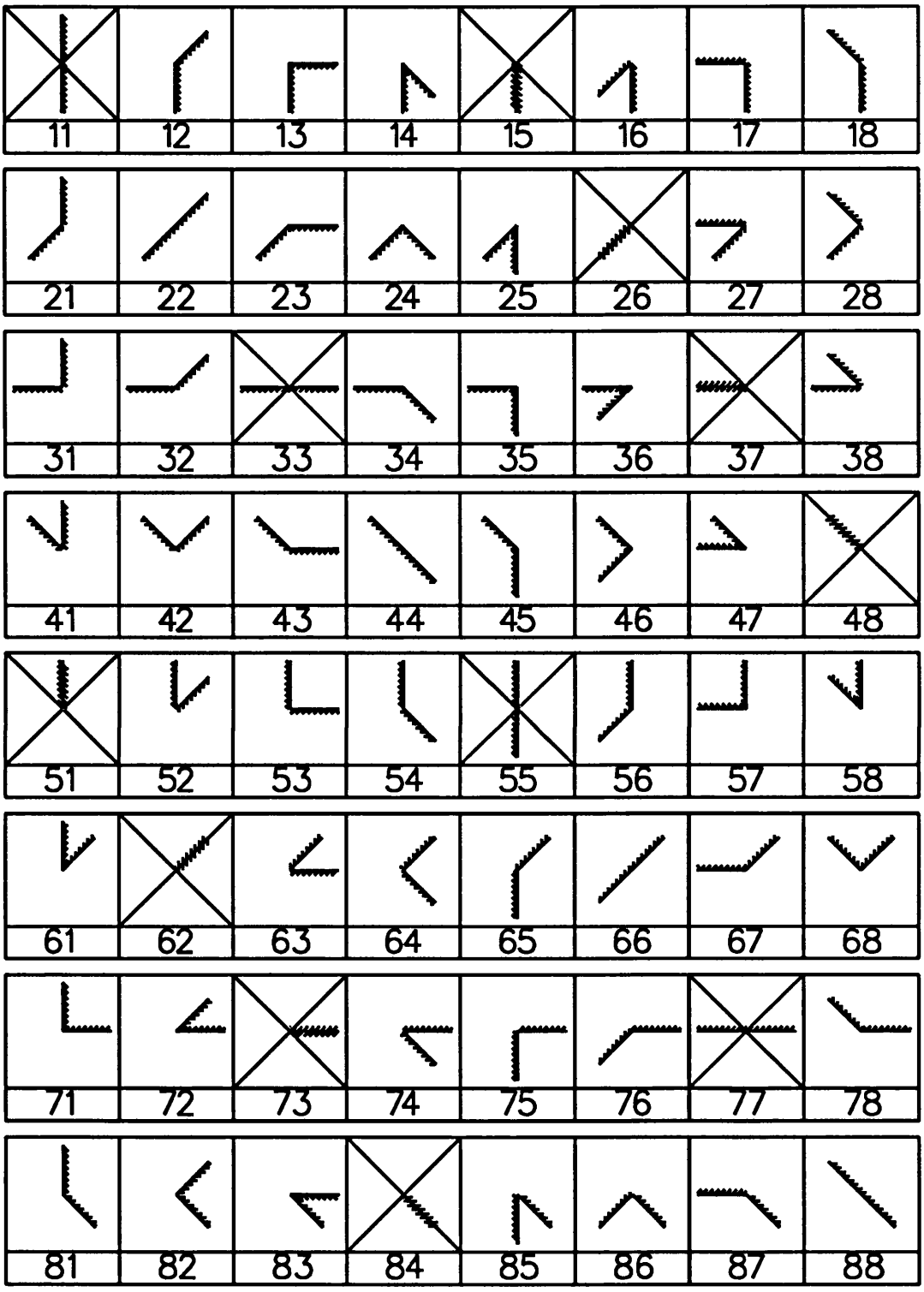

Figure 44. Classification of corners: the shaded side indicates the interior of the polygon

-1	-1	-1	-1	-1	-1	123	13	134	-1	-1	-1
-1	-1	-1	-1	-1	12	0	0	0	14	-1	-1
-1	-1	-1	123	132	0	0	0	0	0	14	-1
113	13	132	0	0	0	0	0	0	0	0	145
181	0	0	0	0	0	0	176	17	17	17	157
-1	18	0	0	0	0	16	-1	-1	-1	-1	-1
-1	-1	178	17	17	167	-1	-1	-1	-1	-1	-1

Figure 45. Initial shape array for the example polygon

7.4 Creation of the Shape Array

Now that the corners and sides have been classified, a two dimensional array containing a representation of the polygon shape is set up. This enables subsequent processing, to proceed as easily as possible. Figure 45 shows the shape array for the example polygon - the rows have been displayed in reverse order so that the shape appears with the same orientation as in previous figures. This array contains the same number of rows as Y grid lines and the same number of columns as X grid lines. The (i,j) entry in the array corresponds to the point with an integer x co-ordinate of i and an integer y co-ordinate of j. Each array entry is an integer which gives information on the location of the corresponding point. The scheme for assigning array entries is shown in Table 9. A point can have one of four types of location. These locations, and their initial array entries, are:

1. Outside the polygon, array entry = -1
2. Inside the polygon, array entry = 0
3. On a side of the polygon, array entry = side label + 10
4. At a corner of the polygon, array entry = corner label + 100

The calculation of the initial array entries is performed as follows:

1. The whole array is filled with zeroes
2. The first side (connecting corners 1 and 2) is selected
3. The array entries corresponding to each of the two corners are set to the correct value (corner label + 100)

Array Entry	Location of Point	Is the Point a Node?
-1	outside polygon	no
0	inside polygon	no
11 - 18	on a side	no
50	inside polygon	yes
51	inside polygon	yes, bondpoint
61 - 68	on a side	yes
111 - 188	at a corner	yes

Table 9. Locations corresponding to array entries

4. The array entries corresponding to the remaining points on the side (if any) are set to the correct value (side label + 10)
5. Steps 2-4 are repeated for all the other sides

When this has been done the array contains the correct values for the perimeter of the polygon and zeroes everywhere else. The next step is to decide which points are inside the polygon and which are outside, counting points on the perimeter of the polygon as outside for the present. This is done by passing along the rows of the array in turn, beginning with the first row. When a side or corner is reached, there are three possibilities:

1. The next point will be inside the polygon. The following array entries indicate that this is the case:
   11, 12, 18, 112, 113, 118, 121-123, 128, 171, 172, 178, 181-183, 188
2. The next point will be outside the polygon. The following array entries indicate that this is the case:
   14-16, 134-136, 144-147, 154, 156, 157, 164-167
3. The next point will not differ from the current point. This is the case if neither of the above conditions holds

The first point is assumed to be outside the polygon, and subsequent points are determined to be inside or outside by using the above rules. If a point is determined to be outside the polygon and its corresponding array entry is 0, the entry is changed to be -1. When all the rows of the array have been processed, all the entries are set correctly.

7.5 Assignment of Nodes

With the shape array completely defined, the next task is to decide where nodes should be placed. The first nodes dealt with are the user-defined bondpoints. Each is taken in turn, and the array entry corresponding to its location is modified in accordance with Table 9:

- If the bondpoint is on a corner, the array entry is not changed.
- If the bondpoint is on a side, 50 is added to the array entry.
- If the bondpoint is an internal point, the array entry is set to 51.

Nodes are then placed as necessary over the remaining points in the polygon. Each circuit node is associated with an intersection of grid lines, but each intersection of grid lines does not have to be associated with a circuit node. As was discussed in section 7.2, each equivalent circuit component should be no more than a tenth of a wavelength in size at the highest frequency of interest. This is also the maximum grid spacing, which the node spacing is never greater than. Other than this, nodes have to be placed at corners and to form a rectangular grid in any particular section of the polygon, so that the equivalent circuit model can be created properly. The following definition is necessary to explain the processing:

> Two points are in the same section of metal if a straight line drawn between them does not leave the polygon, ie. does not pass through any points with an array entry of -1.

Each entry in the shape array is examined in turn to see if it should be a node. Calling the point corresponding to this entry the current point, the following rules are used:

- If the current point has an array entry of -1 then it is outside the polygon and cannot be a node.
- If the current point has an array entry of 50 or more, then it is automatically a node (it is either a corner or has been identified previously as a node), and its value is unchanged.

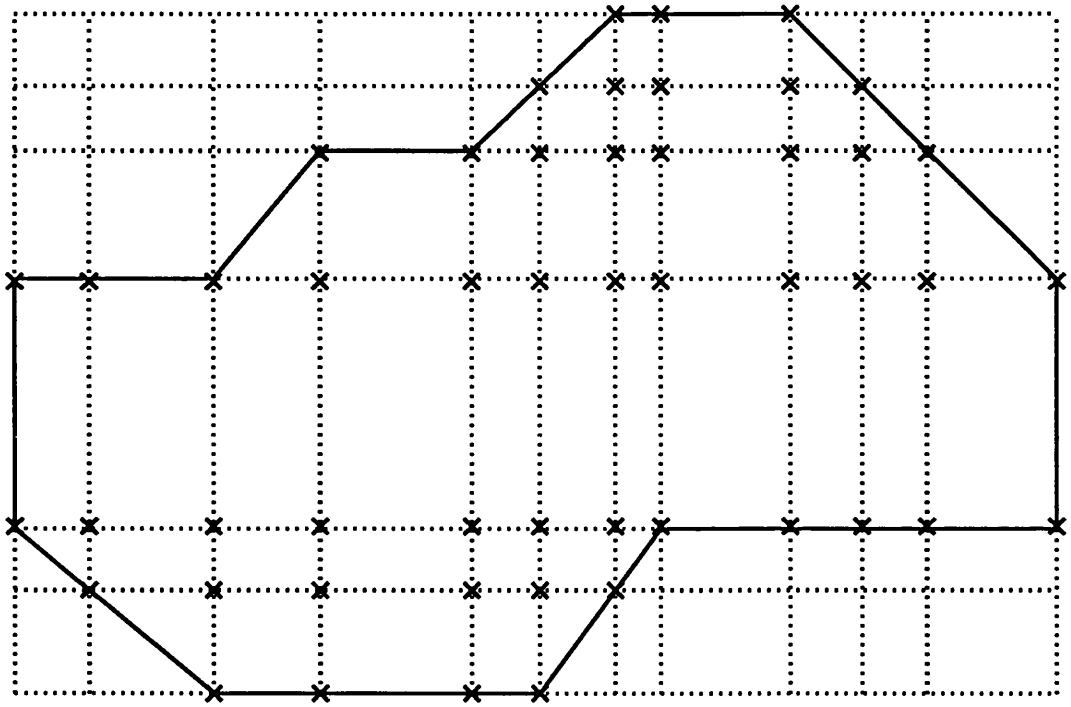

Figure 46. Grid lines and node locations for the example polygon

- If the current point is on a side, it is made a node if there is another node in the same section of metal in one or more of the four directions left, right, up and down. This is signified by adding 50 to its array entry.
- If the current point is an internal point, with an array value of 0, it is made a node if there are one or more nodes in the same section of metal going up or down and there are one or more nodes in the same section of metal going left or right. To signify this, its array entry is changed from 0 to 50.

When all the entries in the array have been examined the above process is repeated, until no new nodes are created. Then a check is made to see if any nodes are spaced by more than the maximum allowed, a tenth of a wavelength. If any are, new nodes are defined one at a time and the above process repeated until all nodes are sufficiently close together.

This process creates the smallest set of nodes possible given that they have to form a rectangular grid within each section of the polygon. In a polygon of simple shape, such as the example being used here, there will be nodes at all internal points. In a polygon of more complex shape however, not all the internal points need have a node associated with them.

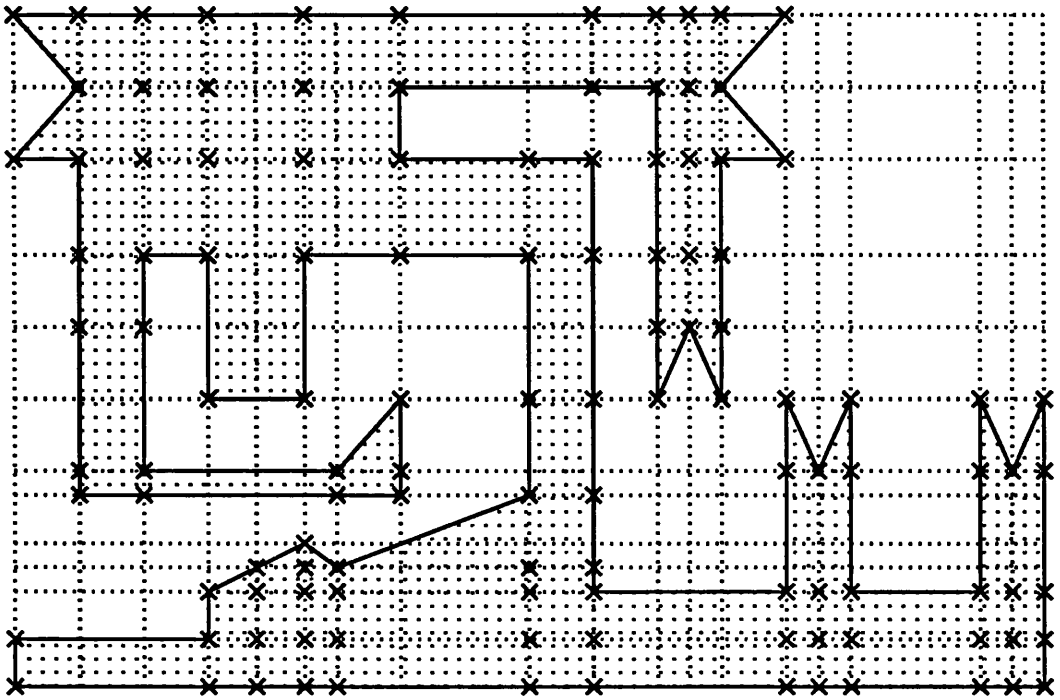

Figure 47. Grid lines and node locations for a complex polygon: interior of polygon shown dotted

Figure 46 shows the node locations for the example polygon - these are marked by crosses, and are at all the intersections of the grid lines within the polygon. Figure 47 shows the same for a rather more complicated polygon. This illustrates the methods described above, reinforcing the point that not all the intersections of grid lines have nodes associated with them.

The final task associated with the nodes is to number them for use in the circuit analysis package. Any nodes associated with bondpoints are given the user-defined node number of the bondpoint. Other nodes are numbered in sequence, starting at the first node in the first row of the shape array and progressing along each row and down the rows. The first number in the sequence is determined elsewhere, and depends on the overall layout geometry: in FACET it is usually 60001 for the first polygon. Each new node number is then just one greater than the last.

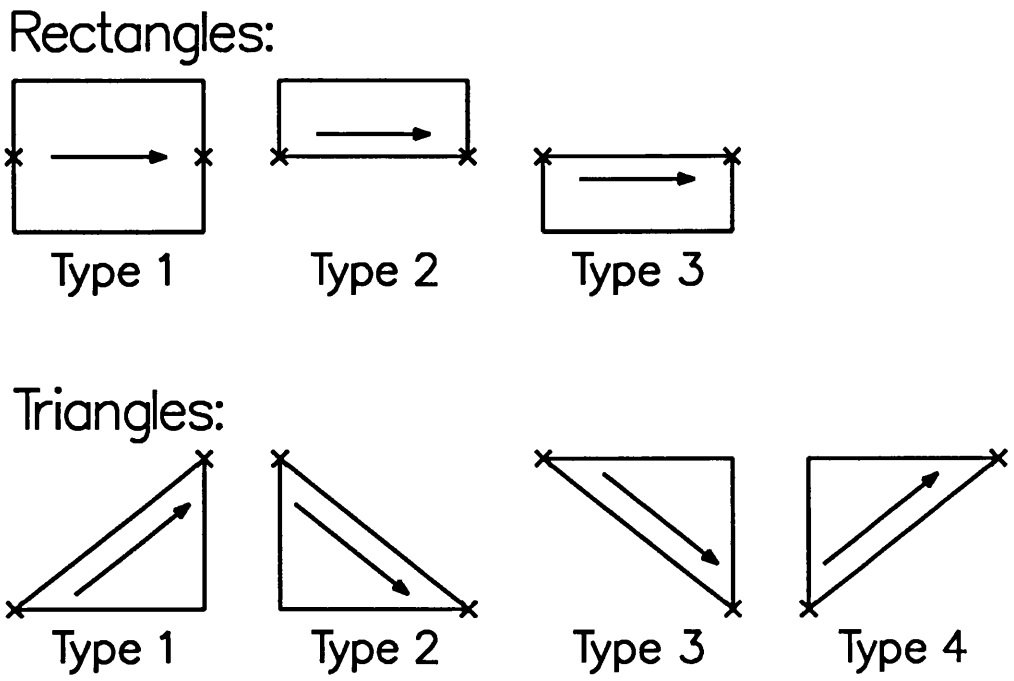

Figure 48. X inductive element types: arrows indicate current flow direction

7.6 Creation of Elements

7.6.1 X Inductive Elements

This set of elements consists of rectangles on which basis functions are defined to represent current flow parallel to the X axis, and right angled triangles on which basis functions are defined to represent current flow parallel to diagonal sides at the edge of the polygon. For convenience, the set is referred to simply as the set of X inductive elements. Figure 48 shows the different types of elements that may be created, showing the direction of current flow within the elements and the two nodes that the element links (marked by crosses). A rectangle connects one node with the node immediately to its right, while a triangle connects one node with the node to the right and one row up or down. Each element represents the series connection of one resistance and one self inductance in the equivalent circuit model. There are three types of rectangle:

- Type 1 is a full width rectangle, used over the interior of the polygon. In width, it extends up halfway to the next row of nodes above, and down halfway to the next row of nodes below.

- Type 2 is a half width rectangle, used at the bottom of a section of a polygon. In width it extends upwards halfway to the next row of nodes above.
- Type 3 is also a half width rectangle, used at the top of a section of a polygon. In width it extends downwards halfway to the next row of nodes below.

In addition, there are four types of right angled triangle, differing in their orientation, with the two nodes connected at opposite ends of the hypotenuse.

Elements are created by stepping through the shape array as before, and considering only those points where nodes are present - these are identified by having a shape label of 50 or more. Next, it is decided for each such point what type(s) of element need to be created - up to two elements may be created, each of which is represented by a separate self inductance and resistance in the equivalent circuit. This is done by examining the shape array. For the present purposes, the current node is called node 1 and the next node along the current row is called node 2.

The following shape labels indicate that node 1 is not at the right hand edge of a section, and hence one or two elements should be created:

50, 51, 61-63, 67, 68, 112, 113, 116-123, 127-132, 138-143, 152, 153, 163, 171-188.

Having decided that elements should be created, it is now necessary to decide which types of elements are required. This is done by examining the shape labels for nodes 1 and 2. Four variables are required, to indicate whether each node is at the top or bottom of a section - these are min_1, min_2, max_1 and max_2. If node 1 is at the bottom of a section, min_1 is set to 1, otherwise it is set to 0. Similarly, if node 1 is at the top of a section, max_1 is set to 1, otherwise it is set to 0. The same process is repeated for node 2 with min_2 and max_2.

Node 1 is counted as being at the bottom of a section if there is no metal below and to the right of it. It is counted as being at the top of a section if there is no metal above and to the right of it. Node 1 is at the bottom of a section for the following values of the shape label:

67, 68, 171-188;

and it is at the top of a section for the following values of the shape label:

62, 63, 112, 113, 122, 123, 132, 142, 143, 152, 153, 163, 172, 182, 183.

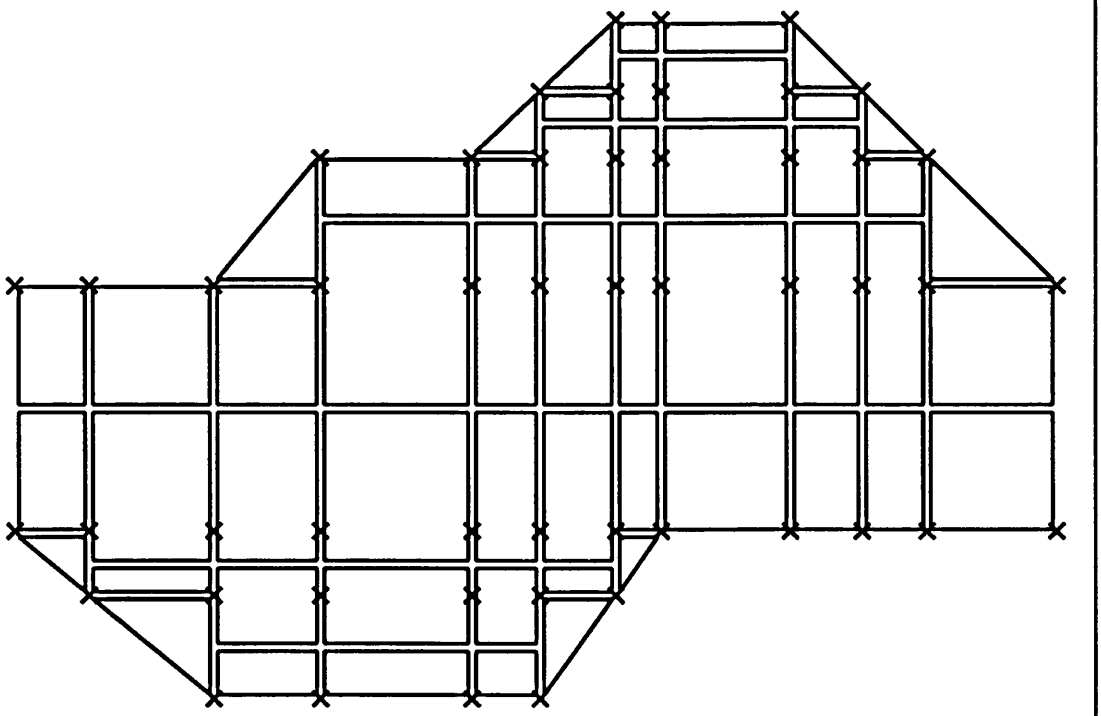

Figure 49. X inductive elements for the example polygon

Slightly different sets of values are used for node 2, this time it is the presence of metal to the left that is important. The resulting set of shape labels indicating that node 2 is at the bottom of a section is:

66, 67, 116, 117, 127, 136, 146, 147, 156, 157, 166, 167, 176, 186, 187;

and the set indicating that node 2 is at the top of a section is:

63, 64, 131-147.

With the four variables set, the required elements can be created. Table 10 shows the elements that are created for different values of the variables min_1, min_2, max_1 and max_2. Figure 49 shows the set of X inductive elements created for the example polygon: they are shown slightly reduced in size to enable them to be distinguished easily.

min_1	min_2	max_1	max_2	Elements created
0	0	0	0	Rectangle type 1
1	0	0	0	Rectangle type 2, triangle type 3
0	1	0	0	Rectangle type 2, triangle type 4
1	1	0	0	Rectangle type 2
0	0	1	0	Rectangle type 3, triangle type 1
1	0	1	0	Triangle types 1 and 3
0	1	1	0	Triangle types 1 and 4
1	1	1	0	Triangle type 1
0	0	0	1	Rectangle type 3, triangle type 2
1	0	0	1	Triangle types 2 and 3
0	1	0	1	Triangle types 1 and 4
1	1	0	1	Triangle type 2
0	0	1	1	Rectangle type 3
1	0	1	1	Triangle type 3
0	1	1	1	Triangle type 4
1	1	1	1	Not possible

Table 10. X inductive elements created in various positions

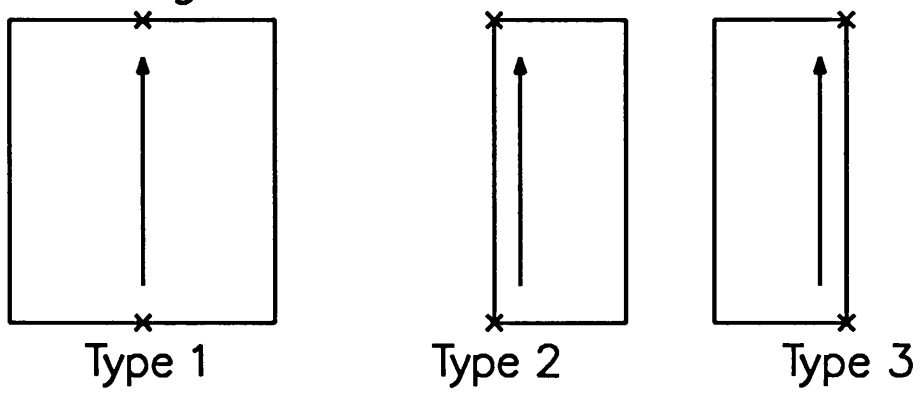

Figure 50. Y inductive element types: arrows indicate current flow direction

7.6.2 Y Inductive Elements

This set of elements consists of rectangles on which basis functions are defined to represent current flow parallel to the Y axis. No triangles are necessary in this set of elements, as they were included with the X inductive elements, and no more than one element is created at each point. A rectangle connects a node with the node immediately above it, and is represented by the series connection of one resistance and one self inductance in the equivalent circuit. There are three types of rectangle which can be created, shown in Figure 50:

- Type 1 is a full width rectangle, used over the interior of the polygon. In width, it extends right halfway to the next column of nodes, and left halfway to the previous column of nodes.
- Type 2 is a half width rectangle, used at the left hand edge of a section of a polygon. In width it extends right halfway to the next column of nodes.
- Type 3 is also a half width rectangle, used at the right of a section of a polygon. In width it extends left halfway to the previous column of nodes.

As before, elements are created by stepping through the shape array and considering those points where nodes are present. For each node, it is decided whether an element will be created, and what type of rectangle it should be. For the present purposes, the current node is called node 1 and the node immediately above it is called node 2.

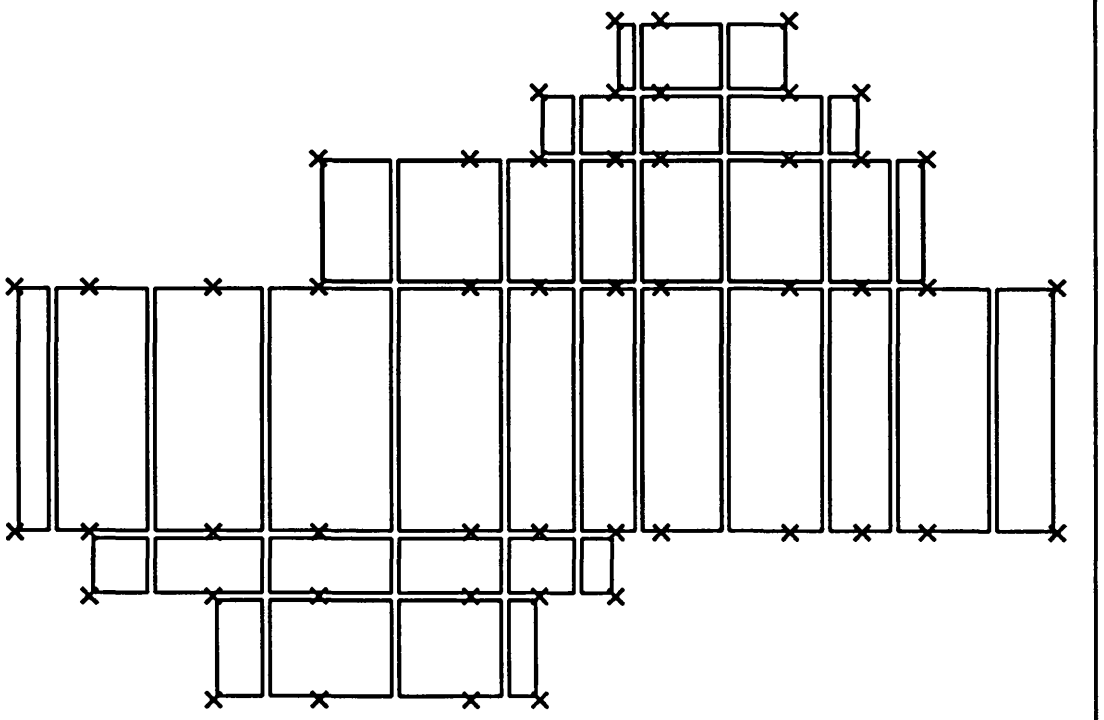

Figure 51. Y inductive elements for the example polygon

No element will be generated if node 2 is at a "triangular peak", with a shape label of:

114, 124, 125

In addition, no element will be generated for certain cases where both nodes are on a diagonal side, or the corner at the end of a diagonal side. The relevant combinations of shape labels are:

node 1: 66, 161-168
node 2: 62, 121-128

or:

node 1: 68, 118, 128, 138, 158, 168, 178, 188
node 2: 64, 114, 124, 134, 144, 154, 164, 174.

For situations not covered by the above, an element will be generated if node 1 is not at the top of a section. The shape labels for which this is the case are:

50, 51, 61, 65-68, 116-121, 127-131, 138, 141, 152-157, 163-167, 171, 174-181, 185-188.

Having decided that an element is to be created, it is necessary to decide which type of element is required. This is done by examining the shape labels for nodes 1 and 2. If there is no metal to the left of either node 1 or node 2, a rectangle of type 2 should be created. The relevant values of the shape label are given below. Only a subset of values are given for node 2, as several values are automatically covered by the value of the label for node 1:

61, 68, 118, 121, 128, 131, 138, 141, 171, 178, 181, 188 for node 1, or
62, 121-128 for node 2.

Similarly, if there is no metal to the right of either node 1 or node 2, a rectangle of type 3 should be created. The relevant values of the shape label are given below, again with only the necessary subset of the values for node 2:

65, 66, 152-157, 163-167 for node 1, or
64, 114, 124, 134, 144, 154, 164, 174 for node 2.

In all other cases, an element of type 1 is created.

Figure 51 shows the set of Y inductive elements created for the example polygon, again shown slightly reduced in size.

7.6.3 Capacitive Elements

The final set of elements to be generated is the capacitive elements. These differ from the X and Y inductive elements in that they have basis functions defined on them to represent the charge density distribution in the vicinity of a node. They also differ in that up to three elements may be created to represent one capacitor plate in the equivalent circuit model. The elements consist of rectangles and right angled triangles. Figure 52 shows the various types of elements that may be created, showing the location of the node for each element as a cross. The type 1 rectangle extends in the X direction from halfway to the previous column of nodes to halfway to the next column of nodes, and in the Y direction from halfway to the row of nodes below to halfway to the row of nodes above. All the other element types can be considered as a subset of the area of the type 1 rectangle, and are drawn to this scale in the figure.

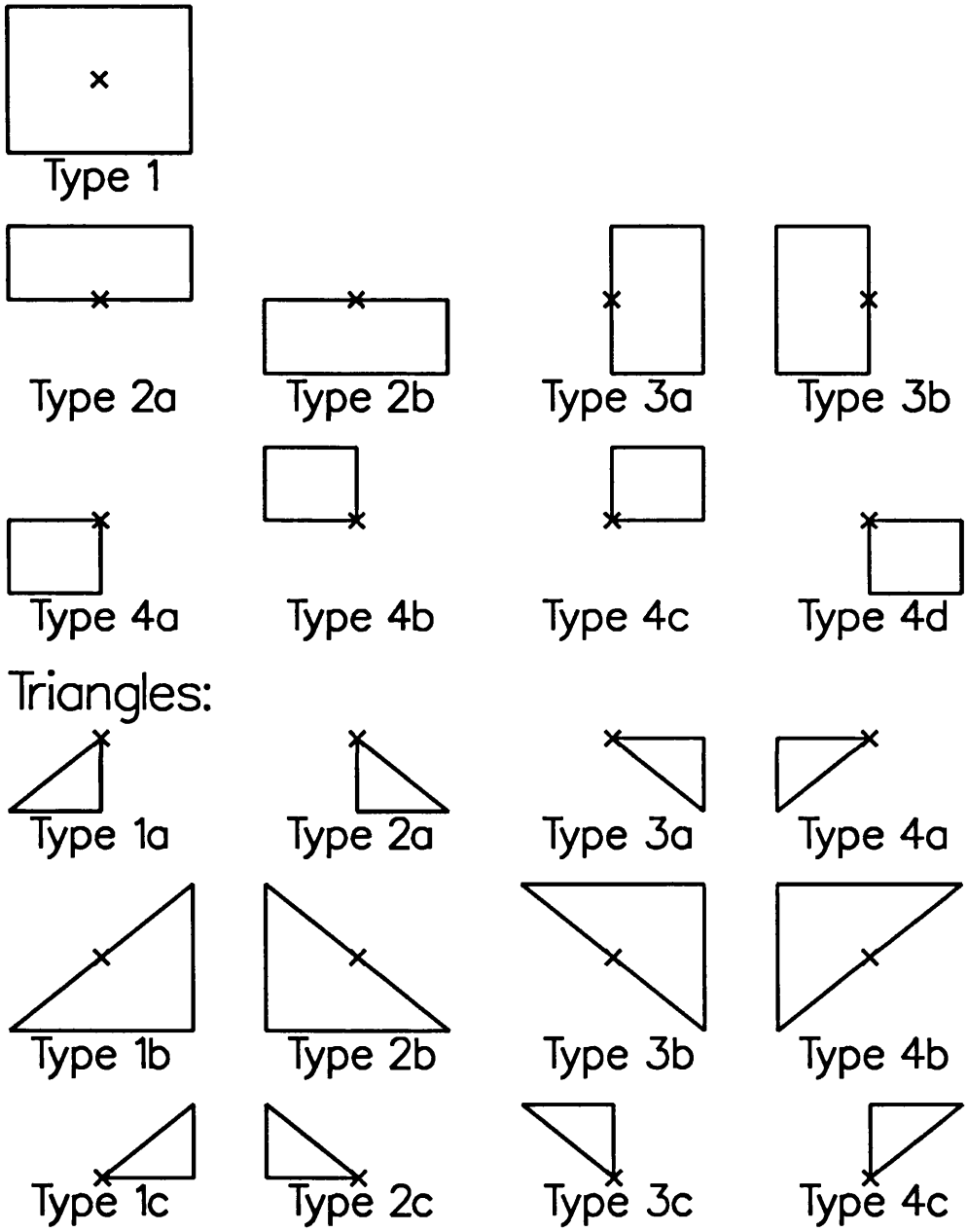

Figure 52. Capacitive element types

As before, elements are created by stepping through the shape array and examining the shape label for each node. The number and types of elements created depends only on the shape label of the current node: one or more elements are always created. Table 11 shows for each element type the shape labels that result in its creation. A particular shape label will result

Element	Shape Labels	Element	Shape Labels
Rectangle type 1	50,51		
Rectangle type 2a	67,116,117,175, 176,185,186,187	Rectangle type 2b	63,131,132,141, 142,143,152,153
Rectangle type 3a	61,118,121, 127,128,138	Rectangle type 3b	65,154,163, 164,165,174
Rectangle type 4a	134,135,138, 144,145,175,185	Rectangle type 4b	127,152,153, 156,157,166,167
Rectangle type 4c	131,141,171, 174,178,181,188	Rectangle type 4d	112,113,116,117, 122,123,163
Triangle type 1a	121 - 128	Triangle type 1b	62
Triangle type 1c	112,122,132,142, 152,172,182	Triangle type 2a	114,124,134,144, 154,164,174
Triangle type 2b	64	Triangle type 2c	141 - 147
Triangle type 3a	181 - 188	Triangle type 3b	68
Triangle type 3c	118,128,138,158, 168,178,188	Triangle type 4a	116,136,146,156, 166,176,186
Triangle type 4b	66	Triangle type 4c	161 - 168

Table 11. Capacitive elements created for various shape labels

in the creation of at most three sub-elements, which together represent one capacitor plate in the equivalent circuit.

Figure 53 shows the set of capacitive elements created for the example polygon, again shown slightly reduced in size.

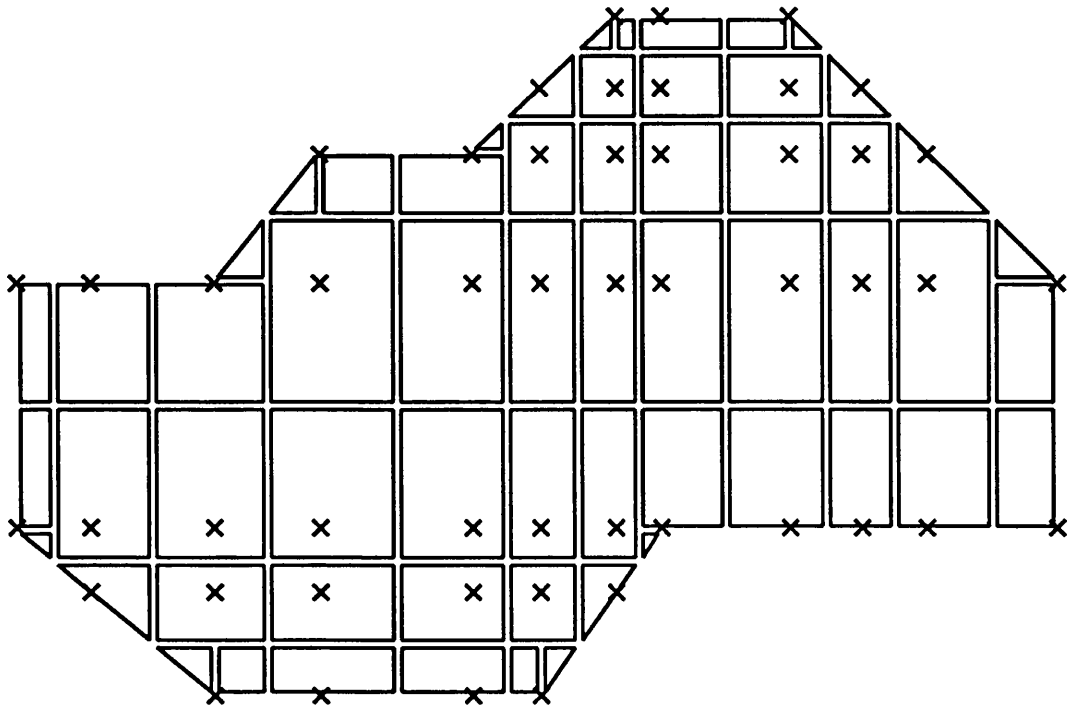

Figure 53. Capacitive elements for the example polygon

7.7 Ways of Improving Efficiency

There are two main sources of inefficiency in the model developed so far. The first is to do with the geometry processing, which in some circumstances can generate an excessive number of elements. The second is to do with the equivalent circuit generated, which can become excessively large. This is particularly the case in modelling non-ideal ground conductors, where all possible couplings must be considered, but can also be a consequence of the first problem.

This section examines briefly ways in which these inefficiencies might be improved. None of these ideas have been fully implemented, and they would form an interesting and useful piece of additional work.

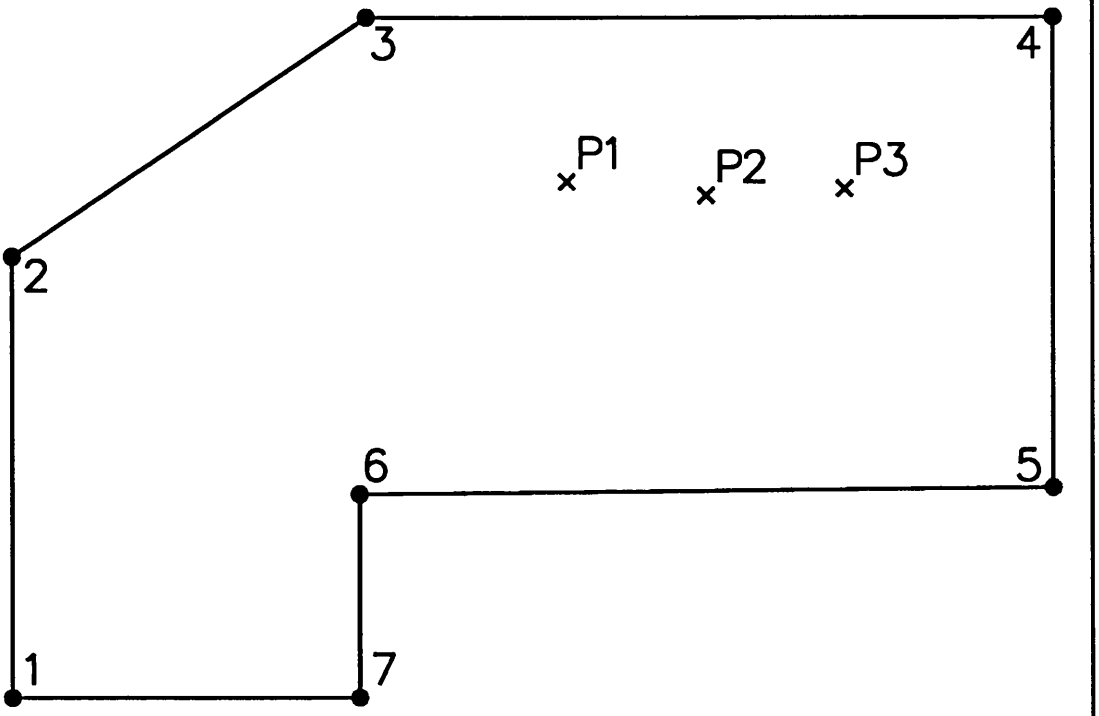

Figure 54. Geometry of polygon example to show excessive subdivision: corners are numbered, bondpoints are marked with a cross and labelled

7.7.1 Improvements to Geometry Processing

Two different ways of modifying the geometry processing have been identified. The first would result in the generation of fewer elements within FACET, while the second would amalgamate several FACET elements into one equivalent circuit element where possible, thus reducing the size of equivalent circuit generated.

7.7.1.1 Generating Fewer Elements

Input geometries with one or more of the following features can result in an excessive number of elements being generated:

- sides which are not quite parallel to the global axes
- corners on different parts of the polygon with almost the same X or Y co-ordinate
- bondpoints with almost the same X or Y co-ordinate as each other or as a corner

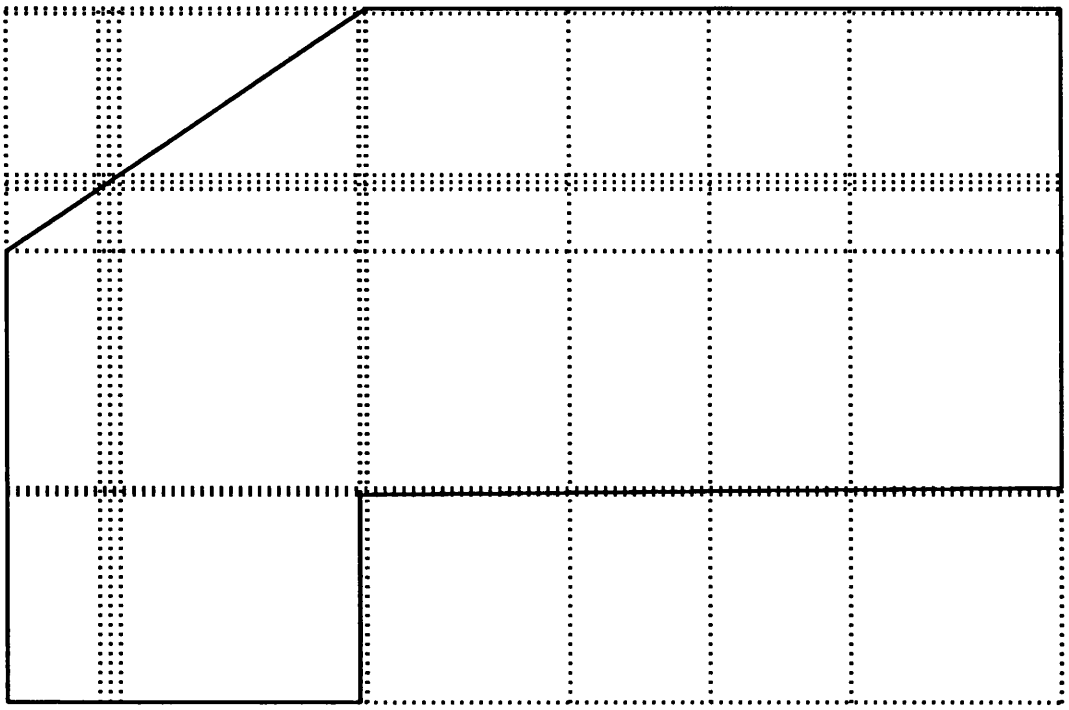

Figure 55. Grid lines generated for the example polygon

An example of a polygon with many of these features is shown in Figure 54. This has seven sides, numbered in a clockwise sense in the figure, and three bondpoints, labelled as Pn (where n is 1, 2 or 3) in the figure. The side between corners 5 and 6 is not quite parallel to the X axis, while corner 3 has a slightly different X co-ordinate to corners 6 and 7. Also (and slightly more obviously), the three bondpoints P1, P2 and P3 all have slightly different Y co-ordinates. Figure 55 shows the effect of this on the geometry processing. An excessive number of grid lines have been generated, some very finely spaced. Because of this, 276 elements were generated, as 177 inductive elements and 99 capacitive elements.

This can be improved by the following steps:

- set the Y co-ordinates of corners 5 and 6 to the mean of their original Y co-ordinates
- set the X co-ordinates of corners 3, 6 and 7 to the mean of their original X co-ordinates
- set the Y co-ordinates of the three bondpoints to the mean of their original Y co-ordinates

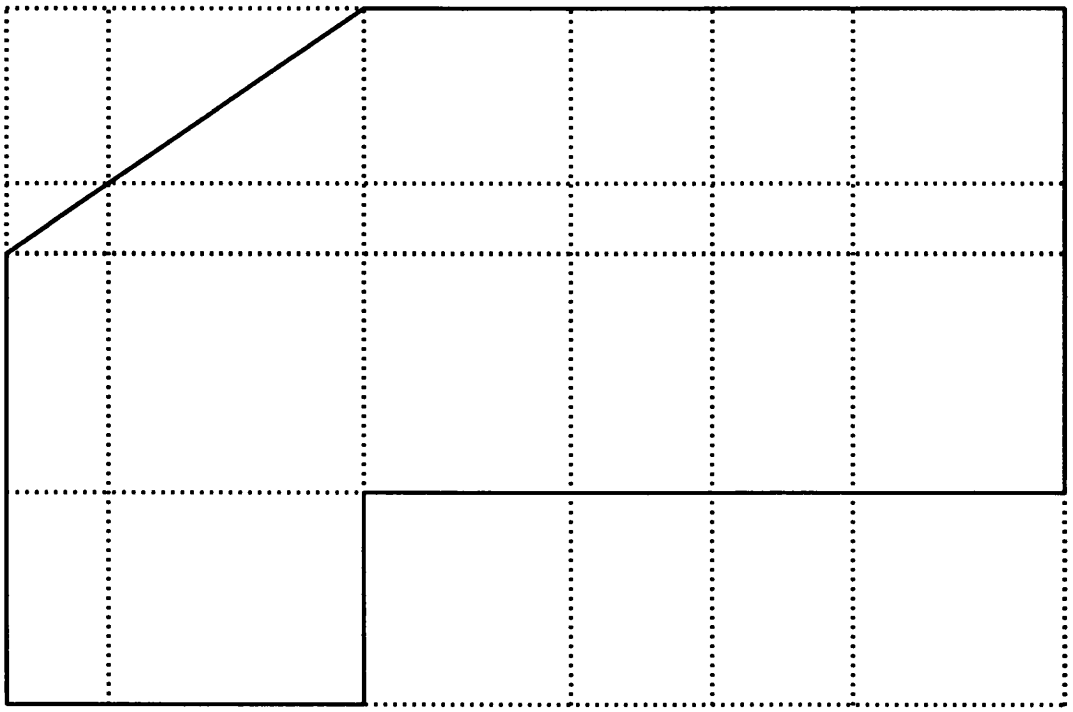

Figure 56. Grid lines generated for the example polygon after realignment of corners and bondpoints

This results in the set of grid lines shown in Figure 56, a considerably smaller set than before. For this modified geometry, 77 elements were generated, as 46 inductive elements and 31 capacitive elements.

This demonstrates that a useful addition to the geometry processing would be a pre-processor, which looked for the sort of problem cases outlined above and realigned the appropriate corners and bondpoints. Rules would need to be built in to this so that features were moved no more than a "reasonable" distance. The definition of a reasonable distance would take account of the size of the polygon, the typical size of other features on the circuit board and the maximum frequency of operation. Such a pre-processor should be relatively simple to implement, and of considerable use.

7.7.1.2 Generating Fewer Components

Even after the steps suggested in the previous section have been taken, there may be more equivalent circuit components generated than are necessary on grounds of electrical length. Components can be up to a tenth of a wavelength square at the highest frequency in the simulation with good accuracy retained. However, the elements within FACET are often smaller than this, either because the geometry of the polygon forces more subdivision or because the greater subdivision is necessary to obtain an accurate representation of the charge and current distributions.

It would therefore be useful to be able to combine several elements together to form one equivalent circuit component where this is appropriate. Such processing is already performed in FACET for track elements, and the same principles could be applied to polygons. A possible procedure could be:

- create the set of grid lines and nodes as described in sections 7.2 to 7.5
- identify a reduced set of nodes spaced up to a tenth of a wavelength apart - these nodes are the ones to which the larger equivalent circuit components will be attached
- generate inductive and capacitive elements as described in section 7.6, but associating them with just the reduced set of nodes

This approach would produce sets of capacitive elements to be combined to form single capacitor plates, and sets of inductive elements to be combined to form single inductances.

The combination of capacitive elements can be handled in the same way as it is for track capacitive elements in FACET already. However, the combination of inductive elements may be more complicated, as there are no simple formulae for combining a sets of series and parallel inductors (together with mutual inductances) into sets of single inductors with mutual inductances between them. The approach suggested in the next section may therefore be more useful in general.

7.7.2 Reducing the Size of the Equivalent Circuit

The equivalent circuit generated for a polygon typically has a large number of components and nodes, but very few of the nodes are connected to anything outside the polygon itself.

In a frequency domain analysis, the effect of all these components could be represented by an N port admittance matrix, where N is the number of external connections.

This relates the column vectors of voltages at circuit nodes, $[V]$ and net (inward) currents at circuit nodes, $[I]$. Denoting the admittance matrix by $[Y]$, the relationship is

$$[I] = [Y][V] \tag{7.1}$$

This matrix contains N^2 entries for each frequency in the simulation, and so can involve many fewer values than the full set of equivalent circuit components for a typical polygon. If it can be generated in less time than PHILPAC or PANACEA takes to analyse the full equivalent circuit, then this could be a useful approach. In fact, even if the time taken is greater than that for the full circuit simulation it may still be useful. This is particularly the case if many different signals are to be applied to the same circuit, when the admittance matrix need only be generated once.

The full admittance matrix for the polygon, involving all the nodes, must first be generated. This consists of four parts:

1. an inductive part $[Y_L]$, which only depends on frequency through the scaling factor $1/\omega$
2. a capacitive part $[Y_C]$, which only depends on frequency through the scaling factor ω
3. an inductive part $[Y_{L_s}]$ due to the skin effect, with more complex frequency dependence
4. a resistive part $[Y_{R_s}]$ also due to the skin effect, with more complex frequency dependence

These parts can then be combined at each frequency to form the full admittance matrix, and the nodes without external connections are compressed out of it, leaving the required N port admittance matrix. These stages are now described in turn.

7.7.2.1 Generation of the Inductive Part of the Admittance Matrix

Given a set of N inductors, the $N \times N$ inductance matrix $[L]$ relates the current flowing in one inductor to the voltage appearing across another. For the i^{th} and j^{th} inductors, this relationship is

$$V_j = L_{ij}\frac{\partial I_i}{\partial t} = j\omega L_{ij} I_i \tag{7.2}$$

where V_j is the voltage induced across the j^{th} inductor; I_i is the current flowing through the i^{th} inductor; L_{ij} is the mutual inductance between the two inductors; and harmonic time dependence of angular frequency ω has been assumed.

To obtain the inductive part of the admittance matrix, what is needed is the relationship between voltages at nodes (rather than between nodes) and currents at nodes (rather than through components). The necessary steps to do this are:

1. Form a list of all the nodes to which one or more inductors are connected.
2. Set the voltage at the first node to 1V and that at all other nodes to 0V. Solve for the currents at all the nodes. This gives the first column of the admittance matrix.
3. Generate the remaining columns of the admittance matrix in the same manner, with each node in turn set to 1V.

To obtain the nodal currents requires N' solutions of the set of equations

$$j\omega [I][L] = [V] \tag{7.3}$$

where the column vector $[V]$ is now the set of unit and zero voltages *across* inductors, and N' is the total number of nodes in the equivalent circuit. Each solution of the above equation provides one column of the inductive part of the full admittance matrix, $[Y_L]$. The only frequency dependence in this part of the admittance matrix is an overall factor of $1/\omega$.

$[Y_L]$ could be regarded as being caused by self inductances alone, so this approach could be used to remove mutual inductances from a circuit if it was necessary, for example if a circuit simulator could only handle a very limited number of them. This equivalent set of self inductances is much larger than the original set, containing in principle a self inductance between each pair of nodes, and some of the values can be negative.

7.7.2.2 Generation of the Remaining Parts of the Admittance Matrix

The remaining parts of the admittance matrix can be calculated much more easily. Take the capacitive part first. The (i,j) element in the admittance matrix is the net inward current at

the j^{th} node with unit voltage applied to the i^{th} node and zero voltage to all other nodes. Hence for the capacitive part of the admittance matrix $[Y_C]$, the element Y_{Cij} is

$$Y_{Cij} = j\omega C_{ij} \tag{7.4}$$

where C_{ij} is the capacitance between the i^{th} and j^{th} nodes. If there is no capacitance present, then the admittance matrix element is zero.

The remaining parts of the admittance matrix are found similarly. The full admittance matrix at angular frequency ω, $[Y]$, is then

$$[Y] = [Y_L] + [Y_C] + [Y_{L_s}] + [Y_{R_s}] \tag{7.5}$$

7.7.2.3 Compression of the Admittance Matrix

The admittance matrix generated in equation 7.5 is an N' port matrix. The final step is to compress this admittance matrix down to the required N port admittance matrix. Writing equation 7.1 in a more explicit form,

$$I_i = \sum_{j=1}^{N'} Y_{ij} V_j \tag{7.6}$$

Assume that only the first N nodes in the set correspond to the required external connections. Hence, there can be no net current at the remaining nodes, ie.

$$I_i = 0 \qquad N+1 \le i \le N' \tag{7.7}$$

Consider the final row of the admittance matrix. Since $I_{N'} = 0$, equation 7.6 can be written as

$$V_{N'} = \sum_{j=1}^{N'-1} \frac{Y_{N'j} V_j}{Y_{N'N'}} \tag{7.8}$$

This enables equation 7.6 to be rewritten as

$$I_i = \sum_{j=1}^{N'-1} Y_{ij}' V_j \tag{7.9}$$

where

$$Y_{ij}' = Y_{ij} - \frac{Y_{iN'} Y_{N'j}}{Y_{N'N'}} \tag{7.10}$$

Y_{ij}' is now an $(N'-1)$ port admittance matrix. Hence, successive application of equation 7.10 can reduce it to the required N port admittance matrix.

7.7.3 Test Results

A short program was written to test out these ideas. It only deals with inductances, converting an inductance matrix of self and mutual inductances to an admittance matrix, compressing this admittance matrix as required, and then converting the reduced admittance matrix to a set of self inductances.

A test run was performed using an example with 175 self inductances, 8141 mutual inductances and 108 nodes. This was compressed to an 8 port admittance matrix, and the simulation times compared. The results were:

- PHILPAC analysis of the full equivalent circuit took about 15 minutes for the first frequency point and 5 minutes for each subsequent point
- Conversion of the inductance matrix to an 8 port admittance matrix and then to a set of 28 self inductances took 14 seconds
- PHILPAC analysis of the resultant circuit took 0.3 seconds for the first frequency point and 0.02 seconds for subsequent points

In this case the compression only needed to be performed once. This is because only inductances were involved, and so the frequency dependence of all the terms in the admittance matrix was the same. The improvement in simulation time is dramatic, and would still be considerable if the conversion had to be performed for every frequency point.

Some effort would be required to set up a scheme for labelling the nodes to be compressed out of the admittance matrix, but apart from this the implementation should be straightforward.

7.8 Conclusions

This chapter has described all the steps taken to process the geometry of the polygon into sets of nodes and elements, to be represented by components in the equivalent circuit. These steps enable the processing to be performed efficiently, generating the smallest possible number of elements.

Some particular input geometries can cause excessive subdivision. These were discussed, together with the problem of excessively large equivalent circuits being generated. Implementation of the pre-processor for the geometry processing and the equivalent circuit compression scheme described should enable the efficiency of simulations to be improved considerably. It would therefore be most worthwhile to investigate these possibilities.

The next chapter examines several examples of the use of these methods, demonstrating their accuracy and discussing efficiency issues where they arise.

Chapter 8

Results

8.1 Introduction

The methods described in this thesis have been incorporated into FACET. This chapter examines several different examples of the many problems which have been modelled using these methods. The results are compared either with experimental data or with previously published work, and give a good indication of the accuracy possible.

As described in Chapters 2 and 7, a given layout is divided into a set of inductive and capacitive elements, representing self inductances and capacitor plates in the equivalent circuit model. The number of inductors or capacitors in the equivalent circuit can be much greater, because there is, in principle, a mutual inductance between each pair of self inductances in the model, and a capacitor formed from each pair of capacitor plates in the model.

8.2 Microstrip Filter

This design is for a low pass filter with a bandwidth of about 2 GHz. The layout is shown as the first picture in Figure 57. It consists of a line about 47mm long and 0.25mm wide, with three wider sections (respectively 5.1mm, 3.1mm and 1.3mm wide) and two stubs, each of which is terminated by a larger area of metal. The input end of the filter is labelled with a "1", and the output end of the filter is labelled with a "2". The substrate is 0.635mm thick alumina, with a dielectric constant of 10.5 and a loss tangent of 0.0025. The tracks are formed from 20μm thick copper, and there is a ground plane, which is assumed here to be ideal, on the bottom face of the substrate. Measurements were made of the attenuation of the filter with 50Ω terminations.

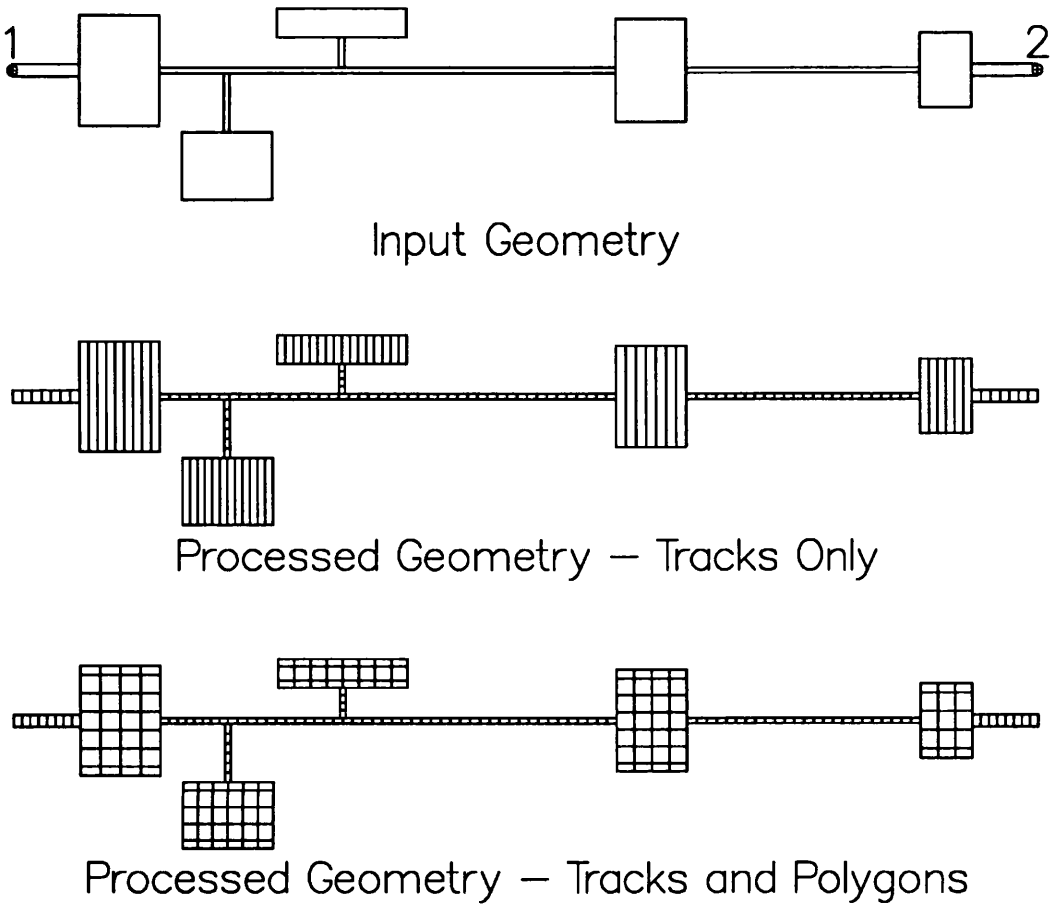

Figure 57. Layout of microstrip filter and subdivision into elements

The filter was modelled in two ways. In the first, all conductors were modelled as tracks, for which only one component of current is allowed. In this example that component is parallel to the long tracks. The subdivision of the layout for this model is shown as the second picture in Figure 57. The subdivision was such that no equivalent circuit component was more than a tenth of a wavelength long at 10 GHz, resulting in 144 elements, grouped into 81 self inductances and 71 capacitor plates.

In the second model, the five larger areas of metal were represented by polygons. This subdivision is illustrated as the third picture in Figure 57. This resulted in 497 elements, grouped into 304 self inductances and 201 capacitor plates.

Model	RADIUS	FACET time (s)	MININD	MINCAP	PHILPAC time (s)
Tracks	5mm	77	10^{-15}H	10^{-18}F	350
Tracks and Polygons	3mm	82	10^{-15}H	10^{-18}F	4830
	5mm	154	10^{-12}H	10^{-15}F	2210
	5mm	154	10^{-15}H	10^{-18}F	14100

Table 12. Simulation times for microstrip filter

The RADIUS parameter in FACET enables the interaction (ie. mutual inductance and capacitance) between elements separated by more than this distance to be ignored, and can reduce considerably the size of the equivalent circuit generated. In addition, there are two parameters, MININD and MINCAP, which are used in the translation of the FACET output of equivalent circuit components into the PHILPAC or PANACEA file. These discard any mutual inductors or capacitors with numerical values smaller than the given values, enabling the PHILPAC file to be considerably reduced in size. All of these parameters need to be used with care. If too many couplings are ignored the simulation will be inaccurate, while if too few are ignored the computation time will be excessive.

Table 12 shows the simulation times for the various cases. The PHILPAC time is for a run with 100 different frequencies. This shows the dramatic difference in times that can result from variations in these three parameters. It is now necessary to determine the relative accuracy of these simulations.

Figure 58 shows results from the tracks only simulation; the tracks and polygons simulation with a RADIUS of 3mm; and experimental measurements. The tracks and polygons simulation is much more accurate than the tracks only simulation. The agreement is almost perfect up to 6 GHz, and still quite close at higher frequencies. The discrepancy above 6 GHz is principally a frequency shift, with the model predicting features at higher frequencies than they are found in the measurements. This may be due to dispersion [Edwards, 1981]. Formulae suggest that for this situation, the effects of dispersion are to increase the effective dielectric constant, and hence the value of the equivalent circuit capacitors, by about 1.5% at 6 GHz and 3.7% at 10 GHz. This would tend to decrease the frequencies from those

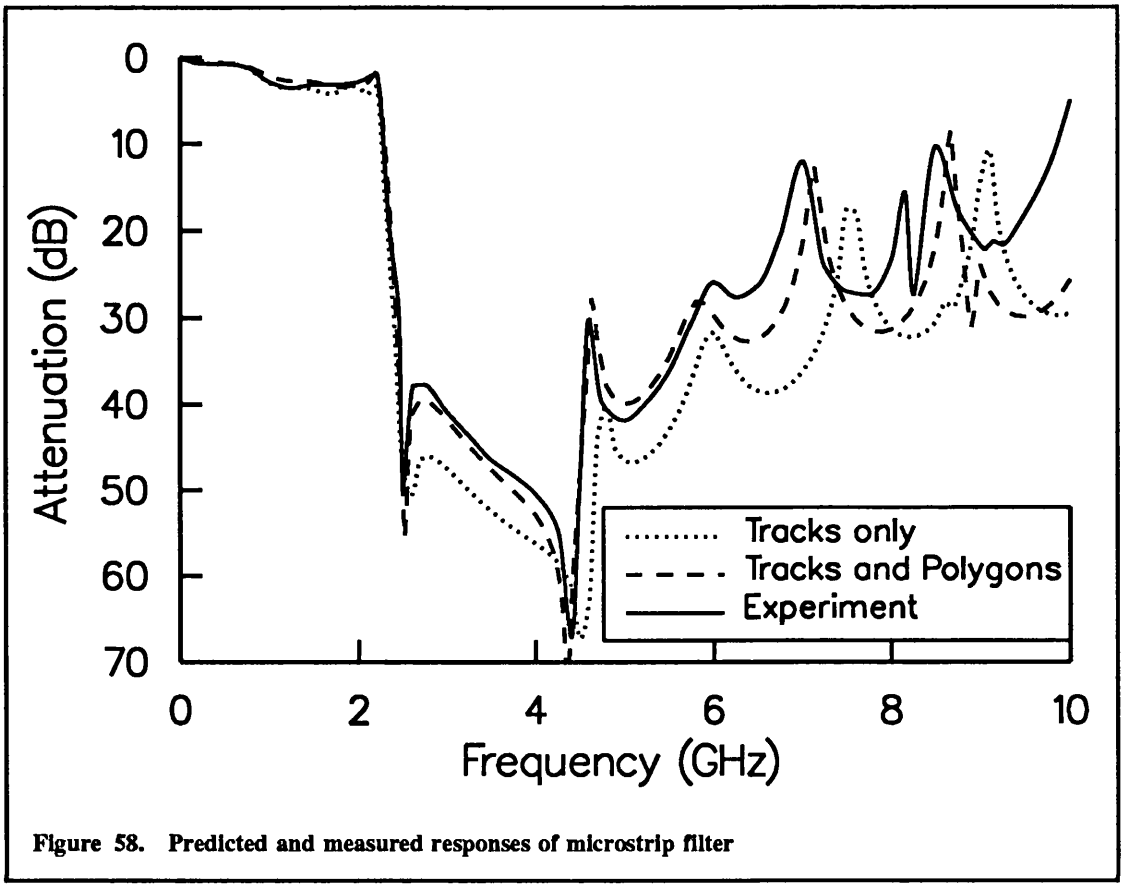

Figure 58. Predicted and measured responses of microstrip filter

predicted by about 0.75% and 1.75% respectively, and would go some way towards explaining the slight discrepancy.

Increasing RADIUS to 5mm was found to have very little effect, demonstrating that 3mm was sufficiently large for this parameter: this is about five times the substrate thickness, at which distance the presence of the ground plane has attenuated the potentials considerably. The table shows that varying the MININD and MINCAP parameters had a dramatic effect on the simulation time. Over the range of values used there was little noticeable effect on the accuracy. Hence, the largest values were used, giving the shortest simulation times.

The difference between the two simulations indicates, as might be expected, that it is not a good approximation to assume that the currents in the five larger areas of metal flow parallel to the axis of the filter. The excellent agreement when these areas are modelled by polygons indicates that the model is good, and the simulation times are not made too excessive.

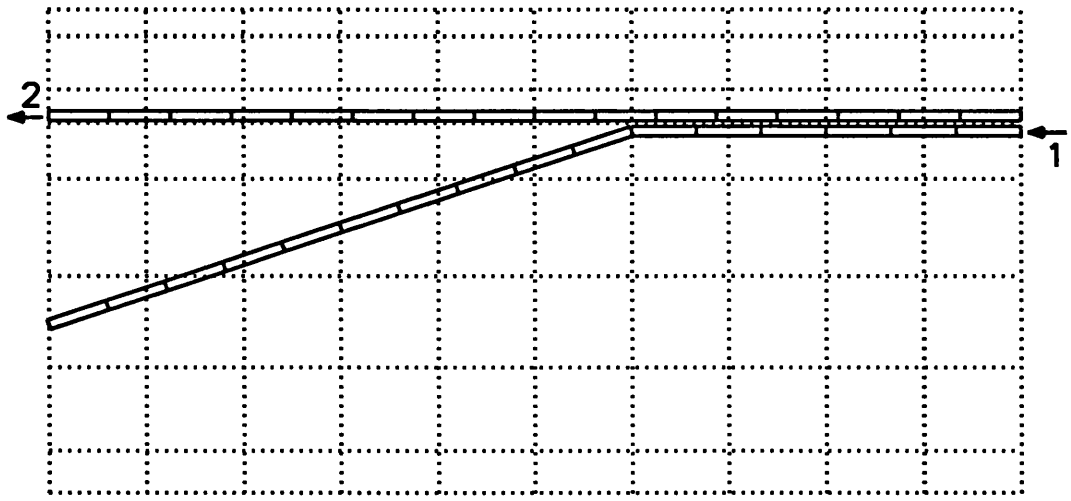

Figure 59. Subdivision of Y type layout with polygon ground plane: X inductive elements in the ground plane are shown dotted, input and output ports are arrowed.

8.3 Y Type Layout

The next example is a specially fabricated test layout. This is shown in Figure 59, and consists of two tracks, each 1mm wide, forming a "Y" shape. The substrate was 1.6mm thick MAS-FR4-74, 100mm long and 50mm wide. Measurements were made to establish its actual dielectric constant and loss tangent at frequencies up to 500 MHz by constructing a parallel plate capacitor: these were found to be 4.90 and 0.017 respectively. There is a ground plane on the bottom face of the substrate, metallised with 15μm of solder on top of 18μm of copper, the same material as the tracks.

With a port formed between each track end and the ground plane, the layout was a four port network. Twoport measurements of the attenuation of this layout were performed, using the port labelled "1" as the input port and the port labelled "2" as the output port. The other two ports had 50Ω chip resistors connected across them. These were found to have a significant inductive impedance at high frequencies, and so measured rather than ideal values for the termination impedances were used in the simulations. This improved the accuracy of the simulations considerably.

The layout was modelled in two ways. The first model treated the ground plane as ideal. The tracks were subdivided into 32 elements, grouped into 18 self inductances and 16

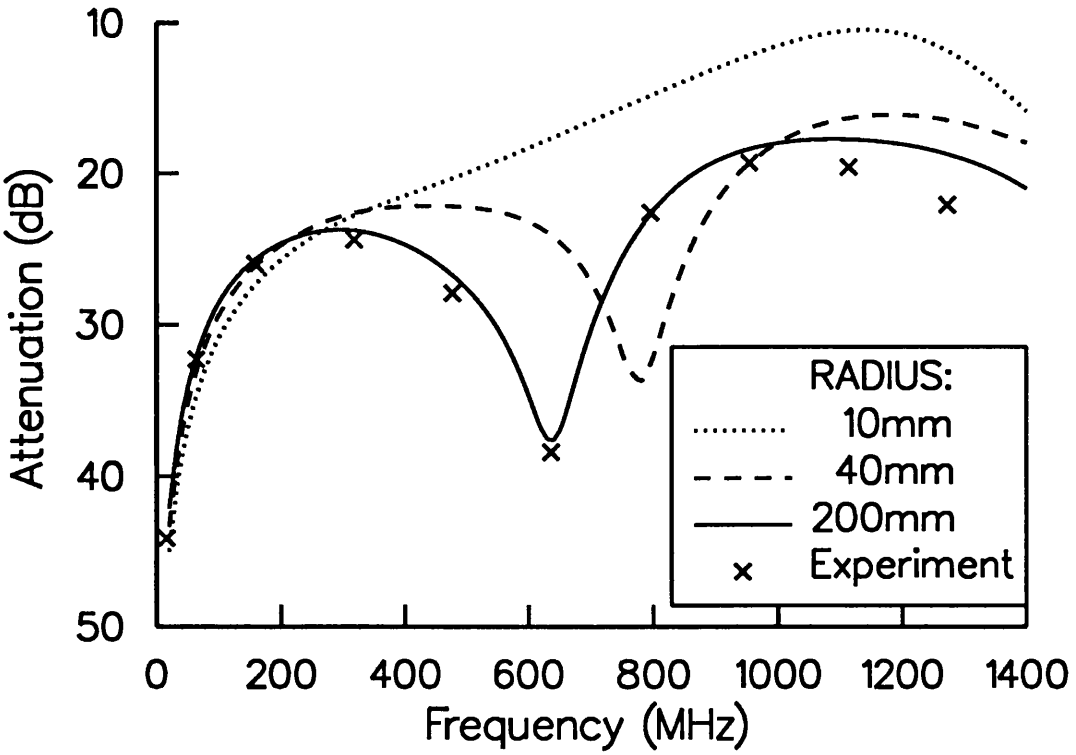

Figure 60. Predicted response of Y type layout with polygon ground plane: showing the effect of varying RADIUS.

capacitor plates. The second model represented the ground plane as a polygon. The subdivision for this model is shown in Figure 59, where the tracks and the polygon ground plane are superimposed, and the elements in the polygon are shown dotted. The subdivision was such that no equivalent circuit component was larger than a tenth of a wavelength at 1 GHz, resulting in 277 elements, grouped into 175 self inductances and 104 capacitor plates.

Model	RADIUS	FACET time (s)	PHILPAC time (s)
Ideal ground plane	10mm	6	7
Polygon ground plane	10mm	20	2100
	40mm	57	18000
	200mm	82	21000

Table 13. Simulation times for Y type layout

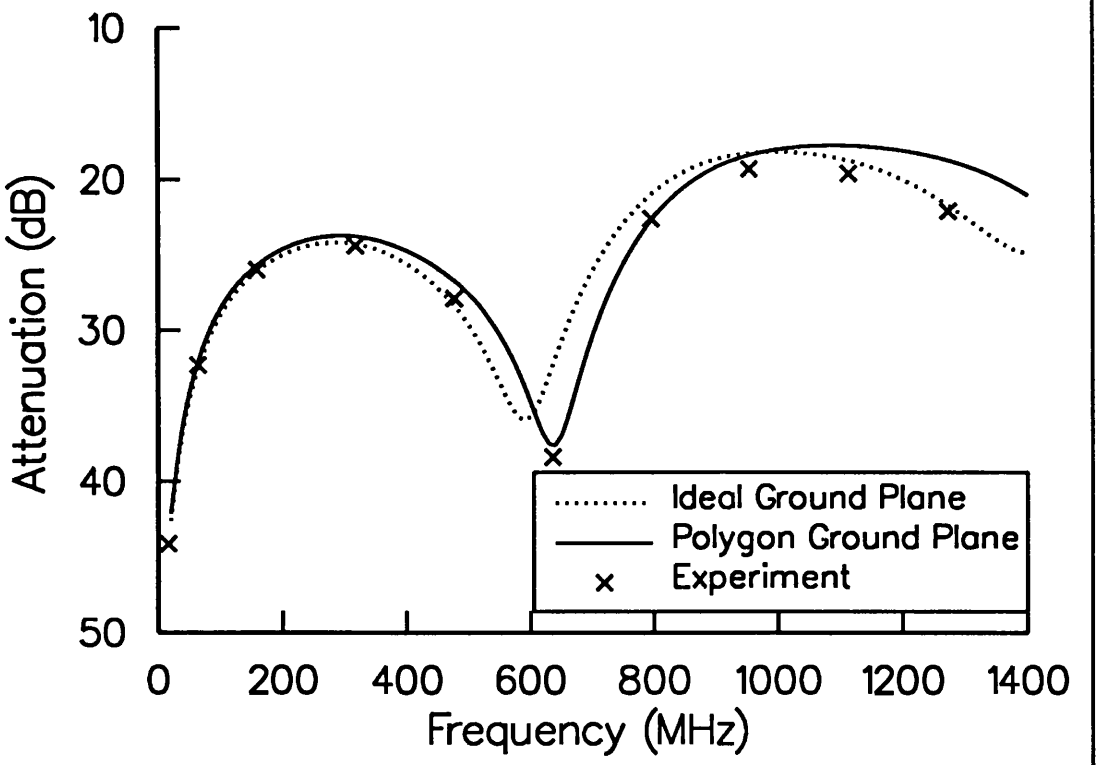

Figure 61. Predicted responses of Y type layout with polygon and ideal ground planes

Table 13 shows the simulation times for the various cases: the PHILPAC time is for a run with 100 different frequencies. For the model with the ideal ground plane, a RADIUS of 10mm was sufficient, and larger values did not alter the simulation results significantly. For this case, both the FACET and PHILPAC simulations were fast.

However, for the model with a polygon ground plane, larger values of RADIUS were necessary. Figure 60 shows the simulation results for several values of RADIUS, compared with the experimental results. This shows that a RADIUS of 200mm is necessary, ie. no couplings can be ignored, if accurate results are needed - although at the lower frequencies (below 400 MHz) the differences are small. It was also found that discarding equivalent circuit components by using MININD and MINCAP changed the results considerably. The FACET run time was still fast, but the PHILPAC run time was rather long, taking nearly six hours to produce 100 results. Ways in which this time could be improved were discussed in Chapter 7.

Figure 61 compares the results from the model with an ideal ground plane to those from the polygon ground plane model. In general, the differences are small, but the polygon ground plane gives significantly better results between 500 MHz and 1000 MHz. At higher frequencies, the ideal ground plane model gives better results. This is probably because the subdivision of the ground plane in the polygon model is not sufficient to resolve all the details of the current flow in the ground plane. However, it is not practicable to increase the subdivision until improvements to the speed of the PHILPAC solution phase of the problem have been made.

These results show that some improvement to the accuracy of a simulation can be made by modelling the ground plane with a polygon. However, the simulation times are rather long at present, so this facility should be used sparingly.

8.4 Current Flow in Ground Conductors

When a circuit board is designed using ground conductors for return current paths, it can be important to know where the current will flow in these. The intuitive answer is that it will take the shortest path possible. In fact, however, it will take the path of lowest impedance, which may or may not be the shortest path. It has been suggested [Barrow, 1989] that even at a relatively low frequency (in RF terms) of 1 MHz, the return current will tend to flow underneath the tracks providing the signal.

This has been investigated with the simple layout shown in Figure 62. This consists of a track in the shape of a "U", with each side having a length of 10mm and a width of 1mm, on the top face of a substrate 1mm thick with a dielectric constant of 5. The bottom face of the substrate has a 20mm square polygon, to represent a ground conductor. One end of the track was connected to the polygon with a via (which is modelled as a single inductor), and the simulation was performed for a voltage source connected between the other end of the track and the ground conductor. The metallisation of the track and polygon was modelled as 15μm of copper. At frequencies below 10 MHz, this has a surface resistance of about 1.15mΩ per square.

The polygon was subdivided finely enough to be able to resolve the details of the current distribution. This resulted in 807 elements, grouped into 514 self inductances and 273 capacitor plates. RADIUS was set to 5mm, since the results for the Y type layout showed

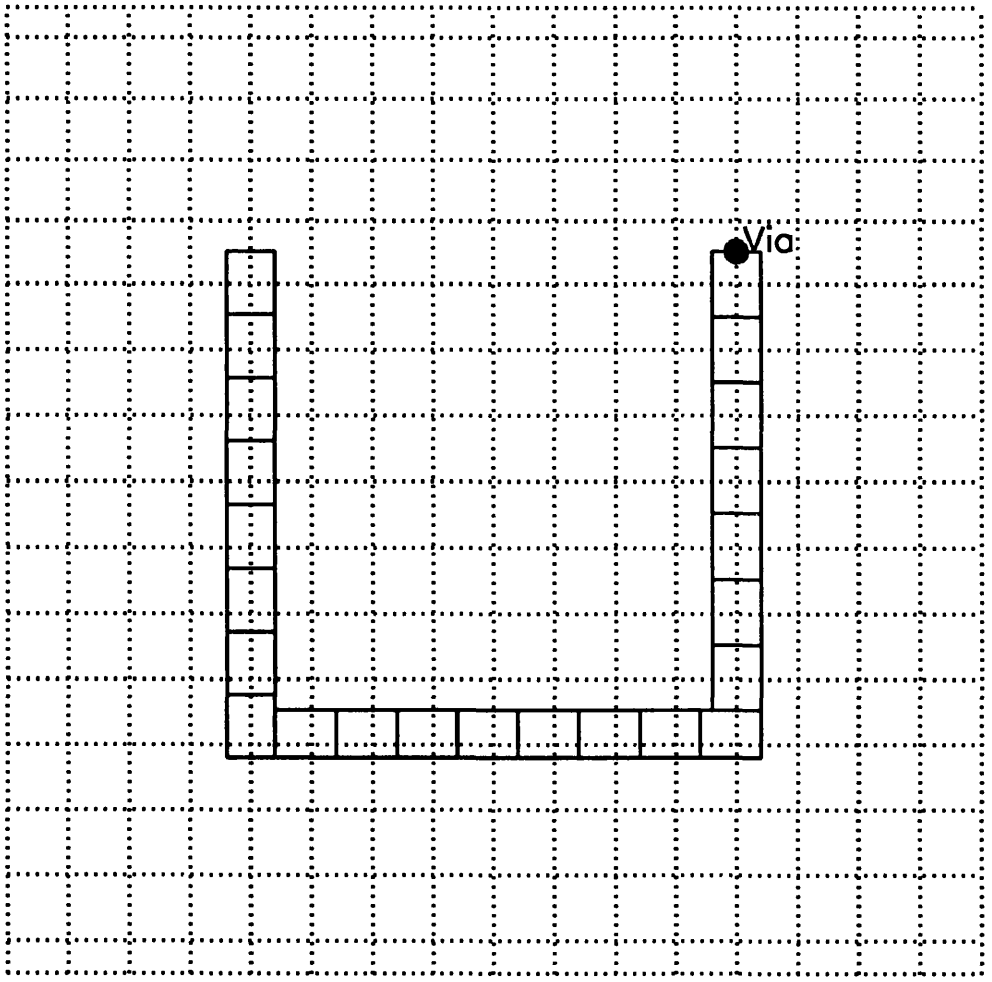

Figure 62. Layout for demonstrating current flow in a ground conductor: X inductive elements in the polygon ground conductor are shown dotted

that at low frequencies a small value for RADIUS is adequate, and this value allows sufficient couplings to be included. As was the case for the Y type layout, discarding equivalent circuit components by using MININD and MINCAP changed the results considerably. The FACET run took 322s, or just over 5 minutes. The PHILPAC run took 15400s, or nearly 260 minutes for just one frequency point.

A modified form of the power flow plot facility in FACET was used to plot the magnitude and direction of the current flowing in the polygon at two different frequencies. Figure 63 shows the current flow at 1 kHz, and Figure 64 shows the current flow at 1 MHz. In both

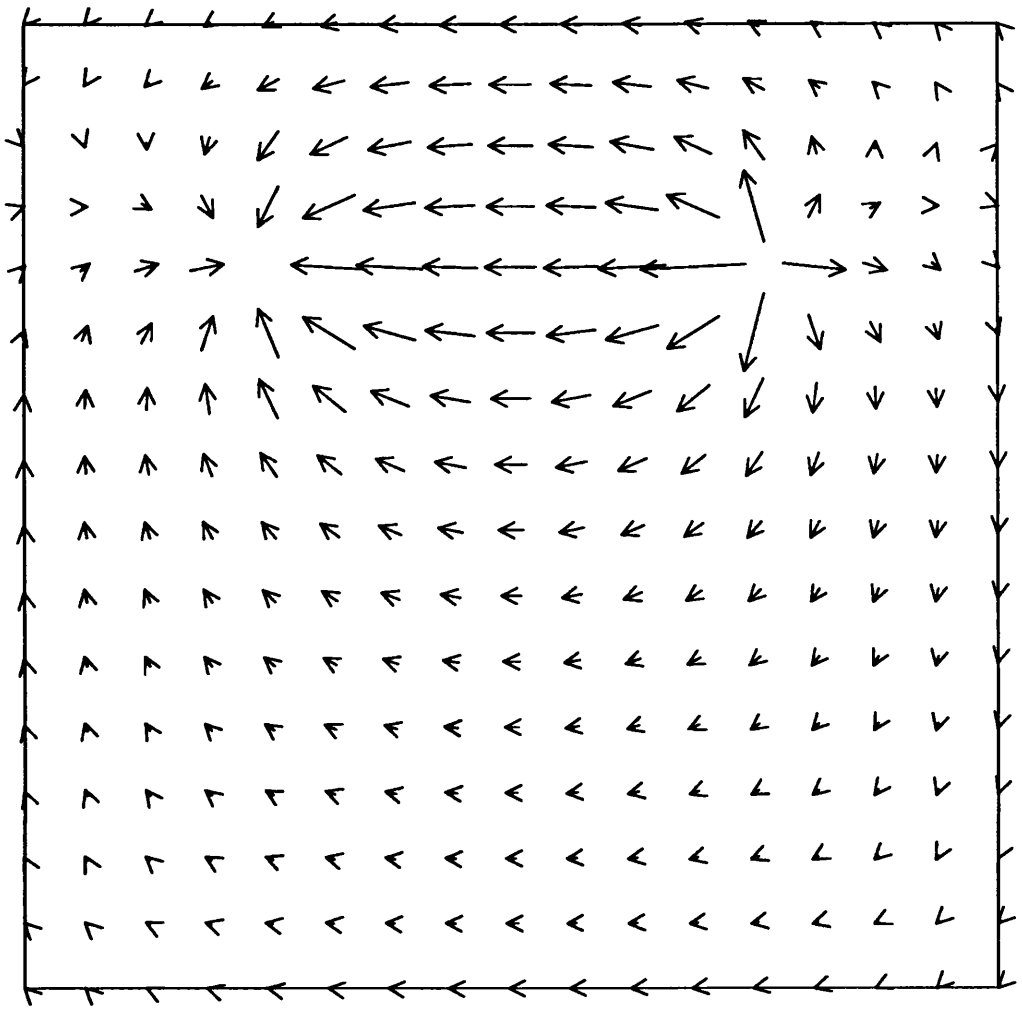

Figure 63. Direction and magnitude of current flow at 1 kHz

figures, the arrows indicate the direction of the current flow by their orientation, and the magnitude of the current (on a linear scale) by their length. At 1 kHz, the current takes the shortest path, while at 1 MHz it principally flows underneath the tracks, as predicted.

The free space wavelength of a 1 MHz radio wave is 300m, so this change has nothing to do with propagation effects. The explanation is in terms of inductance. The area of the loop defined by the route taken by the current at 1 kHz is approximately 100mm^2, while that of the loop defined by the route taken by the current at 1 MHz is approximately 30mm^2. Hence the self inductance of the 1 kHz route would be expected to be rather more than that of the 1 MHz route.

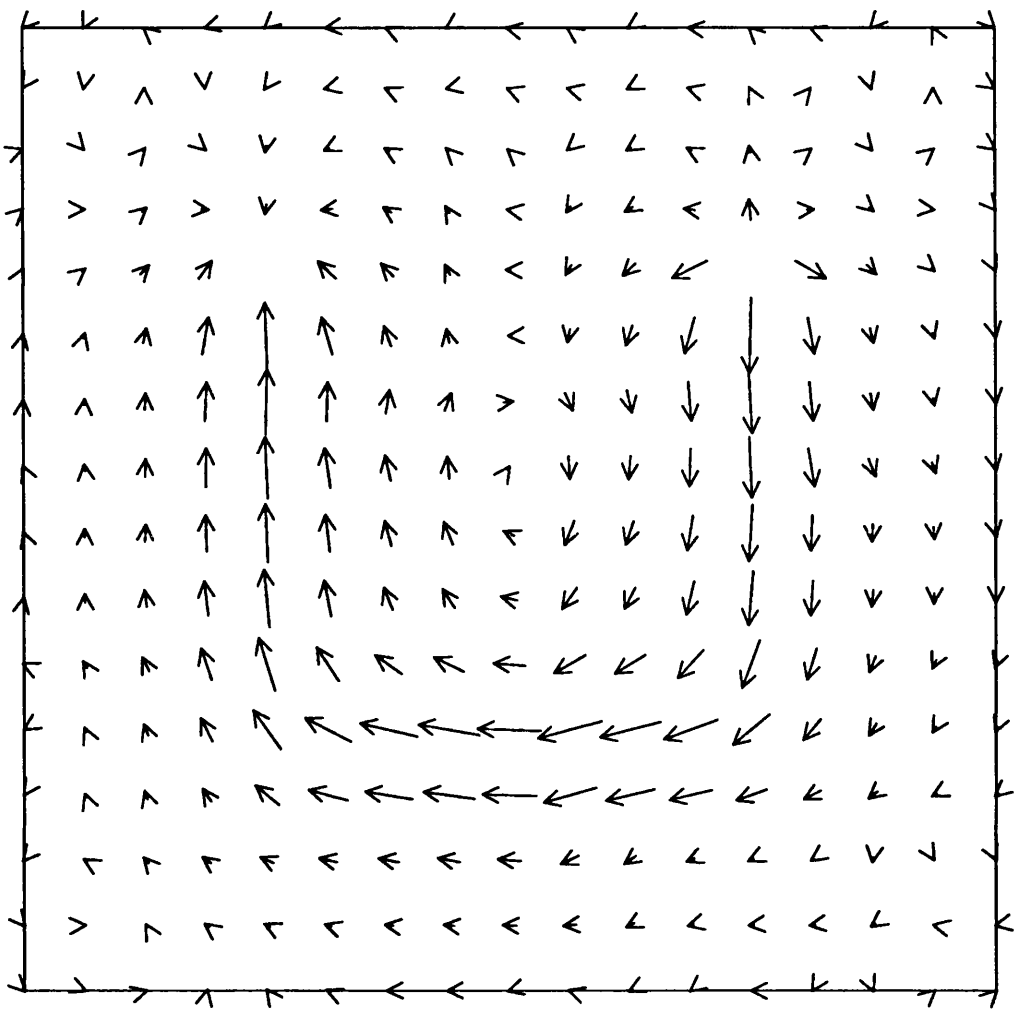

Figure 64. Direction and magnitude of current flow at 1 MHz

Figure 65 shows this effect more clearly. At low frequencies, the inductive component of impedance is negligible, and the current follows the path of least resistance. At 1 kHz this path has a resistance of 36.8mΩ and an inductance of 17.5nH (which represents an impedance of 0.110mΩ). At high frequencies, the inductive component of impedance dominates, and the current follows the path of least inductance. At 1 MHz this path has a resistance of 42.5mΩ and an inductance of 12.1nH (which represents an impedance of 76.0mΩ). Hence, between 1 kHz and 1 MHz, the route taken by the current changes in order to use the path of lowest impedance.

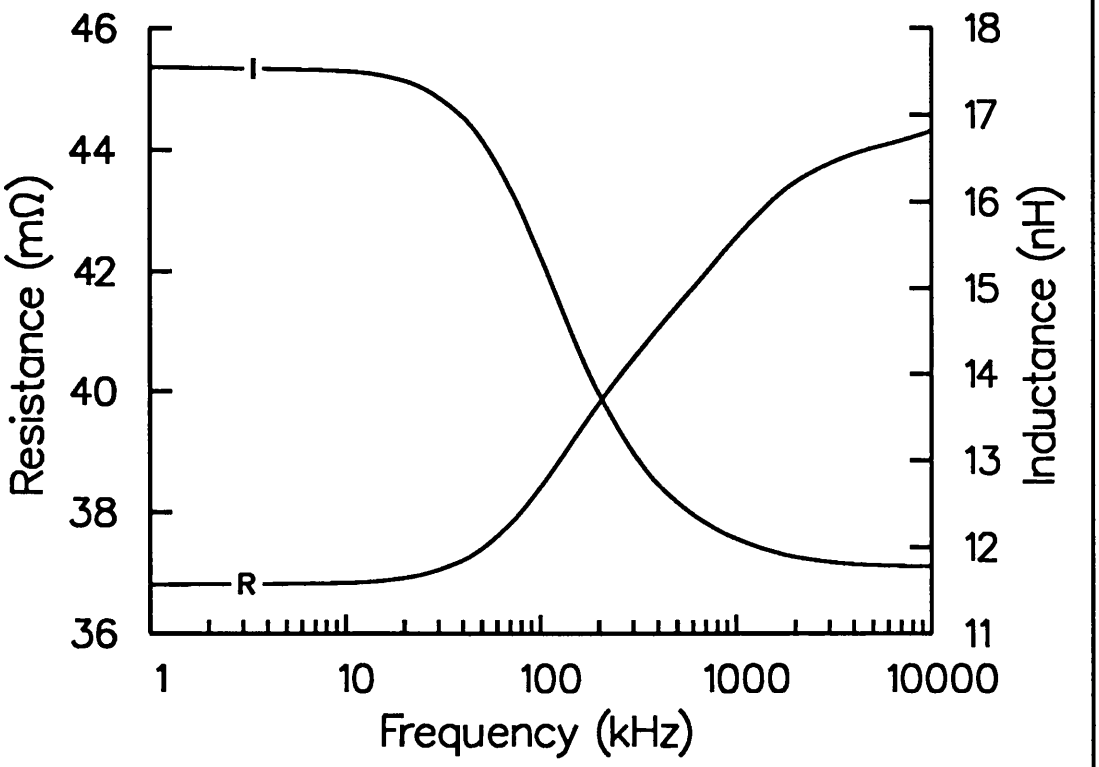

Figure 65. Resistance and inductance of the demonstration layout

8.5 Capacitance of Square Plates

This section examines the capacitance of a square conducting plate in free space, and the capacitance of a similar plate to ground when the ground plane is close. Similar examples are commonly found in the literature, so this provides a check on the accuracy of the capacitance solution developed in this report. The subdivision of the square into capacitive elements is shown in Figure 66. The geometry processing method adopted results in the edge elements being half the width of the other elements, which improves the accuracy of the solution [Ruehli and Brennan, 1973]. This is principally because it enables better modelling of the rapid charge density variations near to the edge of the square.

The first example is the capacitance of a 1m square plate in free space. This was simulated with an ideal ground plane a long distance (1000km) away and adding together all the capacitances to ground of the capacitive elements. The results are shown in Figure 67 for various subdivisions of the square. In all cases RADIUS was set large enough for all couplings to be considered, as otherwise the values calculated were in error. The greatest

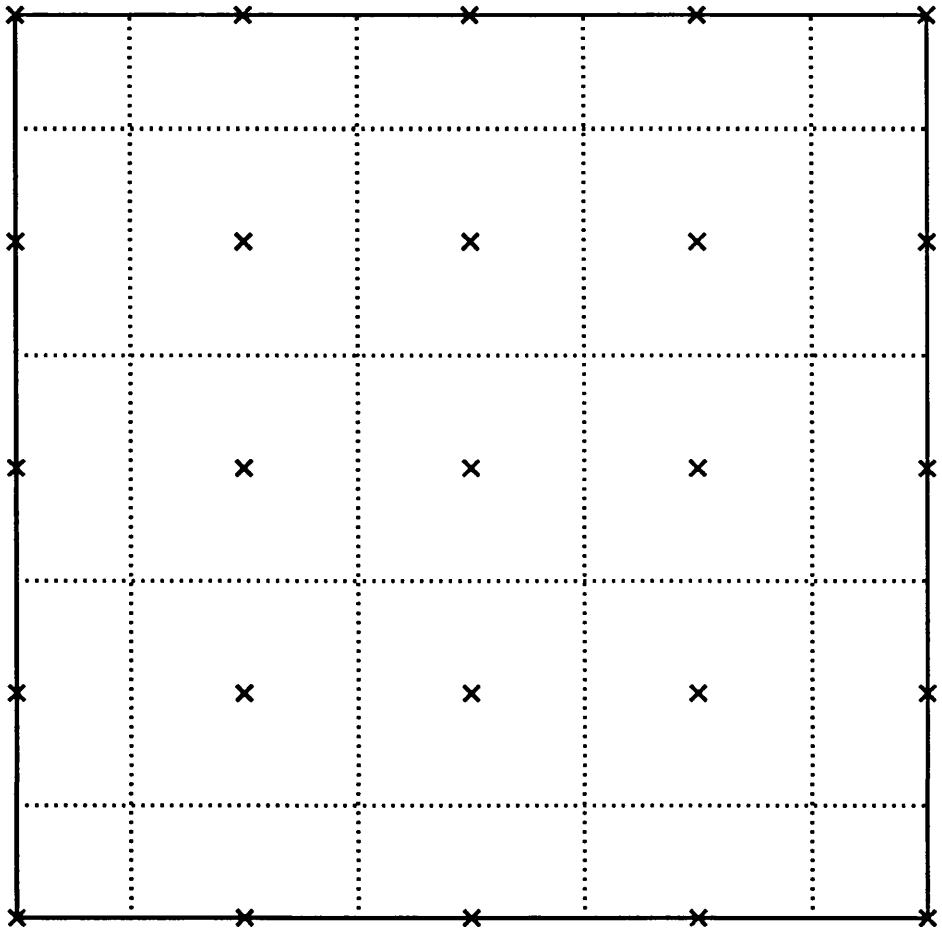

Figure 66. Square plate subdivided into 25 capacitive elements: equivalent circuit nodes shown by crosses

subdivision examined was 31 capacitive elements per side, a total of 961 elements, taking about 1 hour to simulate. Coarser subdivisions took much less time (eg. 1 minute for 13 elements per side). The convergence of the results is quite fast, with a capacitance of 40.58 pF for 31 elements per side. This is close to the result obtained by Ruehli and Brennan [1973] of 40.54 pF. They achieved faster convergence by the use of the Galerkin method rather than the point collocation used here and by the use of narrower edge elements. However, these would increase the computation time considerably, and have little effect on the accuracy of the solution for the intended problems.

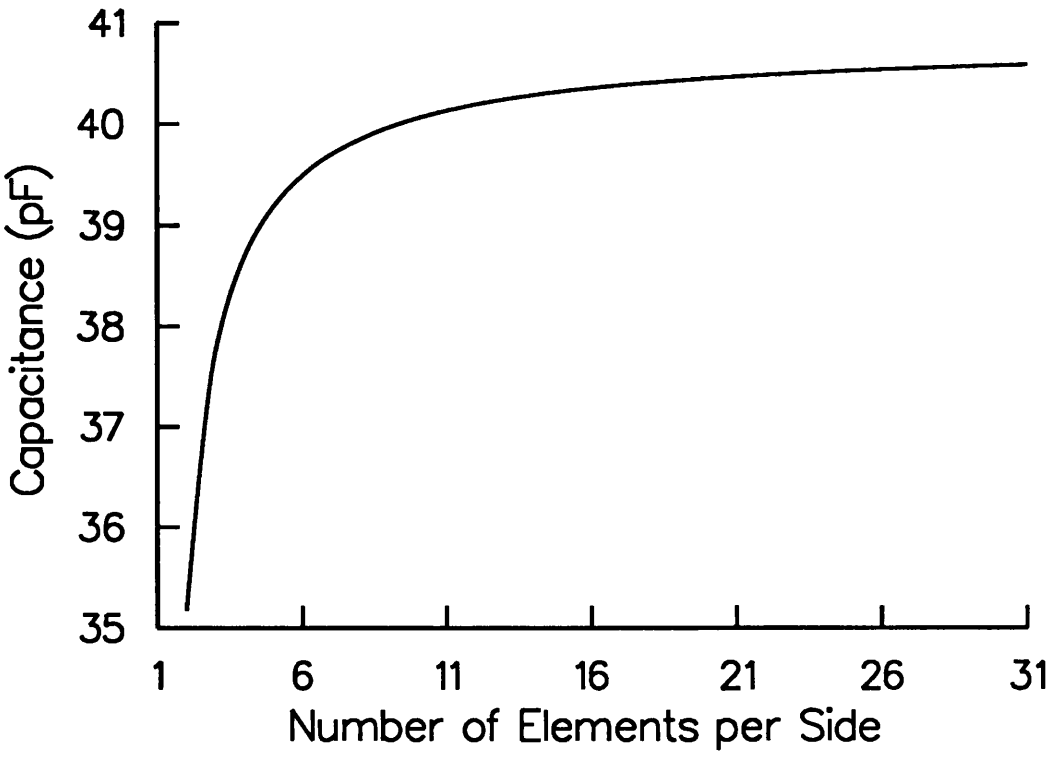

Figure 67. Capacitance of a 1m square plate in free space

The second example is a square with sides of 20mm placed 2mm above an infinite ground plane. The results are shown in Figure 68 for various subdivisions of the square. For a parallel plate capacitor of these dimensions, the expected capacitance would be 1.771 pF. That predicted is 2.725 pF with 31 elements per side, or roughly 50% more, so the effects of fringing capacitance are still considerable. Reitan [1959] modelled parallel plate capacitors by subdividing each plate into 36 equally sized elements with constant charge in each, using approximate relations for the potential.

By the method of images [Bleaney and Bleaney, 1976, pp.48-56], it can be seen that the capacitance to ground of a capacitor plate above an ideal ground plane is double the capacitance of a parallel plate capacitor with two plates of the same size as the original plate, separated by twice the distance between the original plate and the ground plane. Reitan predicts a capacitance of 0.6629 pF for plates 10mm square spaced by 2mm, which scales to 1.3258 pF for plates 20mm square. Hence, the value predicted by Reitan for the configuration examined here is 2.652 pF, in good agreement with the value obtained from FACET.

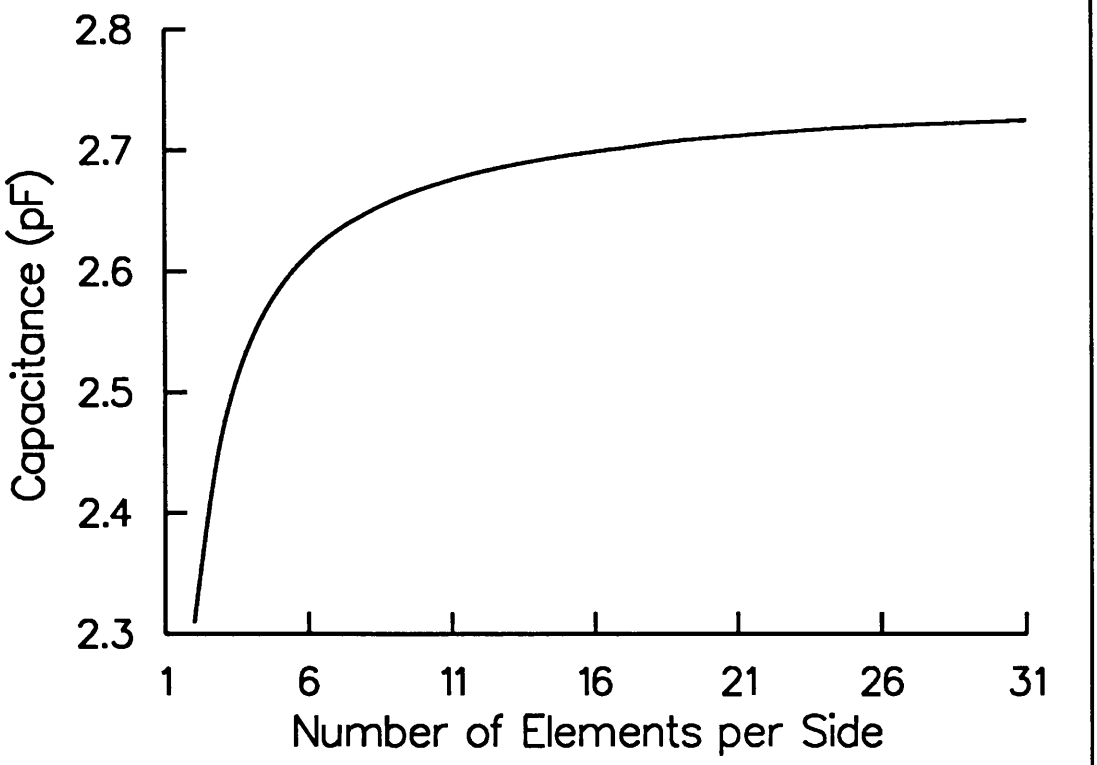

Figure 68. Capacitance to ground of a 20mm square plate: 2mm thick substrate with dielectric constant $\varepsilon_r = 5$

The second example converges less rapidly than the first. This is because the of the presence of the ground plane, which makes the charge density more constant over the majority of the square, with a sharper variation at the edges, and hence a greater subdivision is necessary for the same accuracy. This specific problem could be tackled more efficiently by having more small elements near to the edges, and fewer large elements in the interior. However this would then be less applicable to the more general problems for which FACET is required.

8.6 Conclusions

The four different examples examined in this chapter have demonstrated that the accuracy achievable using polygons in FACET is very good, enabling accurate modelling of layouts that could not be modelled before. The simulation run times are reasonable, except when modelling complex polygon shapes which require extensive subdivision on purely

geometrical grounds, or for simulations with no ideal ground plane, when all couplings must be included at high frequencies. For these cases, improvements to the efficiency would be most worthwhile. Possible methods for achieving this were discussed briefly in Chapter 7.

The combination of the high accuracy achieved and the reasonable simulation times provides the main justification for the approximations introduced into the theory of Chapter 2. The equivalent circuit model is therefore a useful and efficient way of representing the electrical behaviour of circuit boards.

Chapter 9

Conclusions and Future Work

9.1 Conclusions

The work described in this thesis is concerned with modelling the electromagnetic behaviour of metallisation patterns on PCBs. The model selected was an equivalent circuit model, and the derivation of this from Maxwell's equations was described. This derivation involved two main assumptions.

The first assumption is that the effects of retarded potentials can be ignored. This is effectively a quasi-static assumption. Although the vector and scalar potentials used to compute the values of the equivalent circuit components are calculated at zero frequency, they are then linked through the current continuity equation and the equation for the electric field, which do include time variations. This assumption implies that, for accurate results, the dominant coupling effects should take place over relatively small separations, where the retarded potentials are very similar to the static potentials.

The "rule of thumb" which has been used here is that separations of less than five times the distance from the top of the substrate to the ground plane can be considered as small. It was shown in Chapter 3 that the potential falls off rapidly with distance from a source when a ground plane is present, as is usually the case, suggesting that this assumption is likely to be valid for most layouts. As an example, the results for the microstrip filter examined in Chapter 8 were extremely accurate when all couplings over a distance of 3mm or more were ignored. This distance corresponds to about five times the substrate thickness. The results were accurate up to the maximum measured frequency of 10 GHz, with some slight frequency shifts becoming apparent above 6 GHz. These shifts were believed to be caused by dispersion, and are therefore an indication that the retarded potentials are beginning to differ from the static ones over such distances, which might be expected since 3mm corresponds to about a quarter of a wavelength at 10 GHz

The only case for which this approximation seems more questionable is when there is no ground plane present. The Y type layout described in Chapter 8 was modelled both with an ideal ground plane, and with this ground plane represented by a polygon. When modelled with an ideal ground plane, couplings over distances of more than 10mm had virtually no effect, which is less than a tenth of a wavelength at the highest measured frequency of 1.4 GHz. When modelled with a polygon representing the ground plane, however, all couplings had to be included for accurate results to be produced. The largest separation was about 110mm, corresponding to about a wavelength at the maximum frequency. The results produced were slightly more accurate than those with the ideal ground plane model, even at the higher frequencies. This suggests that the errors introduced by the absence of retarded potentials must cancel out to a large extent, so the model is valid at rather higher frequencies than would be expected.

In summary, the quasi-static approximation seems to hold rather well for typical PCB geometries, even into regimes where it might be expected to fail.

The second main approximation is that the actual charge and current distributions are approximated by finite sets of basis functions. The effects of this are reduced considerably by the choice of physically realistic basis functions. For tracks (not the main subject of this thesis) this is done by having singular basis functions in the width to model the effects of the track edges, and polynomial distributions in the length to model other variations.

The model for polygons developed in this thesis used constant basis functions, as the charge and current distributions are only slowly varying in the interior of a typical polygon. These basis functions are likely to be rather less accurate near the edges of the polygon, although helped somewhat by having narrower elements adjacent to edges. The intention was to see how accurate the results produced by this model were before deciding whether it was worth adding in basis functions with the flexibility to model the distributions more accurately. The accuracy of the results presented in Chapter 8 suggests that such refinements are unlikely to yield dramatic improvements in accuracy in most circumstances. It may be worthwhile investigating whether better modelling of the edge behaviour is necessary for particular geometries, and this forms part of the suggested future work.

With the theoretical basis for the model established, the next task was the evaluation of the scalar and vector potentials due to the various charge and current distributions. Chapter 3 detailed the solution to the first part of this problem, calculating the scalar and vector

potential Green's functions, effectively the potential due to point charge and current sources respectively. The method adopted was to take a general class of structures, consisting of three infinite dielectric layers and two infinite, ideal ground planes, and obtain expressions for the potential at any position due to a point source at any position. The solution was obtained in the spectral domain, a fairly standard approach. By manipulating this solution, it was expressed in a form amenable to an inverse Fourier transform, so that the results could be expressed in the spatial domain. These results were obtained in the form of infinite series of point source potentials. For most cases of interest, the series were shown to converge rapidly, so that typically only ten or twenty terms were needed to obtain a solution of good accuracy. As well as being an efficient solution in its own right, this form could be convolved efficiently with the basis functions for charge and current distributions, and in the same way for different PCB structures. This simplified the software creation task considerably.

Chapter 4 showed how the simplest of these solutions, that for the vector potential in free space, could be used to compute the self inductance of a via and the mutual inductance between two vias. Some attention was paid to obtaining an approximate form of the expression for the mutual inductance, the result being an expression which could be evaluated over a hundred times faster than the full expression, but was almost as accurate.

Chapter 5 then tackled the more general task of convolving the Green's functions derived in Chapter 3 with the basis functions for track and polygon elements. For the polygon elements, the basis functions are constant charge and current density, and the convolution integrals were performed analytically. The expressions derived enabled the potentials to be computed very efficiently, many times faster than would be the possible using numerical integration. Analytic expressions were also derived for the self inductance of a rectangular polygon element and the mutual inductance between two parallel rectangular polygon elements. The self inductance could be evaluated very much more rapidly than using a numerical approach. For the mutual inductance the difference was rather less marked, but the analytic expressions still have the advantage of guaranteed accuracy.

For the track elements, the presence of the edge singularities in the basis functions meant that the convolution integrals could not be performed completely analytically. However, much of the integration could be performed analytically, leaving only a single numerical integration to perform. Careful attention to this enabled the potentials for up to six basis functions to be evaluated in little more time than that for one, and the resulting subroutines

were shown to have their speed limited mainly by the time taken to calculate mathematical functions (principally square roots, logarithms and sines) on the computer. Some attention was also paid to the method of numerical integration, the selected method being shown to have good efficiency. The software was written so that other integration methods could easily be slotted into place should ones with better performance be found.

Chapter 6 detailed a series of tests that were performed on the subroutines described in Chapter 5. These checked the internal consistency of routines and showed that the results from different routines joined together properly at the boundaries of their regions. They also checked the results against known solutions, such as the potential due to a point charge. The purpose of these tests was to demonstrate that the routines behaved in the expected manner, so that they could be used with confidence in the rest of the work.

The only remaining task before results could be obtained was the creation of an appropriate set of elements from the geometry of the metallisation pattern on the PCB. Chapter 7 described how the subdivision into elements was performed for areas modelled as polygons. The methods used for other metallisation shapes, and the details of how all the different elements are formed into sets for the overall solution to occur, were not part of this work, and are not described here.

The method developed took advantage of the fact that most polygonal areas on a PCB are found to have straight edges, predominantly parallel to the PCB edges. A grid was formed from the geometry, and around this sets of rectangular and triangular elements were formed. These in turn could be associated with self inductances and capacitor plates in the equivalent circuit model. The method had to deal with rather irregular shapes, and so the grid could not be a simple regular one, as often seems to be used. A comprehensive classification scheme for labelling the different geometrical features was developed, and the method can handle complex shapes, with concave and convex areas and cut-outs.

It was recognised that some geometries caused excessive subdivision, and therefore unacceptably long simulation times. Modifications to the geometry processing were proposed which would solve several of these problems. To address the more general problem of excessively large equivalent circuits being produced, a method for transforming these into a much smaller admittance matrix was proposed, and demonstrated for a simple example. This has the potential for a very large improvement in efficiency, and its full development should have a high priority, since at present the time taken for a circuit analysis

can often be much larger than that taken for the full 3D field analysis performed within FACET.

With the various pieces of the work described, the final (and most important) question was, how well did the simulation results compare with experiment? Chapter 8 addressed this issue for four different examples. Two could be compared directly with experiment, and excellent accuracy was demonstrated. The other two examples were to compare against literature results, again giving results of very high quality.

In conclusion, the results of this work must stand by their accuracy and efficiency. It is hoped that both have been amply demonstrated in this thesis.

9.2 Summary of Achievements

The achievements made during the research were outlined in the main part of this thesis. They are summarised below:

1. The equivalent circuit model developed for the Philips PCB simulator FACET has been extended to model polygonal areas of metal, with arbitrary directions of current flow. It has been shown that this model provides an approximate solution to Maxwell's equations. The approximations are that the treatment is quasi-static, ie. radiation effects are ignored, and that the charge and current distributions can only assume certain forms. Both approximations are well founded, and it was shown that this approximate solution satisfied Kirchhoff's first and second laws exactly.

2. Green's functions have been derived for the electric scalar and magnetic vector potential for a configuration with three layers of dielectric material and two perfectly conducting ground planes. This configuration is able to model the majority of PCB structures. The Green's functions were obtained as infinite series of point sources in the spatial domain, which is a very convenient form for computational purposes.

3. A large set of Green's functions has been derived for simplified structures with fewer ground planes, fewer dielectric layers or a combination of the two. Other simplified Green's functions have also been derived for particular combinations of source and object point locations. All of these have the major advantage of a reduced computational complexity, and are applicable to many cases of interest to PCB

modelling. The convergence of the series derived was examined for several of these cases and shown to be good, often only requiring ten or twenty terms to be computed for results of good accuracy.

4. The Green's functions derived for some of the simpler configurations have been shown to correspond to those derived by other authors using the method of images. The method detailed here has the advantage of being able to derive Green's functions in situations where they would be much too complex to derive readily using the method of images.

5. A model for the self inductance of a via and the mutual inductance between parallel vias has been developed. The expression derived for the self inductance of a via is very fast to compute. An approximate expression has been developed for the mutual inductance that is over a hundred times faster to compute than the exact expression, but is only marginally less accurate.

6. Analytic expressions have been derived for the scalar and vector potentials due to constant charge and current densities defined on rectangular and triangular elements, used within polygon areas. In addition, analytic expressions for the self inductance of a rectangular element and the mutual inductance between two parallel rectangular elements have been derived. These have been presented in a compact form, and a set of subroutines has been developed to incorporate these results. The subroutines were shown to be extremely efficient.

7. Expressions have been derived for the scalar and vector potentials due to the singular charge and current density distributions used within track elements. These have as much as possible of their form derived analytically. Numerical integration techniques have been investigated to make the numerical part of the evaluation as efficient as possible. A set of subroutines has been developed to implement these results. These subroutines have been shown to be efficient, taking only three or four times longer to run than the subroutines implementing the analytic results.

8. A wide range of tests has been performed on the subroutines developed, both on their own and as part of the FACET system. These tests demonstrated that the subroutines gave the answers that would be expected in a variety of special situations, and so giving good confidence that their implementation has been performed correctly.

9. An algorithm for subdividing a polygonal area into the sets of elements required to produce the equivalent circuit model has been developed. This required the development of a detailed classification scheme for the types of corners and sides present in various polygon geometries and the development of algorithms to generate the correct size and shape of elements to model the polygon geometry exactly.

10. Problems which may occur with particular polygon geometries have been identified, and solutions proposed. One partial solution is the creation of an admittance matrix to represent the equivalent circuit produced. This admittance matrix can then have the rows and columns corresponding to the internal nodes (those with no connection to external circuit components) compressed out. This method has been demonstrated to have the potential to improve simulation times dramatically, and to be applicable to all FACET equivalent circuits, not just those containing polygons.

11. Results of FACET simulations on four different designs have been presented, all the designs incorporating areas modelled as polygons. Two of these were compared with experimental results, and two with literature results. The accuracy of the simulations was shown to be very good, thus demonstrating the validity of the models developed in the remainder of the thesis.

9.3 Areas for Further Work

During this research, a preliminary investigation of methods for improving the efficiency of FACET simulations was undertaken. This is worthy of follow-up studies, which are outlined below together with other potential areas for future work.

1. The first problem identified with the use of FACET is that of an excessive number of elements being generated. This is a particular problem for certain polygon geometries, and could be improved somewhat by the development of a pre-processor which detected such types of geometries, principally features which are not quite aligned, and took appropriate action, namely aligning the features if the movement required was not too excessive. Such a pre-processor should be relatively simple to implement, and of considerable usefulness.

2. The second, and more major, problem identified is the production of extremely large equivalent circuits, which are very slow to analyse using circuit simulators. These are

a particular problem when simulating non-ideal ground conductors, when all coupling terms need to be included, but has been found to be a problem in other cases too. The method identified to solve this problem was to convert the equivalent circuit to an admittance matrix and then compress out nodes with no external connections. This method was shown to have the potential for very large gains in speed, and should form a very useful piece of further work.

3. The model developed for polygons assumes constant charge and current density distributions within each element. While this is a good approximation for the majority of elements in a polygon, the distributions are known to approach infinity near the polygon edges. A brief investigation to determine whether there would be useful gains in accuracy by using singular basis functions for elements on the edge of a polygon could be undertaken. If worthwhile improvements were found, such a scheme should then be implemented.

4. A concern which will become increasingly important to PCB designers is the electromagnetic compatibility (EMC) of equipment, which is concerned with the effect that pieces of equipment have on one another. A particular manifestation of this is radiation from PCBs, which is at present excluded from the FACET models. However, most PCBs are not designed as antennas, so radiation should be of secondary importance. It could therefore be predicted by performing a FACET simulation to determine the currents flowing around the PCB metallisation pattern, assuming that radiation does not modify this. The radiation from the current and charge distributions could then be determined by including retarded potentials in the Green's functions. A further refinement would be to determine the small error potentials and then correct the currents and charges accordingly, to enable a more accurate simulation of the circuit performance. In most cases this correction would probably be of secondary importance, but there may be situations where its inclusion is vital.

The above list is by no means exhaustive, but serves to illustrate that there is still much useful work to be done, both to enhance the capabilities of the work performed to date, and to extend the concepts developed into new areas.

Appendix A
Skin Effect

This appendix shows how the finite thickness and conductivity of the metals used as conductors on PCBs give rise to the surface impedance term that is used in Chapter 2. This relates the total current flowing through a given section of metal to the electric field at the surface of the metal.

Consider a sheet of metal of thickness h and conductivity σ. The current density $\mathbf{J}$ at any point in the metal is related to the electric field $\mathbf{E}$ at that point by Ohm's law,

$$\mathbf{J} = \sigma \mathbf{E} \tag{A.1}$$

Using Ohm's law, and assuming harmonic time variation of angular frequency ω, the first two of Maxwell's equations (given in Chapter 2 as equations 2.1 (a) and (b)) become

$$\begin{aligned} \nabla \times \mathbf{E} &= -j\omega \mathbf{B} && (a) \\ \nabla \times \mathbf{H} &= (\sigma + j\omega \varepsilon_0 \varepsilon_r)\mathbf{E} && (b) \end{aligned} \tag{A.2}$$

The dielectric constants of metals are similar to those of dielectrics [Ramo et al, 1965, p.250]. Hence, the $j\omega \varepsilon_0 \varepsilon_r$ term only becomes significant for frequencies approaching the optical, far above those of interest in this work, and can be neglected in this analysis.

Consider now a current propagating along the metal sheet, and assume that the current density is uniform in the plane of the sheet. Take the x and y axes to be in this plane and the z axis in the thickness direction, and assume the current is propagating parallel to the x axis. The current density and electric field therefore only have x-directed components, and these only vary in the z direction (ie. $\mathbf{E} \equiv E_x(z)$). Similarly, the magnetic field only has a y-directed component, $\mathbf{H} \equiv H_y(z)$. Equation A.2 can therefore be rewritten as

$$\begin{aligned} \frac{\partial E_x}{\partial z} &= -j\omega\mu_0 H_y && (a) \\ -\frac{\partial H_y}{\partial z} &= J_x + j\omega D_x && (b) \end{aligned} \tag{A.3}$$

Eliminating H_y from equations A.3 gives an equation for E_x,

$$\frac{\partial^2 E_x}{\partial z^2} - j\omega\mu_0\sigma E_x = 0 \qquad \text{(A.4)}$$

Noting that frequency f and angular frequency ω are related by $\omega = 2\pi f$, set

$$\begin{aligned} \delta &= \frac{1}{\sqrt{\pi f \mu_0 \sigma}} \\ \tau &= (1+j)\sqrt{\pi f \mu_0 \sigma} = \frac{1+j}{\delta} \end{aligned} \qquad \text{(A.5)}$$

so that $\tau^2 = j\omega\mu_0\sigma$. δ is known as the skin depth, as discussed below. Equation A.4 can then be written as

$$\frac{\partial^2 E_x}{\partial z^2} - \tau^2 E_x = 0 \qquad \text{(A.6)}$$

which has the general solution

$$E_x = c_1 e^{\tau z} + c_2 e^{-\tau z} \qquad \text{(A.7)}$$

To proceed further, boundary conditions need to be applied. Those used in FACET are that the electric fields on the top and bottom surfaces of the metal sheet are both equal, ie. $E_x(0) = E_x(h) = E_0$. This assumes that the width of the conductor is small enough for there to be negligible variation in the electric field E_x around its perimeter. The assumption is certainly valid at low frequencies. There is, however, evidence that at microwave frequencies the current in a microstrip line (a track on the top surface of a substrate with a ground plane on the bottom surface) flows principally on its bottom surface (ie. that nearest the ground plane) [Horton et al, 1971; Pucel et al, 1968]. The assumption will also be less valid for polygons than for tracks, as they usually have rather larger widths.

These effects could be allowed for by changing the boundary conditions to more appropriate ones. However, this has little effect on accuracy at the frequencies of interest for the work reported here, and complicates the formulae considerably. Hence, the boundary conditions referred to above will be used, enabling c_1 and c_2 to be found as,

$$c_1 = \frac{E_0(1 - e^{-\tau h})}{e^{\tau h} - e^{-\tau h}}$$
$$c_2 = \frac{E_0(e^{\tau h} - 1)}{e^{\tau h} - e^{-\tau h}} \qquad \text{(A.8)}$$

It can be seen that when the thickness of the metal, h, is rather greater than the skin depth, δ, this parameter is the distance into the metal at which point the fields are reduced to $1/e$ of their value at the surface of the metal. As the frequency is increased, δ decreases, and the fields are confined more and more strongly to a thin surface layer on each side of the metal sheet. As an example, a 15μm thick sheet of copper has a conductivity of $\sigma = 5.8 \times 10^7 \mathrm{Sm}^{-1}$, so that its thickness is equal to the skin depth at a frequency of 19.4 MHz.

Consider a square section of the metal sheet, of unit length and width with sides parallel to the x and y axes. The total current flowing through this section, I, is given by

$$\begin{aligned} I &= \int_0^h J_x \, dx \\ &= \int_0^h \sigma E_x \, dx \\ &= \sigma \int_0^h \{ c_1 e^{\tau z} + c_2 e^{-\tau z} \} \, dx \\ &= \frac{2\sigma E_0}{\tau} \frac{1 - e^{-\tau h}}{1 + e^{-\tau h}} \end{aligned} \qquad \text{(A.9)}$$

The surface impedance, Z_s, is the voltage across a square area for unit total current. The voltage drop along the surface of this unit square of conductor is simply E_0, so the surface impedance is

$$Z_s = \frac{\tau}{2\sigma} \frac{1 + e^{-\tau h}}{1 - e^{-\tau h}} \qquad \text{(A.10)}$$

The units of surface impedance are Ohms per square. The internal impedance of an element, in Ohms, can then readily be found from the surface impedance. For an element of half length a and half width b, the internal impedance Z_{int} is,

$$Z_{int} = \frac{a}{b} Z_s \qquad \text{(A.11)}$$

The surface impedance itself is complex, because the fields inside the metal lag behind those at the surface. Set,

$$\xi = \sqrt{\pi f \mu_0 \sigma} = \frac{1}{\delta} \tag{A.12}$$

so that $\tau = (1+j)\xi$. With this definition, Z_s can be expanded into real and imaginary parts, corresponding to resistance and inductive reactance,

$$\begin{aligned} Z_s &= \frac{(1+j)\xi}{2\sigma} \frac{1 + e^{-\xi h} e^{-j\xi h}}{1 - e^{-\xi h} e^{-j\xi h}} \\ &= \frac{(1+j)\xi}{2\sigma} \frac{1 - e^{-2\xi h} - 2je^{-\xi h} \sin \xi h}{1 - 2e^{-\xi h} \cos \xi h + e^{-2\xi h}} \end{aligned} \tag{A.13}$$

Define R_s as the surface resistance, with $R_s = \mathrm{Re}(Z_s)$, and L_s as the surface (or internal) inductance, with $\omega L_s = \mathrm{Im}(Z_s)$. These are then given by

$$R_s = \frac{\xi}{2\sigma} \frac{1 + 2e^{-\xi h} \sin \xi h - e^{-2\xi h}}{1 - 2e^{-\xi h} \cos \xi h + e^{-2\xi h}} \tag{A.14}$$

$$\omega L_s = \frac{\xi}{2\sigma} \frac{1 - 2e^{-\xi h} \sin \xi h - e^{-2\xi h}}{1 - 2e^{-\xi h} \cos \xi h + e^{-2\xi h}} \tag{A.15}$$

Since $\xi^2 \propto \omega$, at "high frequencies" $R_s \approx \omega L_s$, so the real and imaginary components of the impedance are approximately equal. High frequencies are those for which the skin depth, δ, is much less than the thickness of the metal sheet.

Appendix B

Solution of the Equations for the Scalar Potential

Introduction

This appendix describes the solution of the equations for the scalar potential derived in Chapter 3. The equations are solved in the spectral domain for the source charge in each of the three dielectric layers, giving six distinct potential functions. The method for transforming these back to the spatial domain is then described.

Potentials for the Source Charge in Layer 1

The first case to be considered is that with the source charge located at $z = z_0$ in layer 1. This results in the set of four Laplace's equations of equation 3.12

$$\begin{aligned}
\tilde{\phi}_a(k,z) &= A^+e^{kz} + A^-e^{-kz} && -d_1 \le z \le z_0 \\
\tilde{\phi}_b(k,z) &= B^+e^{kz} + B^-e^{-kz} && z_0 \le z \le 0 \\
\tilde{\phi}_c(k,z) &= C^+e^{kz} + C^-e^{-kz} && 0 \le z \le c \\
\tilde{\phi}_d(k,z) &= D^+e^{kz} + D^-e^{-kz} && c \le z \le c + d_2
\end{aligned} \tag{3.12}$$

together with the Fourier transformed boundary conditions

$$
\begin{aligned}
\tilde{\phi}_a(k,-d_1) &= 0 && (i)\\
\tilde{\phi}_d(k,c+d_2) &= 0 && (ii)\\
\tilde{\phi}_b(k,z_0) &= \tilde{\phi}_a(k,z_0) && (iii)\\
\tilde{\phi}_c(k,0) &= \tilde{\phi}_b(k,0) && (iv)\\
\tilde{\phi}_d(k,c) &= \tilde{\phi}_c(k,c) && (v)\\
\varepsilon_2 \frac{d}{dz}\tilde{\phi}_c(k,0) &= \varepsilon_1 \frac{d}{dz}\tilde{\phi}_b(k,0) && (vi)\\
\varepsilon_3 \frac{d}{dz}\tilde{\phi}_d(k,c) &= \varepsilon_2 \frac{d}{dz}\tilde{\phi}_c(k,c) && (vii)\\
\frac{d}{dz}\tilde{\phi}_b(k,z_0) &= \frac{d}{dz}\tilde{\phi}_a(k,z_0) - \frac{1}{2\pi\varepsilon_0\varepsilon_1} && (viii)
\end{aligned}
\tag{3.13}
$$

The functions A^+ to D^- are all found to contain a factor,

$$
\psi(k) = \frac{1}{\left[(1-\alpha e^{-2kd_1})(1-\beta e^{-2kd_2}) - e^{-2kc}(\alpha - e^{-2kd_1})(\beta - e^{-2kd_2})\right]} \tag{B.1}
$$

which can be rewritten as an infinite sum,

$$
\begin{aligned}
\psi(k) &= \frac{1}{\left[(1-\alpha e^{-2kd_1})(1-\beta e^{-2kd_2})\left(1 - \frac{e^{-2kc}(\alpha - e^{-2kd_1})(\beta - e^{-2kd_2})}{(1-\alpha e^{-2kd_1})(1-\beta e^{-2kd_2})}\right)\right]}\\
&= \sum_{n=0}^{\infty} \frac{(\alpha - e^{-2kd_1})^n}{(1-\alpha e^{-2kd_1})^{n+1}} \frac{(\beta - e^{-2kd_2})^n}{(1-\beta e^{-2kd_2})^{n+1}} e^{-2nkc}
\end{aligned}
\tag{B.2}
$$

Now, the terms in this sum can be expanded further. Looking at the first term, that in α, its two components can be expressed as summations,

$$
\begin{aligned}
(\alpha - e^{-2kd_1})^n &= \sum_{r=0}^{n} (-1)^r \frac{n!}{r!\,(n-r)!} \alpha^{n-r} e^{-2rkd_1}\\
\frac{1}{(1-\alpha e^{-2kd_1})^{n+1}} &= \sum_{s=0}^{\infty} \frac{(n+s)!}{n!\,s!} \alpha^s e^{-2skd_1}
\end{aligned}
\tag{B.3}
$$

These two summations can be combined into a single infinite sum,

$$\frac{(\alpha - e^{-2kd_1})^n}{(1-\alpha e^{-2kd_1})^{n+1}} = \sum_{m=0}^{\infty} K_{mn}(\alpha) e^{-2mkd_1} \tag{B.4}$$

where coefficients of the form $K_{ij}(\eta)$ are given by the summation,

$$K_{ij}(\eta) = \sum_{r=0}^{\min\{i,j\}} (-1)^r \frac{(i+j-r)!}{r!\,(i-r)!\,(j-r)!} \eta^{i+j-2r} \tag{B.5}$$

Interestingly, $K_{ij}(\eta)$ can also be written as a Jacobi polynomial. This derivation is detailed in Appendix C. $\psi(k)$ can now be written as,

$$\psi(k) = \sum_{l=0}^{\infty}\sum_{m=0}^{\infty}\sum_{n=0}^{\infty} K_{mn}(\alpha)\, K_{ln}(\beta)\, e^{-2nkc} e^{-2mkd_1} e^{-2lkd_2} \tag{B.6}$$

This has converted a function of complex form, with no easily found inverse Fourier transform, into a triple summation of terms of a much simpler form. This will enable the inverse transform to be performed analytically, which is a very considerable advantage. With $\psi(k)$ defined above, the functions are found to be,

$$\begin{aligned} A^+ = \frac{1}{4\pi\varepsilon_0\varepsilon_1 k}\Big[& e^{-kz_0} - e^{k(z_0-2c-2d_2)} \\ & + \alpha\left(e^{-k(z_0+2c+2d_2)} - e^{kz_0}\right) \\ & + \beta\left(e^{k(z_0-2c)} - e^{-k(z_0+2d_2)}\right) \\ & + \alpha\beta\left(e^{k(z_0-2d_2)} - e^{-k(z_0+2c)}\right)\Big]\,\psi(k) \end{aligned} \tag{B.7}$$

$$\begin{aligned} A^- = \frac{1}{4\pi\varepsilon_0\varepsilon_1 k}\Big[& e^{k(z_0-2c-2d_1-2d_2)} - e^{-k(z_0+2d_1)} \\ & + \alpha\left(e^{k(z_0-2d_1)} - e^{-k(z_0+2c+2d_1+2d_2)}\right) \\ & + \beta\left(e^{-k(z_0+2d_1+2d_2)} - e^{k(z_0-2c-2d_1)}\right) \\ & + \alpha\beta\left(e^{-k(z_0+2c+2d_1)} - e^{k(z_0-2d_1-2d_2)}\right)\Big]\,\psi(k) \end{aligned} \tag{B.8}$$

$$B^+ = \frac{1}{4\pi\varepsilon_0\varepsilon_1 k}\Big[\; e^{-k(z_0+2c+2d_1+2d_2)} - e^{k(z_0-2c-2d_2)} + \alpha\left(e^{-k(z_0+2d_1)} - e^{kz_0}\right) + \beta\left(e^{k(z_0-2c)} - e^{-k(z_0+2c+2d_1)}\right) + \alpha\beta\left(e^{k(z_0-2d_2)} - e^{-k(z_0+2d_1+2d_2)}\right)\Big]\,\psi(k) \tag{B.9}$$

$$B^- = \frac{1}{4\pi\varepsilon_0\varepsilon_1 k}\Big[\; e^{kz_0} - e^{-k(z_0+2d_1)} + \alpha\left(e^{k(z_0-2c-2d_2)} - e^{-k(z_0+2c+2d_1+2d_2)}\right) + \beta\left(e^{-k(z_0+2d_1+2d_2)} - e^{k(z_0-2d_2)}\right) + \alpha\beta\left(e^{-k(z_0+2c+2d_1)} - e^{k(z_0-2c)}\right)\Big]\,\psi(k) \tag{B.10}$$

$$C^+ = \frac{1-\alpha}{4\pi\varepsilon_0\varepsilon_1 k}\Big[\; e^{-k(z_0+2c+2d_1+2d_2)} - e^{k(z_0-2c-2d_2)} + \beta\left(e^{k(z_0-2c)} - e^{-k(z_0+2c+2d_1)}\right)\Big]\,\psi(k) \tag{B.11}$$

$$C^- = \frac{1-\alpha}{4\pi\varepsilon_0\varepsilon_1 k}\Big[\; e^{kz_0} - e^{-k(z_0+2d_1)} + \beta\left(e^{-k(z_0+2d_1+2d_2)} - e^{k(z_0-2d_2)}\right)\Big]\,\psi(k) \tag{B.12}$$

$$D^+ = \frac{(1-\alpha)(1+\beta)}{4\pi\varepsilon_0\varepsilon_1 k}\Big[\; e^{-k(z_0+2c+2d_1+2d_2)} - e^{k(z_0-2c-2d_2)}\Big]\,\psi(k) \tag{B.13}$$

$$D^- = \frac{(1-\alpha)(1+\beta)}{4\pi\varepsilon_0\varepsilon_1 k}\Big[\; e^{kz_0} - e^{-k(z_0+2d_1)}\Big]\,\psi(k) \tag{B.14}$$

The potential in each of the four regions can now be deduced. As would be expected from the theorem of reciprocity [Morse and Feshbach, 1953, p.883], the potential at $z = z_1$ due to a point charge at $z = z_0$ is found to be the same as the potential at $z = z_0$ due to a point charge at $z = z_1$. Therefore, use z_d and z_s as defined in equation 3.15,

$$z_d = |z - z_0| \quad , \quad z_s = z + z_0 \tag{3.15}$$

The four solutions of equations 3.12 can be reduced to three written in terms of z_d and z_s. Reciprocity then reduces the nine formulae, for the source charge and object point in any of the three layers, to six.

Therefore, write $\tilde{\phi}_{ab}(k,z)$ as the transformed potential in layer b due to a source charge in layer a. Reciprocity means that $\tilde{\phi}_{ab} = \tilde{\phi}_{ba}$, when written in terms of z_d and z_s. Noting that,

$$\frac{1-\alpha}{\varepsilon_1} = \frac{1+\alpha}{\varepsilon_2} \quad , \quad \frac{1+\beta}{\varepsilon_2} = \frac{1-\beta}{\varepsilon_3} \tag{B.15}$$

the three solutions for the transformed potential are,

$$\begin{aligned}
\tilde{\phi}_{11}(k,z) = \frac{1}{4\pi\varepsilon_0\varepsilon_1 k} \sum_{l=0}^{\infty}\sum_{m=0}^{\infty}\sum_{n=0}^{\infty} K_{mn}(\alpha)\, K_{ln}(\beta) \times \\
\Big[\; e^{-k\{2ld_2+2md_1+2nc+z_d\}} + e^{-k\{2(l+1)d_2+2(m+1)d_1+2(n+1)c-z_d\}} \\
- e^{-k\{2ld_2+2(m+1)d_1+2nc+z_s\}} - e^{-k\{2(l+1)d_2+2md_1+2(n+1)c-z_s\}} \\
+ \alpha\Big(e^{-k\{2(l+1)d_2+2md_1+2(n+1)c+z_d\}} + e^{-k\{2ld_2+2(m+1)d_1+2nc-z_d\}} \\
- e^{-k\{2(l+1)d_2+2(m+1)d_1+2(n+1)c+z_s\}} - e^{-k\{2ld_2+2md_1+2nc-z_s\}}\Big) \\
+ \beta\Big(e^{-k\{2(l+1)d_2+2(m+1)d_1+2nc+z_s\}} + e^{-k\{2ld_2+2md_1+2(n+1)c-z_s\}} \\
- e^{-k\{2(l+1)d_2+2md_1+2nc+z_d\}} - e^{-k\{2ld_2+2(m+1)d_1+2(n+1)c-z_d\}}\Big) \\
+ \alpha\beta\Big(e^{-k\{2ld_2+2(m+1)d_1+2(n+1)c+z_s\}} + e^{-k\{2(l+1)d_2+2md_1+2nc-z_s\}} \\
- e^{-k\{2ld_2+2md_1+2(n+1)c+z_d\}} - e^{-k\{2(l+1)d_2+2(m+1)d_1+2nc-z_d\}}\Big)\Big]
\end{aligned} \tag{B.16}$$

$$\begin{aligned}
\tilde{\phi}_{12}(k,z) = \frac{1+\alpha}{4\pi\varepsilon_0\varepsilon_2 k} \sum_{l=0}^{\infty}\sum_{m=0}^{\infty}\sum_{n=0}^{\infty} K_{mn}(\alpha)\, K_{ln}(\beta) \times \\
\Big[\; e^{-k\{2ld_2+2md_1+2nc+z_d\}} + e^{-k\{2(l+1)d_2+2(m+1)d_1+2(n+1)c-z_d\}} \\
- e^{-k\{2ld_2+2(m+1)d_1+2nc+z_s\}} - e^{-k\{2(l+1)d_2+2md_1+2(n+1)c-z_s\}} \\
+ \beta\Big(e^{-k\{2(l+1)d_2+2(m+1)d_1+2nc+z_s\}} + e^{-k\{2ld_2+2md_1+2(n+1)c-z_s\}} \\
- e^{-k\{2(l+1)d_2+2md_1+2nc+z_d\}} - e^{-k\{2ld_2+2(m+1)d_1+2(n+1)c-z_d\}}\Big)\Big]
\end{aligned} \tag{B.17}$$

$$\begin{aligned}
\tilde{\phi}_{13}(k,z) = \frac{(1+\alpha)(1+\beta)}{4\pi\varepsilon_0\varepsilon_2 k} \sum_{l=0}^{\infty}\sum_{m=0}^{\infty}\sum_{n=0}^{\infty} K_{mn}(\alpha)\, K_{ln}(\beta) \times \\
\Big[\; e^{-k\{2ld_2+2md_1+2nc+z_d\}} + e^{-k\{2(l+1)d_2+2(m+1)d_1+2(n+1)c-z_d\}} \\
- e^{-k\{2ld_2+2(m+1)d_1+2nc+z_s\}} - e^{-k\{2(l+1)d_2+2md_1+2(n+1)c-z_s\}}\Big]
\end{aligned} \tag{B.18}$$

Potentials for the Source Charge in Layer 2

Consider now the case with the source charge located at $z = z_0$ in layer 2. The solutions to the four Laplace's equations can be written just as in equation 3.12, but with modified regions of validity for each solution,

$$\begin{aligned}
\tilde{\phi}_a(k,z) &= A^+e^{kz} + A^-e^{-kz} && -d_1 \le z \le 0 \\
\tilde{\phi}_b(k,z) &= B^+e^{kz} + B^-e^{-kz} && 0 \le z \le z_0 \\
\tilde{\phi}_c(k,z) &= C^+e^{kz} + C^-e^{-kz} && z_0 \le z \le c \\
\tilde{\phi}_d(k,z) &= D^+e^{kz} + D^-e^{-kz} && c \le z \le c + d_2
\end{aligned} \tag{B.19}$$

The Fourier transformed boundary conditions are now,

$$\begin{aligned}
\tilde{\phi}_a(k,-d_1) &= 0 && (i) \\
\tilde{\phi}_d(k,c+d_2) &= 0 && (ii) \\
\tilde{\phi}_b(k,0) &= \tilde{\phi}_a(k,0) && (iii) \\
\tilde{\phi}_c(k,z_0) &= \tilde{\phi}_b(k,z_0) && (iv) \\
\tilde{\phi}_d(k,c) &= \tilde{\phi}_c(k,c) && (v) \\
\varepsilon_2 \frac{d}{dz}\tilde{\phi}_b(k,0) &= \varepsilon_1 \frac{d}{dz}\tilde{\phi}_a(k,0) && (vi) \\
\varepsilon_3 \frac{d}{dz}\tilde{\phi}_d(k,c) &= \varepsilon_2 \frac{d}{dz}\tilde{\phi}_c(k,c) && (vii) \\
\frac{d}{dz}\tilde{\phi}_c(k,z_0) &= \frac{d}{dz}\tilde{\phi}_b(k,z_0) - \frac{1}{2\pi\varepsilon_0\varepsilon_2} && (viii)
\end{aligned} \tag{B.20}$$

Note that conditions (i), (ii), (v) and (vii) are still the same as in equation 3.13.

Solving again for the unknown functions A^+ to D^- results in,

$$\begin{aligned}
A^+ = \frac{1+\alpha}{4\pi\varepsilon_0\varepsilon_2 k}\Big[& e^{-kz_0} - e^{k(z_0-2c-2d_2)} \\
& + \beta\left(e^{k(z_0-2c)} - e^{-k(z_0+2d_2)}\right) \Big] \psi(k)
\end{aligned} \tag{B.21}$$

$$\begin{aligned}
A^- = \frac{1+\alpha}{4\pi\varepsilon_0\varepsilon_2 k}\Big[& e^{k(z_0-2c-2d_1-2d_2)} - e^{-k(z_0+2d_1)} \\
& + \beta\left(e^{-k(z_0+2d_1+2d_2)} - e^{k(z_0-2c-2d_1)}\right) \Big] \psi(k)
\end{aligned} \tag{B.22}$$

$$B^{+} = \frac{1}{4\pi\varepsilon_0\varepsilon_2 k}\Big[\; e^{-kz_0} - e^{k(z_0-2c-2d_2)} + \alpha\left(e^{k(z_0-2c-2d_1-2d_2)} - e^{-k(z_0+2d_1)}\right) + \beta\left(e^{k(z_0-2c)} - e^{-k(z_0+2d_2)}\right) + \alpha\beta\left(e^{-k(z_0+2d_1+2d_2)} - e^{k(z_0-2c-2d_1)}\right)\Big]\,\psi(k) \tag{B.23}$$

$$B^{-} = \frac{1}{4\pi\varepsilon_0\varepsilon_2 k}\Big[\; e^{k(z_0-2c-2d_1-2d_2)} - e^{-k(z_0+2d_1)} + \alpha\left(e^{-kz_0} - e^{k(z_0-2c-2d_2)}\right) + \beta\left(e^{-k(z_0+2d_1+2d_2)} - e^{k(z_0-2c-2d_1)}\right) + \alpha\beta\left(e^{k(z_0-2c)} - e^{-k(z_0+2d_2)}\right)\Big]\,\psi(k) \tag{B.24}$$

$$C^{+} = \frac{1}{4\pi\varepsilon_0\varepsilon_2 k}\Big[\; e^{-k(z_0+2c+2d_1+2d_2)} - e^{k(z_0-2c-2d_2)} + \alpha\left(e^{k(z_0-2c-2d_1-2d_2)} - e^{-k(z_0+2c+2d_2)}\right) + \beta\left(e^{k(z_0-2c)} - e^{-k(z_0+2c+2d_1)}\right) + \alpha\beta\left(e^{-k(z_0+2c)} - e^{k(z_0-2c-2d_1)}\right)\Big]\,\psi(k) \tag{B.25}$$

$$C^{-} = \frac{1}{4\pi\varepsilon_0\varepsilon_2 k}\Big[\; e^{kz_0} - e^{-k(z_0+2d_1)} + \alpha\left(e^{-kz_0} - e^{k(z_0-2d_1)}\right) + \beta\left(e^{-k(z_0+2d_1+2d_2)} - e^{k(z_0-2d_2)}\right) + \alpha\beta\left(e^{k(z_0-2d_1-2d_2)} - e^{-k(z_0+2d_2)}\right)\Big]\,\psi(k) \tag{B.26}$$

$$D^{+} = \frac{1+\beta}{4\pi\varepsilon_0\varepsilon_2 k}\Big[\; e^{-k(z_0+2c+2d_1+2d_2)} - e^{k(z_0-2c-2d_2)} + \alpha\left(e^{k(z_0-2c-2d_1-2d_2)} - e^{-k(z_0+2c+2d_2)}\right)\Big]\,\psi(k) \tag{B.27}$$

$$D^{-} = \frac{1+\beta}{4\pi\varepsilon_0\varepsilon_2 k}\Big[\; e^{kz_0} - e^{-k(z_0+2d_1)} + \alpha\left(e^{-kz_0} - e^{k(z_0-2d_1)}\right)\Big]\,\psi(k) \tag{B.28}$$

$\tilde{\phi}_{21}$ is the same as $\tilde{\phi}_{12}$ in equation B.17, as would be expected from reciprocity. The two new cases are,

$$\tilde{\phi}_{22}(k,z) = \frac{1}{4\pi\varepsilon_0\varepsilon_2 k}\sum_{l=0}^{\infty}\sum_{m=0}^{\infty}\sum_{n=0}^{\infty}K_{mn}(\alpha)\,K_{ln}(\beta)\times$$
$$\Big[\; e^{-k\{2ld_2+2md_1+2nc+z_d\}} + e^{-k\{2(l+1)d_2+2(m+1)d_1+2(n+1)c-z_d\}}$$
$$- e^{-k\{2ld_2+2(m+1)d_1+2nc+z_s\}} - e^{-k\{2(l+1)d_2+2md_1+2(n+1)c-z_s\}}$$
$$+\alpha\Big(e^{-k\{2ld_2+2md_1+2nc+z_s\}} + e^{-k\{2(l+1)d_2+2(m+1)d_1+2(n+1)c-z_s\}}$$
$$- e^{-k\{2ld_2+2(m+1)d_1+2nc+z_d\}} - e^{-k\{2(l+1)d_2+2md_1+2(n+1)c-z_d\}}\Big) \qquad \text{(B.29)}$$
$$+\beta\Big(e^{-k\{2(l+1)d_2+2(m+1)d_1+2nc+z_s\}} + e^{-k\{2ld_2+2md_1+2(n+1)c-z_s\}}$$
$$- e^{-k\{2(l+1)d_2+2md_1+2nc+z_d\}} - e^{-k\{2ld_2+2(m+1)d_1+2(n+1)c-z_d\}}\Big)$$
$$+\alpha\beta\Big(e^{-k\{2(l+1)d_2+2(m+1)d_1+2nc+z_d\}} + e^{-k\{2ld_2+2md_1+2(n+1)c-z_d\}}$$
$$- e^{-k\{2(l+1)d_2+2md_1+2nc+z_s\}} - e^{-k\{2ld_2+2(m+1)d_1+2(n+1)c-z_s\}}\Big)\Big]$$

$$\tilde{\phi}_{23}(k,z) = \frac{1+\beta}{4\pi\varepsilon_0\varepsilon_2 k}\sum_{l=0}^{\infty}\sum_{m=0}^{\infty}\sum_{n=0}^{\infty}K_{mn}(\alpha)\,K_{ln}(\beta)\times$$
$$\Big[\; e^{-k\{2ld_2+2md_1+2nc+z_d\}} + e^{-k\{2(l+1)d_2+2(m+1)d_1+2(n+1)c-z_d\}}$$
$$- e^{-k\{2ld_2+2(m+1)d_1+2nc+z_s\}} - e^{-k\{2(l+1)d_2+2md_1+2(n+1)c-z_s\}} \qquad \text{(B.30)}$$
$$+\alpha\Big(e^{-k\{2ld_2+2md_1+2nc+z_s\}} + e^{-k\{2(l+1)d_2+2(m+1)d_1+2(n+1)c-z_s\}}$$
$$- e^{-k\{2ld_2+2(m+1)d_1+2nc+z_d\}} - e^{-k\{2(l+1)d_2+2md_1+2(n+1)c-z_d\}}\Big)\Big]$$

Potentials for the Source Charge in Layer 3

Finally, consider the case with the source charge located at $z = z_0$ in layer 3. As in equation B.19, the solutions to the four Laplace's equations have their regions of validity modified from equation 3.12, giving,

$$\begin{aligned}
\tilde{\phi}_a(k,z) &= A^+e^{kz} + A^-e^{-kz} && -d_1 \le z \le 0\\
\tilde{\phi}_b(k,z) &= B^+e^{kz} + B^-e^{-kz} && 0 \le z \le c\\
\tilde{\phi}_c(k,z) &= C^+e^{kz} + C^-e^{-kz} && c \le z \le z_0\\
\tilde{\phi}_d(k,z) &= D^+e^{kz} + D^-e^{-kz} && z_0 \le z \le c + d_2
\end{aligned} \qquad \text{(B.31)}$$

The Fourier transformed boundary conditions become,

$$
\begin{aligned}
\tilde{\phi}_a(k,-d) &= 0 && (i)\\
\tilde{\phi}_d(k,c+h) &= 0 && (ii)\\
\tilde{\phi}_b(k,0) &= \tilde{\phi}_a(k,0) && (iii)\\
\tilde{\phi}_c(k,c) &= \tilde{\phi}_b(k,c) && (iv)\\
\tilde{\phi}_d(k,z_0) &= \tilde{\phi}_c(k,z_0) && (v)\\
\varepsilon_2 \frac{d}{dz}\tilde{\phi}_b(k,0) &= \varepsilon_1 \frac{d}{dz}\tilde{\phi}_a(k,0) && (vi)\\
\varepsilon_3 \frac{d}{dz}\tilde{\phi}_c(k,c) &= \varepsilon_2 \frac{d}{dz}\tilde{\phi}_b(k,c) && (vii)\\
\frac{d}{dz}\tilde{\phi}_d(k,z_0) &= \frac{d}{dz}\tilde{\phi}_c(k,z_0) - \frac{1}{2\pi\varepsilon_0\varepsilon_3} && (viii)
\end{aligned}
\tag{B.32}
$$

Note that conditions (i)-(iii) and (vi) are unchanged from equation B.20.

Solving again for the unknown functions A^+ to D^- results in,

$$A^+ = \frac{(1+\alpha)(1-\beta)}{4\pi\varepsilon_0\varepsilon_3 k}\left[\, e^{-kz_0} - e^{k(z_0-2c-2d_2)} \,\right] \psi(k) \tag{B.33}$$

$$A^- = \frac{(1+\alpha)(1-\beta)}{4\pi\varepsilon_0\varepsilon_3 k}\left[\, e^{k(z_0-2c-2d_1-2d_2)} - e^{-k(z_0+2d_1)} \,\right] \psi(k) \tag{B.34}$$

$$
\begin{aligned}
B^+ = \frac{1-\beta}{4\pi\varepsilon_0\varepsilon_3 k}\Big[\;& e^{-kz_0} - e^{k(z_0-2c-2d_2)} \\
&+ \alpha\left(e^{k(z_0-2c-2d_1-2d_2)} - e^{-k(z_0+2d_1)}\right) \Big] \psi(k)
\end{aligned}
\tag{B.35}
$$

$$
\begin{aligned}
B^- = \frac{1-\beta}{4\pi\varepsilon_0\varepsilon_3 k}\Big[\;& e^{k(z_0-2c-2d_1-2d_2)} - e^{-k(z_0+2d_1)} \\
&+ \alpha\left(e^{-kz_0} - e^{k(z_0-2c-2d_2)}\right) \Big] \psi(k)
\end{aligned}
\tag{B.36}
$$

$$
\begin{aligned}
C^+ = \frac{1}{4\pi\varepsilon_0\varepsilon_3 k}\Big[\;& e^{-kz_0} - e^{k(z_0-2c-2d_2)} \\
&+ \alpha\left(e^{k(z_0-2c-2d_1-2d_2)} - e^{-k(z_0+2d_1)}\right) \\
&+ \beta\left(e^{-k(z_0+2c+2d_1)} - e^{k(z_0-4c-2d_1-2d_2)}\right) \\
&+ \alpha\beta\left(e^{k(z_0-4c-2d_2)} - e^{-k(z_0+2c)}\right) \Big] \psi(k)
\end{aligned}
\tag{B.37}
$$

$$C^- = \frac{1}{4\pi\varepsilon_0\varepsilon_3 k}\Big[\; e^{k(z_0-2c-2d_1-2d_2)} - e^{-k(z_0+2d_1)} + \alpha\big(e^{-kz_0} - e^{k(z_0-2c-2d_2)}\big) + \beta\big(e^{k(z_0-2d_2)} - e^{-k(z_0-2c)}\big) + \alpha\beta\big(e^{-k(z_0-2c+2d_1)} - e^{k(z_0-2d_1-2d_2)}\big)\Big]\,\psi(k) \tag{B.38}$$

$$D^+ = \frac{1}{4\pi\varepsilon_0\varepsilon_3 k}\Big[\; e^{-k(z_0+2c+2d_1+2d_2)} - e^{k(z_0-2c-2d_2)} + \alpha\big(e^{k(z_0-2c-2d_1-2d_2)} - e^{-k(z_0+2c+2d_2)}\big) + \beta\big(e^{-k(z_0+2d_2)} - e^{k(z_0-4c-2d_1-2d_2)}\big) + \alpha\beta\big(e^{k(z_0-4c-2d_2)} - e^{-k(z_0+2d_1+2d_2)}\big)\Big]\,\psi(k) \tag{B.39}$$

$$D^- = \frac{1}{4\pi\varepsilon_0\varepsilon_3 k}\Big[\; e^{kz_0} - e^{-k(z_0+2d_1)} + \alpha\big(e^{-kz_0} - e^{k(z_0-2d_1)}\big) + \beta\big(e^{k(z_0-2c-2d_1)} - e^{-k(z_0-2c)}\big) + \alpha\beta\big(e^{-k(z_0-2c+2d_1)} - e^{k(z_0-2c)}\big)\Big]\,\psi(k) \tag{B.40}$$

As would be expected from reciprocity, $\tilde{\phi}_{31}$ is the same as $\tilde{\phi}_{13}$ in equation B.18, and $\tilde{\phi}_{32}$ is the same as $\tilde{\phi}_{23}$ in equation B.30. The remaining new case is,

$$\begin{aligned}\tilde{\phi}_{33}(k,z) = \frac{1}{4\pi\varepsilon_0\varepsilon_3 k}\sum_{l=0}^{\infty}\sum_{m=0}^{\infty}\sum_{n=0}^{\infty}K_{mn}(\alpha)\,K_{ln}(\beta)\,\times\\ \Big[\; e^{-k\{2ld_2+2md_1+2nc+z_d\}} + e^{-k\{2(l+1)d_2+2(m+1)d_1+2(n+1)c-z_d\}}\\ - e^{-k\{2ld_2+2(m+1)d_1+2nc+z_s\}} - e^{-k\{2(l+1)d_2+2md_1+2(n+1)c-z_s\}}\\ + \alpha\big(e^{-k\{2ld_2+2md_1+2nc+z_s\}} + e^{-k\{2(l+1)d_2+2(m+1)d_1+2(n+1)c-z_s\}}\\ - e^{-k\{2ld_2+2(m+1)d_1+2nc+z_d\}} - e^{-k\{2(l+1)d_2+2md_1+2(n+1)c-z_d\}}\big)\\ + \beta\big(e^{-k\{2ld_2+2(m+1)d_1+2(n+1)c+z_d\}} + e^{-k\{2(l+1)d_2+2md_1+2nc-z_d\}}\\ - e^{-k\{2ld_2+2md_1+2(n-1)c+z_s\}} - e^{-k\{2(l+1)d_2+2(m+1)d_1+2(n+2)c-z_s\}}\big)\\ + \alpha\beta\big(e^{-k\{2ld_2+2(m+1)d_1+2(n-1)c+z_s\}} + e^{-k\{2(l+1)d_2+2md_1+2(n+2)c-z_s\}}\\ - e^{-k\{2ld_2+2md_1+2(n+1)c+z_d\}} - e^{-k\{2(l+1)d_2+2(m+1)d_1+2nc-z_d\}}\big)\Big]\end{aligned} \tag{B.41}$$

Performing the Inverse Fourier Transform

The Fourier transform pair used in this thesis is,

$$\tilde{f}(k_x, k_y) = \frac{1}{2\pi}\int_{-\infty}^{\infty}\int_{-\infty}^{\infty} f(x,y)\; e^{-jk_x x} e^{-jk_y y}\; dx\; dy$$

and (B.42)

$$f(x,y) = \frac{1}{2\pi}\int_{-\infty}^{\infty}\int_{-\infty}^{\infty} \tilde{f}(k_x, k_y)\; e^{jk_x x} e^{jk_y y}\; dk_x\; dk_y$$

The transformed potentials $\tilde{\phi}(k_x, k_y)$, derived in this appendix, are composed of terms of the form,

$$\tilde{g}(k_x,k_y) = \frac{e^{-z\sqrt{k_x^2+k_y^2}}}{\sqrt{k_x^2+k_y^2}} \qquad \text{(B.43)}$$

The potential $\phi(x,y)$ will therefore have terms of the form,

$$\begin{aligned} g(x,y) &= \frac{1}{2\pi}\int_{-\infty}^{\infty}\int_{-\infty}^{\infty} \tilde{g}(k_x, k_y)\; e^{jk_x x} e^{jk_y y}\; dk_x\; dk_y \\ &= \frac{2}{\pi}\int_{0}^{\infty}\int_{0}^{\infty} \tilde{g}(k_x, k_y)\cos(k_x x)\cos(k_y y)\; dk_x\; dk_y \end{aligned} \qquad \text{(B.44)}$$

since $\tilde{g}(k_x, k_y)$ in equation B.43 is an even function of both k_x and k_y.

Now, formula 3.961.2 in Gradshteyn and Ryzhik [1980] can be written as,

$$\int_0^{\infty} \frac{e^{-z\sqrt{k_x^2+k_y^2}}}{\sqrt{k_x^2+k_y^2}} \cos(k_y y)\, dk_y = K_0\left(k_x\sqrt{y^2+z^2}\right) \qquad \text{(B.45)}$$

and formula 6.671.14 can be written as,

$$\int_0^\infty K_0\left(k_x\sqrt{y^2+z^2}\right)\cos(k_x x)\,dk_x \;=\; \frac{\pi}{2}\frac{1}{\sqrt{x^2+y^2+z^2}} \qquad \text{(B.46)}$$

Substituting equations B.43, B.45 and B.46 into equation B.44 therefore yields the required general term for the potential as,

$$g(x,y)=\frac{1}{\sqrt{x^2+y^2+z^2}} \qquad \text{(B.47)}$$

which can be interpreted as the potential at the point (x,y,z) due to a point charge at the origin, ignoring normalisation constants. This enables the spectral domain potentials given in equations B.16 - B.18, B.29, B.30 and B.41 to be transformed into the spatial domain potentials given in equations 3.17 - 3.22.

Appendix C

Series Coefficients as Jacobi Polynomials

The series coefficient $K_{ij}(\eta)$ was written in Appendix B as,

$$K_{ij}(\eta) = \sum_{r=0}^{\min\{i,j\}} (-1)^r \frac{(i+j-r)!}{r!\,(i-r)!\,(j-r)!}\,\eta^{i+j-2r} \qquad \text{(B.5)}$$

Using table 22.3.3 in Abramowitz and Stegun [1965], take the Jacobi polynomial $G_j(p,q,x)$. Assume that $i \geq j$ and put,

$$p = q = i-j+1 \quad , \quad x=\eta^2 \qquad \text{(C.1)}$$

The polynomial $G_j(i-j+1,i-j+1,\eta^2)$ can then be expressed as,

$$G_j(i-j+1,i-j+1,\eta^2) = \frac{i!\,j!}{(i+j)!} \sum_{r=0}^{j} (-1)^r \frac{(i+j-r)!}{r!\,(i-r)!\,(j-r)!}\,\eta^{2j-2r} \qquad \text{(C.2)}$$

Expression 22.5.2 in Abramowitz and Stegun, relating the Jacobi polynomials $G_j(p,q,x)$ and $P_j^{(\gamma,\delta)}(x)$ can be written as,

$$G_j(i-j+1,i-j+1,\eta^2) = \frac{i!\,j!}{(i+j)!}\,P_j^{(0,i-j)}(2\eta^2-1) \qquad \text{(C.3)}$$

Combining equations C.2 and C.3 results in,

$$P_j^{(0,i-j)}(2\eta^2-1) = \sum_{r=0}^{j} (-1)^r \frac{(i+j-r)!}{r!\,(i-r)!\,(j-r)!}\,\eta^{2j-2r} \qquad \text{(C.4)}$$

Reversing i and j when $j > i$, the $K_{ij}(\eta)$ coefficient given by equation B.5 can therefore be expressed as,

$$K_{ij}(\eta) = \begin{cases} \eta^{i-j} P_j^{(0,i-j)}(2\eta^2 - 1) & (i \geq j) \\ \eta^{j-i} P_i^{(0,j-i)}(2\eta^2 - 1) & (i \leq j) \end{cases} \tag{C.5}$$

Direct evaluation of the K_{ij} coefficients presents a computational problem when i and j exceed about 30, as they are then the very small difference (less than 1) between two very large numbers (10^{30} or more). When they are expressed as Jacobi polynomials, a recurrence relation [Erdelyi, 1953] can be used to compute them, and this does not run into numerical difficulties until i and j exceed about 500, enabling all the necessary coefficients to be computed efficiently.

Appendix D

Efficient Representations for some Potential Formulae

Some of the formulae for the scalar potential derived in Chapter 3 can be rewritten in a form which is more efficient for computation. These cases occur when the source element and object point are both on one of the PCB surfaces, and will be detailed in turn.

Single Sided PCB with Coincident Ground Plane

This case corresponds to setting $d_1 = 0$ and $d_2 = \infty$ in Figure 7. Layer 2 then represents the PCB substrate, and layer 3 represents the free space above the PCB. The potential ϕ_{cc} for this case is given by equation 3.68. Writing this with a finite upper limit of summation, N, and expanding the function ξ gives

$$\begin{aligned}
\phi_{cc} &= \frac{1+\beta}{4\pi\varepsilon_0\varepsilon_2}\sum_{n=0}^{N}(-\beta)^n\left[\frac{1}{\sqrt{x^2+y^2+4n^2c^2}} - \frac{1}{\sqrt{x^2+y^2+4(n+1)^2c^2}}\right] \\
&= \frac{1+\beta}{4\pi\varepsilon_0\varepsilon_2}\left[\sum_{n=0}^{N}\frac{(-\beta)^n}{\sqrt{x^2+y^2+4n^2c^2}} - \sum_{n=1}^{N+1}\frac{(-\beta)^{n-1}}{\sqrt{x^2+y^2+4n^2c^2}}\right] \qquad \text{(D.1)} \\
&= \frac{1+\beta}{4\pi\varepsilon_0\varepsilon_2}\left[\frac{1}{\sqrt{x^2+y^2}} - (1+\beta)\sum_{n=1}^{N}\frac{(-\beta)^{n-1}}{\sqrt{x^2+y^2+4n^2c^2}} - \frac{(-\beta)^N}{\sqrt{x^2+y^2+4(N+1)^2c^2}}\right]
\end{aligned}$$

If a new set of constants P_n is defined by,

$$\begin{aligned} P_0 &= \frac{1+\beta}{4\pi\varepsilon_0\varepsilon_2} \\ P_n &= -P_0(1+\beta)(-\beta)^{n-1} \qquad 1 \le n \le N \\ P_{N+1} &= -P_0(-\beta)^N \end{aligned} \tag{D.2}$$

the potential can be written as the single series,

$$\phi_{cc} = \sum_{n=0}^{N+1} \frac{P_n}{\sqrt{x^2+y^2+4n^2c^2}} \tag{D.3}$$

This has transformed two series of $N+1$ terms each (a total of $2N+2$ terms) into one series of $N+2$ terms. This results in N less terms to compute, and will therefore roughly halve the CPU time needed to calculate the potential.

Double Sided PCB without Ground Plane

This case corresponds to setting $d_1 = \infty$ and $d_2 = \infty$ in Figure 7. Layer 2 then represents the PCB substrate, and layers 1 and 3 represent the free space below and above the PCB. There were three formulae for different cases derived for the potential in Chapter 3:

1. Source element and object point on top surface of the PCB, given by ϕ_{cc} in equation 3.66
2. Source element and object point on bottom surface of the PCB, given by ϕ_{oo} in equation 3.64
3. Source element and object point on opposite surfaces of the PCB given by ϕ_{oc} in equation 3.65

The third case is already in the form of a series with $N+1$ terms, and the first two cases are equivalent with α and β interchanged. Therefore, only the first case will be examined here. The potential ϕ_{cc} is,

$$\phi_{cc} = \frac{1+\beta}{4\pi\varepsilon_0\varepsilon_2}\sum_{n=0}^{N}(\alpha\beta)^n\left[\frac{1}{\sqrt{x^2+y^2+4n^2c^2}} + \frac{\alpha}{\sqrt{x^2+y^2+4(n+1)^2c^2}}\right] \qquad \text{(D.4)}$$

Using exactly the same methods as before, this can be expressed in terms of the single series given by equation D.3 with a different set of P_n constants. These are,

$$\begin{aligned} P_0 &= \frac{1+\beta}{4\pi\varepsilon_0\varepsilon_2} \\ P_n &= P_0(1+\alpha)^2\alpha^n\beta^{n-1} \qquad 1 \le n \le N \\ P_{N+1} &= P_0\,\alpha^{N+1}\beta^N \end{aligned} \qquad \text{(D.5)}$$

Double Sided PCB with Ground Plane

This case corresponds to a non-zero value of d_1 in Figure 7, with $d_2 = \infty$. Again, there were three formulae for different cases derived for the potential in Chapter 3. However, this time all are distinct, and can be made more compact. The potentials all involve double series over m and n, and the upper limits of summation will be taken to be M and N respectively. The three cases are treated in turn.

Source element and object point on top surface of the PCB

The relevant potential is ϕ_{cc}, given by equation 3.63. Writing this with finite upper limits of summation gives,

$$\phi_{cc} = \frac{1+\beta}{4\pi\varepsilon_0\varepsilon_2}\sum_{m=0}^{M}\sum_{n=0}^{N}\beta^n K_{mn}(\alpha)\times\left[\frac{1}{\sqrt{x^2+y^2+4\{md_1+nc\}^2}}\right.$$
$$+\frac{\alpha}{\sqrt{x^2+y^2+4\{md_1+(n+1)c\}^2}}$$
$$-\frac{1}{\sqrt{x^2+y^2+4\{(m+1)d_1+(n+1)c\}^2}} \qquad (D.6)$$
$$\left.-\frac{\alpha}{\sqrt{x^2+y^2+4\{(m+1)d_1+nc\}^2}}\right]$$

where the $K_{mn}(\alpha)$ are a set of constants, defined in Appendix B, equation B.5. The same methods as before can be employed to reduce the above expression to a double sum of just one term. The algebra involved is rather more extensive, so only the results will be shown. The potential can be expressed as,

$$\phi_{cc} = \sum_{m=0}^{M+1}\sum_{n=0}^{N+1}\frac{A_{mn}}{\sqrt{x^2+y^2+4(md_1+nc)^2}} \qquad (D.7)$$

with the set of constants A_{mn} defined by,

$$\begin{aligned}
A_{00} &= \frac{1+\beta}{4\pi\varepsilon_0\varepsilon_2}\\
A_{M+1,0} &= -A_{00}\,\alpha K_{M0}(\alpha)\\
A_{0,N+1} &= A_{00}\,\alpha\beta^N K_{0N}(\alpha)\\
A_{M+1,N+1} &= -A_{00}\,\beta^N K_{MN}(\alpha)\\
A_{m0} &= A_{00}\,[K_{m0}(\alpha)-\alpha K_{m-1,0}(\alpha)]\\
A_{m,N+1} &= A_{00}\,\beta^N[\alpha K_{mN}(\alpha)-K_{m-1,N}(\alpha)]\\
A_{0n} &= A_{00}\,\beta^{n-1}[\beta K_{0n}(\alpha)+\alpha K_{0,n-1}(\alpha)]\\
A_{M+1,n} &= -A_{00}\,\beta^{n-1}[\alpha\beta K_{Mn}(\alpha)+K_{M,n-1}(\alpha)]\\
A_{mn} &= A_{00}\,\beta^{n-1}[\beta K_{m,n}(\alpha)+\alpha K_{m,n-1}(\alpha)-\alpha\beta K_{m-1,n}(\alpha)-K_{m-1,n-1}(\alpha)]
\end{aligned} \qquad (D.8)$$

$1 \le m \le M\ ,\ 1 \le n \le N$

This has transformed four double series, each having $(M+1)\times(N+1)$ terms, into one double series of $(M+2)\times(N+2)$ terms. For large values of M and N this cuts the number

of terms which have to be evaluated by about 75%, a considerable saving. The values actually used in the current version of FACET are $M=N=5$. For this case, the above transformation means that only 49 terms need to be computed instead of 144, reducing the CPU time required by about 66%.

Source element and object point on rear surface of the PCB

The relevant potential is ϕ_{00}, given by equation 3.61. Writing this with finite upper limits of summation gives,

$$\phi_{00} = \frac{1+\alpha}{4\pi\varepsilon_0\varepsilon_2}\sum_{m=0}^{M}\sum_{n=0}^{N}\beta^n K_{mn}(\alpha) \times \left[\frac{1}{\sqrt{x^2+y^2+4\{md_1+nc\}^2}} + \frac{\beta}{\sqrt{x^2+y^2+4\{md_1+(n+1)c\}^2}} - \frac{1}{\sqrt{x^2+y^2+4\{(m+1)d_1+nc\}^2}} - \frac{\beta}{\sqrt{x^2+y^2+4\{(m+1)d_1+(n+1)c\}^2}} \right] \quad \text{(D.9)}$$

As for the previous case, this can be written in the form of equation D.7, with ϕ_{cc} replaced by ϕ_{00}. The set of constants A_{mn} is now defined by,

$$\begin{aligned}
A_{00} &= \frac{1+\alpha}{4\pi\varepsilon_0\varepsilon_2} \\
A_{M+1,0} &= -A_{00}K_{M0}(\alpha) \\
A_{0,N+1} &= A_{00}\beta^{N+1}K_{0N}(\alpha) \\
A_{M+1,N+1} &= -A_{00}\beta^{N+1}K_{MN}(\alpha) \\
A_{m0} &= A_{00}[K_{m0}(\alpha) - K_{m-1,0}(\alpha)] \\
A_{m,N+1} &= A_{00}\beta^{N+1}[K_{mN}(\alpha) - K_{m-1,N}(\alpha)] \\
A_{0n} &= A_{00}\beta^{n}[K_{0n}(\alpha) + K_{0,n-1}(\alpha)] \\
A_{M+1,n} &= -A_{00}\beta^{n}[K_{Mn}(\alpha) + K_{M,n-1}(\alpha)] \\
A_{mn} &= A_{00}\beta^{n}[K_{mn}(\alpha) + K_{m,n-1}(\alpha) - K_{m-1,n}(\alpha) - K_{m-1,n-1}(\alpha)]
\end{aligned} \quad \text{(D.10)}$$

$1 \le m \le M$, $1 \le n \le N$

Source element and object point on opposite surfaces of the PCB

The relevant potential is ϕ_{0c}, given by equation 3.62. Writing this with finite upper limits of summation gives,

$$\phi_{0c} = \frac{1+\alpha}{4\pi\varepsilon_0\varepsilon_2}\sum_{m=0}^{M}\sum_{n=0}^{N}\beta^n K_{mn}(\alpha)\times\left[\frac{1+\beta}{\sqrt{x^2+y^2+\{2md_1+(2n+1)c\}^2}} - \frac{1+\beta}{\sqrt{x^2+y^2+\{2(m+1)d_1+(2n+1)c\}^2}}\right] \tag{D.11}$$

This can be written in a very similar form to equation D.7 as,

$$\phi_{0c} = \sum_{m=0}^{M+1}\sum_{n=0}^{N}\frac{A_{mn}}{\sqrt{x^2+y^2+\{2md_1+(2n+1)c\}^2}} \tag{D.12}$$

The constants A_{mn} for this case are given by,

$$\begin{aligned} A_{0n} &= \frac{(1+\alpha)(1+\beta)}{4\pi\varepsilon_0\varepsilon_2}\beta^n K_{0n}(\alpha) \\ A_{mn} &= A_{00}\,\beta^n[K_{mn}(\alpha)-K_{m-1,n}(\alpha)] \\ A_{M+1,n} &= -A_{00}\,\beta^n K_{Mn}(\alpha) \end{aligned} \tag{D.13}$$

$$1 \le m \le M \;,\; 0 \le n \le N$$

In the FACET subroutine which evaluates these potentials, the second sum in equation D.12 is extended to $N+1$, and the constants $A_{m,N+1}$, with $0 \le m \le M+1$, are set equal to zero. The potential can then be written in exactly the same form as equation D.7, making the subroutine clearer and simpler to implement.

Appendix E

Formula used for the Self Inductance of a Via

The logarithm term in the integration required when equation 4.13 is expanded using equation 4.14 is

$$I = \frac{\mu_0 a}{2\pi^2} \int_0^{\pi} \ln\left[\frac{2a + \sqrt{R^2 + 4a^2}}{-2a + \sqrt{R^2 + 4a^2}} \right] d\theta \qquad \text{(E.1)}$$

Performing the substitution $\alpha = \theta/2$, so that $R = 2b \sin\alpha$, this becomes

$$I = \frac{\mu_0 a}{\pi^2} \int_0^{\frac{\pi}{2}} \ln\left[\frac{a + \sqrt{b^2 \sin^2\alpha + a^2}}{-a + \sqrt{b^2 \sin^2\alpha + a^2}} \right] d\alpha \qquad \text{(E.2)}$$

This can be expressed as the difference of two terms given by

$$\begin{aligned} I_1 &= \frac{\mu_0 a}{\pi^2} \int_0^{\frac{\pi}{2}} \ln\left[\frac{a}{b \sin\alpha} + \sqrt{1 + \frac{a^2}{b^2 \sin^2\alpha}} \right] d\alpha \\ I_2 &= \frac{\mu_0 a}{\pi^2} \int_0^{\frac{\pi}{2}} \ln\left[\frac{-a}{b \sin\alpha} + \sqrt{1 + \frac{a^2}{b^2 \sin^2\alpha}} \right] d\alpha \end{aligned} \qquad \text{(E.3)}$$

Both of these can be expressed in terms of an inverse hyperbolic sine. Since this is an odd function, it follows that

$$\begin{aligned} I_2 &= \frac{\mu_0 a}{\pi^2}\int_0^{\frac{\pi}{2}} \sinh^{-1}\left(\frac{-a}{b\sin\alpha}\right) d\alpha \\ &= -\frac{\mu_0 a}{\pi^2}\int_0^{\frac{\pi}{2}} \sinh^{-1}\left(\frac{a}{b\sin\alpha}\right) d\alpha \\ &= -I_1 \end{aligned} \tag{E.4}$$

and hence

$$I = 2I_1 = -2I_2 \tag{E.5}$$

Formula 8.261 in Gradshteyn and Ryzhik [1980] shows that

$$\int_0^{\frac{\pi}{2}} \ln(2\sin\alpha)\, d\alpha = 0 \tag{E.6}$$

This enables I_1 to be written as

$$\begin{aligned} I_1 &= \frac{\mu_0 a}{\pi^2}\int_0^{\frac{\pi}{2}} \ln\left[\frac{2a}{b} + \sqrt{\frac{4a^2}{b^2} + 4\sin^2\alpha}\right] d\alpha - \int_0^{\frac{\pi}{2}} \ln(2\sin\alpha)\, d\alpha \\ &= \frac{\mu_0 a}{\pi^2}\int_0^{\frac{\pi}{2}} \ln\left[\frac{2a}{b} + \sqrt{\frac{4a^2}{b^2} + 4\sin^2\alpha}\right] d\alpha \end{aligned} \tag{E.7}$$

which is the form needed for use in equation 4.15.

Appendix F

Subroutine Naming Conventions

This appendix describes the consistent naming convention which has been adopted for the subroutines that compute potentials and inductance. There are three sets of subroutines, which compute respectively scalar potentials, vector potentials and inductance. These are detailed in turn.

Scalar Potential Subroutines

The subroutine name is of the form Sesnab. The various parts of the name have the meanings:

- S indicates that the subroutine computes the Scalar potential due to an element
- e indicates the type of element. It can take the values
  - P indicating a polygon element
  - T indicating a track element
- s indicates the shape of the element. It can take the values
  - R indicating a rectangular element
  - T indicating a triangular element (only valid as a polygon element)
- n indicates the number of basis functions included It can take the values 1 or 6.
- a indicates the location of the ground plane. It can take the values
  - C indicates that a ground plane is present coincident with the bottom surface of the PCB ($d_1 = 0$ in Figure 7)
  - G indicates that a ground plane is present parallel to and below the bottom surface of the PCB ($d_1 \neq 0$ in Figure 7)
  - N indicates that there is no ground plane present
- b indicates the location of the source element and object point. It can take the values
  - S indicating both on the top surface of the PCB
  - D indicating both on either surface of the PCB
  - M indicating both either on the surface of or inside the PCB

- B indicating the source element on or inside the PCB, the object point above the PCB

Not all combinations of the above are used. With a coincident ground plane, the subroutines for b=D are identical to those with b=S, and so are not needed. In all other cases, those with b=S are a subset of those with b=D (but no simpler), and so are not needed.

Vector Potential Subroutines

The subroutine name is of the form Vesla. The various parts of the name have the meanings:

- V indicates that the subroutine computes the Vector potential due to an element
- e indicates the type of element. It can take the values
  - P indicating a polygon element
  - T indicating a track element
- s indicates the shape of the element. It can take the values
  - R indicating a rectangular element
  - T indicating a triangular element (only valid as a polygon element)
- 1 indicates that there is only one basis function
- a indicates the location of the ground plane. It can take the values
  - G indicates that a ground plane is present parallel to the bottom surface of the PCB
  - N indicates that there is no ground plane present

Inductance Subroutines

There are two inductance subroutines:

- SIPR, standing for Self Inductance of a Polygon Rectangle
- MIPRPR, standing for Mutual Inductance between Polygon Rectangle and Polygon Rectangle

Appendix G
Integrals for Polygon Elements

Integral for Potential due to a Rectangle

Here the integration required in Chapter 5 is performed. The integral is denoted by I, where

$$I(x_1, x_2, y_1, y_2, z) = \int_{y_1}^{y_2} \int_{x_1}^{x_2} \frac{dx\,dy}{\sqrt{x^2 + y^2 + z^2}} \tag{G.1}$$

Now,

$$\int \frac{dx}{\sqrt{x^2 + y^2 + z^2}} = \ln\left(x + \sqrt{x^2 + y^2 + z^2}\right) \tag{G.2}$$

Hence, setting

$$I_1(x, y_1, y_2, z) = \int_{y_1}^{y_2} \ln\left(x + \sqrt{x^2 + y^2 + z^2}\right) dy \tag{G.3}$$

enables I to be written in the form

$$I(x_1, x_2, y_1, y_2, z) = I_1(x_2, y_1, y_2, z) - I_1(x_1, y_1, y_2, z) \tag{G.4}$$

Now integrate by parts, using

$$\int u \frac{dv}{dy}\, dy = uv - \int v \frac{du}{dx} \tag{G.5}$$

and

$$\begin{aligned} u &= \ln\left(x+\sqrt{x^2+y^2+z^2}\right) \\ \frac{du}{dy} &= \frac{y}{\sqrt{x^2+y^2+z^2}\left(x+\sqrt{x^2+y^2+z^2}\right)} \end{aligned} \qquad \begin{aligned} \frac{dv}{dy} &= 1 \\ v &= y \end{aligned} \tag{G.6}$$

Combining equations G.5 and G.6 gives

$$I_1(x, y_1, y_2, z) = \left[y \ln\left(x+\sqrt{x^2+y^2+z^2}\right)\right]_{y_1}^{y_2} - I_2 \tag{G.7}$$

where

$$I_2 = \int_{y_1}^{y_2} \frac{y^2 dy}{\sqrt{x^2+y^2+z^2}\left(x+\sqrt{x^2+y^2+z^2}\right)} \tag{G.8}$$

Simplifying this with the substitution,

$$\begin{aligned} \xi &= x+\sqrt{x^2+y^2+z^2} \\ y &= \pm\sqrt{\xi^2-2x\xi-z^2} \\ d\xi &= \frac{y\,dy}{\sqrt{x^2+y^2+z^2}} \end{aligned} \tag{G.9}$$

results in

$$I_2 = \int_{\xi_1}^{\xi_2} \frac{\pm\sqrt{\xi^2-2x\xi-z^2}}{\xi}\, d\xi \tag{G.10}$$

where the positive sign is taken for $y \geq 0$ and the negative sign for $y < 0$. Equation G.10 can be integrated by parts. Setting,

$$u = \frac{\pm\sqrt{\xi^2 - 2x\xi - z^2}}{\xi} \qquad \frac{dv}{d\xi} = 1$$
$$\frac{du}{d\xi} = \pm\frac{x\xi + z^2}{\xi^2\sqrt{\xi^2 - 2x\xi - z^2}} \qquad v = \xi \tag{G.11}$$

results in

$$I_2 = \left[\pm\sqrt{\xi^2 - 2x\xi - z^2}\right]_{\xi_1}^{\xi_2} \pm \int_{\xi_1}^{\xi_2} \frac{(x\xi + z^2)\, d\xi}{\xi\sqrt{\xi^2 - 2x\xi - z^2}}$$
$$= [y]_{y_1}^{y_2} - I_3 - I_4 \tag{G.12}$$
$$= y_2 - y_1 - I_3 - I_4$$

The term $y_2 - y_1$ is the independent of x, and so will cancel out in equation G.4. The remaining two integrals will now be tackled in turn. First I_3, which is solved using equations G.9 and G.2,

$$I_3 = \int_{\xi_1}^{\xi_2} \frac{\pm x\, d\xi}{\sqrt{\xi^2 - 2x\xi - z^2}}$$
$$= \int_{y_1}^{y_2} \frac{x\, dy}{\sqrt{x^2 + y^2 + z^2}} \tag{G.13}$$
$$= \left[x \ln\left(y + \sqrt{x^2 + y^2 + z^2}\right)\right]_{y_1}^{y_2}$$

I_4 can be solved using formula 2.266 in Gradshteyn and Ryzhik [1980], and noting that $\arcsin x = -\arcsin(-x)$,

$$I_4 = \int_{\xi_1}^{\xi_2} \frac{\pm z^2 d\xi}{\xi\sqrt{\xi^2 - 2x\xi - z^2}}$$

$$= \pm |z| \left[\arcsin\left(\frac{-x\xi - z^2}{\xi\sqrt{x^2 + z^2}} \right) \right]_{\xi_1}^{\xi_2}$$

$$= \pm |z| \left[\arcsin\left(\frac{x^2+z^2+x\sqrt{x^2 + y^2 + z^2}}{\sqrt{x^2 + z^2}\left(x+\sqrt{x^2 + y^2 + z^2}\right)} \right) \right]_{y_1}^{y_2} \qquad \text{(G.14)}$$

This formula can be simplified somewhat. Consider

$$A = \arcsin\left(\frac{xy}{\sqrt{(x^2 + z^2)(y^2 + z^2)}} \right) + \arcsin\left(\frac{|z|}{\sqrt{y^2 + z^2}} \right) \qquad \text{(G.15)}$$

Formula 1.625.1 in Gradshteyn and Ryzhik can be written as

$$\arcsin\alpha + \arcsin\beta = \arcsin\left(\alpha\sqrt{1-\beta^2} + \beta\sqrt{1-\alpha^2}\right) \qquad \text{(G.16)}$$

provided $\alpha^2 + \beta^2 \le 1$. Setting,

$$\alpha = \frac{x|y|}{\sqrt{(x^2 + z^2)(y^2 + z^2)}} \qquad \sqrt{1-\alpha^2} = \frac{|z|\sqrt{x^2 + y^2 + z^2}}{\sqrt{(x^2 + z^2)(y^2 + z^2)}}$$

$$\beta = \frac{|z|}{\sqrt{y^2 + z^2}} \qquad \sqrt{1-\beta^2} = \frac{|y|}{\sqrt{y^2 + z^2}} \qquad \text{(G.17)}$$

Equation G.16 will always be valid, because

$$\alpha^2 + \beta^2 = \frac{x^2y^2 + y^2z^2 + z^4}{x^2y^2 + x^2z^2 + y^2z^2 + z^4} \le 1 \qquad \text{(G.18)}$$

Combining equations G.15, G.16 and G.17 gives

$$A = \arcsin\left(\frac{x^2+z^2+x\sqrt{x^2+y^2+z^2}}{\sqrt{x^2+z^2}\left(x+\sqrt{x^2+y^2+z^2}\right)} \right) \qquad \text{(G.19)}$$

Combining equations G.14, G.15 and G.19 gives a simpler form for I_4 , noting that $\arcsin|y| = \pm\arcsin y$

$$I_4 = -|z| \left[\arcsin\left(\frac{xy}{\sqrt{(x^2+z^2)(y^2+z^2)}} \right) \pm \arcsin\left(\frac{|z|}{\sqrt{y^2+z^2}} \right) \right]_{y_1}^{y_2} \qquad \text{(G.20)}$$

Note that the second term in the above expression is independent of x , and so will cancel out in equation G.4.

The required result can now be written in full,

$$
\begin{aligned}
I(x_1, x_2, y_1, y_2, z) \;=\; & y_2 \ln\left(\frac{x_2 + \sqrt{x_2^2 + y_2^2 + z^2}}{x_1 + \sqrt{x_1^2 + y_2^2 + z^2}} \right) \\
& - y_1 \ln\left(\frac{x_2 + \sqrt{x_2^2 + y_1^2 + z^2}}{x_1 + \sqrt{x_1^2 + y_1^2 + z^2}} \right) \\
& + x_2 \ln\left(\frac{y_2 + \sqrt{x_2^2 + y_2^2 + z^2}}{y_1 + \sqrt{x_2^2 + y_1^2 + z^2}} \right) \\
& - x_1 \ln\left(\frac{y_2 + \sqrt{x_1^2 + y_2^2 + z^2}}{y_1 + \sqrt{x_1^2 + y_1^2 + z^2}} \right) \\
& - |z| \arcsin\left(\frac{x_2 y_2}{\sqrt{(x_2^2 + z^2)(y_2^2 + z^2)}} \right) \\
& + |z| \arcsin\left(\frac{x_2 y_1}{\sqrt{(x_2^2 + z^2)(y_1^2 + z^2)}} \right) \\
& + |z| \arcsin\left(\frac{x_1 y_2}{\sqrt{(x_1^2 + z^2)(y_2^2 + z^2)}} \right) \\
& - |z| \arcsin\left(\frac{x_1 y_1}{\sqrt{(x_1^2 + z^2)(y_1^2 + z^2)}} \right)
\end{aligned}
\tag{G.21}
$$

Integral for Potential due to a Triangle

Here the integration required in Chapter 5 is performed. The integral is denoted by I', which is similar to I but with one of the limits to the inner integral a function of x. α is the gradient of the hypotenuse, given by

$$\alpha = \frac{y_2 - y_1}{x_2 - x_1} \tag{G.22}$$

With this definition, the integral I' is

$$
\begin{aligned}
I'(x_1, x_2, y_1, y_2, z) &= \int_{x_1}^{x_2} \int_{y_1}^{y_1 + \alpha(x - x_1)} \frac{dy\,dx}{\sqrt{x^2 + y^2 + z^2}} \\
&= \left[\ln\left(y + \sqrt{x^2 + y^2 + z^2}\right) \right]_{y_1}^{y_1 + \alpha(x - x_1)} \\
&= I_6(x_1, x_2, y_1, \alpha, z) - I_1(y, x_1, x_2, z)
\end{aligned}
\tag{G.23}
$$

I_1 was dealt with in the previous section. However, for this section the terms which were cancelled out in equations G.12 and G.20 have to be retained because of the variable integration limit in equation G.23. This results in the following expression for I_1 when x_1 and x_2 have the same sign,

$$
\begin{aligned}
I_1(y, x_1, x_2, z) &= x_2 \ln\left(y_1 + \sqrt{{x_2}^2 + {y_1}^2 + z^2}\right) \\
&\quad - x_1 \ln\left(y_1 + \sqrt{{x_1}^2 + {y_1}^2 + z^2}\right) \\
&\quad + y_1 \ln\left(\frac{x_2 + \sqrt{{x_2}^2 + {y_1}^2 + z^2}}{x_1 + \sqrt{{x_1}^2 + {y_1}^2 + z^2}} \right) - (x_2 - x_1) \\
&\quad - |z| \arcsin\left(\frac{x_2 y_1}{\sqrt{({x_2}^2 + z^2)({y_1}^2 + z^2)}} \right) \\
&\quad + |z| \arcsin\left(\frac{x_1 y_1}{\sqrt{({x_1}^2 + z^2)({y_1}^2 + z^2)}} \right) \\
&\quad \pm |z| \arcsin\left(\frac{|z|}{\sqrt{{x_2}^2 + z^2}} \right) \pm |z| \arcsin\left(\frac{|z|}{\sqrt{{x_1}^2 + z^2}} \right)
\end{aligned}
\tag{G.24}
$$

where the sign of the last two terms depends on the sign of x_1 and x_2. If these are of opposite sign, the integral must be split at $x = 0$, and the sum $I_1(y, x_1, 0, z) + I_1(y, 0, x_2, z)$ taken. The result of this is simply to add a term $\pm\pi$ to the above formula. To simplify the growing number of $\pm$ signs, set the following two constants

$$s_1 = \begin{cases} +1 & \text{if } x_1 \geq 0 \\ -1 & \text{if } x_1 < 0 \end{cases}$$
$$s_2 = \begin{cases} +1 & \text{if } x_2 \geq 0 \\ -1 & \text{if } x_2 < 0 \end{cases} \qquad \text{(G.25)}$$

Using these constants, and noting that $|z| \arcsin |z| = z \arcsin z$, equation G.24 can be written as

$$\begin{aligned} I_1(y, x_1, x_2, z) = {} & x_2 \ln\left(y_1 + \sqrt{x_2^2 + y_1^2 + z^2}\right) \\ & - x_1 \ln\left(y_1 + \sqrt{x_1^2 + y_1^2 + z^2}\right) \\ & + y_1 \ln\left(\frac{x_2 + \sqrt{x_2^2 + y_1^2 + z^2}}{x_1 + \sqrt{x_1^2 + y_1^2 + z^2}}\right) - (x_2 - x_1) \\ & - |z| \arcsin\left(\frac{x_2 y_1}{\sqrt{(x_2^2 + z^2)(y_1^2 + z^2)}}\right) \\ & + |z| \arcsin\left(\frac{x_1 y_1}{\sqrt{(x_1^2 + z^2)(y_1^2 + z^2)}}\right) \\ & - s_2 z \arcsin\left(\frac{z}{\sqrt{x_2^2 + z^2}}\right) + s_1 z \arcsin\left(\frac{z}{\sqrt{x_1^2 + z^2}}\right) \\ & + (s_2 - s_1)\frac{\pi}{2} \end{aligned} \qquad \text{(G.26)}$$

This is now correct for all values of x_1 and x_2. Note that if they have the same sign, the last term is zero.

Turning now to I_6, which is given by

$$I_6(x_1, x_2, y_1, \alpha, z) = \int_{x_1}^{x_2} \ln\left(y_1 + \alpha(x - x_1) + \sqrt{x^2 + (y_1 + \alpha(x - x_1))^2 + z^2}\right) dx \qquad \text{(G.27)}$$

This is somewhat more complicated. The notation is simplified slightly by setting

$$\beta = y_1 - \alpha x_1 \qquad \text{(G.28)}$$

which enables equation G.27 to be written as

$$I_6(x_1, x_2, y_1, \alpha, z) = \int_{x_1}^{x_2} \ln\left(\beta + \alpha x + \sqrt{x^2(1+\alpha^2) + 2\alpha\beta x + \beta^2 + z^2}\right) dx \qquad \text{(G.29)}$$

This can now be integrated by parts, with

$$\begin{aligned} \frac{dv}{dx} &= 1 \qquad v = x \\ u &= \ln\left(\beta + \alpha x + \sqrt{x^2(1+\alpha^2) + 2\alpha\beta x + \beta^2 + z^2}\right) \\ \frac{du}{dx} &= \frac{\alpha\beta + (1+\alpha^2)x + \alpha\sqrt{x^2(1+\alpha^2) + 2\alpha\beta x + \beta^2 + z^2}}{\sqrt{x^2(1+\alpha^2) + 2\alpha\beta x + \beta^2 + z^2}\left(\beta + \alpha x + \sqrt{x^2(1+\alpha^2) + 2\alpha\beta x + \beta^2 + z^2}\right)} \end{aligned} \qquad \text{(G.30)}$$

Applying this to I_6 gives

$$I_6 = \left[x \ln\left(\beta + \alpha x + \sqrt{x^2(1+\alpha^2) + 2\alpha\beta x + \beta^2 + z^2}\right)\right]_{x_1}^{x_2} - I_7 \qquad \text{(G.31)}$$

Expanding some of the terms containing α and β, using equations G.22 and G.28, gives

$$\begin{aligned} \beta + \alpha x_2 &= y_2 \\ \beta + \alpha x_1 &= y_1 \\ \beta^2 + 2\alpha\beta x_2 + (1+\alpha^2){x_2}^2 &= {x_2}^2 + {y_2}^2 \\ \beta^2 + 2\alpha\beta x_1 + (1+\alpha^2){x_1}^2 &= {x_1}^2 + {y_1}^2 \end{aligned} \qquad \text{(G.32)}$$

Use of these formulae simplifies equation G.30 to,

$$I_6 = x_2 \ln\left(y_2 + \sqrt{{x_2}^2 + {y_2}^2 + z^2}\right) - x_1 \ln\left(y_1 + \sqrt{{x_1}^2 + {y_1}^2 + z^2}\right) - I_7 \qquad \text{(G.33)}$$

Consider now I_7, given by

$$
\begin{aligned}
I_7 &= \int_{x_1}^{x_2} \frac{x\left(\alpha\beta + (1+\alpha^2)x + \alpha\sqrt{x^2(1+\alpha^2) + 2\alpha\beta x + \beta^2 + z^2}\right) dx}{\sqrt{x^2(1+\alpha^2) + 2\alpha\beta x + \beta^2 + z^2}\left(\beta + \alpha x + \sqrt{x^2(1+\alpha^2) + 2\alpha\beta x + \beta^2 + z^2}\right)} \\
&= \int_{x_1}^{x_2} \frac{x^2\sqrt{x^2(1+\alpha^2) + 2\alpha\beta x + \beta^2 + z^2} - (\beta x^2 - \alpha z^2 x)}{(x^2+z^2)\sqrt{x^2(1+\alpha^2) + 2\alpha\beta x + \beta^2 + z^2}} dx \\
&= I_8 - I_9
\end{aligned}
\tag{G.34}
$$

I_8 is straightforward,

$$
\begin{aligned}
I_8 &= \int_{x_1}^{x_2} \frac{x^2\,dx}{x^2+z^2} \\
&= \int_{x_1}^{x_2} \left(1 - \frac{z^2}{x^2+z^2}\right) dx \\
&= \left[x - |z| \arctan\left(\frac{x}{|z|}\right)\right]_{x_1}^{x_2}
\end{aligned}
\tag{G.35}
$$

I_9 is first split into two parts,

$$\begin{aligned} I_9 &= \int_{x_1}^{x_2} \frac{(\beta x^2 - \alpha z^2 x)\,dx}{(x^2+z^2)\sqrt{x^2(1+\alpha^2)+2\alpha\beta x+\beta^2+z^2}} \\ &= \beta \int_{x_1}^{x_2} \frac{dx}{\sqrt{x^2(1+\alpha^2)+2\alpha\beta x+\beta^2+z^2}} \\ &\quad - z^2 \int_{x_1}^{x_2} \frac{(\beta+\alpha x)\,dx}{(x^2+z^2)\sqrt{x^2(1+\alpha^2)+2\alpha\beta x+\beta^2+z^2}} \\ &= I_{10} - I_{11} \end{aligned} \tag{G.36}$$

Use equations G.22 and G.28 to simplify two more terms

$$\begin{aligned} (1+\alpha^2)x_2 + \alpha\beta &= x_2 + \alpha y_2 \\ (1+\alpha^2)x_1 + \alpha\beta &= x_1 + \alpha y_1 \end{aligned} \tag{G.37}$$

Using Gradshteyn and Ryzhik formula 2.261 together with the above formulae gives the following result for I_{10},

$$\begin{aligned} I_{10} &= \frac{\beta}{\sqrt{1+\alpha^2}} \left[\ln\left(2\sqrt{(1+\alpha^2)(\beta^2+z^2+2\alpha\beta x+(1+\alpha^2)x^2)} + (1+\alpha^2)x + \alpha\beta \right) \right]_{x_1}^{x_2} \\ &= \frac{y_1 - \alpha x_1}{\sqrt{1+\alpha^2}} \ln\left(\frac{x_2 + \alpha y_2 + \sqrt{(1+\alpha^2)({x_2}^2+{y_2}^2+z^2)}}{x_1 + \alpha y_1 + \sqrt{(1+\alpha^2)({x_1}^2+{y_1}^2+z^2)}} \right) \end{aligned} \tag{G.38}$$

I_{11} is performed with the aid of the following substitution,

$$\begin{aligned} \xi &= \frac{\alpha(\alpha z^2 - \beta x)}{\beta(\alpha x + \beta)} \\ x &= \frac{\alpha^2 z^2 - \beta^2 \xi}{\alpha\beta(\xi + 1)} \\ dx &= -\frac{\alpha z^2 + \beta^2}{\alpha\beta(t+1)^2}\, dt \end{aligned} \tag{G.39}$$

Applying this substitution results in,

$$I_{11} = -\int_{\xi_1}^{\xi_2} \frac{\alpha^2\beta z^2\sqrt{\alpha^2 z^2 + \beta^2}\; d\xi}{(\alpha^2 z^2 + \beta^2\xi^2)\sqrt{\beta^2\xi^2 + \alpha^2(z^2 + \alpha^2 z^2 + \beta^2)}} \tag{G.40}$$

This can be solved using Gradshteyn and Ryzhik formula 2.284, giving

$$\begin{aligned} I_{11} &= \left[-|z| \arctan\left(\frac{\beta\xi\sqrt{\alpha^2 z^2 + \beta^2}}{|z|\sqrt{\beta^2\xi^2 + \alpha^2(z^2 + \alpha^2 z^2 + \beta^2)}} \right) \right]_{\xi_1}^{\xi_2} \\ &= \left[-z \arctan\left(\frac{\alpha z^2 - \beta x}{z\sqrt{(1+\alpha^2)x^2 + 2\alpha\beta x + z^2 + \beta^2}} \right) \right]_{x_1}^{x_2} \\ &= -z \arctan\left(\frac{\alpha(z^2 + x_1 x_2) - x_2 y_1}{z\sqrt{x_2^2 + y_2^2 + z^2}} \right) \\ &\quad + z \arctan\left(\frac{\alpha(z^2 + x_1^2) - x_1 y_1}{z\sqrt{x_1^2 + y_1^2 + z^2}} \right) \end{aligned} \tag{G.41}$$

where use has been made of the fact that $|z| \arctan |z| = z \arctan z$, and of equations G.28 and G.32.

Now equations G.23, G.26, G.33 - G.36, G.38 and G.41 can be combined to give the full result for I' as

$$
\begin{aligned}
I'(x_1, x_2, y_1, y_2, z) \;=\; & x_2 \ln\left(\frac{y_2 + \sqrt{x_2^2 + y_2^2 + z^2}}{y_1 + \sqrt{x_2^2 + y_1^2 + z^2}} \right) \\
& - y_1 \ln\left(\frac{x_2 + \sqrt{x_2^2 + y_1^2 + z^2}}{x_1 + \sqrt{x_1^2 + y_1^2 + z^2}} \right) \\
& + \frac{y_1 - \alpha x_1}{\sqrt{1+\alpha^2}} \ln\left(\frac{x_2 + \alpha y_2 + \sqrt{(1+\alpha^2)(x_2^2 + y_2^2 + z^2)}}{x_1 + \alpha y_1 + \sqrt{(1+\alpha^2)(x_1^2 + y_1^2 + z^2)}} \right) \\
& + z \arctan\left(\frac{x_2}{z} \right) - z \arctan\left(\frac{x_1}{z} \right) \\
& + z \arctan\left(\frac{\alpha(z^2 + x_1 x_2) - x_2 y_1}{z\sqrt{x_2^2 + y_2^2 + z^2}} \right) \\
& - z \arctan\left(\frac{\alpha(z^2 + x_1^2) - x_1 y_1}{z\sqrt{x_1^2 + y_1^2 + z^2}} \right) \\
& + |z| \arcsin\left(\frac{x_2 y_1}{\sqrt{(x_2^2 + z^2)(y_1^2 + z^2)}} \right) \\
& - |z| \arcsin\left(\frac{x_1 y_1}{\sqrt{(x_1^2 + z^2)(y_1^2 + z^2)}} \right) \\
& + s_2 z \arcsin\left(\frac{z}{\sqrt{x_2^2 + z^2}} \right) - s_1 z \arcsin\left(\frac{z}{\sqrt{x_1^2 + z^2}} \right) \\
& - (s_2 - s_1) \frac{\pi}{2}
\end{aligned}
\tag{G.42}
$$

Integrals for Inductance of Rectangles

Two further integrals need consideration to be able to compute the self inductance of a rectangle and the mutual inductance between rectangles. These are both further integrations of the terms derived in the first part of this appendix. The first of these is

$$I_{12} = \int_{x_3}^{x_4} \int_{y_3}^{y_4} y \ln\left(x + \sqrt{x^2 + y^2 + z^2}\right) dy\, dx \tag{G.43}$$

Beginning with the inner integral I_{13},

$$I_{13} = \int_{y_3}^{y_4} y \ln\left(x + \sqrt{x^2 + y^2 + z^2}\right) dy \tag{G.44}$$

Making the substitution,

$$\begin{aligned} \xi &= x + \sqrt{x^2 + y^2 + z^2} \\ y &= \pm\sqrt{\xi^2 - 2x\xi - z^2} \\ d\xi &= \frac{y\, dy}{\sqrt{x^2 + y^2 + z^2}} \end{aligned} \tag{G.45}$$

and noting that

$$\begin{aligned} \int \xi \ln \xi\, d\xi &= \frac{1}{2}\xi^2 \ln \xi - \frac{1}{4}\xi^2 \\ \int \ln \xi\, d\xi &= \xi \ln \xi - \xi \end{aligned} \tag{G.46}$$

I_{13} can now be integrated, giving

$$
\begin{aligned}
I_{13} &= \int_{\xi_3}^{\xi_4} (\xi - x) \ln \xi \, d\xi \\
&= \left[\left(\tfrac{1}{2}\xi^2 - x\xi \right) \ln \xi - \tfrac{1}{4}\xi^2 + x\xi \right]_{\xi_3}^{\xi_4} \\
&= \left[\tfrac{1}{2}(y^2+z^2) \ln\left(x + \sqrt{x^2 + y^2 + z^2} \right) + \tfrac{1}{2} x \sqrt{x^2 + y^2 + z^2} \right. \\
&\quad \left. + \tfrac{1}{2}x^2 - \tfrac{1}{4}(y^2+z^2) \right]_{y_3}^{y_4} \\
&= \tfrac{1}{2}({y_4}^2+z^2) \ln\left(x + \sqrt{x^2 + {y_4}^2 + z^2} \right) + \tfrac{1}{2} x \sqrt{x^2 + {y_4}^2 + z^2} - \tfrac{1}{4}{y_4}^2 \\
&\quad - \tfrac{1}{2}({y_3}^2+z^2) \ln\left(x + \sqrt{x^2 + {y_3}^2 + z^2} \right) - \tfrac{1}{2} x \sqrt{x^2 + {y_3}^2 + z^2} + \tfrac{1}{4}{y_3}^2
\end{aligned}
\qquad \text{(G.47)}
$$

To obtain the required answer, I_{12}, the components of this result need to be integrated with respect to x. These components will now be examined, taking the logarithmic term first.

$$
I_{14} = \tfrac{1}{2}(y^2+z^2) \int_{x_3}^{x_4} \ln\left(x + \sqrt{x^2 + y^2 + z^2} \right) dx \qquad \text{(G.48)}
$$

This can be integrated by parts. Setting,

$$
\begin{aligned}
u &= \ln\left(x + \sqrt{x^2 + y^2 + z^2} \right) & \frac{dv}{dx} &= 1 \\
\frac{du}{dx} &= \frac{1}{\sqrt{x^2 + y^2 + z^2}} & v &= x
\end{aligned}
\qquad \text{(G.49)}
$$

results in

$$
I_{14} = \tfrac{1}{2}(y^2+z^2) \left[x \ln\left(x + \sqrt{x^2 + y^2 + z^2} \right) - \sqrt{x^2 + y^2 + z^2} \right]_{x_4}^{x_3} \qquad \text{(G.50)}
$$

Next the square root term,

$$I_{15} = \frac{1}{2}\int_{x_3}^{x_4} x\sqrt{x^2 + y^2 + z^2}\,dx = \frac{1}{6}\left[(x^2 + y^2 + z^2)^{\frac{3}{2}}\right]_{x_4}^{x_3} \qquad \text{(G.51)}$$

and finally the constant term,

$$I_{16} = -\frac{1}{4}\int_{x_3}^{x_4} y^2\,dx = -\frac{1}{4}y^2(x_4 - x_3) \qquad \text{(G.52)}$$

Equations G.43, G.47 and G.50 - G.52 can now be combined to give I_{12} as

$$\begin{aligned}
I_{12} = {} & \frac{1}{2}x_4(y_4^2+z^2)\ln\left(x_4+\sqrt{x_4^2 + y_4^2 + z^2}\right) \\
& - \frac{1}{2}x_3(y_4^2+z^2)\ln\left(x_3+\sqrt{x_3^2 + y_4^2 + z^2}\right) \\
& - \frac{1}{2}x_4(y_3^2+z^2)\ln\left(x_4+\sqrt{x_4^2 + y_3^2 + z^2}\right) \\
& + \frac{1}{2}x_3(y_3^2+z^2)\ln\left(x_3+\sqrt{x_3^2 + y_3^2 + z^2}\right) \\
& + \frac{1}{6}(x_4^2-2y_4^2-2z^2)\sqrt{x_4^2 + y_4^2 + z^2} \\
& - \frac{1}{6}(x_3^2-2y_4^2-2z^2)\sqrt{x_3^2 + y_4^2 + z^2} \\
& - \frac{1}{6}(x_4^2-2y_3^2-2z^2)\sqrt{x_4^2 + y_3^2 + z^2} \\
& + \frac{1}{6}(x_3^2-2y_3^2-2z^2)\sqrt{x_3^2 + y_3^2 + z^2} \\
& - \frac{1}{4}x_4y_4^2 + \frac{1}{4}x_3y_4^2 + \frac{1}{4}x_4y_3^2 - \frac{1}{4}x_3y_3^2
\end{aligned} \qquad \text{(G.53)}$$

The second integral required is

$$I_{17} = \int_{x_3}^{x_4}\int_{y_3}^{y_4} \arcsin\left(\frac{xy}{\sqrt{(x^2 + z^2)(y^2 + z^2)}}\right)dy\,dx \qquad \text{(G.54)}$$

Tackle this by considering the following problem,

$$
\begin{aligned}
D &= \frac{\partial^2}{\partial x \partial y}\left(xy \arcsin\left(\frac{xy}{\sqrt{(x^2+z^2)(y^2+z^2)}} \right) \right) \\
&= \frac{\partial}{\partial y}\left(y \arcsin\left(\frac{xy}{\sqrt{(x^2+z^2)(y^2+z^2)}} \right) + \frac{xy^2|z|}{(x^2+z^2)\sqrt{x^2+y^2+z^2}} \right) \\
&= \arcsin\left(\frac{xy}{\sqrt{(x^2+z^2)(y^2+z^2)}} \right) + \frac{xy|z|}{(y^2+z^2)\sqrt{x^2+y^2+z^2}} \\
&\quad + \frac{xy|z|(2x^2+y^2+2z^2)}{(x^2+z^2)\sqrt{(x^2+y^2+z^2)^3}}
\end{aligned}
\tag{G.55}
$$

If the two terms after the arcsin in equation G.55 can be integrated, then the problem can be solved. Consider first

$$
\begin{aligned}
I_{18} &= \int\int \frac{y|z|}{y^2+z^2} \frac{x\,dx}{\sqrt{x^2+y^2+z^2}}\,dy \\
&= \int \frac{|z|y\sqrt{x^2+y^2+z^2}}{y^2+z^2}\,dy
\end{aligned}
\tag{G.56}
$$

This is simplified by the substitution

$$
\begin{aligned}
\xi^2 &= x^2+y^2+z^2 \\
\xi\,d\xi &= y\,dy
\end{aligned}
\tag{G.57}
$$

which enables I_{18} to be written as

$$
\begin{aligned}
I_{18} &= |z| \int \frac{\xi^2}{\xi^2 - x^2}\, d\xi \\
&= |z| \int \left(1 + \frac{x}{2}\left(\frac{1}{\xi - x} - \frac{1}{\xi + x}\right)\right) d\xi \\
&= |z|\xi + \frac{|z|x}{2} \ln\left(\frac{\xi - x}{\xi + x}\right) \\
&= |z|\sqrt{x^2 + y^2 + z^2} + \frac{|z|x}{2} \ln\left(\frac{\sqrt{x^2 + y^2 + z^2} - x}{\sqrt{x^2 + y^2 + z^2} + x}\right)
\end{aligned}
\tag{G.58}
$$

The second term to be integrated from equation G.55 is

$$
\begin{aligned}
I_{19} &= \int\int \frac{|z|x}{x^2 + z^2}\, y\, \frac{(2x^2 + y^2 + 2z^2)}{\sqrt{(x^2 + y^2 + z^2)^3}}\, dy\, dx \\
&= \int \frac{|z|x}{x^2 + z^2}\, \frac{y^2}{\sqrt{x^2 + y^2 + z^2}}\, dx \\
&= \frac{|z|y}{2} \ln\left(\frac{\sqrt{x^2 + y^2 + z^2} - y}{\sqrt{x^2 + y^2 + z^2} + y}\right)
\end{aligned}
\tag{G.59}
$$

by the same methods used for I_{18}.

I_{17} can now be evaluated, using equations G.55, G.58 and G.59. This results in

$$
\begin{aligned}
I_{17} \;=\; & x_4 y_4 \arcsin\left(\frac{x_4 y_4}{\sqrt{(x_4^{\,2} + z^2)(y_4^{\,2} + z^2)}} \right) \\
& - x_3 y_4 \arcsin\left(\frac{x_3 y_4}{\sqrt{(x_3^{\,2} + z^2)(y_4^{\,2} + z^2)}} \right) \\
& - x_4 y_3 \arcsin\left(\frac{x_4 y_3}{\sqrt{(x_4^{\,2} + z^2)(y_3^{\,2} + z^2)}} \right) \\
& + x_3 y_3 \arcsin\left(\frac{x_3 y_3}{\sqrt{(x_3^{\,2} + z^2)(y_3^{\,2} + z^2)}} \right) \\
& - |z| \sqrt{x_4^{\,2} + y_4^{\,2} + z^2} \;+\; |z| \sqrt{x_3^{\,2} + y_4^{\,2} + z^2} \\
& + |z| \sqrt{x_4^{\,2} + y_3^{\,2} + z^2} \;-\; |z| \sqrt{x_3^{\,2} + y_3^{\,2} + z^2} \\
& - \frac{1}{2} x_4 |z| \ln\left(\frac{\sqrt{x_4^{\,2} + y_4^{\,2} + z^2} - x_4}{\sqrt{x_4^{\,2} + y_4^{\,2} + z^2} + x_4} \right) \\
& + \frac{1}{2} x_3 |z| \ln\left(\frac{\sqrt{x_3^{\,2} + y_4^{\,2} + z^2} - x_3}{\sqrt{x_3^{\,2} + y_4^{\,2} + z^2} + x_3} \right) \\
& + \frac{1}{2} x_4 |z| \ln\left(\frac{\sqrt{x_4^{\,2} + y_3^{\,2} + z^2} - x_4}{\sqrt{x_4^{\,2} + y_3^{\,2} + z^2} + x_4} \right) \\
& - \frac{1}{2} x_3 |z| \ln\left(\frac{\sqrt{x_3^{\,2} + y_3^{\,2} + z^2} - x_3}{\sqrt{x_3^{\,2} + y_3^{\,2} + z^2} + x_3} \right) \\
& - \frac{1}{2} y_4 |z| \ln\left(\frac{\sqrt{x_4^{\,2} + y_4^{\,2} + z^2} - y_4}{\sqrt{x_4^{\,2} + y_4^{\,2} + z^2} + y_4} \right) \\
& + \frac{1}{2} y_4 |z| \ln\left(\frac{\sqrt{x_3^{\,2} + y_4^{\,2} + z^2} - y_4}{\sqrt{x_3^{\,2} + y_4^{\,2} + z^2} + y_4} \right) \\
& + \frac{1}{2} y_3 |z| \ln\left(\frac{\sqrt{x_4^{\,2} + y_3^{\,2} + z^2} - y_3}{\sqrt{x_4^{\,2} + y_3^{\,2} + z^2} + y_3} \right) \\
& - \frac{1}{2} y_3 |z| \ln\left(\frac{\sqrt{x_3^{\,2} + y_3^{\,2} + z^2} - y_3}{\sqrt{x_3^{\,2} + y_3^{\,2} + z^2} + y_3} \right)
\end{aligned}
\tag{G.60}
$$

Formulae for the Self Inductance of a Rectangle

In order to compute the self inductance of a rectangle, equations G.21, G.53 and G.60 need to be combined. The rectangle has a length (x dimension) of $2a$ and a width (y dimension) of $2b$. With the centre of the rectangle being taken as the co-ordinate origin, the x component of the vector potential, A_x, at the point (x,y) in the rectangle is given by

$$A_x = \frac{\mu_0}{8\pi b} I(-a-x, a-x, -b-y, b-y, 0) \tag{G.61}$$

where I is given by equation G.21, with $z=0$ as the potential is required on the rectangle itself. The self inductance of the rectangle is then

$$L = \frac{1}{2b}\int_{-a}^{a}\int_{-b}^{b} A_x \, dy \, dx \tag{G.62}$$

For $I(x_1, x_2, y_1, y_2, 0)$ in the above integration, the values of x_1 etc. are

$$\begin{aligned} -2a \le x_1 \le 0 \qquad & 0 \le x_2 \le 2a \\ -2b \le y_1 \le 0 \qquad & 0 \le y_2 \le 2b \end{aligned} \tag{G.63}$$

I contains eight logarithm terms, all of the form

$$f(x,y,z) = y \ln\left(x + \sqrt{x^2 + y^2 + z^2}\right) \tag{G.64}$$

In terms of this function,

$$\begin{aligned} \int_{-a}^{a}\int_{-b}^{b} I \, dy \, dx = & \int_{0}^{2a}\int_{0}^{2b} f(x,y,0)\, dy\, dx - \int_{-2a}^{0}\int_{0}^{2b} f(x,y,0)\, dy\, dx \\ & - \int_{0}^{2a}\int_{-2b}^{0} f(x,y,0)\, dy\, dx + \int_{-2a}^{0}\int_{-2b}^{0} f(x,y,0)\, dy\, dx \\ & + \int_{0}^{2b}\int_{0}^{2a} f(x,y,0)\, dy\, dx - \int_{-2b}^{0}\int_{0}^{2a} f(x,y,0)\, dy\, dx \\ & - \int_{0}^{2b}\int_{-2a}^{0} f(x,y,0)\, dy\, dx + \int_{-2b}^{0}\int_{-2a}^{0} f(x,y,0)\, dy\, dx \end{aligned} \tag{G.65}$$

Each of these integrals is given by equation G.53, which is simplified by having two of the limits and z equal to zero. The first four integrals are therefore,

$$\int_0^{2a}\int_0^{2b} f(x,y,0)\,dy\,dx = 4ab^2\ln\left(2a+2\sqrt{a^2+b^2}\right) + \frac{4}{3}(a^2-2b^2)\sqrt{a^2+b^2} + \frac{8}{3}b^3 - \frac{4}{3}a^3 - 2ab^2 \tag{G.66}$$

$$-\int_{-2a}^{0}\int_0^{2b} f(x,y,0)\,dy\,dx = -4ab^2\ln\left(-2a+2\sqrt{a^2+b^2}\right) + \frac{8}{3}b^3 + \frac{4}{3}(a^2-2b^2)\sqrt{a^2+b^2} - \frac{4}{3}a^3 + 2ab^2 \tag{G.67}$$

$$-\int_0^{2a}\int_{-2b}^{0} f(x,y,0)\,dy\,dx = 4ab^2\ln\left(2a+2\sqrt{a^2+b^2}\right) - \frac{4}{3}a^3 + \frac{4}{3}(a^2-2b^2)\sqrt{a^2+b^2} + \frac{8}{3}b^3 - 2ab^2 \tag{G.68}$$

$$\int_{-2a}^{0}\int_{-2b}^{0} f(x,y,0)\,dy\,dx = -4ab^2\ln\left(-2a+2\sqrt{a^2+b^2}\right) - \frac{4}{3}a^3 + \frac{8}{3}b^3 + \frac{4}{3}(a^2-2b^2)\sqrt{a^2+b^2} + 2ab^2 \tag{G.69}$$

Noting that

$$\begin{aligned}\ln\left(-2a+2\sqrt{a^2+b^2}\right) &= \ln\left(-2a+2\sqrt{a^2+b^2}\right) + \ln\left(2a+2\sqrt{a^2+b^2}\right) \\ &\quad - \ln\left(2a+2\sqrt{a^2+b^2}\right) \\ &= \ln 4b^2 - \ln\left(2a+2\sqrt{a^2+b^2}\right) \\ &= 2\ln 2b - \ln\left(2a+2\sqrt{a^2+b^2}\right)\end{aligned} \tag{G.70}$$

the sum of the first four integrals in equation G.65, S, is

$$\begin{aligned}S &= 16ab^2\ln\left(2a+2\sqrt{a^2+b^2}\right) - 16ab^2\ln 2b + \frac{16}{3}(a^2-2b^2)\sqrt{a^2+b^2} \\ &\quad - \frac{16}{3}a^3 + \frac{32}{3}b^3 \\ &= 16ab^2\ln\left(\frac{a+\sqrt{a^2+b^2}}{b}\right) + \frac{16}{3}(a^2-2b^2)\sqrt{a^2+b^2} - \frac{16}{3}a^3 + \frac{32}{3}b^3\end{aligned} \tag{G.71}$$

The last four integrals in equation G.65 are the same as the first four with a and b interchanged. From equations G.61 and G.62, the self inductance of a rectangle is therefore,

$$L = \frac{\mu_0}{\pi b^2}\left(ab^2 \ln\left(\frac{a+\sqrt{a^2+b^2}}{b} \right) - \frac{1}{3}(a^2+b^2)\sqrt{a^2+b^2} + a^2 b \ln\left(\frac{b+\sqrt{a^2+b^2}}{a} \right) + \frac{1}{3}(a^3+b^3) \right) \tag{G.72}$$

If a ground plane is present, the mutual inductance between the rectangle and its image must be subtracted from its self inductance. This is more complicated as z is no longer zero as in equation G.61 - for the simplest case of a ground plane on the back of a PCB with thickness c, then $z=2c$. This case will now be examined. The mutual inductance between source and image rectangle is

$$L_{im} = \frac{\mu_0}{16\pi b^2} \int_{-a}^{a} \int_{-b}^{b} I(-a-x, a-x, -b-y, b-y, 2c)\, dy\, dx \tag{G.73}$$

I still contains eight logarithm terms, in almost the same form as equation G.65. In addition, there are now four arcsin terms to be considered. Setting

$$g(x,y,z) = |z| \arcsin\left(\frac{xy}{\sqrt{(x^2+z^2)(y^2+z^2)}} \right) \tag{G.74}$$

enables the integral of I to be written as

$$\begin{aligned} \int_{-a}^{a}\int_{-b}^{b} I\, dy\, dx = & \int_{0}^{2a}\int_{0}^{2b} f(x,y,2c)\, dy\, dx - \int_{-2a}^{0}\int_{0}^{2b} f(x,y,2c)\, dy\, dx \\ & - \int_{0}^{2a}\int_{-2b}^{0} f(x,y,2c)\, dy\, dx + \int_{-2a}^{0}\int_{-2b}^{0} f(x,y,2c)\, dy\, dx \\ & + \int_{0}^{2b}\int_{0}^{2a} f(x,y,2c)\, dy\, dx - \int_{-2b}^{0}\int_{0}^{2a} f(x,y,2c)\, dy\, dx \\ & - \int_{0}^{2b}\int_{-2a}^{0} f(x,y,2c)\, dy\, dx + \int_{-2b}^{0}\int_{-2a}^{0} f(x,y,2c)\, dy\, dx \\ & - \int_{0}^{2a}\int_{0}^{2b} g(x,y,2c)\, dy\, dx + \int_{-2a}^{0}\int_{0}^{2b} g(x,y,2c)\, dy\, dx \\ & + \int_{0}^{2a}\int_{-2b}^{0} g(x,y,2c)\, dy\, dx - \int_{-2a}^{0}\int_{-2b}^{0} g(x,y,2c)\, dy\, dx \end{aligned} \tag{G.75}$$

The first four of these integrals are,

$$\int_0^{2a}\int_0^{2b} f(x,y,2c)\,dy\,dx = 4a\Big((b^2+c^2)\ln\Big(2a+2\sqrt{a^2+b^2+c^2}\Big) - c^2\ln\Big(2a+2\sqrt{a^2+c^2}\Big) \Big) + \frac{4}{3}\Big((a^2-2b^2-2c^2)\sqrt{a^2+b^2+c^2} + 2(b^2+c^2)\sqrt{b^2+c^2} - (a^2-2c^2)\sqrt{a^2+c^2} - 2c^3 \Big) - 2ab^2 \tag{G.76}$$

$$-\int_{-2a}^{0}\int_0^{2b} f(x,y,2c)\,dy\,dx = 4a\Big(-(b^2+c^2)\ln\Big(-2a+2\sqrt{a^2+b^2+c^2}\Big) + c^2\ln\Big(-2a+2\sqrt{a^2+c^2}\Big) \Big) + \frac{4}{3}\Big(2(b^2+c^2)\sqrt{b^2+c^2} + (a^2-2b^2-2c^2)\sqrt{a^2+b^2+c^2} - 2c^3 - (a^2-2c^2)\sqrt{a^2+c^2} \Big) + 2ab^2 \tag{G.77}$$

$$-\int_0^{2a}\int_{-2b}^{0} f(x,y,2c)\,dy\,dx = 4a\Big(-c^2\ln\Big(2a+2\sqrt{a^2+c^2}\Big) + (b^2+c^2)\ln\Big(2a+2\sqrt{a^2+b^2+c^2}\Big) \Big) + \frac{4}{3}\Big(-(a^2-2c^2)\sqrt{a^2+c^2} - 2c^3 + (a^2-2b^2-2c^2)\sqrt{a^2+b^2+c^2} + 2(b^2+c^2)\sqrt{b^2+c^2} \Big) - 2ab^2 \tag{G.78}$$

$$\int_{-2a}^{0}\int_{-2b}^{0} f(x,y,2c)\,dy\,dx = 4a\Big(c^2 \ln\big(-2a+2\sqrt{a^2+c^2}\big) - (b^2+c^2)\ln\big(-2a+2\sqrt{a^2+b^2+c^2}\big)\Big) + \frac{4}{3}\Big(-2c^3 - (a^2-2c^2)\sqrt{a^2+c^2} + 2(b^2+c^2)\sqrt{b^2+c^2} + (a^2-2b^2-2c^2)\sqrt{a^2+b^2+c^2}\Big) + 2ab^2 \tag{G.79}$$

In the same way as in equation G.70,

$$\ln\big(-2a+2\sqrt{a^2+b^2+c^2}\big) = 2\ln 2\sqrt{b^2+c^2} - \ln\big(2a+2\sqrt{a^2+b^2+c^2}\big)$$
$$\ln\big(-2a+2\sqrt{a^2+c^2}\big) = 2\ln 2c - \ln\big(2a+2\sqrt{a^2+c^2}\big) \tag{G.80}$$

The sum of the first four integrals in equation G.75, S', reduces to

$$S' = 16a(b^2+c^2)\ln\left(\frac{a+\sqrt{a^2+b^2+c^2}}{\sqrt{b^2+c^2}}\right) - 16ac^2\ln\left(\frac{a+\sqrt{a^2+c^2}}{c}\right) + \frac{16}{3}(a^2-2b^2-2c^2)\sqrt{a^2+b^2+c^2} - \frac{32}{3}c^3 + \frac{32}{3}(b^2+c^2)\sqrt{b^2+c^2} - \frac{16}{3}(a^2-2c^2)\sqrt{a^2+c^2} \tag{G.81}$$

As before, the last four integrals in equation G.74 are the same as the first four with a and b interchanged. Consider now the four arcsin integrals in equation G.75. Each of these is given by I_{17} in equation G.60, simplified by having two of the limits equal to zero for each integral. These four integrals are

$$
\begin{aligned}
-\int_0^{2a}\int_0^{2b} g(x,y,2c)\,dy\,dx \;=\; & -8abc\,\arcsin\left(\frac{ab}{\sqrt{(a^2+c^2)(b^2+c^2)}}\right) \\
& + 8c^2\left(\sqrt{a^2+b^2+c^2} - \sqrt{b^2+c^2} - \sqrt{a^2+c^2} + c\right) \\
& + 4ac^2\left(\ln\left(\frac{\sqrt{a^2+b^2+c^2}-a}{\sqrt{a^2+b^2+c^2}+a}\right) - \ln\left(\frac{\sqrt{a^2+c^2}-a}{\sqrt{a^2+c^2}+a}\right)\right) \\
& + 4bc^2\left(\ln\left(\frac{\sqrt{a^2+b^2+c^2}-b}{\sqrt{a^2+b^2+c^2}+b}\right) - \ln\left(\frac{\sqrt{b^2+c^2}-b}{\sqrt{b^2+c^2}+b}\right)\right)
\end{aligned}
\tag{G.82}
$$

$$
\begin{aligned}
\int_{-2a}^{0}\int_0^{2b} g(x,y,2c)\,dy\,dx \;=\; & -8abc\,\arcsin\left(\frac{ab}{\sqrt{(a^2+c^2)(b^2+c^2)}}\right) \\
& + 8c^2\left(-\sqrt{b^2+c^2} + \sqrt{a^2+b^2+c^2} + c - \sqrt{a^2+c^2}\right) \\
& + 4ac^2\left(-\ln\left(\frac{\sqrt{a^2+b^2+c^2}+a}{\sqrt{a^2+b^2+c^2}-a}\right) + \ln\left(\frac{\sqrt{a^2+c^2}+a}{\sqrt{a^2+c^2}-a}\right)\right) \\
& + 4bc^2\left(-\ln\left(\frac{\sqrt{b^2+c^2}-b}{\sqrt{b^2+c^2}+b}\right) + \ln\left(\frac{\sqrt{a^2+b^2+c^2}-b}{\sqrt{a^2+b^2+c^2}+b}\right)\right)
\end{aligned}
\tag{G.83}
$$

$$
\begin{aligned}
\int_0^{2a}\int_{-2b}^{0} g(x,y,2c)\,dy\,dx \;=\; & -8abc\,\arcsin\left(\frac{ab}{\sqrt{(a^2+c^2)(b^2+c^2)}}\right) \\
& + 8c^2\left(-\sqrt{a^2+c^2} + c + \sqrt{a^2+b^2+c^2} - \sqrt{b^2+c^2}\right) \\
& + 4ac^2\left(-\ln\left(\frac{\sqrt{a^2+c^2}-a}{\sqrt{a^2+c^2}+a}\right) + \ln\left(\frac{\sqrt{a^2+b^2+c^2}-a}{\sqrt{a^2+b^2+c^2}+a}\right)\right) \\
& + 4bc^2\left(-\ln\left(\frac{\sqrt{a^2+b^2+c^2}+b}{\sqrt{a^2+b^2+c^2}-b}\right) + \ln\left(\frac{\sqrt{b^2+c^2}+b}{\sqrt{b^2+c^2}-b}\right)\right)
\end{aligned}
\tag{G.84}
$$

$$
\begin{aligned}
-\int_{-2a}^{0}\int_{-2b}^{0} g(x,y,2c)\,dy\,dx \;=\; & -8abc\arcsin\left(\frac{ab}{\sqrt{(a^2+c^2)(b^2+c^2)}}\right) \\
& + 8c^2\left(c - \sqrt{a^2+c^2} - \sqrt{b^2+c^2} + \sqrt{a^2+b^2+c^2}\right) \\
& + 4ac^2\left(\ln\left(\frac{\sqrt{a^2+c^2}+a}{\sqrt{a^2+c^2}-a}\right) - \ln\left(\frac{\sqrt{a^2+b^2+c^2}+a}{\sqrt{a^2+b^2+c^2}-a}\right)\right) \\
& + 4bc^2\left(\ln\left(\frac{\sqrt{a^2+c^2}+b}{\sqrt{a^2+c^2}-b}\right) - \ln\left(\frac{\sqrt{a^2+b^2+c^2}+b}{\sqrt{a^2+b^2+c^2}-b}\right)\right)
\end{aligned}
\qquad \text{(G.85)}
$$

L_{tm} can now be found by adding S' from equation G.81, S' with a and b reversed and the four integrals given in equations G.82 - G.85. After simplification of the logarithm terms, the result is given by equation G.86. Note that if $c = 0$, this reduces to the same formula as that for L in equation G.72. The self inductance of the rectangle, taking the ground plane into account, is simply $L - L_{tm}$.

$$
\begin{aligned}
L_{im} = \frac{\mu_0}{\pi b^2}\Bigg(& ab^2 \ln\left(\frac{a+\sqrt{a^2+b^2+c^2}}{\sqrt{b^2+c^2}}\right) \\
& + a^2 b \ln\left(\frac{b+\sqrt{a^2+b^2+c^2}}{\sqrt{a^2+c^2}}\right) \\
& + ac^2 \ln\left(\frac{\sqrt{b^2+c^2}\left(a+\sqrt{a^2+c^2}\right)}{c\left(a+\sqrt{a^2+b^2+c^2}\right)}\right) \\
& + bc^2 \ln\left(\frac{\sqrt{a^2+c^2}\left(b+\sqrt{b^2+c^2}\right)}{c\left(b+\sqrt{a^2+b^2+c^2}\right)}\right) \\
& + \frac{1}{3}(a^2-2c^2)\sqrt{a^2+c^2} + \frac{1}{3}(b^2-2c^2)\sqrt{b^2+c^2} \\
& - \frac{1}{3}(a^2+b^2-2c^2)\sqrt{a^2+b^2+c^2} + \frac{2}{3}c^3 \\
& - abc \arcsin\left(\frac{ab}{\sqrt{(a^2+c^2)(b^2+c^2)}}\right)\Bigg)
\end{aligned}
\qquad \text{(G.86)}
$$

Formula for the Mutual Inductance Between Two Parallel Rectangles

As for the self inductance, the mutual inductance between two parallel rectangles is computed by combining equations G.21, G.53 and G.60. The first rectangle has its centre at the origin of co-ordinates, with a length of $2a_1$ and a width of $2b_1$. The x component of the vector potential, A_x, at the point (x,y,z) is given in a similar way to equation G.61 as

$$A_x = \frac{\mu_0}{8\pi b_1} I(-a_1-x, a_1-x, -b_1-y, b_1-y, z) \qquad \text{(G.87)}$$

The second rectangle has its centre at (x_0, y_0, z), with a length of $2a_2$ and a width of $2b_2$. The mutual inductance between the two rectangles is then found as

$$M = \frac{1}{2b_2}\int_{x_0-a_2}^{x_0+a_2}\int_{y_0-b_2}^{y_0+b_2} A_x\,dy\,dx \tag{G.88}$$

For $I(x_1, x_2, y_1, y_2, z)$ in the above integration, the values of x_1 etc. are

$$\begin{aligned} -a_1-a_2-x_0 \le\ & x_1 \le -a_1+a_2-x_0 \qquad a_1-a_2-x_0 \le x_2 \le a_1+a_2-x_0 \\ -b_1-b_2-y_0 \le\ & y_1 \le -b_1+b_2-y_0 \qquad b_1-b_2-y_0 \le y_2 \le b_1+b_2-y_0 \end{aligned} \tag{G.89}$$

To clarify the notation, some constants are introduced for the limits above. These are

$$\begin{aligned} d_{x_1} &= -a_1-a_2-x_0 \qquad & d_{y_1} &= -b_1-b_2-y_0 \\ u_{x_1} &= -a_1+a_2-x_0 \qquad & u_{y_1} &= -b_1+b_2-y_0 \\ d_{x_2} &= a_1-a_2-x_0 \qquad & d_{y_2} &= b_1-b_2-y_0 \\ u_{x_2} &= a_1+a_2-x_0 \qquad & u_{y_2} &= b_1+b_2-y_0 \end{aligned} \tag{G.90}$$

With $f(x,y,z)$ and $g(x,y,z)$ as defined in equations G.64 and G.74, the integral of I can be written in a similar way to equation G.75 as

$$\begin{aligned} \int_{-a}^{a}\int_{-b}^{b} I\,dy\,dx = & \int_{d_{x_2}}^{u_{x_2}}\int_{d_{y_2}}^{u_{y_2}} f(x,y,z)\,dy\,dx - \int_{d_{x_1}}^{u_{x_1}}\int_{d_{y_2}}^{u_{y_2}} f(x,y,z)\,dy\,dx \\ & - \int_{d_{x_2}}^{u_{x_2}}\int_{d_{y_1}}^{u_{y_1}} f(x,y,z)\,dy\,dx + \int_{d_{x_1}}^{u_{x_1}}\int_{d_{y_1}}^{u_{y_1}} f(x,y,z)\,dy\,dx \\ & + \int_{d_{y_2}}^{u_{y_2}}\int_{d_{x_2}}^{u_{x_2}} f(x,y,z)\,dy\,dx - \int_{d_{y_1}}^{u_{y_1}}\int_{d_{x_2}}^{u_{x_2}} f(x,y,z)\,dy\,dx \\ & - \int_{d_{y_2}}^{u_{y_2}}\int_{d_{x_1}}^{u_{x_1}} f(x,y,z)\,dy\,dx + \int_{d_{y_1}}^{u_{y_1}}\int_{d_{x_1}}^{u_{x_1}} f(x,y,z)\,dy\,dx \\ & - \int_{d_{x_2}}^{u_{x_2}}\int_{d_{y_2}}^{u_{y_2}} g(x,y,z)\,dy\,dx + \int_{d_{x_1}}^{u_{x_1}}\int_{d_{y_2}}^{u_{y_2}} g(x,y,z)\,dy\,dx \\ & + \int_{d_{x_2}}^{u_{x_2}}\int_{d_{y_1}}^{u_{y_1}} g(x,y,z)\,dy\,dx - \int_{d_{x_1}}^{u_{x_1}}\int_{d_{y_1}}^{u_{y_1}} g(x,y,z)\,dy\,dx \end{aligned} \tag{G.91}$$

As for the self inductance, the integrals in the above equation are given by equations G.53 and G.60. The resultant expressions are rather more complicated than before, since none of the limits on the integrals are zero. They are therefore broken down into various sets of terms, grouped by type. The first of these groupings is the logarithmic terms, themselves divided into four sets. The first of these groups, L_1, is the terms from equation G.53 corresponding to the first four integrals in equation G.91, leaving out the terms involving multiplication by z.

$$
\begin{aligned}
2L_1 = {} & u_{y_2}{}^2\left(u_{x_2}\ln\left(u_{x_2}+\sqrt{u_{x_2}{}^2+u_{y_2}{}^2+z^2}\right)-d_{x_2}\ln\left(d_{x_2}+\sqrt{d_{x_2}{}^2+u_{y_2}{}^2+z^2}\right)\right)\\
& -d_{y_2}{}^2\left(u_{x_2}\ln\left(u_{x_2}+\sqrt{u_{x_2}{}^2+d_{y_2}{}^2+z^2}\right)-d_{x_2}\ln\left(d_{x_2}+\sqrt{d_{x_2}{}^2+d_{y_2}{}^2+z^2}\right)\right)\\
& -u_{y_2}{}^2\left(u_{x_1}\ln\left(u_{x_1}+\sqrt{u_{x_1}{}^2+u_{y_2}{}^2+z^2}\right)-d_{x_1}\ln\left(d_{x_1}+\sqrt{d_{x_1}{}^2+u_{y_2}{}^2+z^2}\right)\right)\\
& +d_{y_2}{}^2\left(u_{x_1}\ln\left(u_{x_1}+\sqrt{u_{x_1}{}^2+d_{y_2}{}^2+z^2}\right)-d_{x_1}\ln\left(d_{x_1}+\sqrt{d_{x_1}{}^2+d_{y_2}{}^2+z^2}\right)\right)\\
& -u_{y_1}{}^2\left(u_{x_2}\ln\left(u_{x_2}+\sqrt{u_{x_2}{}^2+u_{y_1}{}^2+z^2}\right)-d_{x_2}\ln\left(d_{x_2}+\sqrt{d_{x_2}{}^2+u_{y_1}{}^2+z^2}\right)\right)\\
& +d_{y_1}{}^2\left(u_{x_2}\ln\left(u_{x_2}+\sqrt{u_{x_2}{}^2+d_{y_1}{}^2+z^2}\right)-d_{x_2}\ln\left(d_{x_2}+\sqrt{d_{x_2}{}^2+d_{y_1}{}^2+z^2}\right)\right)\\
& +u_{y_1}{}^2\left(u_{x_1}\ln\left(u_{x_1}+\sqrt{u_{x_1}{}^2+u_{y_1}{}^2+z^2}\right)-d_{x_1}\ln\left(d_{x_1}+\sqrt{d_{x_1}{}^2+u_{y_1}{}^2+z^2}\right)\right)\\
& -d_{y_1}{}^2\left(u_{x_1}\ln\left(u_{x_1}+\sqrt{u_{x_1}{}^2+d_{y_1}{}^2+z^2}\right)-d_{x_1}\ln\left(d_{x_1}+\sqrt{d_{x_1}{}^2+d_{y_1}{}^2+z^2}\right)\right)
\end{aligned}
\tag{G.92}
$$

The second of these groups, L_2, is the terms from equation G.53 corresponding to the second four integrals in equation G.91, leaving out the terms involving multiplication by z. This is the same as L_1, but with x and y interchanged.

$$
\begin{aligned}
2L_2 = {} & u_{x_2}{}^2\left(u_{y_2}\ln\left(u_{y_2}+\sqrt{u_{x_2}{}^2+u_{y_2}{}^2+z^2}\right)-d_{y_2}\ln\left(d_{y_2}+\sqrt{u_{x_2}{}^2+d_{y_2}{}^2+z^2}\right)\right)\\
& -d_{x_2}{}^2\left(u_{y_2}\ln\left(u_{y_2}+\sqrt{d_{x_2}{}^2+u_{y_2}{}^2+z^2}\right)-d_{y_2}\ln\left(d_{y_2}+\sqrt{d_{x_2}{}^2+d_{y_2}{}^2+z^2}\right)\right)\\
& -u_{x_2}{}^2\left(u_{y_1}\ln\left(u_{y_1}+\sqrt{u_{x_2}{}^2+u_{y_1}{}^2+z^2}\right)-d_{y_1}\ln\left(d_{y_1}+\sqrt{u_{x_2}{}^2+d_{y_1}{}^2+z^2}\right)\right)\\
& +d_{x_2}{}^2\left(u_{y_1}\ln\left(u_{y_1}+\sqrt{d_{x_2}{}^2+u_{y_1}{}^2+z^2}\right)-d_{y_1}\ln\left(d_{y_1}+\sqrt{d_{x_2}{}^2+d_{y_1}{}^2+z^2}\right)\right)\\
& -u_{x_1}{}^2\left(u_{y_2}\ln\left(u_{y_2}+\sqrt{u_{x_1}{}^2+u_{y_2}{}^2+z^2}\right)-d_{y_2}\ln\left(d_{y_2}+\sqrt{u_{x_1}{}^2+d_{y_2}{}^2+z^2}\right)\right)\\
& +d_{x_1}{}^2\left(u_{y_2}\ln\left(u_{y_2}+\sqrt{d_{x_1}{}^2+u_{y_2}{}^2+z^2}\right)-d_{y_2}\ln\left(d_{y_2}+\sqrt{d_{x_1}{}^2+u_{y_2}{}^2+z^2}\right)\right)\\
& +u_{x_1}{}^2\left(u_{y_1}\ln\left(u_{y_1}+\sqrt{u_{x_1}{}^2+u_{y_1}{}^2+z^2}\right)-d_{y_1}\ln\left(d_{y_1}+\sqrt{u_{x_1}{}^2+d_{y_1}{}^2+z^2}\right)\right)\\
& -d_{x_1}{}^2\left(u_{y_1}\ln\left(u_{y_1}+\sqrt{d_{x_1}{}^2+u_{y_1}{}^2+z^2}\right)-d_{y_1}\ln\left(d_{y_1}+\sqrt{d_{x_1}{}^2+d_{y_1}{}^2+z^2}\right)\right)
\end{aligned}
\tag{G.93}
$$

The third of these groups, L_3, is the terms from equation G.53 involving multiplication by z corresponding to the first four integrals in equation G.91. These are combined with similar terms from equation G.60 (ie. those multiplied by x_3 or x_4) corresponding to the last four integrals in equation G.91.

$$\begin{aligned}
\frac{2L_3}{z^2} &= u_{x_2}\ln\left(\sqrt{u_{x_2}^2+u_{y_2}^2+z^2}-u_{x_2}\right) - d_{x_2}\ln\left(\sqrt{d_{x_2}^2+u_{y_2}^2+z^2}-d_{x_2}\right) \\
&- u_{x_2}\ln\left(\sqrt{u_{x_2}^2+d_{y_2}^2+z^2}-u_{x_2}\right) + d_{x_2}\ln\left(\sqrt{d_{x_2}^2+d_{y_2}^2+z^2}-d_{x_2}\right) \\
&- u_{x_1}\ln\left(\sqrt{u_{x_1}^2+u_{y_2}^2+z^2}-u_{x_1}\right) + d_{x_1}\ln\left(\sqrt{d_{x_1}^2+u_{y_2}^2+z^2}-d_{x_1}\right) \\
&+ u_{x_1}\ln\left(\sqrt{u_{x_1}^2+d_{y_2}^2+z^2}-u_{x_1}\right) - d_{x_1}\ln\left(\sqrt{d_{x_1}^2+d_{y_2}^2+z^2}-d_{x_1}\right) \\
&- u_{x_2}\ln\left(\sqrt{u_{x_2}^2+u_{y_1}^2+z^2}-u_{x_2}\right) + d_{x_2}\ln\left(\sqrt{d_{x_2}^2+u_{y_1}^2+z^2}-d_{x_2}\right) \\
&+ u_{x_2}\ln\left(\sqrt{u_{x_2}^2+d_{y_1}^2+z^2}-u_{x_2}\right) - d_{x_2}\ln\left(\sqrt{d_{x_2}^2+d_{y_1}^2+z^2}-d_{x_2}\right) \\
&+ u_{x_1}\ln\left(\sqrt{u_{x_1}^2+u_{y_1}^2+z^2}-u_{x_1}\right) - d_{x_1}\ln\left(\sqrt{d_{x_1}^2+u_{y_1}^2+z^2}-d_{x_1}\right) \\
&- u_{x_1}\ln\left(\sqrt{u_{x_1}^2+d_{y_1}^2+z^2}-u_{x_1}\right) + d_{x_1}\ln\left(\sqrt{d_{x_1}^2+d_{y_1}^2+z^2}-d_{x_1}\right)
\end{aligned} \tag{G.94}$$

The final group of logarithmic terms, L_4, is the terms from equation G.53 involving multiplication by z corresponding to the second four integrals in equation G.91. These are combined with similar terms from equation G.60 (ie. those multiplied by y_3 or y_4) corresponding to the last four integrals in equation G.91.

The result is the same as L_3, but with x and y interchanged:

$$\begin{aligned}
\frac{2L_4}{z^2} &= u_{y_2}\ln\left(\sqrt{u_{x_2}^2+u_{y_2}^2+z^2}-u_{y_2}\right) - d_{y_2}\ln\left(\sqrt{u_{x_2}^2+d_{y_2}^2+z^2}-d_{y_2}\right) \\
&- u_{y_2}\ln\left(\sqrt{d_{x_2}^2+u_{y_2}^2+z^2}-u_{y_2}\right) + d_{y_2}\ln\left(\sqrt{d_{x_2}^2+d_{y_2}^2+z^2}-d_{y_2}\right) \\
&- u_{y_1}\ln\left(\sqrt{u_{x_2}^2+u_{y_1}^2+z^2}-u_{y_1}\right) + d_{y_1}\ln\left(\sqrt{u_{x_2}^2+d_{y_1}^2+z^2}-d_{y_1}\right) \\
&+ u_{y_1}\ln\left(\sqrt{d_{x_2}^2+u_{y_1}^2+z^2}-u_{y_1}\right) - d_{y_1}\ln\left(\sqrt{d_{x_2}^2+d_{y_1}^2+z^2}-d_{y_1}\right) \\
&- u_{y_2}\ln\left(\sqrt{u_{x_1}^2+u_{y_2}^2+z^2}-u_{y_2}\right) + d_{y_2}\ln\left(\sqrt{u_{x_1}^2+d_{y_2}^2+z^2}-d_{y_2}\right) \\
&+ u_{y_2}\ln\left(\sqrt{d_{x_1}^2+u_{y_2}^2+z^2}-u_{y_2}\right) - d_{y_2}\ln\left(\sqrt{d_{x_1}^2+d_{y_2}^2+z^2}-d_{y_2}\right) \\
&+ u_{y_1}\ln\left(\sqrt{u_{x_1}^2+u_{y_1}^2+z^2}-u_{y_1}\right) - d_{y_1}\ln\left(\sqrt{u_{x_1}^2+d_{y_1}^2+z^2}-d_{y_1}\right) \\
&- u_{y_1}\ln\left(\sqrt{d_{x_1}^2+u_{y_1}^2+z^2}-u_{y_1}\right) + d_{y_1}\ln\left(\sqrt{d_{x_1}^2+d_{y_1}^2+z^2}-d_{y_1}\right)
\end{aligned} \tag{G.95}$$

The next set of terms is the algebraic terms, P. When terms corresponding to the first and second four integrals in equation G.91 are combined, the following cancellation takes place

$$\begin{aligned}
&\frac{1}{6}\left((x_4^2-2y_4^2-2z^2) + (y_4^2-2x_4^2-2z^2)\right)\sqrt{x_4^2+y_4^2+z^2} \\
&\qquad = -\frac{1}{6}(x_4^2+y_4^2+4z^2)\sqrt{x_4^2+y_4^2+z^2}
\end{aligned} \tag{G.96}$$

and when the appropriate term from the final four integrals is added in, another cancellation takes place

$$\begin{aligned}
&-\frac{1}{6}(x_4^2+y_4^2+4z^2)\sqrt{x_4^2+y_4^2+z^2} + z^2\sqrt{x_4^2+y_4^2+z^2} \\
&\qquad = -\frac{1}{6}(x_4^2+y_4^2-2z^2)\sqrt{x_4^2+y_4^2+z^2}
\end{aligned} \tag{G.97}$$

To make the notation slightly more compact, introduce the function η

$$\eta(x,y,z) = \frac{1}{6}(x^2+y^2-2z^2)\sqrt{x^2+y^2+z^2} \tag{G.98}$$

With the use of the three equations G.96, G.97 and G.98, the algebraic terms P can be written as

$$\begin{aligned} P = & -\eta(u_{x_2}, u_{y_2}, z) + \eta(d_{x_2}, u_{y_2}, z) + \eta(u_{x_2}, d_{y_2}, z) - \eta(d_{x_2}, d_{y_2}, z) \\ & + \eta(u_{x_1}, u_{y_2}, z) - \eta(d_{x_1}, u_{y_2}, z) - \eta(u_{x_1}, d_{y_2}, z) + \eta(d_{x_1}, d_{y_2}, z) \\ & + \eta(u_{x_2}, u_{y_1}, z) - \eta(d_{x_2}, u_{y_1}, z) - \eta(u_{x_2}, d_{y_1}, z) + \eta(d_{x_2}, d_{y_1}, z) \\ & - \eta(u_{x_1}, u_{y_1}, z) + \eta(d_{x_1}, u_{y_1}, z) + \eta(u_{x_1}, d_{y_1}, z) - \eta(d_{x_1}, d_{y_1}, z) \end{aligned} \tag{G.99}$$

The final terms to be incorporated from equation G.53 are

$$\frac{1}{4}\left(-x_4 y_4^{\,2} + x_3 y_4^{\,2} + x_4 y_3^{\,2} - x_3 y_3^{\,2}\right) \tag{G.100}$$

for each of the first four integrals in equation G.91, and the same for the second four integrals with x and y reversed. When the actual values for x_3 and x_4 are applied for each set of four integrals, these terms all cancel out.

The final terms to be incorporated from equation G.60 are the arcsin terms T, corresponding to the final four integrals in equation G.91. To make the notation more compact, introduce the function λ

$$\lambda(x,y,z) = xyz \arcsin\left(\frac{xy}{\sqrt{(x^2 + z^2)(y^2 + z^2)}}\right) \tag{G.101}$$

In terms of this function, the arcsin terms T are

$$\begin{aligned} T = & -\lambda(u_{x_2}, u_{y_2}, z) + \lambda(d_{x_2}, u_{y_2}, z) + \lambda(u_{x_2}, d_{y_2}, z) - \lambda(d_{x_2}, d_{y_2}, z) \\ & + \lambda(u_{x_1}, u_{y_2}, z) - \lambda(d_{x_1}, u_{y_2}, z) - \lambda(u_{x_1}, d_{y_2}, z) + \lambda(d_{x_1}, d_{y_2}, z) \\ & + \lambda(u_{x_2}, u_{y_1}, z) - \lambda(d_{x_2}, u_{y_1}, z) - \lambda(u_{x_2}, d_{y_1}, z) + \lambda(d_{x_2}, d_{y_1}, z) \\ & - \lambda(u_{x_1}, u_{y_1}, z) + \lambda(d_{x_1}, u_{y_1}, z) + \lambda(u_{x_1}, d_{y_1}, z) - \lambda(d_{x_1}, d_{y_1}, z) \end{aligned} \tag{G.102}$$

Equations G.87 - G.102 can now be combined to give the mutual inductance M as

$$M = \frac{\mu_0}{16\pi b_1 b_2}(L_1 + L_2 + L_3 + L_4 + P + T) \tag{G.103}$$

References

M. Abramowitz and I.A. Stegun.

1965 "Handbook of Mathematical Functions". Dover Publications, New York.

J. Barrow.

1989 "Avoiding Ground Problems in High-Speed Circuits". RF Design, July 1989, pp.32-34.

B.I. Bleaney and B. Bleaney.

1976 "Electricity and Magnetism" (Third Edition). Oxford University Press, Oxford.

Y.L. Chow.

1980 "An Approximate Dynamic Green's Function in Three Dimensions for Finite Length Microstripline". IEEE Transactions on Microwave Theory and Techniques, **MTT-28**, pp.393-397.

W.J. Cody.

1965 "Chebyshev Approximations for the Complete Elliptic Integrals K and E". Mathematics of Computation, **19**, pp.105-112.

R. Crampagne, M. Ahmadpanah and J-L. Guiraud.

1978 "A Simple Method for Determining the Green's Function for a Large Class of MIC Lines Having Multilayered Dielectric Structures". IEEE Transactions on Microwave Theory and Techniques, **MTT-26**, pp.82-87.

T.C. Edwards.

1981 "Foundations for Microstrip Circuit Design". pp.67-77, John Wiley and Sons.

EEsof.

EEsof Inc., 5795 Lindero Canyon Road, Westlake Village, CA 91362, USA.

A. Erdelyi.

1953 "Higher Transcendental Functions". Volume 2, McGraw-Hill, New York, p.169, formula 10.8(11).

A. Farrar and A.T. Adams.

1974 "Multilayer Microstrip Transmission Lines". IEEE Transactions on Microwave Theory and Techniques, **MTT-22**, pp.889-891.

I.S. Gradshteyn and I.M. Ryzhik.

1980 "Table of Integrals, Series, and Products". Academic Press.

R.F. Harrington.

1968 "Field Computation by Moment Methods". Macmillan, New York.

H. Horton, B. Easter and A. Gopinath.

1971 "Variation of Microstrip Losses with Thickness of Strip". Electronics Letters, **7**, pp.490-491.

M. Kobayashi.

1985 "Longitudinal and Transverse Current Distributions on Microstriplines and their Closed-Form Expression". IEEE Transactions on Microwave Theory and Techniques, **MTT-33**, pp.784-788.

S. Koike, N. Yoshida and I. Fukai.

1987 "Transient Analysis of Coupling Between Crossing Lines in Tree-Dimensional Space". IEEE Transactions on Microwave Theory and Techniques, **MTT-35**, pp.67-71.

J. Matthews and R.L. Walker.

1970 "Mathematical Methods of Physics" (Second Edition). pp.349-353, Benjamin/Cummings, California.

J.C. Maxwell.

1893 "A Treatise on Electricity and Magnetism" (Third Edition). Volume 1, pp.148-154, Oxford University Press, London.

R.F. Milsom, K.J. Scott, G. Clark, J.C. McEntegart, S. Ahmed and F.N. Soper.

1989 "FACET - A CAE System for RF Analogue Simulation Including Layout". Proceedings of the 26th ACM/IEEE Design Automation Conference, pp.622-625, Las Vegas, 25-29 June 1989.

R. Mittra and S.W. Lee.

1971 "Analytical Techniques in the Theory of Guided Waves". pp.4-11, Macmillan, New York.

J. Moore and R. Pizer.

1984 (Editors). "Moment Methods in Electromagnetics". Research Studies Press, Letchworth, UK.

P.M. Morse and H. Feshbach.

1953 "Methods of Theoretical Physics". Part I, McGraw-Hill, New York.

NAG.

1988 "The NAG Fortran Library Manual - Mark 13". NAG Ltd, Wilkinson House, Jordan Hill Road, Oxford, UK, OX2 8DR

A.G. van Nie.

1977 "On Fields and Waves in Microstrips". Journal of Applied Science and Engineering A, **2**, pp.205-212.

T.N.L. Patterson.

1968 "The Optimum Addition of Points to Quadrature Formulae". Mathematics of Computation, **22**, pp.847-856.

R.A. Pucel, D.J. Massé and C.P. Hartwig.

1968 "Losses in Microstrip". IEEE Transactions on Microwave Theory and Techniques, **MTT-16**, pp.342-350.

Quantic.

Quantic Laboratories Inc., 222 Osborne St., S. Winnipeg, Canada, R31 1Z3.

S. Ramo, J.R. Whinnery and T. van Duzer.

1965 "Fields and Waves in Communication Electronics". John Wiley and Sons, New York.

D.K. Reitan, and T.J. Higgins.

1957 "Accurate Determination of the Capacitance of a Thin Rectangular Plate". Transactions of the AIEE, **75**, pp.761-766.

D.K. Reitan.

1959 "Accurate Determination of the Capacitance of Rectangular Parallel-Plate Capacitors". Journal of Applied Physics, **30**, pp.172-176.

A.E. Ruehli.

1972 "Inductance Calculations in a Complex Integrated Circuit Environment". IBM Journal of Research and Development, **16**, pp.470-481.

1979 "Survey of Computer-Aided Electrical Analysis of Integrated Circuit Interconnections". IBM Journal of Research and Development, **23**, pp. 626-639.

1987 (Editor). "Circuit Analysis, Simulation and Design". Part 2, pp.235-253, North-Holland, Amsterdam.

A.E. Ruehli and P.A. Brennan.

1973 "Efficient Capacitance Calculations for Three-Dimensional Multiconductor Systems". IEEE Transactions on Microwave Theory and Techniques, **MTT-21**, pp.76-82.

P. Silvester.

1968 "TEM mode properties of microstrip transmission lines". Proceedings of the IEE, **111**, pp.43-48.

P. Silvester and P. Benedek.

1973 "Microstrip Discontinuity Capacitances for Right-Angle Bends, T Junctions and Crossings". IEEE Transactions on Microwave Theory and Techniques, **MTT-21**, pp.341-346.

J.J.H. Wang and C.J. Drane.

1982 "Numerical Analysis of Arbitrarily Shaped Bodies Modeled by Surface Patches". IEEE Transactions on Microwave Theory and Techniques, **MTT-30**, pp.1167-1173.

C. Wei, R.F. Harrington, J.R. Mautz and T.K. Sarkar.

1984 "Multiconductor Transmission Lines in Multilayered Dielectric Media". IEEE Transactions on Microwave Theory and Techniques, **MTT-32**, pp.439-449.

E. Yamashita.

1968 "Variational Method for the Analysis of Microstrip-Like Transmission Lines". IEEE Transactions on Microwave Theory and Techniques, **MTT-16**, pp.529-535.

O.C. Zienkiewicz and K. Morgan.

1983 "Finite Elements and Approximation". Wiley, New York.

Additional Material

The following publications have arisen in part from work described in this thesis. They are included after this page.

1. "Radio Frequency Simulation of a Complex Printed Circuit Board Layout by the Quasi-Static Boundary Element Method", R.F. Milsom and K.J. Scott, International Journal of Numerical Modelling, **1**, pp.63-68, 1988.

2. "Electrical Simulation of Multi Layer PCB with Non-Parallel Tracks and Printed Components", R.F. Milsom, K.J. Scott and G. Clark, Proceedings of the 8th International Zurich Symposium on Electromagnetic Compatibility, pp.63-68, Zurich, 7-9 March 1989.

3. "FACET - A CAE System for RF Analogue Simulation Including Layout", R.F. Milsom, K.J. Scott, G. Clark, J.C. McEntegart, S. Ahmed and F.N. Soper, Proceedings of the 26th ACM/IEEE Design Automation Conference, pp.622-625, Las Vegas, 25-29 June 1989.

INTERNATIONAL JOURNAL OF NUMERICAL MODELLING : ELECTRONIC NETWORKS, DEVICES AND FIELDS,
Vol. 1, 165–170 (1988)

RADIO FREQUENCY SIMULATION OF A COMPLEX PRINTED CIRCUIT BOARD LAYOUT BY THE QUASI-STATIC BOUNDARY ELEMENT METHOD

R. F. MILSOM AND K. J. SCOTT

Philips Research Laboratories, Redhill, Surrey RH1 5HA, U.K.

SUMMARY

A method for analysing the electrical effect of a set of conducting strips is presented. This method is applied to modelling the electrical behaviour of conducting tracks on a printed circuit board (PCB). Unlike most other published work, this analysis is not restricted to the case where the tracks are parallel. The problem is formulated in terms of an admittance matrix. A boundary element method incorporating image theory is used to produce a system of linear equations. These are solved to yield the required admittance matrix, which can then be incorporated into a standard circuit analysis package. Comparisons between measured and predicted circuit performance for a complex layout show close agreement up to at least 1 GHz.

INTRODUCTION

The electrical behaviour of a radio frequency (RF) circuit implemented on a printed circuit board (PCB) is typically quite different from that expected from the schematic circuit. One reason for this discrepancy is that the circuit does not take account of the printed substrate, which is itself a multi-terminal component with very complex transfer characteristics rather than the set of ideal, lossless, uncoupled connecting strips assumed at the initial design stage. The ideal model may be a reasonable approximation at audio frequency (AF), but is a poor approximation at RF. The outline of an admittance matrix model based on electromagnetic field analysis is presented here. This model is applicable to a randomly orientated set of conducting strips printed on one or both surfaces of a dielectric substrate, and is very accurate up to 1 GHz and reasonably accurate up to 10 GHz. The 3D geometries under consideration are too complex for analytical solutions to Maxwell's equations, so the field problem must be solved by numerical analysis. Such computer simulations are usually very CPU-intensive, even for much simpler boundary conditions. The solution described here uses the boundary element method[1] (BEM), which requires a very much smaller number of linear equations than the more common finite difference method[2] (FDM) or finite element method[3] (FEM) as applied to the same problem. The number of equations is further reduced by using image theory and building in a number of assumptions about the expected form of the current density and potential distributions. Some of these assumptions follow from a quasi-static approximation to Maxwell's equations.

PROBLEM DESCRIPTION

A PCB (without its components soldered on) consists of alternating layers of dielectric sheet and conductor pattern, typical features of which are shown in Figure 1. There is usually a conducting plane, either coincident with or parallel to the PCB, which can be regarded as ground. The metallization patterns are predominantly tracks and solder pads, the latter forming the points at which the external components (either surface mounted devices — SMDs — or wire-ended devices) are soldered to the board. Other features such as vias and partial ground planes are not considered here. Published methods of analysis of printed tracks are applicable only to parallel tracks,[4, 5] whereas the method described here applies to tracks of arbitrary orientation relative to each other.

0894–3370/88/030165–06$05.00

Received 26 April 1988
Revised 18 August 1988

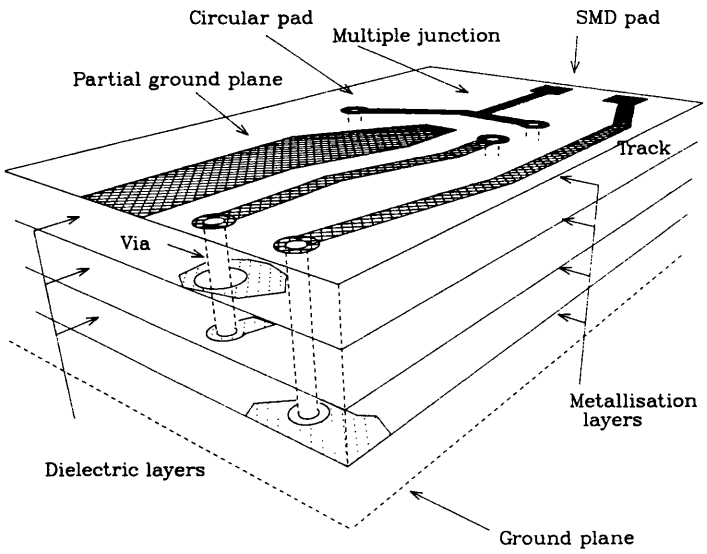

Figure 1. Features of a PCB

If there are N solder pads and a ground plane, the board is a passive N-port device. In this analysis the ground plane is assumed to be parallel to, but not necessarily coincident with, a surface of the PCB. The influence of incident radiation is ignored. Since the materials are, to a good approximation, linear, this device may be represented electrically by an $N \times N$ complex admittance matrix [Y]. When the external circuit is operating, a set of voltages V_i (i = 1,2,. . .,N) relative to ground will appear at the pads, and currents I_i (i = 1,2,. . .,N) will flow into the tracks connected to these pads. The solution for the current in the tracks implicitly gives the current distribution in the ground plane by the appropriate choice of image series in the Green's function, as described below. The column vectors of voltages [V] and currents [I] are related by

$$[\mathbf{I}] = [\mathbf{Y}][\mathbf{V}] \tag{1}$$

Note that [Y] is a unique electrical description of the PCB which depends only on its geometry, materials and frequency, but is independent of the external components. The solution for [Y] is used, along with external component values, in a standard analogue circuit simulator to determine the behaviour of the circuit, including layout effects.

CHOICE OF SOLUTION METHOD

Inspection of equation (1) shows that the jth column of [Y] is given by the currents at all N pads when there is unit alternating voltage between the jth pad and ground, with all other pads shorted to ground. The currents are found by solving Maxwell's equations subject to these applied voltages and the boundary conditions imposed by the geometry. The net currents are extracted from the field solution.

Standard methods of numerical analysis such as FEM and FDM discretize the field problem by transforming the continuum partial differential equations into a finite set of linear equations, each equation typically corresponding to one node of a mesh in 3D space. Because of the rapid spatial variation of the field in the problem of interest, hundreds of millions of such equations would be required. Although the left-hand side matrix is sparse, such solution methods based on differential formulations are not really feasible. An integral formulation is therefore used. This leads to the numerical solution known as the BEM. To reduce the number of equations for a large complex layout to a manageable level, some special assumptions are still required. The essentials of the method are described here.

INTEGRAL EQUATION FORMULATION

Maxwell's equations[6] are first expressed in terms of scalar potential ϕ and vector potential $\mathbf{A}$:

$$\nabla^2\phi - \epsilon\mu\frac{\partial^2\phi}{\partial t^2} = -\frac{\rho}{\epsilon} \tag{2}$$

$$\nabla^2\mathbf{A} - \epsilon\mu\frac{\partial^2\mathbf{A}}{\partial t^2} = -\mu\mathbf{J} \tag{3}$$

where ϵ and μ are the permittivity and permeability, ρ and $\mathbf{J}$ are charge and current density, and t is time.

The time-dependent terms in equations (2) and (3) are now neglected. This amounts to ignoring radiation from the board, which has little effect on the couplings in most PCBs. The solutions of equations (2) and (3) for ϕ and $\mathbf{A}$ can now be written as

$$\phi(\mathbf{r}) = \iiint G_\phi(\mathbf{r}|\mathbf{r}')\rho(\mathbf{r}')\,d^3\mathbf{r}' \tag{4}$$

$$\mathbf{A}(\mathbf{r}) = \iiint G_\mathbf{A}(\mathbf{r}|\mathbf{r}')\,\mathbf{J}(\mathbf{r}')\,d^3\mathbf{r}' \tag{5}$$

where the Green's functions G_ϕ and $G_\mathbf{A}$ are respectively the scalar and vector potentials at position r due to a point charge and point current at position $\mathbf{r}'$. These are considered further below. A harmonic time dependence of angular frequency ω is now assumed. The current continuity condition, which relates charge and current, can be written as

$$\nabla\cdot\mathbf{J} = -j\omega\rho \tag{6}$$

The electric field $\mathbf{E}$ is now given by

$$\mathbf{E} = -\nabla\phi - j\omega\mathbf{A} \tag{7}$$

Equations (6) and (7) couple together the static potentials, and result in the quasi-static approximation. Substituting equations (4)–(6) into equation (7) gives the integral representation of the induced electric field $\mathbf{E}_i(\mathbf{r})$ as

$$\mathbf{E}_i(\mathbf{r}) = \iiint_{D_c} G_\mathbf{E}(\mathbf{r}|\mathbf{r}')\mathbf{J}(\mathbf{r}')\,d^3\mathbf{r}' \tag{8}$$

where the integral is over the domain of the conductors D_c, and the Green's function $G_\mathbf{E}$ is given by

$$G_\mathbf{E}(\mathbf{r}|\mathbf{r}') = -j[\omega G_\mathbf{A}(\mathbf{r}|\mathbf{r}') + \frac{1}{\omega}\nabla G_\phi(\mathbf{r}|\mathbf{r}')\nabla.] \tag{9}$$

There is also an applied field $\mathbf{E}_a(\mathbf{r})$ due to the external power source. The total field $\mathbf{E}_t(\mathbf{r})$ is given by

$$\mathbf{E}_t(\mathbf{r}) = \mathbf{E}_i(\mathbf{r}) + \mathbf{E}_a(\mathbf{r}) \tag{10}$$

This field and the current density field must satisfy the continuum equivalent of Ohm's law in the conductors. Therefore

$$\mathbf{E}_t(\mathbf{r}) = \frac{\mathbf{J}(\mathbf{r})}{\sigma(\mathbf{r})} \tag{11}$$

where $\sigma(\mathbf{r})$ is the conductivity at $\mathbf{r}$. Substituting equations (9) and (10) into equation (11) and rearranging gives

$$\frac{\mathbf{J}(\mathbf{r})}{\sigma(\mathbf{r})} - \iiint_{D_c} G_\mathbf{E}(\mathbf{r}|\mathbf{r}')\mathbf{J}(\mathbf{r}')\,d^3\mathbf{r}' = \mathbf{E}_a(\mathbf{r}) \tag{12}$$

in the domain of the conductors.

Equation (12) constitutes the electric field integral equation[7] (EFIE) which contains only one unknown variable, the current density $\mathbf{J}(\mathbf{r})$. The EFIE is used in the BEM to obtain the solution for this current. As with other numerical methods, the continuum equations are transformed into a set of linear equations. However, because the current is non-zero over only a small finite volume, the total number of these equations is relatively small.

First, $\mathbf{J}(\mathbf{r})$ is expanded over a set of known real vector basis functions $\mathbf{j}_k(\mathbf{r})$ defined in the conductors. Thus,

$$\mathbf{J}(\mathbf{r}) = \sum_{k=1}^{K} C_k \mathbf{j}_k(\mathbf{r}) \tag{13}$$

where C_k are unknown complex constants. A set of weighting functions $\mathbf{W}_n(\mathbf{r})$ ($n = 1,2,\ldots,K$) are also introduced to multiply equation (12). Thus, substituting equation (13) into equation (12), multiplying by the weights and integrating over D_c gives

$$\sum_{k=1}^{K} C_k \iiint_{D_c} \mathbf{W}_n(\mathbf{r}) \cdot \left[\frac{\mathbf{j}_k(\mathbf{r})}{\sigma(\mathbf{r})} - \iiint_{D_c} G_{\mathbf{E}}(\mathbf{r}|\mathbf{r}') \mathbf{j}_k(\mathbf{r}') d^3\mathbf{r}' \right] d^3\mathbf{r} \tag{14}$$

$$= \iiint_{D_c} \mathbf{W}_n(\mathbf{r}) \cdot \mathbf{E}_a(\mathbf{r}) d^3\mathbf{r}, \quad n = 1,2,\ldots,K$$

This equation is used to derive two sets of linear equations. The first set enforces the boundary condition of zero longitudinal electric field on the tracks. Each $\mathbf{W}_n(\mathbf{r})$ in this set is the product of a unit vector in the local axial direction of the track with a Dirac delta function, and the set of weighting functions is defined on a grid within the tracks. Since there is no incident radiation, $\mathbf{E}_a(\mathbf{r})$ is zero for this set. For the second set, equation (14) is integrated along a line normal to the PCB surface at each port, with the $\mathbf{W}_n(\mathbf{r})$ directed parallel to this line. Here the integral of $\mathbf{E}_a(\mathbf{r})$ is equal to the applied voltage at the port. These linear equations are solved for the C_k. Then the net current at each pad, and hence the entries in the admittance matrix $[\mathbf{Y}]$, are found by analytical integration of equation (13).

QUASI-STATIC BOUNDARY ELEMENT METHOD

In the BEM the pattern of conductors is divided into elementary domains and a separate current density basis function set defined in each element. This set is also constrained to satisfy the continuity equation (6) at boundaries between elements. Strictly, the domains should be on the conductor surfaces (hence boundary elements). However, since conductors are thin, use of volume elements together with the concept of surface impedance[8] reduces the equations to boundary element form.

Figure 2 shows the subdivision of the PCB layout for a mobile radio antenna filter. Rectangular elements are used to approximate all the conductors, which in this example are on both surfaces. There is also a ground plane, the package surface, parallel to the PCB. The need for subdividing this ground plane into elements, which would very greatly increase the number of elements, is

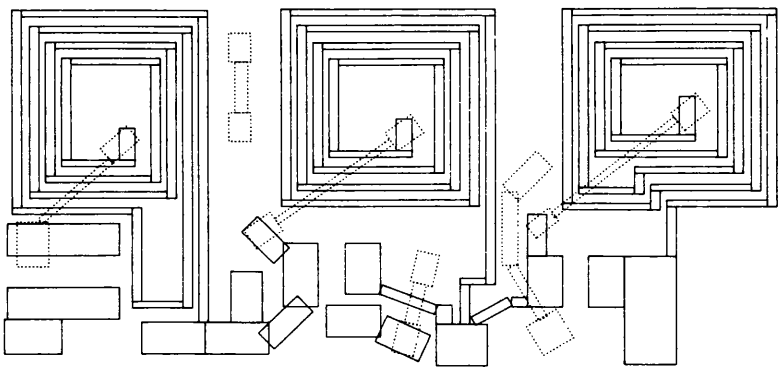

Figure 2. Layout of mobile radio antenna filter: tracks on back surface shown dotted

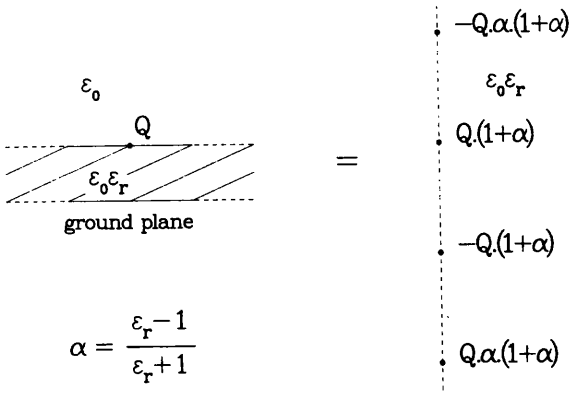

Figure 3. Infinite image series for PCB with coplanar ground

avoided by including its effect in the Green's function G_E. In fact both the ground plane and the discontinuities in ϵ between the PCB and free space are taken into account by using image theory, as described by Chow,[9] in the solution for G_ϕ, which is the scalar potential due to a point charge on one PCB surface. There are an infinite number of images, the first four of which are shown schematically in Figure 3 for the simpler case where the ground plane is on one of the PCB surfaces. The actual point charge Q is shown on the left, and the equivalent series of image charges, valid for the potential within the PCB or on its surface, is shown on the right; ϵ_0 is the permittivity of free space, and ϵ_r ($= \epsilon/\epsilon_0$) is the relative permittivity of the PCB. The more complex case of a remote ground gives a doubly infinite set, but this can normally be truncated after about 20 terms. The series for G_A has only two terms because there is no discontinuity in μ.

A quasi-static approximation can be made when the ground plane is much closer than a wavelength at the highest relevant frequency. This approximation has a very significant bearing on computational efficiency because the integrals in equations (14) are then frequency independent and real valued.

As well as the reduction in the required number of linear equations through this use of image theory, an additional reduction is achieved by building knowledge of the expected behaviour into the current density expansion per element, as referred to in equation (13). In local co-ordinates, this expansion is of the form

$$j_x = \frac{1}{\sqrt{(b^2 - y^2)}} \sum_i \sum_j x^i y^j, \qquad j_y = 0, j_z = 0 \tag{15}$$

where x, y and z are the local longitudinal, transverse, and thickness directions, and b is the half-width of the element. The current is assumed to be in the x direction since it has been shown that the other components of current are negligible at the frequencies of interest.[10] The edge singularity factor removes the need for multiple elements across the width of a track. In addition, the coefficients C_k are constrained to enforce the continuity of both j_x and $\partial j_x/\partial x$ at junctions between elements.

COMPARISON WITH EXPERIMENT

The BEM solution has been built into a suite of computer programs and used to simulate a variety of circuits. These simulations have been compared with measurement and also with circuit analysis, ignoring layout effects, for example using SPICE.

One such circuit is the filter whose layout is shown in Figure 2, and which contains three printed spiral inductors. The filter response predicted with a standard circuit simulator using the design values of printed and discrete components, but ignoring parasitic effects, is shown dotted in Figure 4. When the admittance matrix of the PCB, which includes the inductors, is included in the analysis the predicted response is that shown by the continuous line. This shows a substantial deviation from the original design. The response measured on a network analyser is shown by the broken line. Clearly, there is a high level of agreement between this measurement and the new simulation

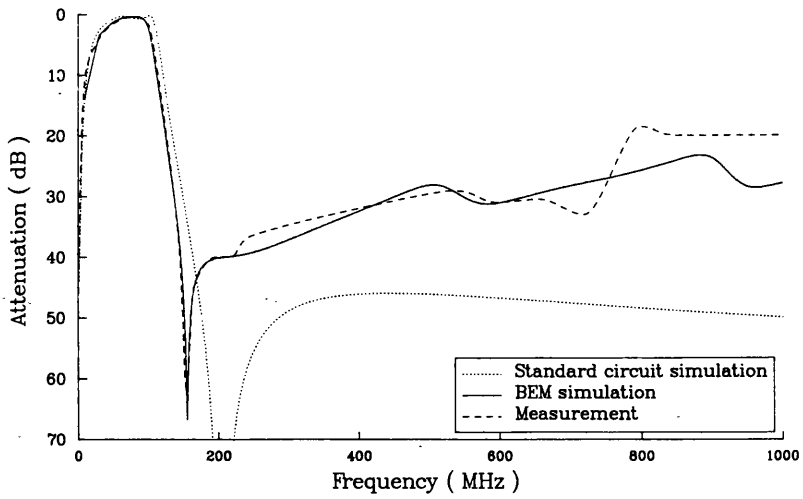

Figure 4. Mobile radio antenna filter: measured and simulated responses

method described here. The number of linear equations used in the BEM was about 800, and the CPU time was about 1 h on an IBM 4381 computer. This computing time is dominated by the integrations, rather than the solution of the linear equations. For a number of other geometries similar or even better levels of agreement between simulation and measurement have been obtained, in some cases up to 5 GHz, with agreement to within a few dB up to 10 GHz.

CONCLUSIONS

A method of circuit analysis which takes PCB layout effects into account has been developed. This method, based on an integral equation formulation of Maxwell's equations, requires the solution of many hundreds or even thousands of linear equations. This compares with the hundreds of millions of equations that would be needed using FEM or FDM for the same problem. High accuracy has been achieved, despite a number of assumptions made in order to reduce the amount of computation. Circuit designers can now be confident that layout effects are known to good accuracy before PCBs are made and tested. Therefore, with this model, many time-consuming and costly design iterations in hardware will be avoided.

ACKNOWLEDGEMENTS

The authors would like to acknowledge the contribution of software engineers from Philips ISA/ UK CAD group and the support of Philips Radio Communication Systems Ltd.

REFERENCES

1. M. H. Lean and A. Wexler, 'Accurate field computation with the boundary element method', *IEEE Trans. Magn.*, **MAG-18**, 331–335 (1982).
2. O. C. Zienkiewicz and K. Morgan, *Finite Elements and Approximation*, Wiley, New York, 1983, Chapter 1.
3. O. C. Zienkiewicz and K. Morgan, *Finite Elements and Approximation*, Wiley, New York, 1983, Chapters 3 and 4.
4. J. Poltz and A. Wexler, 'Transmission line analysis of PC boards', *VLSI Syst. Des.*, March, 38–43 (1986).
5. R. F. Harrington, J. R. Mautz and T. K. Sarkar, 'Multiconductor transmission lines in multilayer dielectric media', *IEEE Trans. Microwave Theory Techniques*, **MTT-32**, 439–450 (1984).
6. S. Ramo, J. R. Whinnery and T. Van Duzer, *Fields and Waves in Communication Electronics*, Wiley, New York, 1965.
7. J. J. H. Wang and C. J. Drane, 'Numerical analysis of arbitrary shaped bodies modelled by surface patches', *IEEE Trans. Microwave Theory Techniques*, **MTT-30**, 1167–1173 (1982).
8. E. M. Deeley and J. Xiang, 'Improved surface impedance methods for 2-D and 3-D problems', *IEEE Trans. Magn.*, **MAG-24**, 209–211 (1988).
9. Y. L. Chow, 'An approximate dynamic Green's function in three dimensions for finite length microstripline', *IEEE Trans. Microwave Theory Techniques*, **MTT-28**, 393–397 (1980).
10. A. G. Van Nie, 'On fields and currents in microstrips', *J. Appl. Sci. Eng. A*, **2**, 205–212 (1977).

ELECTRICAL SIMULATION OF MULTI LAYER PCB WITH NON-PARALLEL TRACKS AND PRINTED COMPONENTS

R.F.Milsom, K.J.Scott and G. Clark
Philips Research Laboratories
Redhill, U.K.

Summary

A Boundary Element Method (BEM) solution for the 3D electromagnetic fields in a variety of printed circuit board structures is presented. These structures include multi-layer boards, with or without a parallel conducting plane, which need not be coincident with a surface of the PCB. Any number of metallisation layers with different conductivities are allowed, and these may contain a large number of non-parallel tracks, rectangular or circular solder pads, and printed components such as spiral inductors or interdigital capacitors Good agreement between the model and measurement is demonstrated.

Introduction

CAD tools are commonly used to create the layout of a printed circuit board, but to date tools for the electrical simulation of a PCB are very limited. The major reason for this is the need for an efficient numerical solution to Maxwell's equations where the 3D fields and boundary conditions are very complex. Here we present a numerical model which allows the simulation of a variety of PCB structures. Only internal parasitic effects including electromagnetic coupling are modelled. The effect of external radiation is not considered.

A printed circuit board (without its components soldered on) comprises alternating layers of dielectric sheet and conductor pattern. There is usually a conducting plane, either coincident with or parallel to it. The metallisation patterns are predominantly tracks and rectangular or circular pads, the latter forming the points at which the external components are soldered to the board. Many published methods of analysis of printed tracks are applicable only to parallel tracks [1,2], whereas the method described here applies to a set of arbitrarily orientated tracks. An outline of the theory is presented, with special attention given to a numerical stability problem at the frequencies of most interest. Comparisons with measurements are also described.

Solution

The requirement is for an electrical model of the PCB, which is compatible with SPICE-like circuit simulators. Such a model must therefore ultimately be derived in terms of the circuit variables, voltage and current. However it is necessary to first obtain a solution to a field problem. The solution described here is based on the BEM [3] (Boundary Element Method), which uses an integral formulation of the field equations. Maxwell's equations are first expressed in terms of scalar potential ϕ and vector potential $\mathbf{A}$. Thus, at position $\mathbf{r}$,

$$\nabla^2 \phi(\mathbf{r}) - \epsilon(\mathbf{r})\,\mu(\mathbf{r})\,\frac{\partial^2 \phi(\mathbf{r})}{\partial t^2} = -\frac{\rho(\mathbf{r})}{\epsilon(\mathbf{r})} \qquad (1)$$

$$\nabla^2 \mathbf{A}(\mathbf{r}) - \epsilon(\mathbf{r})\,\mu(\mathbf{r})\,\frac{\partial^2 \mathbf{A}(\mathbf{r})}{\partial t^2} = -\mu(\mathbf{r})\,\mathbf{J}(\mathbf{r}) \qquad (2)$$

where ϵ and μ are permittivity and permeability, ρ and $\mathbf{J}$ are charge and current density and t is time At frequencies of greatest interest electromagnetic wavelength is of the order of tens of centimetres, whereas spatial variations of fields due to discontinuities at conductor edges occur over distances of a few millimetres. Therefore, to a good approximation, the second term in each of equations 1 and 2 may be ignored.

Green's functions

Solving equations 1 and 2 for ϕ and **A** gives the integral formulation,

$$\phi(\mathbf{r}) = \int\int\int G_\phi(\mathbf{r}|\mathbf{r}')\,\rho(\mathbf{r}')\,d^3\mathbf{r}' \qquad (3)$$

$$\mathbf{A}(\mathbf{r}) = \int\int\int G_\mathbf{A}(\mathbf{r}|\mathbf{r}')\,\mathbf{J}(\mathbf{r}')\,d^3\mathbf{r}' \qquad (4)$$

where the Green's functions G_ϕ and $G_\mathbf{A}$ are respectively the scalar and vector potentials due to a point charge and point current in the configuration appropriate to the vertical structure of the PCB under consideration.

Figure 1 shows the configuration of interest. $G_\phi(\mathbf{r}|\mathbf{r}')$ is the scalar potential at $\mathbf{r} = (x,y,z)$ due to unit point charge at $\mathbf{r}' = (x',y',z')$, where both points are within or on the dielectric sheet, which has thickness c. An ideal conducting plane is parallel to, and at a distance d from the dielectric. If harmonic time dependence of angular frequency ω is assumed, then from the Method of Images [4] it can be shown that,

$$G_\phi(\mathbf{r}|\mathbf{r}') = \sum_{m=1}^{\infty}\sum_{n=1}^{\infty} K_{mn} \times \frac{e^{-j\omega t}}{\sqrt{(x-x')^2 + (y-y')^2 + (h_{mn} \pm z \pm z')^2}} \qquad (5)$$

where K_{mn} are constants which depend only on the permittivity of free space ϵ_o and the complex relative permittivity ϵ_r of the PCB material, and h_{mn} are constants which depend only on c and d. The signs of z and z' depend on m and n.

Since there is no discontinuity in any component of the magnetic field at the interfaces between free space and dielectric, only a single image representing the effect of the conducting plane is required for the magnetic vector potential Green's function. Thus,

$$G_\mathbf{A}(\mathbf{r}|\mathbf{r}') = \frac{\mu_o}{4\pi}\left[\frac{1}{|\mathbf{r}-\mathbf{r}'|} - \frac{1}{\sqrt{(x-x')^2 + (y-y')^2 + (z+z')^2}}\right] e^{-j\omega t} \qquad (6)$$

where μ_o is the permeability of free space. The derivation of equations 5 and 6 is a generalisation of a method reported earlier [5]. The double summation in equation 5 can normally be truncated to about 5×5 terms without significant loss of accuracy.

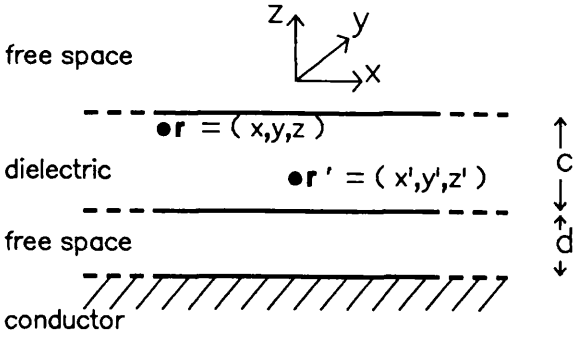

Fig.1: PCB configuration showing general source and object point locations **r'** and **r**

The omission of the time-dependent terms in equations 1 and 2 is equivalent to ignoring retarded potentials, which leads to the above omission of spatial variation of the phase term in equations 5 and 6. This is a better approximation if all conductors are close to the conducting plane. If $(c + d)$ is less than a tenth of a wavelength at the highest frequency of interest (say 2 GHz for mobile communications equipment), then there is rapid spatial attenuation of G_ϕ and $G_\mathbf{A}$ such that the magnitude is very small at distances $|\mathbf{r} - \mathbf{r}'|$ for which the phase of the retarded potential would be significantly different from zero. The error in the solution due to this approximation is usually comparable to the error resulting from truncation of the series in equation 5.

Despite this quasi-static approximation it is still necessary to consider coupling between the electric and magnetic fields. Equations 3 and 4 are coupled firstly by the current continuity equation, and secondly by the relationship between electric field **E** and the two potentials. Thus,

$$\nabla \cdot \mathbf{J} = -\frac{\partial \rho}{\partial t} \qquad (7)$$

$$\mathbf{E} = -\nabla\phi - \frac{\partial \mathbf{A}}{\partial t} \qquad (8)$$

Admittance matrix

The electrical model of the PCB described here is a frequency-dependent order N admittance matrix $[\mathbf{Y}]$ given by,

$$[\mathbf{Y}] = [\mathbf{I}][\mathbf{V}]^{-1} \qquad (9)$$

where $[\mathbf{I}]$ and $[\mathbf{V}]$ are the column vectors of currents and voltages at the N solder pads. $[\mathbf{Y}]$ is independent of the discrete components or ICs soldered to the pads.

These voltages and currents are defined by,

$$V_k = -\int_{-d}^{Z_k} E_z(X_k, Y_k, z)\, dz \qquad (10)$$

where (X_k, Y_k, Z_k) is the centre of the k^{th} pad, and

$$I_k = \sum \int\int \mathbf{J} \cdot d\mathbf{S} \qquad (11)$$

where the summation is taken over all tracks connected to the k^{th} pad, each surface integral is taken over the cross-section of the track at its junction with the pad. **S** is directed parallel to the track edges and away from the pad. If there is no ideal conducting plane d is infinite.

Since all conductors of the PCB are thin, **J** is assumed parallel to the $x-y$ plane, so from equation 2, the z-component of **A** is zero. Thus, from equations 8 and 10,

$$V_k = \phi(X_k, Y_k, Z_k) \qquad (12)$$

at all frequencies. Pads are electrically very short, so voltage is assumed constant on each pad.

Quasi-static BEM

The solution for **J** is obtained by the BEM , with an important quasi-static modification. It is known [6] that such integral methods are numerically unstable at frequencies for which typical feature size is electrically small. This is because only a small component of **J** contributes to $\nabla \cdot \mathbf{J}$, the remaining contribution being a solenoidal field. Therefore, a small error in **J** may give a large error in $\nabla \cdot \mathbf{J}$ and hence in ρ. This numerical problem is dealt with here as follows.

Equation 9 shows that the m^{th} column of [**Y**] is equal to [**I**] , as found from equation 11, where the solution for **J** has been found for applied voltages,

$$\begin{aligned} V_n &= 0 \quad (n = 1....m-1, m+1....N) \\ V_m &= 1 \end{aligned} \qquad (13)$$

The quasi-static solution proceeds by first finding a solution for the charge density ρ. This is obtained by making an estimate Φ for the scalar potential on the tracks from the known potentials (1 and 0) on the pads, and the expected slow spatial variation of ϕ on conductors. On tracks, a piecewise linear fit to ϕ along the length and constant ϕ in the cross-section is a good approximation if pads are separated by track sections no more than a tenth of a wavelength long at the highest frequency of interest. If longer tracks or junctions are present, then these are subdivided by the creation of N' infinitesimal pseudo-pads, which are treated in the same way as pads except that external components are not connected. A larger admittance matrix of order $N + N'$ is then obtained, but this is compressed down to the required order N by applying the current continuity condition at the pseudo-pads to eliminate the appropriate N' rows and columns.

The current density is now conveniently separated into solenoidal and divergent contributions, $\mathbf{J}_S$ and $\mathbf{J}_D$ respectively. Both contributions are approximated by expanding over finite sets of vector basis functions. Thus,

$$\begin{aligned} \mathbf{J}_S(\mathbf{r}) &= \sum_{i=1}^{S} A_i \mathbf{f}_i(\mathbf{r}) \\ \mathbf{J}_D(\mathbf{r}) &= \sum_{i=1}^{R} B_i \mathbf{g}_i(\mathbf{r}) \end{aligned} \qquad (14)$$

where the functions $\mathbf{f}_i$ and $\mathbf{g}_i$ have zero and non-zero divergence respectively, and A_i and B_i are unknown coefficients.

From equations 7 and 14, the solution for charge density at angular frequency ω is given by,

$$\rho(\mathbf{r}) = -\frac{1}{j\omega} \sum_{i=1}^{R} B_i \nabla \cdot \mathbf{g}_i(\mathbf{r}) \qquad (15)$$

Therefore, substituting equation 15 and the estimate Φ into equation 3 in the domain of the conductors D_c,

$$\frac{-1}{j\omega} \sum_{i=1}^{R} B_i \int\int\int_{D_c} G_\phi(\mathbf{r} \mid \mathbf{r}') \nabla \cdot \mathbf{g}_i(\mathbf{r}')\, d^3\mathbf{r}' = \Phi \qquad (16)$$

The coefficients B_i are now found by the Method of Weighted Residuals [7]. Thus,

$$\begin{aligned} -\frac{1}{j\omega} \sum_{i=1}^{R} B_i \int\int\int_{D_c} w_i(\mathbf{r}) \times \\ \int\int\int_{D_c} G_\phi(\mathbf{r} \mid \mathbf{r}') \nabla \cdot \mathbf{g}_i(\mathbf{r}')\, d^3\mathbf{r}'\, d^3\mathbf{r} \\ = \Phi \int\int\int_{D_c} w_i(\mathbf{r})\, d^3\mathbf{r} \end{aligned} \qquad (17)$$

where w_j $(j = 1,2..R)$ is a defined set of R weighting functions. After evaluation of the integrals, the R linear equations 17 are solved for B_i.

The remaining unknowns A_i are then found as follows. In the domain D_c,

$$\mathbf{E}(\mathbf{r}) = \frac{\mathbf{J}(\mathbf{r})}{\sigma(\mathbf{r})} \tag{18}$$

where $\sigma(\mathbf{r})$ is the conductivity at $\mathbf{r}$. Substituting equation 4 and the estimate Φ into equation 8 and then into equation 18 gives, in D_c,

$$-\frac{\mathbf{J}(\mathbf{r})}{\sigma(\mathbf{r})} - \nabla\Phi - j\omega \int\int\int_{D_c} G_{\mathbf{A}}(\mathbf{r}\,|\,\mathbf{r}')\,\mathbf{J}(\mathbf{r}')\,d^3\mathbf{r}' = 0 \tag{19}$$

Current density $\mathbf{J}$ is now separated into the expansions in equation 14, and these are substituted into equation 19 which is rearranged with known quantities on the right hand side. Thus,

$$\sum_{i=1}^{S} A_i \left[-\frac{\mathbf{f}_i(\mathbf{r})}{\sigma(\mathbf{r})} - j\omega \int\int\int_{D_c} G_{\mathbf{A}}(\mathbf{r}\,|\,\mathbf{r}')\,\mathbf{f}_i(\mathbf{r}')\,d^3\mathbf{r}' \right] = \sum_{k=1}^{R} B_k \left[\frac{\mathbf{g}_k(\mathbf{r})}{\sigma(\mathbf{r})} + j\omega \int\int\int_{D_c} G_{\mathbf{A}}(\mathbf{r}\,|\,\mathbf{r}')\,\mathbf{g}_k(\mathbf{r}')\,d^3\mathbf{r}' \right] + \nabla\Phi \tag{20}$$

The Method of Weighted Residuals is then applied to equation 20 to find the A_i.

Elements, basis functions and weighting functions

In the general BEM domain boundaries are divided into elementary sub-regions (elements), and basis function sets are defined in each element with appropriate field continuity conditions enforced at element junctions. Here the conductors of the PCB are subdivided into three types of element characterised by geometrical shape and basis function set as follows:

1. Rectangular track element - current density vector parallel to principal track edges with amplitude distribution given by bi-variate polynomial in $x-y$ plane, edge singularity factor [8] in the width, and skin-effect factor [9] in the thickness.

2. Rectangular pad element - solenoidal current assumed zero, and charge density given by bi-variate polynomial in $x-y$ plane with edge singularity factor.

3. Circular pad element - solenoidal current assumed zero, and charge density given by harmonic function of angle in $x-y$ plane with edge singularity factor.

The basis function sets are also constrained such that current density and its first derivative are continuous between track elements. The use of high order polynomials reduces the number of elements because long track elements can then be used. Strictly, all elements have finite thickness. However, the very small thickness of conductors compared to other dimensions allows all integrals to be reduced to surface integrals so the solution has the same form as the BEM. The use of the edge singularity factors ensures that the spatial convolution of basis functions and Green's functions gives smooth and slowly varying potentials on the conductors, and this allows the use of scalar and vector Dirac delta function weights (Point Collocation Method [10]) to multiply equations 16 and 20 respectively.

Comparison with measurement

The numerical model described has been built into a suite of computer programs linked to a PCB layout CAD system and a SPICE-like circuit analysis package. Figure 2 shows a layout designed to test the accuracy of the method for non-parallel tracks, which is the case not treated by available PCB simulators. Two non-parallel transmission lines each comprising a pair of parallel tracks are printed on opposite faces of the PCB which is mounted above a copper ground plane. S-parameters between the two ports shown were measured and simulated. The unused ports were terminated with 50 Ohm chip resistors. Figure 3 shows the level of agreement for the magnitude of reflection $|S_{11}|$ and transmission $|S_{21}|$. Corresponding agreement was obtained for the phase.

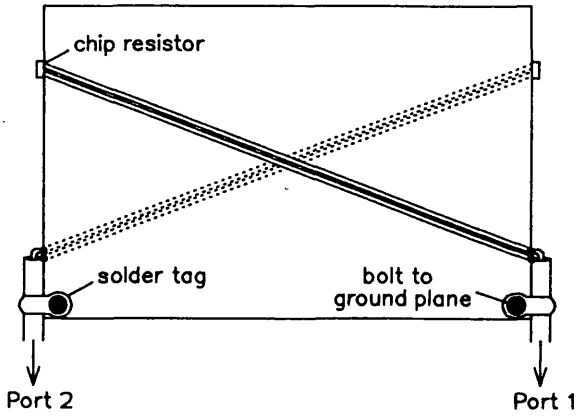

Fig.2: Layout of non-parallel transmission lines on different layers

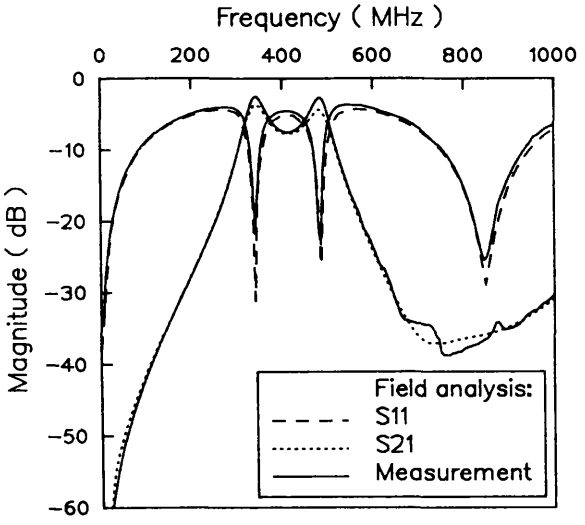

Fig.3: Measured and simulated S-parameters of non-parallel transmission lines

Figure 4 shows the layout for a more practical application of the analysis, namely a Private Mobile Radio (PMR) antenna filter. This PCB also has conductors on both faces. There are three non-standard spiral inductors and a number of pins which allow the module to be plugged into its socket. The latter are not strictly part of the printed conductor pattern, but may nevertheless be included in the simulation. The pins used are those indicated for the transmitter output and antenna

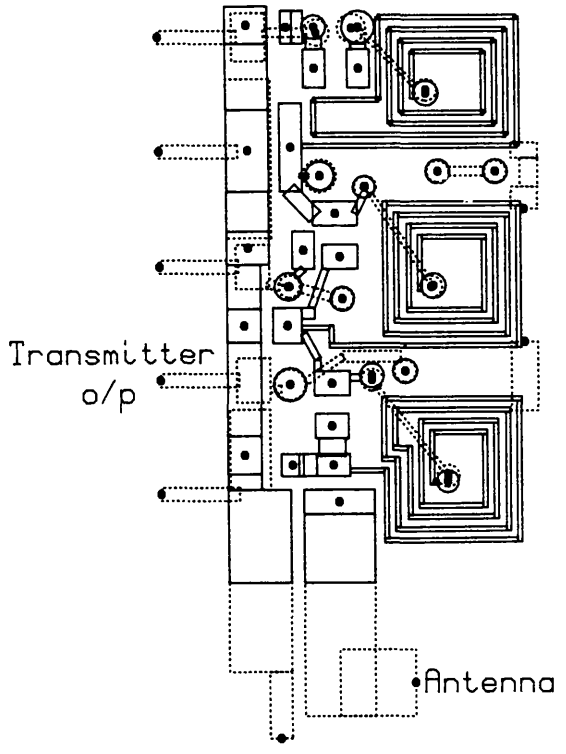

Fig.4: Antenna filter PCB Layout, with two layers superimposed

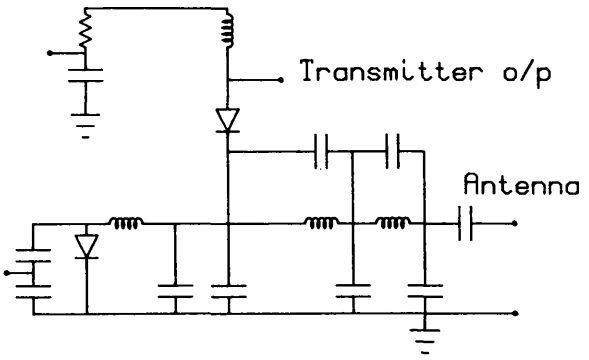

Fig.5: Antenna filter schematic circuit

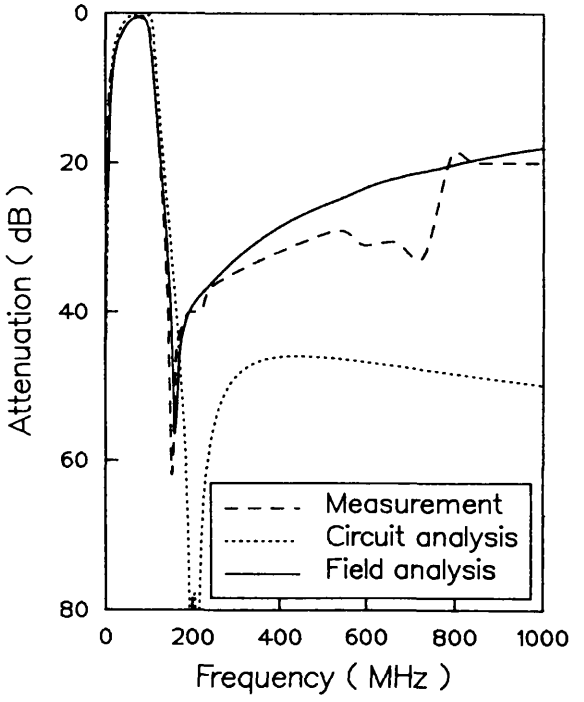

Fig.6: Measured and simulated frequency responses of antenna filter

connections. Filled circles indicate where the conductors are connected to discrete components or to other modules. In the simulation the conducting plane is taken as the closest surface of the metal package. Vias are modelled as small discrete inductors between appropriate pads.

Figure 5 shows the schematic circuit for this filter, and Figure 6 illustrates the responses obtained by measurement, circuit analysis of the schematic circuit, and by field analysis taking account of the layout. The latter clearly gives a more accurate representation of the passband and the general stopband level.

Conclusions

A new method of analysis of an analogue circuit on a PCB has been described. This is a quasi-static implementation of the Boundary Element Method which eliminates the problem of numerical instability in the frequency range applicable to mobile communications. Complex layouts including non-parallel tracks and multi-layer boards can be simulated. It is well known that the number of linear equations required for the BEM is much fewer than say for the Finite Element Method. However, the method here reduces the number further by using high-order basis functions with special functional form based on expected behaviour of the current and charge distributions, and by the use of the Method of Images which eliminates the need for elements on the ideal conducting plane and on the dielectric/free space interfaces. The quasi-static approximation has the additional advantage of ensuring that all the numerical integrals are frequency-independent, and this greatly increases numerical efficiency. Simulations have been compared with measurement and good agreement was obtained.

Acknowledgements

The authors would like to acknowledge the contribution of Philips ISA-UK CAD Group who designed and coded much of the software, and the support of Philips Radio Communications Systems Ltd.

References

[1] Poltz,J. and Wexler,A.: VLSI Systems Design (USA), 38-43, March 1986.

[2] Harrington,R.F., Mautz,J.R. and Sarkar,T.K.: IEEE Transactions on Microwave Theory and Techniques (USA), MTT-32, 439-450 (1984)

[3] Lean,M.H. and Wexler,A.: IEEE Transactions on Magnetics (USA), MAG-18, 331-335 (1982)

[4] Bleaney,B.I. and Bleaney,B., "Electricity and Magnetism", Third Edition, pp.48-56, Clarendon Press, Oxford, 1976.

[5] Chow,Y.L.: IEEE Transactions on Microwave Theory and Techniques (USA), MTT-28, 393-397 (1980)

[6] Mautz,J.R. and Harrington,R.F.: IEEE Transactions on Antennas and Propagation (USA), AP-32, 330-339 (1984)

[7] Zienkiewicz,O.C. and Morgan,K., "Finite Elements and Approximation", Chapter 2, Wiley, New York, 1983

[8] Kobayashi M.: IEEE Transactions on Microwave Theory and Techniques (USA), MTT-33, 784-788 (1985)

[9] Ramo,S., Whinnery,J.R. and Van Duzer,T., "Fields and Waves in Communication Electronics", pp.298-301, Wiley, New York, 1965

[10] Zienkiewicz,O.C. and Morgan,K., "Finite Elements and Approximation", pp.96-99, Wiley, New York, 1983.

FACET - a CAE System for RF analogue simulation including layout

R.F.Milsom, K.J.Scott, G.Clark, J.C.McEntegart, S.Ahmed and F.N.Soper

Philips Research Laboratories, Redhill, Surrey, RH1 5HA, U.K.

Abstract

FACET, a CAE system for RF analogue simulation is described. Layout-dependent effects such as parasitic electromagnetic coupling are included. The method of analysis provides accurate electrical modelling of multilayer PCB structures with a large number of arbitrarily-orientated tracks and printed components, without excessive demands on CPU and memory. This is achieved by building in knowledge of the frequencies of interest and the expected charge and current distributions. FACET is linked automatically to a layout CAD system and a circuit analysis package.

Introduction

In many areas of electronics there is a need for higher frequencies than have been used in the past. For example in mobile communication systems 1 GHz is now common and frequencies up to 3 GHz are probable in the next decade [1]. In such systems the layout of components and connections in the equipment is of prime importance. At these frequencies the effects of electromagnetic coupling in the interconnections can seriously degrade performance, and lead to many repeated attempts at layout if not properly understood. FACET, Functional Analysis of Circuits by Electromagnetic Theory, is a CAE package for analogue simulation taking account of PCB layout. In contrast to other PCB simulators FACET can model the mutual coupling of a very large number of conductors, e.g. 10,000 non-parallel track sections with 16 Mbytes of main memory. This package allows RF engineers to observe layout-dependent electromagnetic effects and make appropriate corrections to the layout, without time-consuming iterations with hardware. Mask-making proceeds only when FACET indicates acceptable performance.

Figure 1 shows how FACET integrates with other CAE/CAD tools. The geometry of the conductor patterns is extracted from MEDUSA which is a CAD system used for layout. Additionally, the user inputs the schematic circuit, the physical properties of the conductors and insulating material of the PCB, the upper frequency limit of the simulation and the required output options. FACET then uses the geometrical, physical and frequency data to create an electrical equivalent circuit model of the printed board which is automatically merged with the schematic circuit and loaded into a circuit analysis package, PHILPAC, which runs the simulation. Graphical output options allow the user to inspect the layout geometry sub-division and equivalent circuit node positions before simulation, and the spatial distribution of electromagnetic field quantities after the simulation.

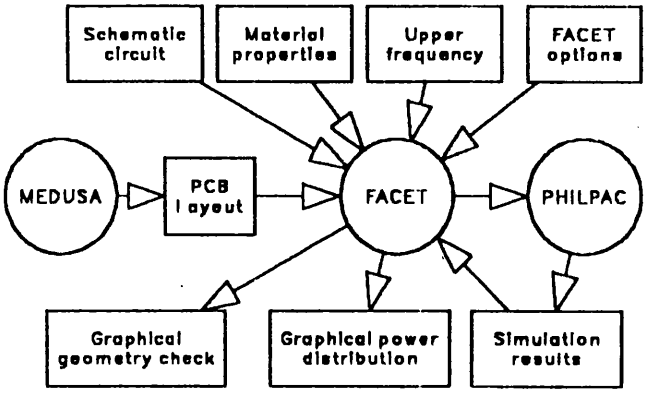

Fig. 1 FACET environment

Figure 2 shows typical features of an analogue PCB, which in general comprises alternating dielectric sheets and printed conductor patterns. Conductors include tracks, junctions, pads, vias, and polygonal partial ground planes. FACET models all the features shown including an optional continuous ground plane parallel to the PCB, which typically represents the closest surface of a metal package. Only the track conductors are considered here. Printed components such as spiral inductors and interdigital capacitors are special cases of this general model for tracks.

Layout CAD systems typically produce geometrical output designed primarily for the manufacturing process i.e. mask-making, machining, soldering and component placement, and not for simulation using electromagnetic

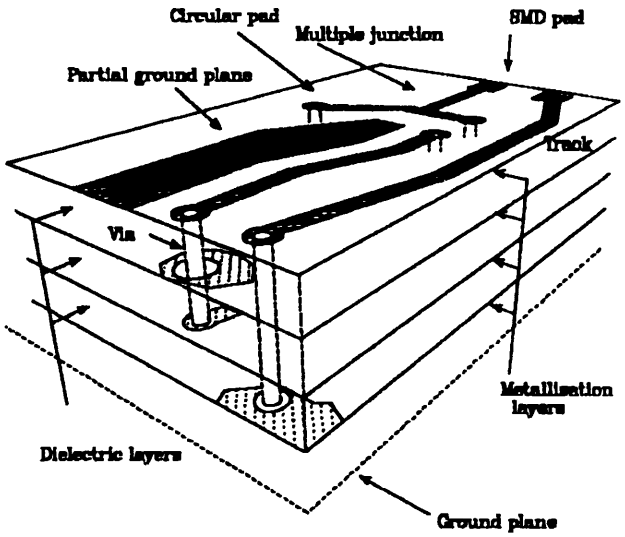

Fig. 2 PCB features simulated

field analysis. In particular, many features of the conductor patterns are built into the photomask using overlapping primitive shapes, which if used directly would lead to simulation errors. FACET therefore has a geometric pre-processor which operates on the extracted geometry to remove unwanted overlap and transform the patterns into a set of elementary shapes and connectivity information that the analysis program can use. A large set of rules is used to handle the subdivision and trimming for the many cases that can arise. Figure 3 shows the processed geometry of two superimposed metallisation layers on the PCB of a portable radio antenna filter. Small circles indicate positions of the nodes used in the equivalent circuit.

The Electromagnetic Model

The combination of conductors and insulators shown in Figure 2 form a passive linear multi-terminal component. Solving for the 3D fields in such a component demands exceptionally large computer memory and processing power if a standard method of numerical analysis such as the Finite Element Method [2] is used. The Boundary Element Method has been used successfully to reduce computing requirements[3]. However in order to fully model a complete analogue PCB using, for example a VAX 8800 computer, further efficiency improvements are required. At frequencies of greatest interest (less than 3 GHz) the spatial variation of the electromagnetic field resulting from discontinuities at conductor edges is much greater than that due to wave propagation. Therefore a quasi-static approximation to Maxwell's equations is made, and this is shown to lead automatically to a lumped equivalent circuit model of the PCB, the coupling between electric and magnetic fields being effectively provided by the network topology. Such lumped models have been reported earlier [4,5]. However, to improve the numerical efficiency, the method described here takes account of both the highest frequency required in the simulation and the expected current and charge distributions for the type of physical structure employed.

The quasi-static approximation is initially expressed in integral form,

$$\phi(\mathbf{r}) = \int\int\int G_{\phi}(\mathbf{r}\,|\,\mathbf{r}')\,\rho(\mathbf{r}')\,d^3\mathbf{r}' \qquad (1)$$

$$\mathbf{A}(\mathbf{r}) = \int\int\int G_{A}(\mathbf{r}\,|\,\mathbf{r}')\,\mathbf{J}(\mathbf{r}')\,d^3\mathbf{r}' \qquad (2)$$

where ϕ and $\mathbf{A}$ are respectively scalar and vector potentials, ρ and $\mathbf{J}$ are charge and current density, and $\mathbf{r}$ and $\mathbf{r}'$ are position vectors. The Green's functions G_{ϕ} and G_{A} depend on the layer structure of the PCB [6,7]. The integrals are over the domain of the conductors, excluding the continuous ground plane which is allowed for in the Green's functions. Harmonic time-dependence of angular frequency ω is assumed throughout. In the domain of the conductors, the field variables in equations 1 and 2 are also required to satisfy,

$$\mathbf{E} = -\nabla\phi - j\omega\mathbf{A} = \frac{\mathbf{J}}{\sigma} \qquad (3)$$

where $\mathbf{E}$ is electric field and σ is the local value of conductivity. $\mathbf{J}$ and ρ must also satisfy the current continuity condition. The following analysis considers all PCB tracks. The other conductors are dealt with by a generalisation of the method. Voltage V on conductors is defined as being equal to scalar potential ϕ, and current I is the surface integral (over the conductor cross-section) of $\mathbf{J}$, which is assumed parallel to the longitudinal direction in each track. The entire layout of tracks is divided into N two-terminal sections, where each terminal is either a multiple junction or a pad. At frequencies of interest the spatial variation of both V and I along tracks is much slower than the general variation of field quantities. Therefore, by expressing the solution in terms of approximations to these two quantities, relatively few unknowns are required. It is also shown that only a small part of the field solution is frequency-dependent, so only one CPU-intensive 3D field analysis is performed for the entire frequency range.

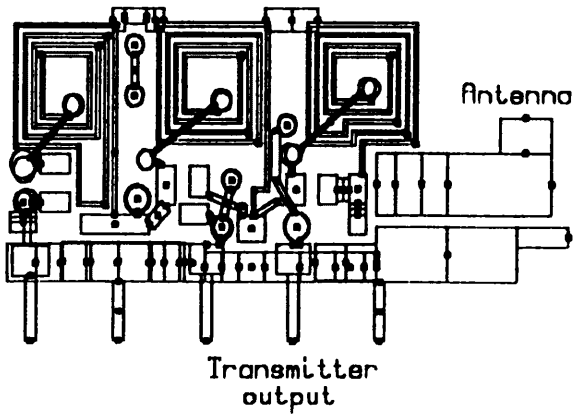

Fig. 3 Processed layout geometry

V and I are approximated by piecewise constant functions along these sections. The constant current and constant voltage intervals overlap, and are chosen to be about $0.1\lambda_m$ in length, apart from a $0.05\lambda_m$ constant current interval at each end of a section, where λ_m is wavelength at the maximum frequency of interest. The net currents and voltages on these intervals are respectively I_k ($k = 1,2...M_I$) and V_k ($k = 1,2...M_V$) . Current and charge density, on the k^{th} constant current and voltage intervals respectively, are approximated by,

$$\mathbf{J}(\mathbf{r}) = I_k \, \mathbf{n}(\mathbf{r}) \, \tau_k(\mathbf{r}) \tag{4}$$

$$\rho(\mathbf{r}) = Q_k \, \psi_k(\mathbf{r}) \tag{5}$$

where $\mathbf{n}$ is a unit vector parallel to the local longitudinal direction, Q_k is the net charge on the k^{th} constant voltage interval, and τ_k and ψ_k are assumed normalised spatial distributions such that,

$$\int\int_{S_k^C} \tau_k \, d^2\mathbf{r} = 1 \tag{6}$$

$$\int\int\int_{D_k^V} \psi_k \, d^3\mathbf{r} = 1 \tag{7}$$

where the surface integral in equation 6 is over the cross section S_k^C of the k^{th} constant current interval and the volume integral in equation 7 is over the domain of conductors D_k^V of the k^{th} constant voltage interval. Substituting equation 5 into 1 and applying the Method of Weighted Residuals [2],

$$\sum_{k=1}^{M_V} H_{lk} \, Q_k = V_l \qquad (l = 1,2.....M_V) \tag{8}$$

where

$$H_{lk} = \int\int\int_{D_l^V} W_l(\mathbf{r}) \int\int\int_{D_k^V} G_\phi (\mathbf{r} | \mathbf{r}') \, \psi(\mathbf{r}') \, d^3\mathbf{r}' \, d^3\mathbf{r} \tag{9}$$

and where V_l is the weighted mean potential in D_l^V given by,

$$V_l = \int\int\int_{D_l^V} W_l(\mathbf{r}) \; \phi(\mathbf{r}) \; d^3\mathbf{r} \tag{10}$$

and W_l ($l = 1,2...M_V$) are chosen weighting functions for which,

$$\int\int\int_{D_k^V} W_k(\mathbf{r}) \; d^3\mathbf{r} = 1 \tag{11}$$

Inverting equation 8,

$$Q_k = \sum_{l=1}^{M_V} C_{kl} \, V_l \qquad (k = 1,2.....M_V) \tag{12}$$

C is a capacitance matrix equal to the inverse of H.

Substituting equation 5 into the current continuity equation in the domain D_k^C of the conductors of the k^{th} constant current interval,

$$\nabla \cdot \mathbf{J} = -j\omega \, Q_k \, \psi_k \tag{13}$$

Applying the Divergence Theorem to the left hand side and substituting equations 7 and 12 into the right hand side of equation 13,

$$I_{2k} - I_{1k} = -j\omega \sum_{l=1}^{M_V} C_{kl} \, V_l \qquad (k = 1,2.....M_V) \tag{14}$$

Now, since tracks have electrically small cross-section, it is assumed that the longitudinal tangential component of $\mathbf{E}$ is approximately constant around the perimeter of the cross-section, and therefore that it is sufficient to enforce equation 3 in an average sense over this perimeter. Thus, taking the appropriate line integrals in the cross-sectional plane at distance a_k measured along the k^{th} constant current interval,

$$\frac{\oint_{p(a_k)} \mathbf{J} \, dp(a_k)}{\oint_{p(a_k)} \sigma \, dp(a_k)} + \nabla\phi(a_k) + j\omega \, \frac{\oint_{p(a_k)} \mathbf{A} \, dp(a_k)}{\oint_{p(a_k)} dp(a_k)} = 0 \tag{15}$$

where $p(a_k)$ is the path around the perimeter at a_k . and ϕ is assumed constant on $p(a_k)$. Now, substituting equations 2, 4 and 6 into 15 and integrating along the k^{th} constant current interval,

$$I_k \, Z_k + V_{2k} - V_{1k} + j\omega \sum_{l=1}^{M_C} L_{kl}^e \, I_l = 0 \quad (k = 1,2..M_C) \tag{16}$$

where V_{1k} and V_{2k} are the voltages at the ends of the interval,

$$Z_k = \int_k \frac{\oint_{p(a_k)} \tau_k(a_k) \, \mathbf{n}(a_k) \, dp(a_k)}{\oint_{p(a_k)} \sigma_k(a_k) \, dp(a_k)} \cdot da_k \tag{17}$$

and

$$L_{kl}^e = \int_k \frac{\oint_{p(a_k)} \int\int\int_{D_l'} G_A(\mathbf{r}_k | \mathbf{r}_l') \tau_l(\mathbf{r}_l') \mathbf{n}(\mathbf{r}_l') \, d^3\mathbf{r}_l' dp(a_k)}{\oint_{p(a_k)} dp(a_k)} . da_k \tag{18}$$

Z_k is the internal impedance (resistance plus internal reactance) of the k^{th} constant current interval, and L_{kl}^e is mutual inductance between sections k and l (or the external component of self inductance if $k = l$). Equations 14 and 16 are equivalent to Kirchoff's network equations and determine the lumped equivalent circuit topology. The solutions obtained for the component values depend on the choice of ψ_k , τ_k and W_k. For example, ψ_k and τ_k are chosen to exhibit the Maxwell distribution [8] in the transverse direction in tracks. The variation of τ_k in the thickness direction is frequency-dependent, due to skin-effect , and FACET approximates this dependence to that in an infinite metal

layer of the same composition and thickness as the track. Z_k are therefore also frequency-dependent. However, the frequency-dependence of r_k has negligible effect in equation 18, so both C_{kl} and L^e_{kl} are independent of frequency. This is very significant for CPU time.

FACET computes both the equivalent circuit topology and the lumped equivalent component values, and then creates a file in the format required for PHILPAC. This is automatically merged with a second file containing the information on the components to be soldered to the PCB. Node numbering is organised so that each terminal of such a component is connected to the node associated with its solder pad.

Application of FACET

Figure 4 illustrates the schematic circuit of the antenna filter whose PCB layout was shown in Figure 3. Three of the inductors were implemented using non-standard printed spirals. FACET, in effect, breaks all the connections in this schematic circuit, and replaces the ideal inductors and connections with the additional components generated. In Figure 5, the FACET simulation is compared with the ideal response of the schematic circuit and with the measured response. The filter input and output are respectively the transmitter output pin and the antenna pin as indicated in Figure 3. The corresponding nodes of the schematic circuit are shown in Figure 4. Both the measured width of the passband and general stopband level differ significantly from the ideal wanted behaviour indicated by the schematic circuit response. FACET predicts the non-ideal behaviour well.

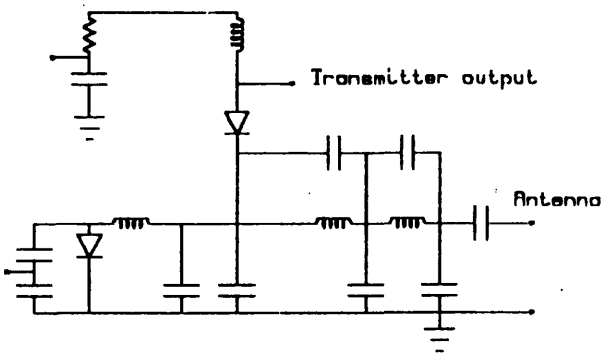

Fig. 4 Schematic circuit of filter

Summary

FACET, a new CAE package for electrical simulation of an analogue circuit on a PCB has been described. The effect of the layout on performance is included. FACET is interfaced to a layout CAD system for extraction of the geometry, and automatically interprets this geometry for the simulation. A lumped equivalent network model for the printed dielectric is derived, and this is merged automatically with the network of components soldered to the board. There is an automatic interface to a circuit analysis package. Complex layouts including non-parallel tracks and multi-layer boards can be simulated. The number of linear equations required for the method is much fewer than in commonly used numerical analysis techniques for 3D fields. The computing requirement is therefore modest for such a complex boundary value problem. The model is accurate throughout the frequency range applicable to civil mobile communications, but would not be valid at higher microwave frequencies where line widths are more comparable to wavelength. FACET can graphically display the power or stored energy distribution in the layout to help users diagnose causes of layout-related problems.

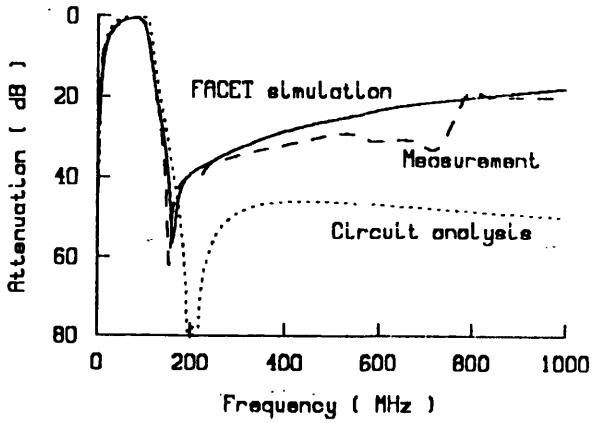

Fig. 5 Filter response

Acknowledgements

The authors would like to acknowledge the support of Philips Radio Communications Systems Ltd. and the contribution of Philips ISA-UK.

References

1. MacNamee,R.J.G., Vadgama,S.K. and Gibson,R.W., "Universal Mobile Telecommunication System - A Concept", Proc. Land Mobile Radio, Univ. of Warwick, IERE Publication No.78, 15-17 Dec. 1987.
2. Zienkiewicz,O.C. and Morgan,K., "Finite Elements and Approximation", Wiley, New York, 1983
3. Lean,M.H. and Wexler,A., "Accurate field computation with the Boundary Element Method", IEEE Trans. on Magnetics, MAG-18, pp.331-335, 1982.
4. Ruehli,A.E., "Survey of computer-aided electrical analysis of integrated circuit interconnections", IBM J.Res.Develop., 23, pp.626-639, 1979
5. Ruehli,A.E., "Equivalent circuit models for three-dimensional multiconductor systems", IEEE Trans. on Microwave Theory and Techniques, MTT-22, pp.216-221, 1974
6. Milsom,R.F. and Scott,K.J., "Radio frequency simulation of a complex printed circuit board layout by the quasi-static Boundary Element Method", Int.J.Numerical Modelling: Electronic Networks, Devices and Fields, Vol.1, pp.165-170, 1988
7. Chow,Y.L., "An approximate dynamic Green's function in three dimensions for finite length microstripline", IEEE Trans. on Microwave Theory and Techniques, MTT-28, pp.393-397, 1980
8. Kobayashi M., "Longitudinal and transverse current distributions on microstriplines and their closed form expression", IEEE Trans. on Microwave Theory and Techniques, MTT-33, pp.784-788, 1985